UNIVERSITY OF SOUTHAMPTON

FACULTY OF ENGINEERING AND THE ENVIRONMENT

School of Engineering Science

Thermal Stability and Current Transfer in Twisted-pair Helium Gas-cooled MgB_2 DC Cables

by

Jessica Spurrell

Thesis for the degree of Doctor of Engineering

August 26, 2017

UNIVERSITY OF SOUTHAMPTON

ABSTRACT

FACULTY OF ENGINEERING AND THE ENVIRONMENT

Institute of Cryogenics

Doctor of Engineering

Thermal Stability and Current Transfer in Twisted-pair Helium Gas-cooled MgB_2 DC Cables.

by Jessica Charlotte Spurrell

CERN's helium gas-cooled, twisted-pair superconducting cable design, typically consisting of intercalated superconducting and copper (stabilising) tapes, is a novel design which offers low cable inductance for high-current DC power transmission. The electrical and thermal contacts between the copper and superconducting tapes, which are given by wrapping the complete 'sandwich stack' of tapes together in Kapton, are important parameters for current sharing, cryogenic stability and quench propagation. Observation of both I_C and superconductor-stabiliser contact inhomogeneities due to the mechanical twisting process and the gas-cooling regime has shed light on overcoming the unique challenges these create in cable operation.

Both an MgB_2 twisted-pair cable assembly manufactured at CERN and a short-length single-sandwich strand made at the University of Southampton have been studied and a novel method for measuring contact resistance *in situ* has be designed and validated. Tests included measuring thermal runaway propagation velocity (v_p) and minimum quench energy (MQE) plus long-period stability tests for the cable, along with characterisation of current transfer as well as contact resistance measurements between the superconductor and stabiliser layers in the single-sandwich. The results suggest that an optimised cable operation strategy may exist, being a trade-off between: high stabilisation with lower superconductor-stabiliser contact resistance; and fast propagation resulting in easier quench detection with higher superconductor-stabiliser contact resistance. The results of the investigations are relevant to both the CERN LHC High Luminosity upgrade and future superconducting power transmission projects.

Academic Thesis: Declaration of Authorship

I, Jessica Spurrell, declare that this thesis, and the work presented in it, are my own and has been generated by me as the result of my own original research.

Thermal Stability and Current Transfer in CERN Twisted-pair Helium Gas-cooled MgB_2 DC Cables.

I confirm that:

1. This work was done wholly or mainly while in candidature for a research degree at this University;

2. Where any part of this thesis has previously been submitted for a degree or any other qualification at this University or any other institution, this has been clearly stated;

3. Where I have consulted the published work of others, this is always clearly attributed;

4. Where I have quoted from the work of others, the source is always given. With the exception of such quotations, this thesis is entirely my own work;

5. I have acknowledged all main sources of help;

6. Where the thesis is based on work done by myself jointly with others, I have made clear exactly what was done by others and what I have contributed myself;

7. Either none of this work has been published before submission, or parts of this work have been published as: [please list references below]:

Signed:

Date: August 26, 2017

Spurrell, J., et al. "Quench Property of Twisted-Pair MgB_2 Superconducting Cables in Helium Gas." IEEE Transactions on Applied Superconductivity 25.3 (2015): 1-5.

Contents

List of Figures

LIST OF FIGURES

List of Tables

Glossary

B_c Critical magnetic field or magnetic flux density: property of a superconducting component which is a function of component temperature and applied current; for Type I superconductors, in a magnetic field below this value the component will be superconducting and above this value it will be in the normal or resistive state; for Type II superconductors two critical values H_{c1} and H_{c2} exist between which the magnetic field is able to penetrate the superconductor (breakdown of the Meissner effect) but a superconducting current is still able to flow. 3, 4, 6, 9, 12, 13, 56

H_c Critical magnetic field strength: property of a superconducting component which is a function of component temperature and applied current; for Type I superconductors, in a magnetic field of strength below this value the component will be superconducting and above this value it will be in the normal or resistive state; for Type II superconductors two critical values H_{c1} and H_{c2} exist between which the magnetic field is able to penetrate the superconductor (breakdown of the Meissner effect) but a superconducting current is still able to flow. 4, 9

I_c Critical current: property of a superconducting component which is a function of component temperature and applied magnetic field; if a current less than this is applied and flows through the component it will do so in the superconducting state; if a current equal to or greater than this is applied and flows through the component then it will begin the transition from the superconducting to the normal or resistive state. 3, 6, 12, 13, 31, 34, 49, 56, 63, 69, 94, 102, 103, 123, 128, 141, 156, 175, 176, 199, 202, 205, 206

I_{quench} Quench current: value of current which, when applied to a superconducting component, instigates a quench or thermal runaway event; characterised by non-

linear increase in both voltages measured across the component and local component temperature. 102, 124, 126, 128, 146, 156, 163, 175–177, 199, 205

J_c Critical current density: critical current (I_c) divided by cross-sectional area; cross-sectional area is usually that of the whole superconducting component i.e. including both the superconducting material and the normal metal matrix - if cooling infrastructure and component housing are also included, it is generally referred to as J_e; property of a superconducting component which is a function of component temperature and applied magnetic field; if a current density less than this is applied and flows through the component it will do so in the superconducting state; if a current density equal to or greater than this is applied and flows through the component then it will begin the transition from the superconducting to the normal or resistive state. 3

J_e Engineering critical current density: critical current (I_c) divided by cross-sectional area; cross-sectional area is usually that of the whole superconducting component i.e. including both the superconducting material and the normal metal matrix plus that of the cooling infrastructure and component housing i.e. the working critical current density; see also J_c. 3, 65

R_C Contact resistance: electrical resistance between two electrical conductors in contact; function of contact surface area; measured in Ωcm^2. 96, 97, 101–105, 109, 110, 112, 113, 119–121, 125, 126, 134, 136, 141, 146, 151, 156, 171, 175–177, 194, 197, 198, 200, 201, 211

T_c Critical temperature: property of a superconducting component; below this temperature the component will be superconducting; above this temperature it will be in the normal or resistive state. 3, 6, 10, 12, 45, 56, 79, 102–105, 130, 134, 141, 151

2 m preliminary cable test Tests carried out on the 2 m MgB_2-Cu CERN cable in the 5 m Nexans semi-flexible cryostat at the University of Southampton. The cable was that initially used in [1]. 39, 40, 56, 58, 74, 94

AC Alternating Current. 30, 203

AMSC American Superconductor
`http://www.amsc.com/`. 17

BCS Bardeen-Cooper-Schrieffer Theory: first complete microscopic theory of low temperature superconductivity devised in 1957; predicts the breakdown of the superconducting state at temperatures greater than 30-40 K and does not describe the mechanisms of high temperature superconductivity. 10

Belleville washer Frusto-conical shaped washer which deflects a known amount under a given force; also known as a Belleville spring, coned-disc spring, conical spring washer, cupped spring washer or disc spring. 87, 88, 101, 125

BL Bolts Loosened. 101, 125, 126, 136, 141, 146, 151, 156, 163, 167, 171, 175–177, 194, 197–199

BSCCO Bismuth Strontium Calcium Copper Oxide. 19, 20

BT Bolts Tightened. 101, 102, 125, 126, 130, 136, 141, 146, 151, 156, 163, 167, 171, 175–177, 194, 197–199

Bus-bar Electrical links in which cable assemblies feeding multiple circuits are routed together to form a single current transport system to a common connection. 22, 26, 30

Cable *General context*: Electrical connector including conductor(s), electrical and thermal insulation e.g. dielectric, coolant (if necessary) and cable housing. *Specifically in the context of this project*: See entry for strand twisted-pair. May also be referred to as a 'sub-cable'. 17, 20–26, 28, 30, 31, 33–36, 39, 40, 42, 45, 48–50, 53, 56–58, 63, 71, 74, 75, 77, 81, 94, 124, 175, 202–206

Cable assembly Link or bus-bar consisting multiple cables or sub-cables. 3, 28, 30, 31, 40, 49, 52, 53, 63, 199

CDA Copper Development Association. 105

CERN Formerly Conseil Européen pour la Recherche Nucléaire, now European Organisation for Nuclear Research. 15, 20, 22, 25, 26, 28, 30, 31, 33, 35, 36, 39, 40, 50, 56–58, 71, 74, 77, 81, 86, 95, 202, 203, 205

Cernox Thin film resistance temperature sensor with high sensitivity at cryogenic temperatures. 50, 83, 99

Constantan A copper-nickel alloy, often used with copper to make Type T thermocouples (TCs). 99, 100, 200

Cryostat A device or vessel in which a very low temperature can be maintained. 12, 13, 22, 26, 27, 39, 40, 42–46, 48–50, 56–58, 75, 81, 96, 100

CTL Current Transfer Length. 79, 94, 95, 136, 151

Cu Copper. 28, 36, 39, 50, 61, 63, 71, 74, 75, 89, 92, 94–97, 99–101, 104, 105, 107, 109, 110, 112, 113, 115, 118–120, 123, 126, 130, 132–136, 141, 146, 151, 156, 175, 176, 207

DC Direct Current. 30, 63, 203

Dewar Vacuum-insulated vessel used in this context to contain cryogenic liquids. Named after inventor, Sir James Dewar. 46

FCL Fault Current Limiter. 15, 25

FSU-CAPS Florida State University Center for Advanced Power Systems. 22

G-10 Grade of glass-reinforced epoxy laminate electrically insulating material. 83, 86

GE varnish Insulating varnish often used to insulate or thermally anchor electrical wires to solid surfaces in cryogenic applications due to its good electrical and chemical resistance and good resistance to thermal cycling. See [2–4]. 58, 83, 97, 100

H-Phase Heated current sharing phase; used to describe current sharing between a superconducting tape and a normal metal tape when a tape heater in the centre of the tape is used to force a temperature gradient so that the centre of the tape is at a higher temperature (and therefore quenches at a lower current) than the ends of the tape; the majority of current transfers from the superconducting tape to and from the normal metal tape close to the centre (around the heated point), causing the zero-point to be in or around the tape centre. 115, 135, 177

High Temperature Superconductor(s) (HTS) Superconducting materials that become superconducting at 'high' temperatures, generally considered to be those achievable with liquid nitrogen i.e. the critical temperature of the conductor is above the freezing point of nitrogen, 63 K (and usually above the boiling point of nitrogen, 77 K); however, may also be considered to refer to materials with a critical temperature above approximately 35 K at which point the BCS theory predicts that superconductivity should not be possible. 10, 11, 14, 15, 17, 20–23, 25, 26, 28, 30, 45, 48, 50, 65, 81, 83

HiLumi CERN LHC High Luminosity Upgrade Design Study. `http://hilumilhc.web.cern.ch/about/fp7-hilumi-lhc`. 27, 28, 31, 35, 39, 71, 203

HL-LHC High Luminosity Large Hadron Collider (LHC). 20, 22, 26–28, 30, 31, 35, 48, 71, 203, 205

ID Inner Diameter. 43

Kapton Electrically insulating polyimide film with good thermal conductivity for a non-metallic solid at cryogenic temperatures. 34, 35, 52, 56, 58, 61, 75, 86, 92, 97, 198, 203

Knot Fixed point in a spline curve approximation or points between which the curve generated can be described using separate, independent functions. 110, 112, 113, 115, 117, 120, 134

L-Phase Left-hand current sharing phase; used to describe current sharing between a superconducting tape and a normal metal tape when the majority of current transfers from the superconducting tape to the normal metal tape on the Left-hand side (LHS) causing the zero-point to be left of the tape centre. 115, 130, 132, 133, 151, 156, 163, 167, 175

LHC Large Hadron Collider. 15, 20, 22, 25–27, 35, 36, 39, 40, 43, 45, 50, 71, 203

LHS Left-hand side. 96, 99, 109, 132, 136, 141, 146, 151, 156, 175, 197, 198

Link Cables or cable assemblies connecting two or more components electrically. 22, 26–28, 30, 35, 39, 50, 71, 205

LIPA Long Island Power Authority. 23

LNG Liquid Natural Gas. 24

Low Temperature Superconductor(s) (LTS) Superconducting materials that become superconducting at 'low' temperatures, generally considered to be those unachievable with liquid nitrogen i.e. the critical temperature of the conductor is below the boiling point of nitrogen, 77 K (and usually below the freezing point of nitrogen, 63 K); however, may also be considered to refer to materials with a critical temperature below approximately 35 K at which point the BCS theory predicts that superconductivity should not be possible. 10, 11, 14, 20, 22, 26, 65

MATLAB® High-level language and interactive environment for numerical computation, visualization, and programming.
`http://www.mathworks.co.uk/products/matlab/`. 110, 112, 113, 201, 207

MQE Minimum Quench Energy. 63–65, 67, 71, 74, 203, 204

MRE Maximum Recovery Energy. 63, 64

MRI Magnetic Resonance Imaging. 15

MSS Arc skew sextupole magnets [5]. 27

Nexans Manufacturer of cables and cabling solutions.
`http://www.nexans.com`. 39, 40, 50

NMR Nuclear Magnetic Resonance. 15

Normal metal matrix Part of a superconducting material which is made from a non-superconducting or 'normal' metal such as copper, nickel or silver; usually takes the form of an outer structure containing superconducting filaments or a substrate as part of several layers of materials; enhances both structural and thermal stability. 14, 19, 30

OD Outer Diameter. 43

PID Proportional-Integral-Derivative. 48, 83

Platform Removable cryostat-sample interface and sample holder that allows for ease in connection and changing of samples; provides both thermal link to cryocooler and electrical link to current leads (see section 4.2.2). 81, 83, 86, 89, 92, 94, 97, 99–101

PPMS Physical Property Measurement System. 105

PTFE Polytetrafluoroethylene. 52, 92

Quench Term commonly used to describe the process which occurs when part of a superconductor or superconducting component undergoes a transition from the superconducting to the normal or resistive state with exponential voltage increase and tape heating or thermal runaway; may cause irrecoverable system damage; see, for example, p. 200 [6]. 11, 14, 15, 28, 56–58, 63, 67, 69, 71, 74, 102, 117, 126, 130, 175, 199, 200, 203–206

R-Phase Right-hand current sharing phase; used to describe current sharing between a superconducting tape and a normal metal tape when the majority of current transfers from the superconducting tape to the normal metal tape on the Right-hand side (RHS) causing the zero-point to be right of the tape centre. 115, 130, 132, 133, 167, 175, 176

RHS Right-hand side. 96, 109, 121, 133, 136, 141, 146, 151, 156, 171, 175, 197, 198

RRR Residual Resistance Ratio: Usually defined as the ratio of the resistivity of a material at room temperature ($\rho(300K)$) to that at 0 K ($\rho(0K)$); however for the CDA cryogenic properties of copper data as shown in figure 4.18, RRR is defined by the following ratio: $\frac{\rho(273K)}{\rho(4K)}$. 105

Sandwich Alternating layers of superconductor and stabiliser tapes; a 'single-sandwich' is comprised of three tapes in a stabiliser-superconductor-stabiliser formation and

a sandwich stack refers to a formation of alternating stabiliser and superconductor tapes with more than one superconductor layer. 30, 36, 39, 71, 75, 83, 86, 94–97, 101, 123, 124, 202, 204

Sandwich stack Alternating layers of superconductor and stabiliser tapes; in the context of this project, the structure of three layers of MgB_2 and four layers of copper held together by being wrapped in layers of Kapton tape is generally assumed unless stated otherwise. 30, 31, 33–36, 56, 77, 86, 199

SC Superconductor. Here, unless otherwise stated, refers to MgB_2. 89, 92, 94–97, 99–101, 104, 107, 109, 110, 112, 115, 117, 118, 120, 123, 130, 132–135, 141, 151, 156, 175, 176, 205, 207

SHETL Scotish Hydro-Electric Transmission Ltd. 23

SLM Shape Language Modelling: method of producing functions from datasets which allows for extensive control of the curve shape. `http://uk.mathworks.com/matlabcentral/fileexchange/24443-slm-shape-language-modeling`. 110, 112, 120, 201, 207, 210, 211

SMES Superconducting Magnetic Energy Storage. 15, 25

Spline The Oxford Dictionary definition of a mathematical spline is, "a continuous curve constructed so as to pass through a given set of points and have a certain number of continuous derivatives". 110, 112, 120

SS Stainless Steel. 31, 52, 87

SS-Phase Settled Sharing current sharing phase; used to describe current sharing between a superconducting tape and a normal metal tape when the majority of current transfers from the superconducting tape to the normal metal tape on the LHS, remains in the normal metal tape for the majority of the length of the tape, then returns to the superconducting tape on the RHS, with the zero-point being in or around the tape centre. 115, 130, 132, 134–136, 141, 146

SSE Scottish and Southern Energy plc. 23

Strand Single length of conductor; in this context a 'conductor' is comprised of a sandwich stack of layers of superconductor and stabiliser tapes; two strands twisted together form a twisted-pair or cable. 30, 31, 34–36, 39, 40, 49, 50, 52, 53, 56, 58, 61, 63, 69, 71, 74, 75, 86, 95, 124, 202–204, 206

TC Thermocouple (in this instance Type T, copper-constantan). 69, 83, 97, 99–101, 105, 200, 201

Thermal runaway Positive feedback heating loop resulting from quench. 11, 14, 15, 28, 56, 71, 94, 96, 102, 123, 146, 177, 200

Twisted-pair Two strands (or, occasionally, referring to instrumentation wires), electrically insulated from each other but in thermal contact, twisted together to reduce inductive voltages. 31, 33–35, 39, 40, 50, 52, 53, 58, 71, 203, 206

US-Phase Unsettled Sharing current sharing phase; used to describe current sharing between a superconducting tape and a normal metal tape when the current transfers to and from the superconducting tape and the normal metal tape multiple times over the tape length, causing three zero-points to be observed. 115, 133, 134, 141, 156, 163, 176

V-tap Voltage-tap; wire(s) attached to components/samples to measure the voltage difference across them. xii, 50, 56, 58, 61, 65, 69, 71–74, 77, 95, 97, 99–101, 105, 107, 109, 112, 176

WPD Western Power Distribution. 23

YBCO Yttrium Barium Copper Oxide. 10, 19, 20

Zero-point Position along the length of the sandwich sample at which no current is transferring between the superconducting and normal metal tapes; also position at which current transfer direction is changing and the cumulative voltage in the superconducting tape is equal to that in the normal metal tape or the voltage difference between the two tapes is equal to zero. 130, 132, 133, 146, 151, 176, 177

Acknowledgements

I would like to thank my supervisors Professor Yifeng Yang and Doctor Edward Young, and all at the University of Southampton Institute of Cryogenics and the Research Institute for Industry Cryogenics team, namely Professor Carlo Beduz, Doctor Iole Falorio, Doctor Jorge Pelegrín-Mosquera, Doctor Maurizio Paollela, Doctor Wendell Bailey, Mike Webb, Ian Mears, Thom Bostock, Rob Loades and Qingbo Zhang, without whom this work would not have been possible.

I would also like to thank Jon Trembley, from Air Products, for his continued mentoring and support; and Terry Webster and Dave Williams from the University of Southampton Engineering Design and Manufacturing Centre who taught me not only how to make things but how to make things work.

To Doctor Emily Matthews, it is no exaggeration to say that your friendship and encouragement made this journey possible.

And to all my family and all my adoptive families, the Spurrells, the Bensteads, the Daveys and the Wilsons, thank you for everything - you are cooler than liquid helium and carry more energy, enthusiasm and kindness than any cable, superconducting or otherwise.

1

Introduction

1.1 Introduction to Superconductivity

1.1.1 Discovery and Superconducting Properties

In 1908 at the University of Leiden in The Netherlands, Professor of Experimental Physics Heike Kamerlingh Onnes and team liquefied helium gas in his purpose-built, renowned cryogenics laboratory [7]. This was the first time that helium had been liquefied; and helium, having at 4.2 K (-268.8 °C) the lowest boiling point of the gases naturally occurring in the atmosphere, was considered the last gas to be liquefied. The advances that Onnes' experiments enabled in the understanding of thermodynamics were paramount and for this he was awarded the Nobel Prize for Physics in 1913 [8].

As well as thermodynamics, the ability to reach such low temperatures allowed scientists to further investigate their understanding of the electrical properties of materials. The relation between temperature and electrical resistance of metals was of particular interest at the time and it was during his investigations into this property of mercury that Onnes made another, very important discovery.

As can be seen in figure 1.1, as a sample of mercury measured by Onnes was cooled, its resistance decreased. Initially the decrease was linear; however, around the boiling temperature of helium, 4.2 K, within a temperature change of 0.01 K the resistance decreased dramatically and by several orders of magnitude from around 1×10^{-1} Ω to what is marked in figure 1.1 as 1×10^{-5} Ω, before disappearing entirely. Figure 1.1 comes from the repeat of the original experiment, some 6 months before, in which it was observed that between 4.3 K and 4.2 K the resistance decreased by a factor of almost

400; then at 4.13 K and below, no resistance at all was measured using equipment capable of around 30 nV resolution (by Ohm's Law, resistance, R, is equal to voltage, V, divided by current, I, see equation 1.1) [9].

$$R = \frac{V}{I} \tag{1.1}$$

Figure 1.1 therefore shows the first recorded example of the transition of mercury from the resistive state to the non-resistive state or from being a standard electrical conductor to a perfect electrical conductor exhibiting a flow of electrical current without resistance: a superconductor [10]. Initially described by Onnes in his notes as 'supraconductivity', the phenomenon came to be known as *superconductivity*. Onnes went on to observe superconductivity in other elemental metals such as tin and lead which made the transition at 3.7 K and 7.2 K respectively [11].

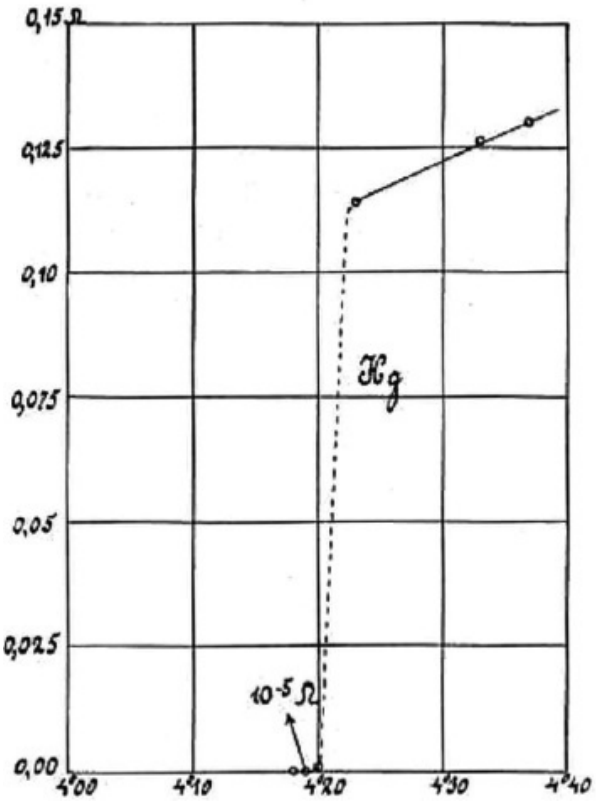

Figure 1.1: Historic graph from [10] showing the resistance of the mercury sample tested by Onnes as a function of temperature, including the first documented transition to a superconducting (zero-resistance) state [12].

The temperature at which the transition to the superconducting state occurs is known as the *critical temperature* or T_c. This temperature is a material property and is one of the three defining characteristics of a superconductor, the others being *critical magnetic field*, B_c, and *critical current*, I_c. If a temperature, magnetic field and current below the critical values is applied then the material will be superconducting; above these values and it will be resistive. The transition between the superconducting and resistive states due to a change in temperature above or below T_c is direct and instantaneous. The nature of the transition due to a change in magnetic field above or below B_c is dependent on whether or not the material is a Type I or Type II superconductor as described in the following section. The transition due to a change in applied current above or below I_c is not instantaneous and the subject of much in-depth study.

These three critical properties are interdependent and as such form a critical surface defining the conditions under which the superconducting state can be achieved for a given material. An example of a typical critical surface is shown in figure 1.2a while the critical surface of the first commercially available superconducting compound, NbTi, developed by Westinghouse Research Laboratories in 1962 [13], is plotted with that of the later developed Nb_3Sn in figure 1.2b. Note that the critical properties can be written in alternative forms, as in figure 1.2. Instead of I_c, critical current density, J_c can be used. Equation 1.2 shows the general relationship between current (I) and current density (J) where A is cross-sectional area of the conductor:

$$J = \frac{I}{A}. \tag{1.2}$$

J_c is found by using I_c in equation 1.2. In a superconductor, the cross-sectional area, A, could be:

- The cross-sectional area of the superconducting material only (rarely used),
- The cross-sectional area of the superconducting material plus the rest of the superconducting component e.g the normal metal matrix - as described in section 1.2.2 (most common definition of J_c), or,
- The cross-sectional area of the cable assembly including cooling infrastructure, most commonly referred to as 'engineering critical current density' or J_e.

Likewise, instead of critical magnetic flux density B_c measured in Tesla, the property critical magnetic field strength H_c measured in Am^{-1} is often referred to.

The superconducting state is defined, however, by *two* characteristics:

- **Perfect electrical conductivity** — or zero electrical resistance as first observed by Onnes in 1911 [10], as discussed above, and,
- **The Meissner effect** — or the complete expulsion of a magnetic field, as observed by Walther Meissner and Robert Oschenfeld in 1933 [16].

Meissner and Oschenfeld observed the latter characteristic while investigating the effects of magnetism on materials in the zero-resistance or superconducting state. In particular, they were interested in the effect of diamagnetism.

It is known from the Maxwell-Faraday equation that a magnetic field changing with time is always accompanied by an electric field changing in space; the addition by Lenz of the minus sign ensures that the conservation of energy or Newton's Third Law is obeyed and gives us the Maxwell-Faraday-Lenz equation, equation 1.3, where $\mathbf{E}$ is the electric field vector, $\mathbf{B}$ is the magnetic field vector and t is time.

$$\nabla \times \mathbf{E} = -\frac{\partial \mathbf{B}}{\partial t} \tag{1.3}$$

If applied to an electrical conductor, the electric field caused by the changing magnetic field will cause electrons to flow by way of the Lorentz Force (equation 1.4) and electric currents will be induced, known as eddy currents. The induced current will in turn create a magnetic field which, thanks to the addition by Lenz, will oppose the original magnetic field. In equation 1.4, $\mathbf{F}$ is the Lorentz Force vector which causes a charged particle (in this case and electron) to move, q is the charge on the particle and $\mathbf{v}$ is the velocity vector of the particle.

$$\mathbf{F} = q[\mathbf{E} + (\mathbf{v} \times \mathbf{B})] \tag{1.4}$$

In materials with a high magnetic permeability, or ferromagnetic materials such as iron, nickel and cobalt, the induced current is significant; indeed, this is the principle of an electric generator. All materials, however, respond in some way to an applied,

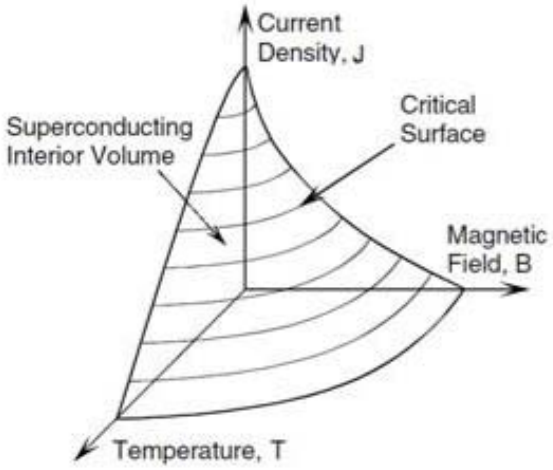

(a) Typical critical surface for a Type II superconductor. [14]

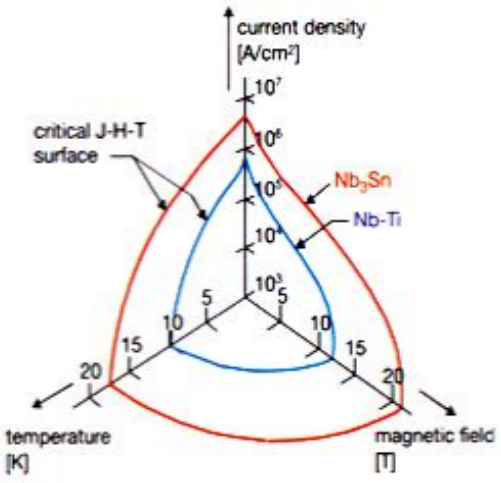

(b) Critical surfaces for niobium-tin (Nb_3Sn) and niobium-titanium (NbTi) superconductors, the latter being the first commercially available superconducting compound (both Type II). [15]

Figure 1.2: Examples of superconducting critical surfaces (3D plots showing interdependence of critical values).

changing magnetic field either by attraction (paramagnetism) or repulsion (diamagnetism), as demonstrated by Faraday in 1845. This response is generally very small and, often, negligible compared to the ferromagnetic response where this is present.

The effects of diamagnetism can, however, be seen and felt with a strong enough magnetic field. Figure 1.3 shows a ball of water and a live, un-harmed frog diamgentically levitating in a magnetic field of about 16 T at the Nijmegen High Field Magnet Laboratory. With such a high magnetic field, the vertical component of the diamagnetic effect on the frog and the water is enough to counter the effect of gravity on them, causing them to levitate [17].

In a perfect electrical conductor, such as a superconductor, one would expect that sufficiently large eddy currents could be generated by a moving magnetic field, that the magnetic field that such currents induce would be enough to completely counteract the original magnetic field. In other words, a superconductor is often described as a *perfect diamagnet*. However, what Meissner and Oschenfeld observed was not only perfect diamagnetism in the presence of a changing magnetic field but the complete expulsion of a magnetic field, whether changing or constant, even if the field were applied before the transition to the superconducting state had occurred. This effect is known as the Meissner effect [16]. Figure 1.4a shows a magnet resting on a superconducting pellet at room temperature. Figure 1.4b shows the effect of cooling the pellet below its critical temperature with liquid nitrogen: the magnetic field of the stationary magnet, which could penetrate the pellet whilst it was in the normal or resistive state, is expelled from the pellet once it becomes superconducting; its effects are counteracted, causing the magnet to levitate.

In summary, a material is considered to be a superconductor if can be shown to exhibit both the effects of perfect electrical conductivity (or zero-resistance) and not only perfect diamagnetism but also the complete expulsion of a magnetic field (or the Meissner effect) within the conditions bound by its critical properties, T_c, I_c and B_c. As well as the materials mentioned here, namely mercury, tin, lead, NbTi and Nb_3Sn, many others have been shown to exhibit superconductivity in this way. Those materials relevant to this project are discussed in more detail in section 1.2.2.

(a) Diamagnetic levitation of a ball of water.

(b) Diamagnetic levitation of a live, un-harmed frog.

Figure 1.3: Examples of diamagnetic levitation in a 16 T magnetic field at the Nijmegen High Field Magnet Laboratory, Radboud University, The Netherlands [17].

(a) Disc magnet resting on a superconducting pellet in the resistive state.

(b) Disc magnet levitating above a superconducting pellet in the superconducting state, levitating due to the complete expulsion of the magnetic field, known as the Meissner effect.

Figure 1.4: Meissner effect demonstration, before and after the transition to the superconducting state by cooling with liquid nitrogen; demonstration designed and built at the University of Southampton.

1.1.2 Superconducting Theory and Application

1.1.2.1 From London to Gorkov

It took many years after the discovery of the phenomenon of superconductivity to theorise the mechanisms driving it. In 1935 brothers London and London were able to show that the Meissner effect was dependent on the presence of a superconducting current [18]. In 1950 Landau and his student Ginzburg described the macroscopic properties of superconductivity in terms of phase transitions in what became known as the Ginzburg-Landau theory. This theory accurately predicted the presence of Type I and Type II superconductors. In the same year Maxwell and Reynolds made important progress that pointed towards the electron-phonon interaction mechanism [19] [20].

The difference between Type I and Type II superconductors comes from the way in which they make the transition to the normal state when exposed to a magnetic field greater than or equal to B_c. In a Type I superconductor this transition is immediate and both the Meissner effect and the perfect conductivity immediately break down. Type I superconductors are all elemental metals and since they possess relatively low B_c values they were not greatly developed.

Type II superconductors possess not one critical magnetic field value but two: B_{c1} and B_{c2}, often referred to in terms of critical magnetic field strengths, H_{c1} and H_{c2}. If exposed to a magnetic field of strength equal to or greater than H_{c1} but less than H_{c2}, the Meissner effect will break down in the Type II superconductor; however, a superconducting current will still be able to flow. Between H_{c1} and H_{c2} the superconductor is in a mixed state also known as the 'vortex state' in which regions of normal or resistive material are surrounded by vortices of superconducting current as demonstrated in figure 1.5. This allows penetration of the magnetic field without loss of the superconducting current as is experienced in Type I conductors since the magnetic field is still excluded from the superconducting regions. As figure 1.5 shows the resistive regions are evenly spaced throughout the material. As H_{c2} is approached the resistive cores grow and so become more closely packed together; however, as long as the vortices are stationary a superconducting or zero-resistance current can still flow. Note that, given the interdependence of the critical properties of a superconductor, H_{c2} can be approached not only by increasing the applied magnetic field strength but also by increasing the applied current or temperature. At H_{c2} the force of the superconducting

current is such that it can cause the vortices to move and the superconducting state is lost. At this point the material has made the transition to the resistive state and exhibits neither the Meissner effect nor perfect electrical conductivity.

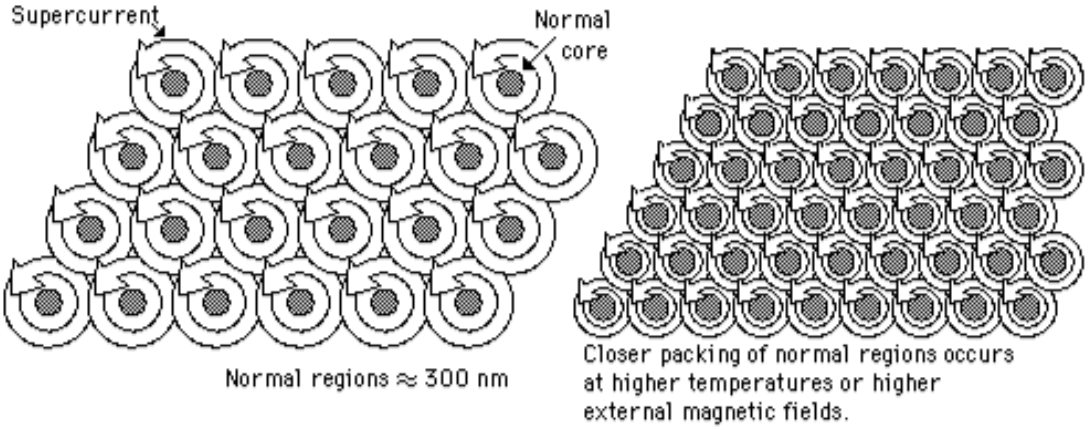

Figure 1.5: Superconducting current vortices surrounding normal or resistive regions in a Type II superconductor in the mixed or vortex state [21].

In 1957, some 46 years after superconductivity was discovered, Bardeen, Cooper and Schrieffer described the microscopic theory of superconductivity known as BCS theory, involving Cooper pairs and electron-phonon interaction [22]. In 1959 Gorkov showed that BCS theory reduced to the Ginzburg-Landau theory close to the critical temperature; in fact the Ginzburg-Landau theory can be derived from BCS theory [23].

BCS theory does not account for superconductivity above approximately 30-40 K, which was first observed by Bednorz and Müller in 1986 in a group of materials known as the cuprates [24]. For this reason superconducting materials with a T_c above this temperature region are often referred to as 'High Temperature Superconductors' or HTS and those with a T_c below this as 'Low Temperature Superconductors' or LTS.

For the first 75 years of superconductor technology, all discovered superconductors had to be cooled with either complex and costly liquid helium systems (the most common), liquid hydrogen (boiling point -253 °C or 20 K) systems which were rarer due to safety issues or, by the late 1970s, cryocoolers. In 1987 however, Wu and a team at the University of Alabama in collaboration with Chu and a team at the University of Houston observed superconductivity in Yttrium Barium Copper Oxide (YBCO) at 93

K. This was the first superconducting material that could be cooled with liquid nitrogen (boiling point -196 °C or 77 K) [25]. Liquid nitrogen is much cheaper to produce than liquid helium given its availability, the primary source being the air, and its higher boiling temperature. Once used the nitrogen gas boil-off can return to the atmosphere so the only limits to the supply of liquid nitrogen are the energy required to liquefy it, unlike liquid helium for which there is only a finite and diminishing source of gaseous helium available to liquefy [26]. Furthermore, nitrogen, unlike hydrogen, is completely inert and therefore the safety systems it requires are much less complex. For this reason it is also common to distinguish between HTS and LTS materials as those with critical temperatures above and below the boiling point of nitrogen, 77 K.

1.1.2.2 Quench and Thermal Runaway

The behaviour of the material near its critical regions and the nature of its transition between the superconducting and the resistive states, in particular the phenomena known as 'quench' and 'thermal runaway', are also important when differentiating between LTS and HTS, as well as leading to important design considerations for all superconducting applications.

Working at such low temperatures and with such high current densities, the main problem that any superconducting system is likely to face is that of a disturbance to the system resulting in thermal instability and, hence, a positive feedback heating loop which may result in irrecoverable damage to the system. This heating scenario is referred to as *thermal runaway* and it is caused by a *quench*.

The thermal stability of a superconducting component or system is dependent on the system cooling and any Joule or electrical resistance heating that may occur. When an electrical current flows through a conductor of finite electrical resistance, said resistance causes the dissipation of energy as heat, given by equation 1.5, where P is Joule or resistance heating power, I is current and V is voltage.

$$P = IV \tag{1.5}$$

Combining with Ohm's law, equation 1.1, the relation between heating power and electrical resistance is:

$$P = I^2R = \frac{V^2}{R}. \tag{1.6}$$

Under normal working conditions, a superconducting component is cooled to and maintained at a temperature below its T_c and it is working within its other critical values, I_c and B_c, so that the electrical resistance and, therefore, the Joule heating of the component is zero. The sources of heat in the system in this situation would therefore be:

- Resistive joints between components if there is more than one superconducting component in the system,
- Resistive joints between the component(s) and the current source,
- Radiation from outside the cryostat or other component housing.

Counteracting the heating effects of the above on the component should all be within the capacity of the cooling system. Therefore, under normal working conditions no temperature change within the component should occur.

However, as discussed in the previous section, superconductivity is a microscopic phenomenon and, as such, subtle differences in behaviour or critical properties may occur within any given section of superconducting material. Furthermore, temperature, upon which superconductivity is supremely dependent, is almost impossible to accurately control on such a small scale for much larger components or systems (see section 1.2.3).

It is possible, therefore, for some disturbance or local or global change in the temperature, magnetic field or applied current experienced by a superconducting component, to force all or part of it to be in a state outside of its critical range i.e. above the critical surfaces described in figure 1.2. Examples of such disturbances include:

- **Temperature increase** — caused by, for example:
  - A loss of or change in flow of a cooling fluid (*global*),
  - A failure of system insulation (*global*),
  - A disturbance in the flow of a cooling fluid (*local*),
  - A breakage or fault in the insulation causing a part of the component to be more susceptible to heating from the external environment (*local*),

  - A joint between components or between a component and the current supply which is or becomes more resistive than the other joint(s) and therefore heats at a greater rate under what would otherwise be normal working conditions e.g. due to bad soldering (*local*),
  - A section of the component(s) where the I_c or B_c is lower than the rest of the component(s) so that it becomes resistive and therefore heat-generating under what would otherwise be normal working conditions (*local*);

- **Current increase** — caused by, for example:
  - A current supply disturbance, fault or input error (*global*),
  - Current diverting from one component to another due to a local increase in temperature or a lower local I_c or B_c (*local*);

- **Magnetic field or field strength increase** — caused by, for example, a surge or fault in a magnet or magnetic component in the vicinity of the superconducting component (which could include the component itself) (*global or local*);

- **A mechanical disturbance to the system** — caused by, for example, an impact by an external body on the cryostat or component housing, which could cause, directly or indirectly, any of the above.

As described in [6], these disturbances can be classified in one of four categories within a 'disturbance spectrum' encompassing the spacial and temporal domains. These are described in table 1.1 which also gives the standard units of measurement of such disturbances.

[Units of measurement]		**Space**	
		Point	Distributed
Time	Transient	J	$J\ m^{-3}$
	Continuous	W	$W\ m^{-3}$

Table 1.1: The 'disturbance spectrum' as described in [6]. Disturbances are categorised as either discrete (point, transient) or continuous (distributed, continuous) in space and time. Suggested units of measurement of each disturbance category are given.

Should a disturbance such as those described above occur, some or all of the current flowing will no longer be superconducting but resistive and, as such, some Joule

or resistive heating will occur. As many superconducting materials are poor electrical conductors when not in the superconducting state, this resistive current will often be carried by the normal metal matrix or stabilising component of the superconductor design (see section 1.2.2). The resistivity of the normal metal and the current transfer resistance between the superconducting and normal metal components become important factors in understanding and predicting system behaviour at this point.

If the disturbance is transient and a combination of the system cooling and current sharing with the normal metal are sufficient, the system may recover and return to normal working conditions. However, if this is not the case, the area around the disturbance will continue to exhibit Joule or resistive heating which will spread to neighbouring areas. As the temperature rises in these areas, even if no other disturbance or change of conditions occurs, they too will be forced into the resistive state and further heating will therefore occur. Heat will continue to spread throughout the system causing more and more of it to become resistive and thus a positive feedback heating loop is set up, known as a *thermal runaway* event as the system temperature increases exponentially. Exponential increases in voltage are indicative of this occurring and this self-perpetuating transition to the resistive state with such characteristic signatures is known as *quench*.

Usually, whether due to the local nature of the disturbance or some local inhomogeneity in component critical values, the initial resistive zone which initiates a quench will be small compared to overall component or system size; and the spreading of the heat and, hence, transition to the resistive state will propagate from this initial zone throughout the component. By recording voltage and temperature in a component undergoing a quench, it is possible to measure the propagation velocity of the resistive zone. Factors such as superconducting and stabilising normal metal materials, component design, cooling and contact resistance between superconducting and stabilising components all have an effect on resistive zone propagation and, hence, quench behaviour. The effects are complex but, in terms of materials at least, this can be characteristic; as a general rule, the lower the critical temperature of the superconducting material, the sharper the transition to the resistive state or the steeper the increase in measured component voltage and temperature with applied current, magnetic field or system temperature, or for fixed conditions over time. Thus LTS can also be classified by a sharp quench or thermal runaway and HTS by a slower or smoother transition.

The majority of superconducting applications are designed to work well below their critical conditions so as to avoid quench and thermal runaway. However, the consequences are so drastic (often resulting in irreversible system damage) that the addition of stabilising materials as well as quench detection mechanisms are a vital part of superconducting application design (see, for example, section 1.3.3.1).

1.1.2.3 Transporting People and Power

Although the most common application of superconductors is in the form of very strong magnets such as those used in Magnetic Resonance Imaging (MRI) scanning machines, Nuclear Magnetic Resonance (NMR) spectroscopy and particle accelerators such as the CERN LHC, the ability to cool superconductors with cryogens other than liquid helium has opened the door to many more applications. Such applications already in development include Fault Current Limiters(FCLs), energy storage in the form of very large magnets such as Superconducting Magnetic Energy Storage (SMES) and flywheels, transformers, and generators such as for use with wind turbines. Other applications on the horizon but requiring further development include motors for all electric aircraft (see figure 1.6).

However, the main application made feasible due to the discovery of Type II HTS materials is, in fact, the one that Onnes himself envisioned would be the primary use of the perfect electrical conductor, but which unfortunately had to wait nearly a century to become a reality: electrical power transmission.

1.2 Superconducting Power Transmission

1.2.1 Overview of Power Transmission Research Projects

Since Onnes' discovery of superconductivity in 1911, it has been anticipated that the ability to transmit electrical power without resistive losses would revolutionise modern society. However, due to the complex and costly nature of cooling with liquid helium, it was not until the discovery of superconducting materials which could be cooled by liquid nitrogen, which didn't occur until the late 1980s, that this became a real possibility.

Transmission losses have a major effect on our energy consumption today. In the financial year 2011/12, the recorded value of electrical transmission losses alone for Great Britain was 6.12 TWh [28]. Of these the main component was resistive heating

Figure 1.6: Design concept for E-Thrust all electric aircraft; currently the only electric motor with a high enough power density to generate enough lift for a passenger aircraft would be superconducting [27].

losses, caused by Joule heating due to the electrical resistance of the cables and components. Resistive heating losses accounted for nearly 80 % of the total system losses of the UK National Grid in financial year 2011/12 and it is estimated that this will increase over the next 5 years [29]. Further to this are the more complex distribution losses discussed, for example, in [30]. Leading superconducting cable manufacturer, AMSC, have suggested that, for 1,000 km of cable, even whilst taking into account the required cooling power, superconducting cables would lose only a third as much energy in transmission as conventional ones [31]. On a smaller scale, a 35 % reduction in transmission losses compared to conventional cables has been estimated for a 20-m long, 18.5 kA HTS cable cooled using an optimised two stage turbo-Brayton cryocooler [32].

It is not just the reduced losses that make HTS power transmission systems a truly viable long-term solution but also their high current density. Many urban areas around the world are reaching the capacity of their current electrical power transmission systems. Power consumption has increased to a level well beyond that expected when the power transmission networks were designed 30-50 years ago [33]. In order to meet the demand the systems need to be upgraded. To do this using conventional conductor technology would require vast increases of space taken up by underground ducts or overhead pylons which is both impractical and unsustainable. HTS cables can achieve a practical current density (i.e. taking into account the cross-sectional area of cooling systems, insulation and stabilising materials as well as that of the superconductor) at least two to five times greater than that of conventional cables [34]. Therefore, simply by retrofitting existing underground ducts, up to five times more energy can be brought to an urban area. Saving weight as well as space is also an important factor and a recent study suggests that an HTS transmission system including 20 m of cable could result in a 93 % decrease in system weight compared to a conventional system using copper cables at ambient temperature [32].

For these reasons many governments, electrical power suppliers and research institutes around the world have been investigating the plausibility of HTS power transmission systems and their integration into national power grids since c.1991. The main projects identified are documented in table 1.2. Note that superconducting cables still require a voltage rating in order to integrate with conventional circuits.

Project	Country	Cable Length (m)	Voltage (kV)	Current (kA)	AC/DC	Material	Publication Dates
AmpaCity	Germany	1000	10	4	AC	BSCCO/YBCO	2011-2012
LIPA I	USA	600	138	2.4	AC	BSCCO	2005-2010
LIPA II	USA	600	138	2.4	AC	YBCO	2011
SuperACE	Japan	500	66-77	3-5	AC	BSCCO	2002-2007
Albany I	USA	350	34.5	2.3	DC	BSCCO	2005-2008
Albany II	USA	350	34.5	2.3	DC	320 m BSCCO 30 m YBCO	2009-2011
Yokohama	Japan	250	66	3	AC	BSCCO	2009-2011
Bixby	USA	200	13.2	4.9	DC	BSCCO/YBCO	2005-2007
Moscow	Russia	200	20	1.5-2	AC	BSCCO	1998-2012
Superpoli	France	200	20	28	AC	BSCCO/YBCO	1999-2008
Edison	USA	120	24	4.2	AC	BSCCO	1999-2002
Gochang	S. Korea	100	22.9	2.2	AC	BSCCO	2006-2011
htpFF	USA	50	115	3.3	DC	BSCCO	1993-2001
Chongwan	S. Korea	30	29	1.7	DC	BSCCO	2005-2006
Chongwan II	S. Korea	TBC	154	3.2	AC	BSCCO	2007
NKT	Denmark	30	36	2	AC	BSCCO	1991-2002
Querétaro	Mexico	5	23	10	DC	BSCCO	2003

Table 1.2: HTS power transmission projects identified, in order of descending cable length.

1.2.2 Superconducting Materials for Power Transmission

There are many materials which have been shown to exhibit superconducting properties and many more are constantly being discovered. For the purposes of this project, which is concerned with the application of superconductivity for power transmission, only those materials deigned suitable for this purpose are discussed. It is noted, of course, that these materials are also used and being developed for applications other than power transmission.

1.2.2.1 YBCO and BSCCO

The majority of superconducting power transmission projects, such as those listed in table 1.2, use either YBCO or BSCCO cooled by liquid nitrogen. They are both commercially available on a large scale and have critical currents of 93 K (YBCO), 92 K (Bi-2212) and 110 K (Bi-2223) where the numbers refer to the element coefficients of bismuth, strontium, calcium and copper in the compound. Examples of YBCO and BSCCO tapes are shown in figures 1.7 and 1.8 respectively.

It is noted that the conductors do not consist purely of the superconducting material; rather a combination of superconductor, normal metal conductor and, in the case of YBCO, other stabilising materials as required. As can be seen from figures 1.7 and 1.8, the final YBCO-based conductor takes the form of a tape made up of laminated substrates, whereas BSCCO architecture tends to take the form of superconducting filaments in a normal metal matrix. The normal metal conductor part of the overall compound may be referred to as the 'matrix' (as in normal metal matrix) or 'sheath'.

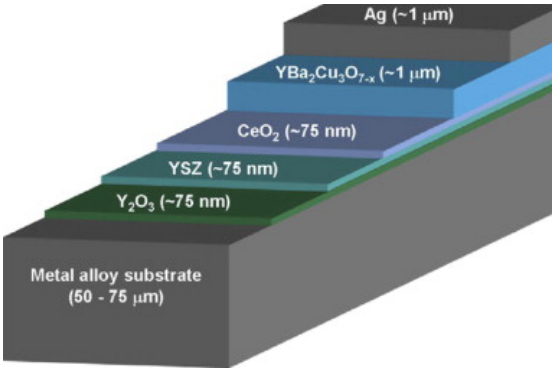

Figure 1.7: Architecture of YBCO cable manufactured by AMSC. [35]

Figure 1.8: Sample of standard BSCCO tapes consisting of HTS layers 200 μm thick (superconducting filaments in a normal metal matrix); shown with and without copper reinforcements. [36]

1.2.2.2 MgB_2

Magnesium diboride, or MgB_2, was first reported to be superconducting at temperatures below 39 K by Nagamatsu et al. in 2001 [37]. Whether or not it is considered to be HTS depends on the chosen definition as discussed previously in section 1.1.2.

However, a critical temperature of 39 K is sufficiently high that it can be cooled with cold helium gas as opposed to liquid helium. Therefore, although liquid helium is in short supply globally [26], where cold gaseous helium is readily available, MgB_2 becomes a viable contender as a power transmission cable material. Where gaseous helium is not available, liquid hydrogen has also been considered as a potential coolant [38].

MgB_2 also has many other preferential properties in terms of both cost and performance. Its properties in magnetic fields are highly favourable compared to those of the more traditional niobium-based LTS materials [39]. Furthermore, it is estimated that the cost/performance ratio (measured in US Dollars per kiloampere-metre product) could be approximately four times less than that of YBCO and 20 times less than that of BSCCO [40] due to the following properties:

- Consists of two readily available elements,
- Requires relatively low-temperature manufacturing processes,
- Can be drawn into wires or manipulated into other usable forms using variants of already-established techniques,
- Works effectively with a copper sheath rather than the silver sheath often required by HTS materials.

It has therefore been studied in particular detail with regards to the CERN High Luminosity LHC (HL-LHC) upgrade [41] (as discussed in section 1.3) and all tests

carried out as part of this project have concentrated on MgB_2. An example of an MgB_2 superconducting tape as used in this project, including its constituent parts, their surface area and overall tape dimensions, is shown in figure 1.9.

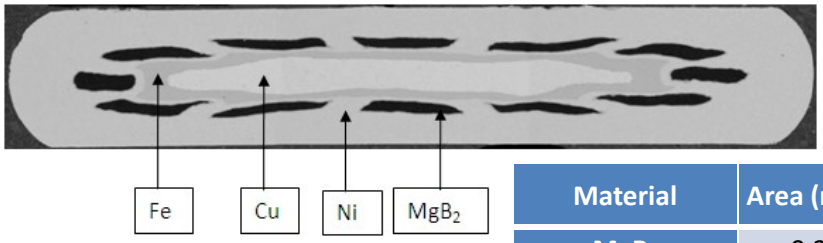

Material	Area (mm^2)	%
MgB_2	0.23	10
Ni	1.55	65
Iron	0.23	10
Copper	0.36	15
Total	2.37	100
Dimension	3.5 x 0.65	

Figure 1.9: Architecture of MgB_2 tape including stabilising components and normal metal (nickel) matrix. [42]

1.2.3 Cooling Methods for Superconducting Power Transmission Cables

The majority of HTS power transmission projects use liquid nitrogen as the cable coolant. However, gas-cooling has been considered in some contexts.

Unlike liquid-cooling, gas-cooling poses the challenge of temperature inhomogeneity. As the gas flows along a cable absorbing heat from it (thus, cooling it) its temperature increases creating a temperature gradient along the gas flow, potentially resulting in a temperature gradient along the cable length. Furthermore, both the gas flow itself and its interaction with the cable are complex and create further temperature

inhomogeneities which are difficult to predict. Depending on the cooling system, the interaction of multiple gas streams can also add complexity.

Despite these complications, gas-cooling has its advantages and helium gas-cooled superconducting cables were investigated as part of the CERN HL-LHC upgrade (discussed in more detail in section 1.3). In this instance gaseous helium is readily available for cooling HTS cables as the LHC cryogenic system provides [43]:

- **Liquid and superfluid helium** — for the cooling of the magnets and LTS magnet links,
- **Helium gas at 4.5-20 K** — for the cooling of the beam screen and resistive parts of the HTS current leads,
- **Helium gas at 50 K** — for the cooling of the cryostat thermal screens.

As well as availability, using a gas as a coolant as opposed to a liquid is advantageous in the CERN LHC upgrade case as it is unusual in requiring long lengths of vertical cable housing over a large elevation [44], which is less suitable for liquid cooling. Furthermore, a greater range of temperatures will be available and an improved range of superconductor properties will therefore be achievable. A potential bus-bar cooling method for use of gas-cooled HTS power transmission cables in the LHC upgrade is given on p. 26 of [45].

Cold gas-cooled power transmission lines have also been investigated outside of the LHC, albeit much less extensively than their liquid-cooled counterparts. In 2000, Anghel et al. published a study on a prototype neon gas-cooled system. A Joule-Thomson valve was used to reduce the temperature of the neon to approximately 45 K and, by adjusting the operating pressures of the system and introducing a heater, a temperature range of 30-70 K was shown to be possible [46].

In 2011 and 2012 the Florida State University Center for Advanced Power Systems (FSU-CAPS) tested the feasibility of a helium gas-cooled HTS cable. Focusing on the cooling capabilities of the system, a superconducting cable was simulated by a stainless steel bar of an approximately similar thermal mass. The cryostat was tested and the temperature gradients studied and compared to a theoretical model. The experimental and theoretical results showed good agreement. It was identified that though the system could remove up to 20 W of heat per m of simulated cable without

substantial temperature gradients, a greater helium gas flow rate would be required for large-scale applications such as naval and aeronautical applications [47]. In addition, a feasibility study of pressurised gaseous helium as a dielectric was also carried out. A partial discharge inception voltage of approximately 16 kV was shown, which was well within the design requirements and the dielectric performance of the helium gas-cooled cables described as 'promising' [48].

1.2.4 Integration into Current Power Transmission Systems

Given the scale of national and regional electricity networks and the immense disruption to society that any interruption of their services would cause, any changes to such systems would need to be gradual. For that reason the majority of projects concentrate on the integration of superconducting components into existing power transmission systems. One of the key projects demonstrating the feasibility of HTS power transmission is the Long Island Power Authority (LIPA) project. The 600 m-long HTS power transmission cable installed into the LIPA grid in 2008 is still connected to this day, efficiently providing electricity to thousands of people [49].

Taking the UK as an example, a preliminary investigation into the form this transition may take and the role of superconductors in it has been carried out in collaboration with both transmission and distribution companies, namely The National Grid, Scottish and Southern Energy plc (SSE)/Scotish Hydro-Electric Transmission Ltd (SHETL) and Western Power Distribution (WPD).

From the perspective of the National Grid, the most promising potential application of superconducting technology would be in the upgrade of conductors connecting micro-generation circuits to the main grid. Creating new connections to what is already considered to be a 'saturated' grid is expensive due to the required reinforcement of the main grid. However, retrofitting existing connections with superconductors to increase their capacity would not require the same modification of the main grid. Furthermore, the increase in development of HTS technology production is allowing it to become a more and more economical option [50].

Two potential areas for superconducting applications were identified in discussion with SSE/SHETL, namely 'congested corridors' and offshore wind farms. As in the LIPA case described in [49], the high current density of superconductors makes them highly favourable as short-length 'joints' in circuits where it is required to carry a

large current through a small space, generally in urban and industrial areas. The term 'congested corridors' has been coined to describe this scenario. Proving the technology and familiarising the electrical network industry with it via projects like this could work as a good stepping stone to further integrate it into the system in the future. In a current offshore wind farm system, multiple turbines are currently connected to one circuit by 33 kV cables. Each circuit is connected to land by approximately 40-50 m of 132 kV or 200 kV cables. An immediate superconducting application in this area could therefore be the replacement of the short turbine-turbine connections in order to improve efficiency [51].

From the perspective of a distribution company, reliability is the most important factor to consider - even more so than cost. Superconductors could potentially be used as security or 'back-up' cables to carry anticipated spikes in the network load. Although it is aimed for the future grid system to be managed in such a way that a fairly constant demand and supply are produced (for example with increased use of energy storage and 'smart' devices), in the transition period there may be even greater 'load swings' than exist already. Cables of greater capacity may therefore be required to cope with this, if not to be in constant operation [52].

1.2.5 Further Power Transmission System Development

As the electrical transmission grids strive to take on the challenges of greater capacity in a reduced space and increased interconnectivity, in the long term it is anticipated that a radical re-design of such systems will be required. Some such concepts in development are 'SuperGrids' and 'micro-grids' in which superconducting components are predicted to play an important role.

It is likely that fuels such as fossil fuels (while the resources remain) and hydrogen will continue to be part of the future energy economy. As such, the issue of transmission from source to point of use, typical of such geographically-limited energy sources (unlike, for example, domestic solar generation), will therefore continue to exist [53]. A solution to the combined transmission problems of both electricity and fuels has been given the name 'SuperGrid' [38] and consists of a very long superconducting cable or 'SuperCable' [54], for example stretching between the East and West coasts of the USA, cooled by liquid hydrogen, liquid methane or Liquid Natural Gas (LNG). Electricity and fuels

could then be tapped off at various strategic points along the cable for distribution or immediate use [55].

As mentioned, the loss problem of transmission (and of step-up/step-down transformers) exists because energy generation rarely takes place on or near the point of consumption. However, with the development of generation techniques that can be incorporated into or very close to a populated environment, such as solar panels and small-scale wind turbines, electricity can be taken directly from the point of generation to the consumer, bypassing national-scale grids [56]; this network design is known as a 'micro-grid'. If the majority of generation within a micro-grid is based on renewable energy sources which provide non-constant power (such as wind and solar) then energy storage also becomes a significant component of such a system. On the micro-grid scale, superconducting storage systems such as SMES could significantly enhance the dynamic system stability [57]. Superconducting FCLs are also being investigated as components in a stabilised micro-grid [58]. Although the majority of studies focus the role of superconductors in these areas of storage and current-limiting components, superconducting cables are also being considered.

As micro-grids aim to reduce transmission distances and keep generation close to consumption regions, the transmission infrastructure will be in close proximity to populated areas. The reduced spacial requirements of a high-current-density conductor and the increased safety of low voltage transmission, as well as the increased efficiency, make superconducting cables an attractive option [59].

1.3 Superconducting Power Transmission at CERN

1.3.1 Pioneering a New Technology

In the early days of the CERN LHC development, HTS technology still posed the following problems:

- Poor mechanical properties,
- Low critical current density,
- Sensitivity to magnetic field at high temperatures.

However, it was nevertheless envisaged that HTS technology would have a significant role to play and was considered by CERN to be worth investing in - which proved an auspicious approach. The introduction of HTS current leads in the LHC design, which provided a thermal break between the liquid helium-cooled magnet circuits and the power input at room temperature, reduced the heat leak into the helium bath by a factor of 10 and, consequently, the cooling power consumption by a factor of three [60]. Furthermore, the project pioneered HTS technology by being the "largest current lead project ever undertaken" at the time [61].

As the materials developed, so did their potential applications within the LHC. During the review process of the planned upgrades of the LHC, the following potential HTS applications were identified: switches, cables and, in the long-term, magnets [62]. This project concentrates on the use of HTS cables in the LHC upgrade(s).

LTS cable links are already in use at the LHC, connecting magnet systems. These links typically operate at the same narrow temperature range as the magnet circuits and share a common refrigerant of liquid or supercritical helium. HTS links or busbars, however, would operate at a wider temperature range with cooling by exhaust helium boil-off gas and integrate smoothly with the current lead systems up to room temperature [44].

1.3.2 The LHC High Luminosity Upgrade Phases I and II

The HL-LHC upgrade was originally to be rolled out in two phases. The Phase-I upgrade aimed to increase luminosity to 2-3 $\times$ 10^{34} cm^{-2} s^{-1}. This would have caused an increase in electromagnetic radiation in the LHC tunnel, posing a danger to any electronic equipment housed there such as control valves, level gauges and other devices housed in the current lead cryostats which are sensitive to radiation. Such equipment would have needed to be moved to a relatively radiation-free area away from the beam [45]. HTS cables could have been used to form the link between the magnet circuits and the current lead systems as they are less susceptible to degradation from the radiation than LTS cables [63]. HTS cables could also have been used to replace LTS links between magnets. These applications would have required links of between approximately 30 and 100 m in length and 10 m in elevation.

The Phase-I upgrade was merged with the Phase-II upgrade which aimed to increase the luminosity by a further factor of 10 to values above 10^{35} cm^{-2} s^{-1} [64]. To ensure

that all sensitive devices and components, including power converters, were unaffected by the increased radiation, it was suggested that they be moved above ground, requiring superconducting links of up to 500 m in length and 150 m in elevation. Removal of power converters, current leads and their cryostats from the underground area would also increase the space around the accelerator and allow quicker access to the power system components for maintenance [41]. The combined upgrades of Phase-I and Phase-II are known as the HL-LHC (High-Luminosity LHC) and the Design Study programme of the upgrade as 'HiLumi'.

After further evaluation, a power transmission system for the LHC requiring 10 superconducting links was designed as part of the HiLumi programme. The link specifications were as follows (see figure 1.10):

- 4 × links at Point 1 and 4 × links at Point 5:
  - Multi-purpose:
    - Removal of current leads and their cryostats to a safe distance from the beam
    - Upgrade of high luminosity (magnet) triplets
    - Feeding of arc and MSS magnets
  - Vertical (surface to tunnel installations)
  - 300 m-long
  - 156 kA total current-carrying capacity in the form of:
    - 12 × 120 A conductors
    - 28 × 600 A conductors
    - 23 × 6 kA conductors
- 2 × links at Point 7:
  - Single purpose: Removal of current leads and their cryostats to a safe distance from the beam
  - Semi-horizontal (tunnel installation)
  - 500 m-long
  - 29 kA total current-carrying capacity in the form of:

* 48 × 600 A conductors

The use of HTS in the proposed links, as opposed to conventional Cu or aluminium based cables, would also have the advantage of removing the large, warm, heavy standard power transmission cables, increasing the space around the accelerator and decreasing the heat leak into the system. For example, in one original design for individual magnet-feeding power links at Point 1, it was estimated that over 70 tonnes of copper would be required if conventional copper cables were used [45]. Based on this reasoning, extensive research has been carried out into the design and operation of HTS cable assembly links for use in the HL-LHC upgrade through the HiLumi project.

1.3.3 Cable Designs

1.3.3.1 Design Considerations

The following considerations were important when designing the CERN cable assembly structure:

- **Compact design** — Space is limited both in the tunnels and tunnel alcoves and in the channels that the cable assembly will pass through during installation. Therefore a compact design was required not only to allow the cable to fit but also to allow access for installation, connection and maintenance.

- **Reducing induced voltages** — Conductor lengths were to be twisted both into pairs and around formers where possible to reduce induced voltages. Discussed in more detail below.

- **Thermal stability** — Sufficient stabilising material was to be included to minimise the possibility of thermal runaway occurring and to ensure that the cable assembly was recoverable should a thermal runaway event occur. This was even more critical than in other HTS power transmission projects given the reduced access to the cables available for maintenance or repair should damage occur.

- **Quench detection** — A system must be put in place to detect a quench or thermal runaway event should it occur.

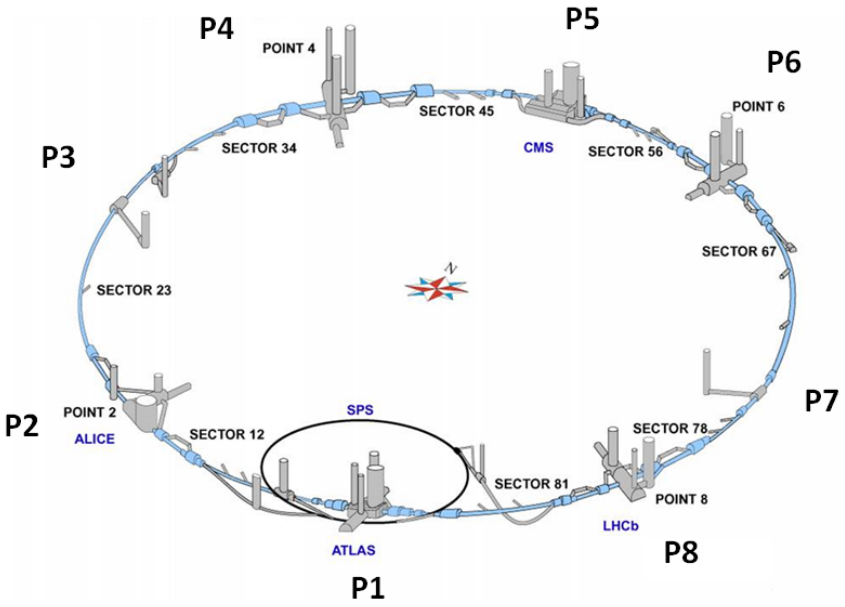

(a) LHC map showing detectors and positions of 'Points'.

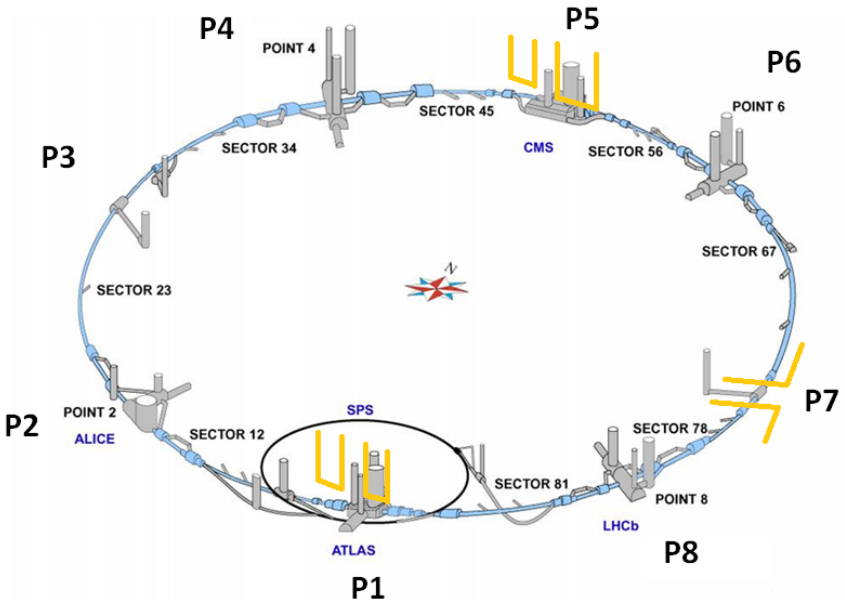

(b) LHC map showing proposed superconducting links (yellow).

Figure 1.10: LHC maps with and without superconducting links shown. [65]

- **Conductor material and form** — A number of suitable superconducting materials exist which can be manufactured as both wires and tapes, depending on their individual material properties, and the unique behaviour of each form needed to be considered.

- **Cooling system requirements** — The cable was to be cooled using the helium boil-off gas from the liquid and superfluid helium used to cool the magnet circuits posing the dual challenges of gas-cooling and integrating the cable cooling system not only into the magnet cooling system but also the helium recovery system.

1.3.3.2 Strands and Twisted-Pairs

Both superconducting wires and tapes have been considered in the design process. In particular, the formation of stabilised 'sandwich' strands using tapes has been studied. A strand in this context consists of alternating layers of superconducting and stabilising tapes, the stabilising tapes being made of a normal metal conductor such as copper. This strand configuration is also referred to as a 'sandwich stack', an example of which can be seen in figure 1.11. These stabilisation layers are additional to the normal metal matrix already incorporated into superconducting tapes.

The requirements of the CERN HL-LHC cables are unusual in that, unlike most commercial and national network transmission cables, they are operating with a Direct Current (DC). The cable requirement is therefore simply two conductors per magnet circuit carrying 'current in' and 'current out', as opposed to standard conventional conductor three-phase Alternating Current (AC) power transmission cables.

The magnetic inductance due to the transport of such high currents is significant, yet its exact calculation is complex, as with all inductance calculations - there is to take into account the self-inductance of each conductor, the mutual inductance between current-in and current-out conductor pairs and, in a bus-bar link feeding multiple magnet circuits with a single cable assembly, the mutual inductance between neighbouring conductor pairs [66]. This is known as a 'self-field' scenario in which no external magnetic fields are applied but the induced fields are taken into account.

Such an induced self-field scenario was modelled for a cable consisting of two conductors carrying a DC current in and out as part of investigations by CERN into the feasibility of using HTS cables [67]. The conductors modelled were strands in the form

of sandwich stack layers of tapes such as those described above and the results showed that when the two conductors were parallel, the induced fields forced a non-uniform current distribution among the tapes in each strand, resulting in locally reduced I_c values. However, by twisting the conductors together, each surface alternates between being an inner and outer surface so that, over the length of the cable, the induced fields are cancelled out. The twisting together of paired instrumentation wires to minimise signal noise due to induced voltages is fairly standard practice and the modelling in [67] shows that, by applying this to the current transport conductors in the CERN HL-LHC cables, a significant degradation of I_c can be avoided. This 'twisted-pair' configuration has therefore been integrated into the cable design.

However, laying two or more twisted-pairs parallel to each other would nullify the effect and induced fields would still be experienced. Therefore, all the twisted-pairs in a cable assembly are also twisted about a former or central support tube, generally made of Stainless Steel (SS), to further reduce induction.

Unlike conventional, ductile, normal metal wires and cables, a superconducting component cannot be easily drawn, formed or twisted, for various reasons. All of the superconducting materials considered for the HiLumi project are brittle and can snap or break during bending, stretching or twisting. Furthermore, the superconducting properties of a material depend on its microscopic structure, which is also affected by bending, stretching and twisting. Each material therefore comes with a recommended minimum bending radius, bending above which its superconducting properties should still be effective. In the HiLumi cable designs, a twist pitch of 0.4 m was generally adhered to in order to reduce any degradation of the superconducting properties. However, it is still possible that damage could have occurred during the twisting process, causing an inhomogeneous I_c distribution or other degradations in the cable properties.

1.3.3.3 Initial Designs

An early design for a 26 × 600 A-rated twisted-pair (52 × strands) cable assembly, where each strand consisted of 2 × superconducting tapes and 1 × copper stabilisation tape, is shown in figure 1.12.

A series of later designs based on MgB_2 wire, as opposed to tapes, is shown in figure 1.13. Similar designs based on the other superconducting materials studied and validation of the cable concept can be found in [68], in which the concentric designs of

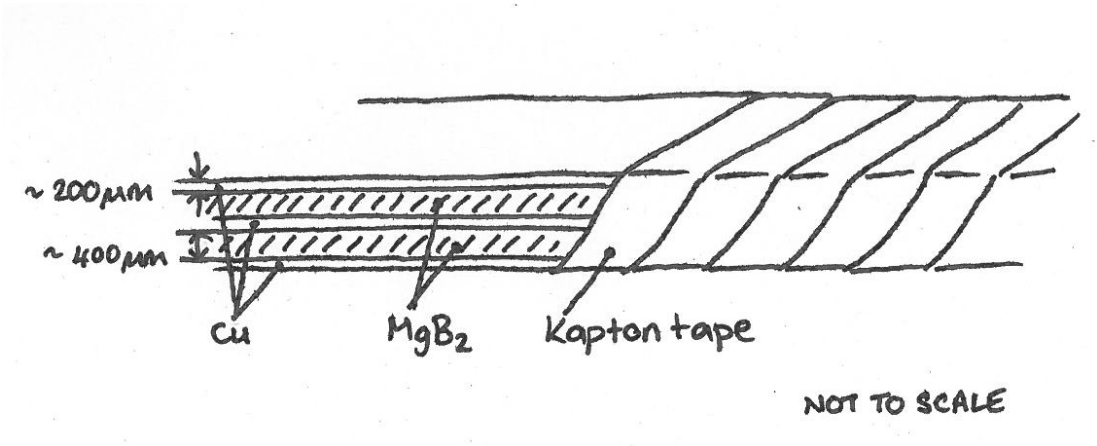

Figure 1.11: An example of a sandwich stack strand formation consisting of 2 × superconducting (MgB_2) and 3 × stabilising (Cu) tapes wrapped in Kapton tape.

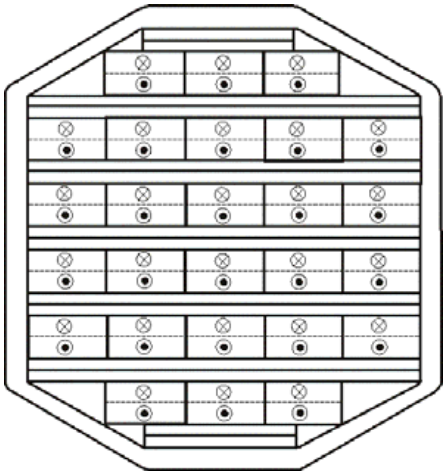

Figure 1.12: Initial cable designs: 26 × 600 A twisted-pairs cable assembly structure; crosses denote current-in strand and circles denote current-out strands; each strand consists of 2 × superconducting tapes (of Y-123 or Bi-2223) and 1 × copper stabilisation tape [43].

figure 1.13, which lend themselves well to a twisted-pair formation, are favoured over the grid-like design of figure 1.12. However, the use of sandwich stacks of alternating superconducting and normal-metal stabilising tapes has been generally favoured over the use of wires.

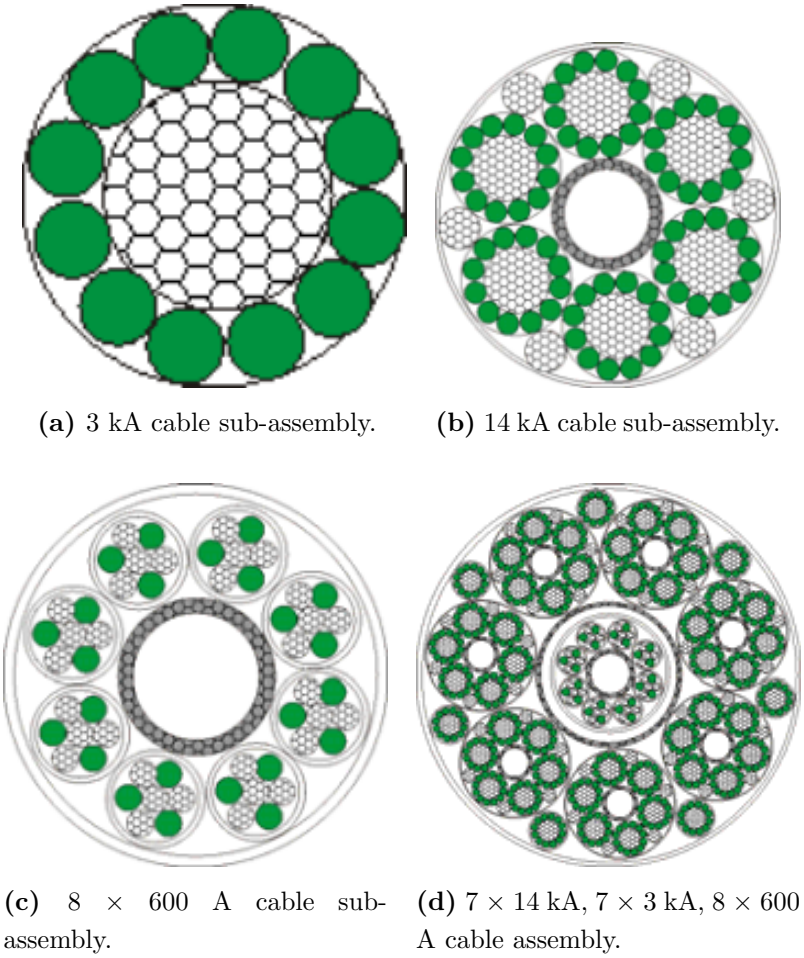

(a) 3 kA cable sub-assembly.

(b) 14 kA cable sub-assembly.

(c) 8 × 600 A cable sub-assembly.

(d) 7 × 14 kA, 7 × 3 kA, 8 × 600 A cable assembly.

Figure 1.13: Various MgB_2 wire cable assembly configuration concepts with copper stabiliser where MgB_2 is solid (green) and copper is hatched (white) [41].

The performance of 2 m-long sample cables were tested in a collaboration between CERN and the University of Southampton [1, 67]. The cable unit was a twisted-pair assembly of two cables, each made from sandwich stacks of three superconducting and four stabilising tapes. The sandwich stacks were electrically insulated from each other and then twisted together to form a pair. Five cable 'Types' were tested and their configurations are summarised in table 1.3.

'Type'	Conductor	Supplier	$\mathbf{I}_{C,av,77K}$ (A)	$\mathbf{I}_{C,av,4.2K}$ (A)
Type-1	Bi-2223	Bruker HTS	260	1270
Type-2	Bi-2223	Sumitomo	493	2885
Type-3	YBCO	SuperPower	295	4410
Type-4	YBCO	AMSC	310	3220
Type-5	MgB_2	Columbus	n/a	4205

Table 1.3: Summary of properties of 2 m-long, single twisted-pair sample cables studied in a collaboration between CERN and the University of Southampton [1, 67].

Each of the cables tested incorporated a sandwich stack of 3 × superconducting layers intercalated with 4 × copper layers (of dimensions 4 × 0.2 mm^2), giving a total of approximately 3.2 mm^2 (4 × 0.8 mm^2) cross-sectional area of copper stabiliser, per unit length. The copper laminations took the following forms:

- **Type-1, Type-3 and Type-5** — copper tapes interleaved between superconducting tapes during the preparation of the strands to form sandwich stacks; electrical contact between superconductor and stabiliser made by pressure of Kapton tape wrapped around the sandwich stack,
- **Type-2 and Type-4** — copper alloy laminations soldered onto both sides of each superconducting tape.

The electrical insulation of each strand was provided by Kapton tape (6 mm × 50 μm), wrapped with 50 % overlapping back and forth around each strand and again around each twisted-pair. The twist pitch of each twisted-pair cable unit was 0.4 m for all types.

Critical currents were established at 4.2 K for all samples and at 77 K for the cuprate conductors only, both under self-field and in a homogeneous external field of up to 10 T. The averages of the values found for the two strands of each material tested are given in table 1.3. Further investigations ascertained critical currents of the sample cables as a function of temperature between 10 and 77 K, as seen in figure 1.14, and it was verified that the cables remained stable with 80-95 % of I_c applied for 5 minutes [1].

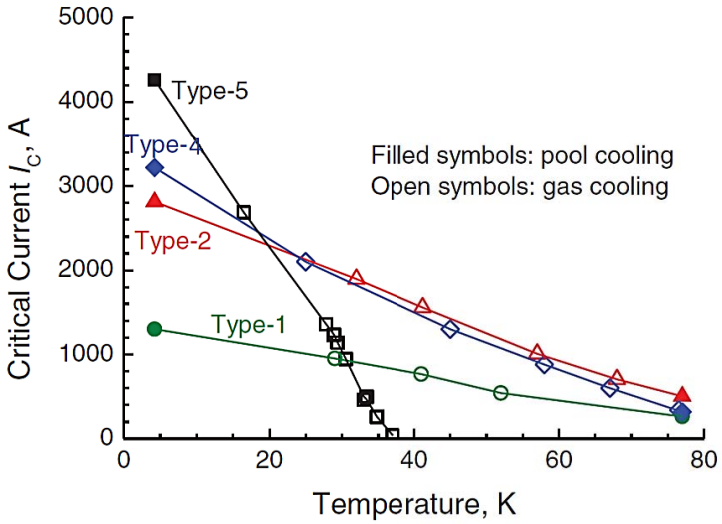

Figure 1.14: Critical current as a function of temperature for several 2 m-long, single twisted-pair sample cables as summarised in table 1.3 [1].

1.3.3.4 MgB_2 Sandwich-stack Cable Design for LHC Point 7 Links

The final chosen cable configuration designed specifically for the requirements of the links at Point 7 in the HL-LHC (see figure 1.10), namely a 29 kA-rated cable made up of 48 × 600 A-rated conductors, is known as the MgB_2-Cu sandwich stack design and is based on the Type-5 design described above and in table 1.3 and figure 1.14. It is a novel superconducting power transmission cable concept developed by CERN in line with the requirements of the CERN LHC combined Phase I and Phase II upgrade or HiLumi/HL-LHC projects described previously and uses assemblies of twisted-pair strands [64].

As described above, each strand consists of alternating layers of superconducting material (MgB_2) and stabilising tapes made of a normal metal conductor (copper). Two strands, electrically insulated from each other by being wrapped in Kapton tape, are twisted together to form a twisted-pair. The Kapton wrapping also holds the superconducting and stabilising layers together, providing the pressure contact which is the only contact between the tape layers since they are not soldered or adhered to

each other in any other way. This pressure-only contact is another unique feature of the CERN cable design. The normal metal layers are added for enhanced electrical and thermal stabilisation due to the inaccessibility of the cables once installed in the LHC tunnels. In the configuration presented here each strand is comprised of three layers of MgB_2 and four layers of Cu as shown in figure 1.15.

Note also that 'single-sandwich' refers to three tapes in a stabiliser-superconductor-stabiliser formation and a 'sandwich stack' refers to a formation of alternating stabiliser and superconductor tapes with more than one superconductor layer, such as the strands described above. A 'half-sandwich' refers to two tapes, one stabiliser and one superconductor.

It is this cable concept which has been tested at the University of Southampton, forming the basis of this body of work, and described in the following chapters.

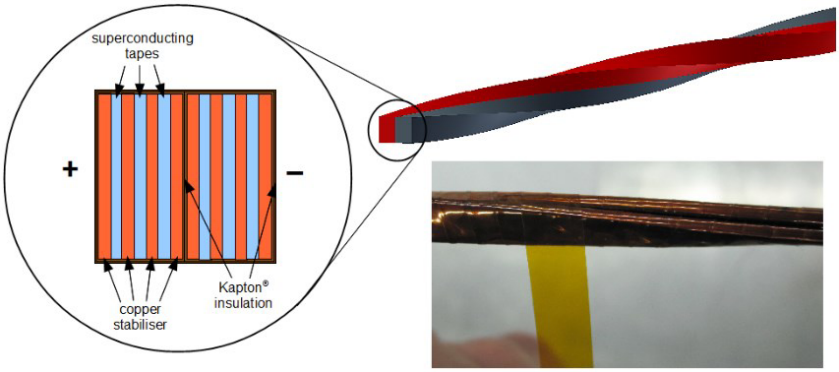

(a) Left: Schematic of a pair of MgB_2-Cu strands including individual Kapton wrapping. Right: (upper) schematic of two strands twisted together to form a twisted-pair; (lower) twisted-pair Kapton wrapping process. [68]

(b) Portion of sandwich stack in cable assembly tested at University of Southampton with Kapton pulled back to reveal Cu and MgB_2 tapes.

Figure 1.15: Kapton-wrapped MgB_2-Cu strands as tested at the University of Southampton.

2

Preliminary Tests and Motivation: CERN Cable Testing Facilities at Southampton

2.1 Introduction

As a continuation of the collaboration between CERN and the University of Southampton to investigate superconducting power transmission cable designs for use in the LHC Point 7 link as part of the HiLumi upgrade design project, a purpose-built vessel referred to as the '5 m Nexans semi-flexible cryostat' was designed and built. This was designed for the testing of up to 5 m-long, multi-strand prototype cables following on from the 2 m-long, single twisted-pair sample cables described in the previous chapter and in [1, 44, 67].

Before the full multi-strand prototype cable tests were carried out, the Type-5 MgB_2-Cu 2 m-long, single twisted-pair sample cable from [1, 44, 67] was used to test the workings of the 5 m Nexans semi-flexible cryostat. These tests, which are henceforth referred to as the '2 m preliminary cable tests', allowed the cryostat cooling configuration and behaviour to be tested and optimised. These tests also lead to two further series of experiments from which the two main research threads of this body of work are derived, namely 5 m-long, multi-strand cable stability tests and 200 mm-long single- or half-sandwich current transfer tests.

This chapter therefore describes: the test facilities designed and built by CERN and

the University of Southampton to test 5 m-long multi-strand cable prototypes; and the results of the 2 m preliminary cable tests that led to the two main research questions behind this body of work.

2.2 Test Facilities

2.2.1 The Cryostat

In order to carry out thermal stability and quench characterisation tests on a cable assembly of the design described in section 1.3.3.4, the 5 m Nexans semi-flexible cryostat was designed and assembled at the University of Southampton [1]. Cable assemblies of up to 50 strands or 25 twisted-pairs connected in series could be tested in the cryostat. Strands were connected in series so that they could be tested using one pair of current leads and one power source which significantly simplified the cryostat design. Further work outside the scope of this project is being carried out by the University of Southampton and CERN to design and build a test facility for 24 independently loaded twisted-pairs, simulating the context in which the cable will be used in the LHC i.e. powering 24 individual magnet circuits.

2.2.1.1 General Structure

A schematic showing all major inputs and outputs of the cryostat is given in figure 2.1. Figure 2.2a shows the cryostat in the laboratory environment at the Institute of Cryogenics, University of Southampton. Figure 2.2b highlights some of the main features of the general structure of the cryostat.

The top of the cryostat (as labelled in figures 2.1 and 2.2b) features the main entry and exit ports and the connections to the sample. It is also at the top that the cryostat opens for the loading and connection of samples. The main cable housing of the cryostat can be seen as the long, black, corrugated middle section in figure 2.2.

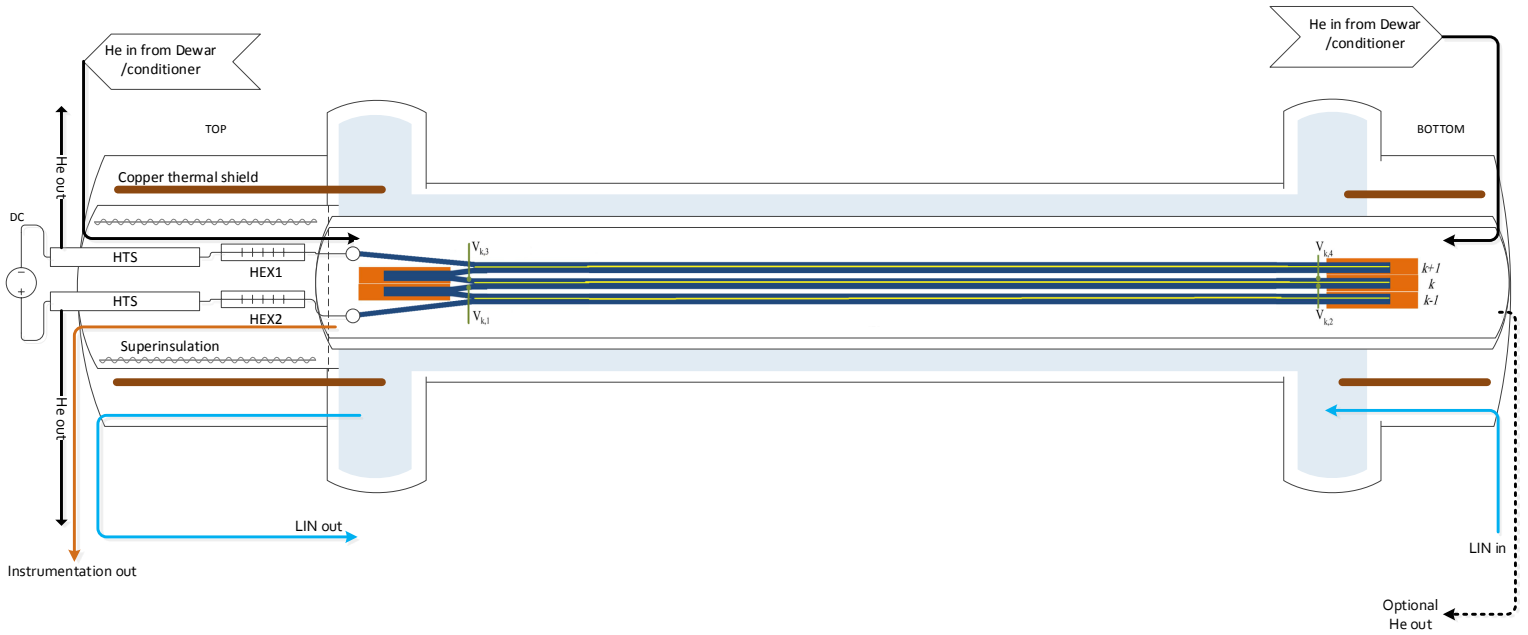

Figure 2.1: Schematic of 5 m Nexans semi-flexible cryostat at the University of Southampton showing all entry/exit ports apart from vacuum ports. Vertical dashed line represents flange at which cryostat opens for loading and connection of sample. Superconducting cable to be tested represented by schematic from [44]. HEX = Heat exchanger, LIN = Liquid Nitrogen, other abbreviations as in Glossary.

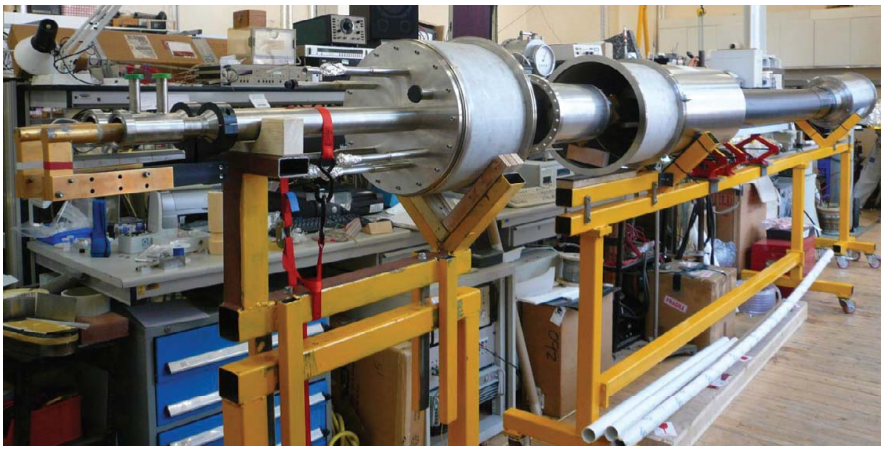

(a) In the laboratory.

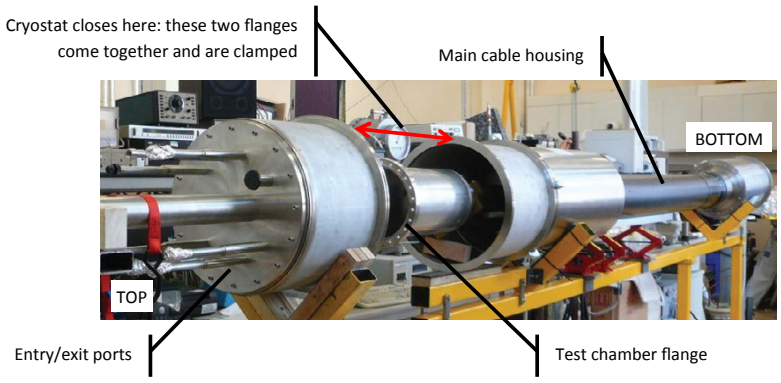

(b) Main features.

Figure 2.2: 5 m Nexans semi-flexible cryostat at the University of Southampton [1].

2.2.1.2 Thermal Shielding

To ensure that the sample could be efficiently maintained at the required low temperatures in the cryostat, multiple thermal shielding techniques were used.

The main cable housing consists of four concentric flexible tubes incorporating a vacuum environment, a liquid nitrogen jacket and a corrugated pipe in which the superconducting cable to be tested was placed. The external diameter of this section is

220 mm and the ID/OD of the corrugated pipe is 84/92 mm (see figure 2.3). This set-up represents the current baseline for proposed future LHC applications [44].

Radiative heat transfer is governed by the Stefan-Boltzmann law which states that, for the case of 'a pipe passing through an enclosure large in size relative to the pipe diameter' [69], heat exchange by radiation is determined by equation 2.1:

$$\dot{Q}_{radiation} = A_{pipe} \times \varepsilon_{pipe} \times \sigma \times (T^4_{pipe} - T^4_{enclsoure}) \tag{2.1}$$

where $Q_{radiation}$ is the rate of heat transfer between the 'pipe' and the 'enclosure', A_{pipe} is the radiating surface area of the 'pipe', ε_{pipe} is the emissivity of the 'pipe' surface, σ is the Stefan-Boltzmann constant (5.67×10^{-8} W m^{-2} K^{-4}), T_{pipe} is the temperature of the 'pipe' surface and $T_{enclosure}$ is the temperature in the 'enclosure' at the surface of the 'pipe'.

However, here, unlike in most conventional heat transfer cases, the 'pipe' represents the cryostat, the temperature within which is very low, and the 'enclosure' is the warm body or cryostat surroundings, i.e. the laboratory. Heat therefore transfers from the 'enclosure' to the 'pipe', so we can rewrite equation 2.1 as:

$$\dot{Q}_{radiation} = A_{enclosure} \times \varepsilon_{enclsoure} \times \sigma \times (T^4_{enclosure} - T^4_{pipe}) \tag{2.2}$$

where $A_{enclosure}$ is the surface area of the 'enclosure' in contact with the 'pipe' surface and $\varepsilon_{enclsoure}$ is the emissivity of the 'enclosure' at the surface of the 'pipe'.

Without a thermal shield, $T_{enclosure}$ would be the temperature of the laboratory environment, ∼300 K. By surrounding the inner chamber of the cryostat (in which the sample is held) by a jacket of liquid nitrogen to form a thermal shield, $T_{enclosure}$ is significantly reduced to the temperature of the liquid nitrogen or 77 K. For T_{pipe} values of 10-40 K, the addition of the liquid nitrogen thermal shield results in a decrease in radiative heat transfer into the internal cryostat chamber by a factor of between 230 and 250, before taking into account the effects on emissivity.

It is noted that it is also possible to use gaseous helium at 20-50 K, such as that which would be produced by the cooling of magnet circuits in the LHC, as the low-temperature fluid in the cooling jacket.

This significant reduction in heat transfer into the system from the surroundings would be compromised by conduction and convection heat transfer if the cryogen jacket

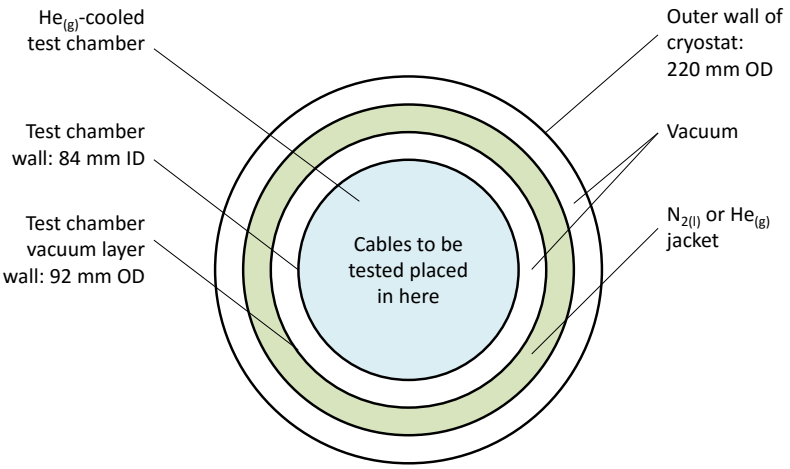

Figure 2.3: Cross-section of the main cable housing of the 5 m Nexans semi-flexible cryostat at the University of Southampton.

was in direct contact with the test chamber outer wall. However, as can be seen in figure 2.3, vacuum layers are used to prevent this.

Furthermore, the liquid nitrogen does not come into direct contact with the outer flanges at either end of the cryostat. A series of insulated pipes carry the liquid nitrogen from wells at either end of the main chamber into and out of the cryostat. In place of the liquid nitrogen jacket thermal shield at each end, then, there is instead a copper shield which sits with one end in the nitrogen wells and so is cooled to the liquid nitrogen temperature by conduction.

This copper thermal shield is particularly important at the top of the cryostat as the majority of entry and exit ports are housed here. In particular the connection to the current supply here creates an unavoidable direct thermal connection to equipment at room temperature. Therefore, at the top of the cryostat, as well as the copper thermal shield, superinsulation is used. The superinsulation consists of alternating layers of:

- **Aluminised Mylar** — a thin, light, plastic sheet coated in aluminium whose reflective properties reduce heat transfer by radiation,

- **Synthetic (e.g. Nylon) netting** — which prevent the Mylar sheets from being in contact with each other to prevent heat transfer by conduction via the thermally conductive aluminium layers; a thermally resistive material, often synthetic, such as nylon, is chosen and a design which significantly reduces the contact area between layers such as netting so as to continue to reduce conductive heat transfer (see equation 2.3).

Rate of heat transfer by conduction, $\dot{Q}_{conduction}$, is given by Fourier's law:

$$\dot{Q}_{conduction} = -\frac{\Delta T \times A}{\rho_{thermal} \times \Delta x} \tag{2.3}$$

where ΔT is the temperature difference between the two bodies in contact, A is the contact area, $\rho_{thermal}$ is the thermal resistivity of the material and Δx is the material thickness or length along which heat has conducted.

2.2.1.3 HTS Current Leads

As mentioned previously, the top section of the cryostat separates from the main body of the cryostat to allow samples to be inserted. This extra joint, along with the connection to the current supply, means that reducing heat transfer into the system at this point is particularly important. To this end, as well as the thermal shielding described above, HTS current leads were used, as in the LHC itself as described in section 1.3.1. Figure 2.4 shows the top section of the cryostat, which houses the current leads, separated from the main cryostat body.

As mentioned, the electrical connection between the sample and the power supply creates an unavoidable thermal link between the cold system inside the cryostat and ambient conditions. The use of HTS current leads reduces the heat entering the system at this point in two ways:

- **Thermal break** — The current leads, kept at an interim temperature by the cold $He_{(g)}$ exiting the cryostat, provide a thermal break, reducing the temperature difference seen by the sample cable to be tested, and helping to reduce heat entering the system via conduction,

- **Reduced heat generation** — The current leads, being maintained below their T_c and therefore in the superconducting or non-resistive state, do not produce any Joule heating and so do not add to the heat entering the system at this point.

Therefore the use of current leads is more advantageous than simply using conventional current connections cooled to the same temperature.

Furthermore, helium gas heat exchangers within the current lead unit further reduce heat leak into the system via conduction along the current leads. The heater exchangers unconnected to a sample are shown in figure 2.5a and with a sample connected in figure 2.5b.

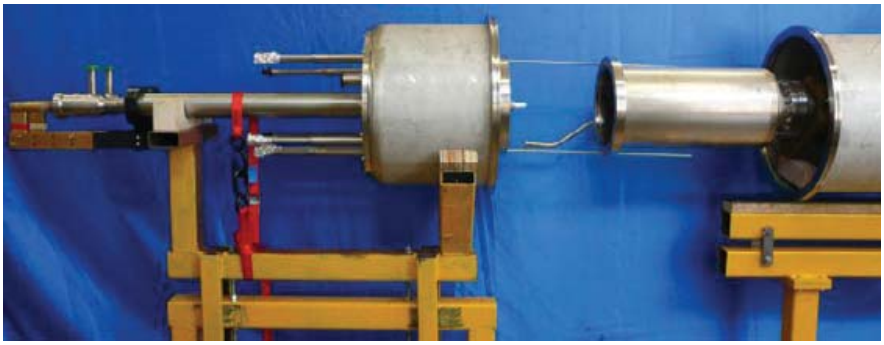

Figure 2.4: 5 m Nexans semi-flexible cryostat: current lead unit separated from main body of cryostat; test chamber flange also visible [1].

2.2.1.4 Helium Gas Cooling

The sample in the test chamber is cooled using helium gas for which there are two independent entry/exit ports, one at each end of the cryostat. The majority of the cooling is done by the bottom gas feed. The top feed was originally installed as an optional flow, mainly used for counteracting the remaining heat leak into the system via the connection to the power supply. However, it has since been seen that a mixing of the two gas feeds can help to provide a homogeneous temperature inside the vessel.

The helium gas is supplied by Dewars of liquid helium. In each Dewar a resistance heater is inserted into the liquid to control the helium boil-off rate by manually controlling the power applied to the heater. The pressure of the gas leaving the Dewar

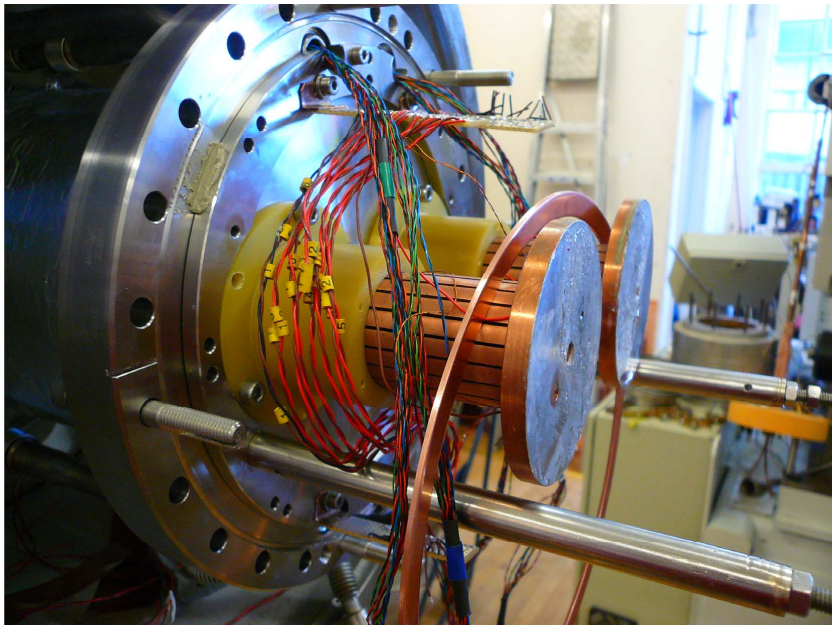

(a) Without sample connected.

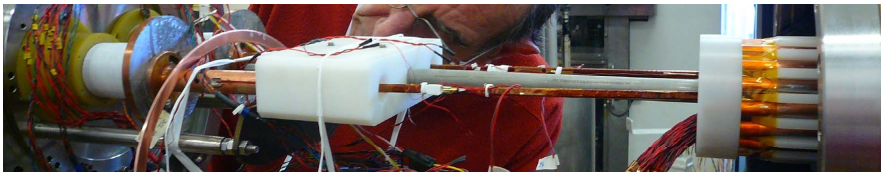

(b) With sample connected.

Figure 2.5: Current lead heat exchangers in 5 m Nexans semi-flexible cryostat at the University of Southampton.

is monitored. Before entering the cryostat, the helium gas passes through a gas 'conditioner' used to adjust the temperature and flow-rate of the helium gas entering the cryostat for which purpose it contains a second resistance heater and a thermometer. The power applied to the conditioner heater can be controlled manually or by using a suitable control device, such as a PID controller, whose inputs can be the gas pressure or the gas temperature. This is shown schematically in figure 2.6. The combined helium flow is channelled out via the HTS current leads, to maintain them below their critical temperature, on its return to ambient temperature.

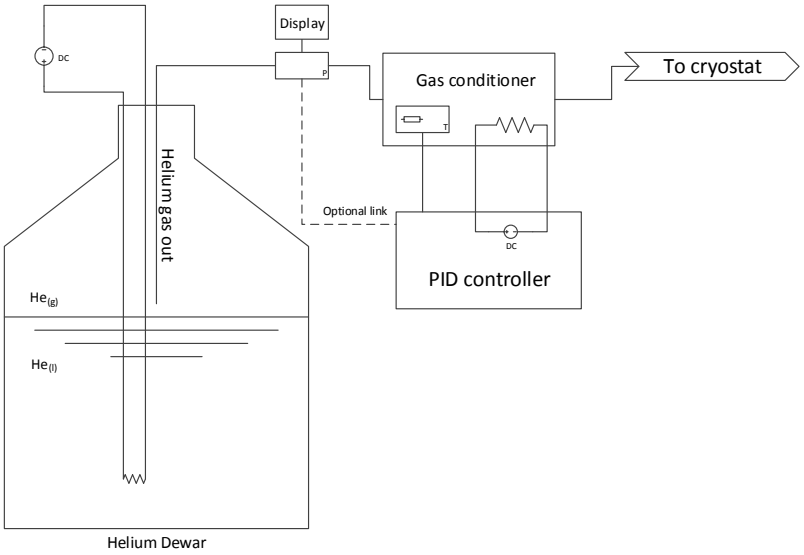

Figure 2.6: Schematic for control of helium gas feeding 5 m semi-flexible Nexans cryostat at the University of Southampton. Configuration used for both top and bottom gas feeds.

Gas-cooling is used here to simulate the HL-LHC environment in which the cables will be cooled using boil-off gas from the magnet-cooling helium feeds. However, compared to conventional cooling by liquid cryogens, the heat transfer coefficient for gas cooling is typically lower by at least an order of magnitude. While such a reduced heat transfer capability is an important design and operation consideration for gas-cooled superconducting cables, it becomes particularly challenging for the cable testing. Electrical and thermal characterisation tests must be conducted with applied currents that are near and above the critical current and in scenarios in which the heat dissipation

in the superconductor exceeds the cooling capability. Furthermore, by definition, there will always be a temperature gradient with forced-flow cooling since the temperature of the coolant increases along the direction of flow as it absorbs the heat energy of the body which it is cooling. Therefore, assessing cable characteristics such as the isothermal determination of critical current (I_c) over a long length of sample cable is not straightforward.

It was seen in the preliminary tests that the following operational steps helped to mitigate the difficulties of low heat transfer by gas cooling in this cryostat and minimise the temperature gradient along the length of the cryostat in order to attempt to homogenise the temperature of the sample and were therefore used in all following experiments:

- **Increase main gas flow** — It was seen that the temperature gradient along the 5 m test vessel could be reduced to 1 K or less by increasing the main gas flow rate (bottom gas feed).
- **Use of secondary gas flow** — By maintaining the secondary gas flow (top gas feed) at a lower temperature than that of the main gas flow, it was able to compensate for the temperature increase in the main flow.
- **Encourage mixing of gas flows** — The mixing of the two gas flows at different temperatures produced strong natural convection currents which travelled in the opposite direction to the main flow with a substantial penetration into the main vessel, resulting in a further reduction of the temperature gradient. This had been observed as the temperature measured in the middle or bottom of the vessel reacted to a change in the conditions of the top gas feed.

It was also originally intended that the the ends of a cable assembly to be tested, where the inter-strand joints were situated, were maintained at a lower temperature than the rest of the cable in order to compensate for heat generation due to resistive joint components such as solder and copper. To this end a heater was installed at the top of a baffle situated in the cryostat at the bottom end; samples would be loaded into the cryostat so that the baffle was positioned between the joints and the main cable. The gas would therefore flow past the joints at a low temperature governed by the gas conditioner, then be forced around the baffle and past the heater which would control

the temperature of the gas seen by the cable. However, it was soon determined that the strong natural convection currents of the combined flow were far more dominant in controlling the flow temperature than the heater which therefore became redundant and was not used.

2.2.2 The 2 m-long, Single Twisted-Pair Sample Cable Assembly

The 2 m-long, single twisted-pair sample cable used in the preliminary tests in the 5 m semi-flexible Nexans cryostat was that used in [1] of the design described in section 1.3.3.4 with the alterations described below.

The two strands of the twisted-pair cable were labelled 'V' and 'N' and additional voltage taps or 'v-taps' were placed at the positions shown in figure 2.7. Voltage differences between various v-tap pairs could be read with the use of external junction boxes. Voltage taps V3, V4, N3 and N4 were those connected to the cable at the University of Southampton in addition to those connected at CERN and used during the tests described in [1].

Temperature was measured at the following points on the cable using cernox thermometers:

- V strand, top,
- N strand, top,
- Unspecified strand, middle,
- Unspecified strand, bottom.

A resistance heater, H1, was installed in the middle of the cable, as per figure 2.8.

2.2.3 The 5 m-long, Multi-Strand Prototype Cable Assembly

To test the design of the HTS links required at Point 7 of the LHC, an assembly of 23 twisted-pairs, each rated at 600 A, of MgB_2-Cu strands (a cable) was designed and built at CERN for testing at the University of Southampton. It is noted that the original specification was for 24 × twisted-pairs or 48 × strands. However, during the manufacturing and assembly processes, two of the strands were damaged, namely #5 and #6. The damaged strands were shorted out so that a joint between strands #4

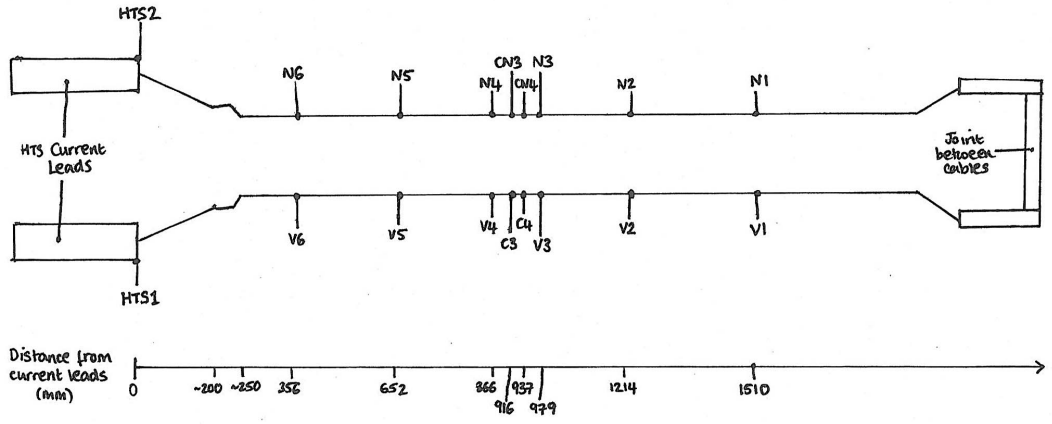

Figure 2.7: Voltage tap positions on 2 m-long, single twisted-pair sample cable.

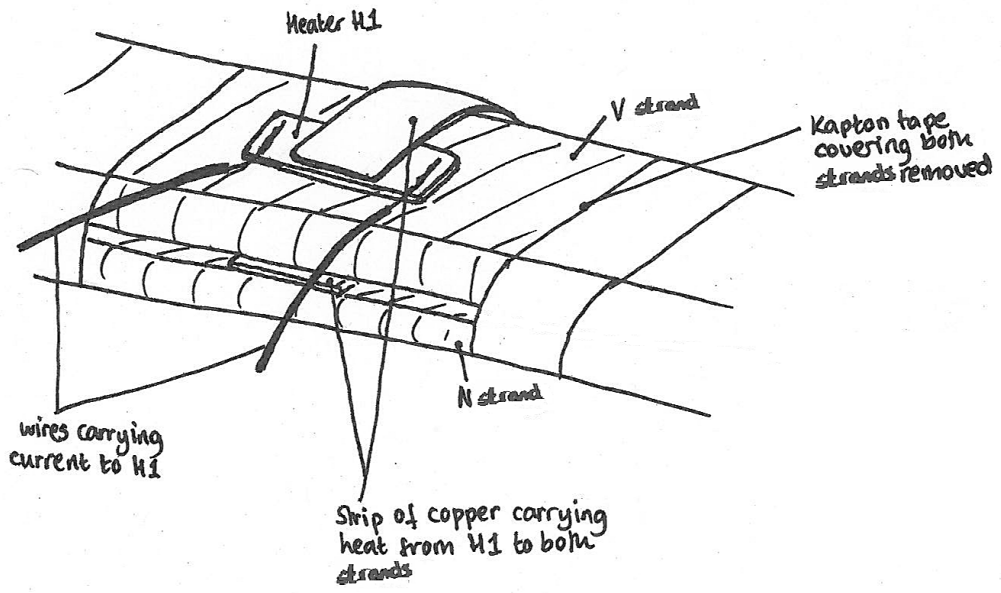

Figure 2.8: Attachment method of resistance heater H1 to 2 m-long, single twisted-pair sample cable.

and #7 was made. It is noted, therefore, that while all 48 strands were present and strands retained their original numbering for reference, only 46 of the 48 strands were actually tested.

2.2.3.1 Strands and Twisted-pairs

In the cable assembly configuration as tested: each strand was wrapped in a layer of electrically insulating Kapton tape (as described in figure 1.15a); each twisted-pair was then also wrapped in Kapton; and, finally, the whole cable assembly was wrapped in a last layer of Kapton. The cable assembly was structurally supported by being twisted around a SS former. Figure 2.9 shows the top of the cable assembly in which all the Kapton wrapping processes can be seen as well as other cable features.

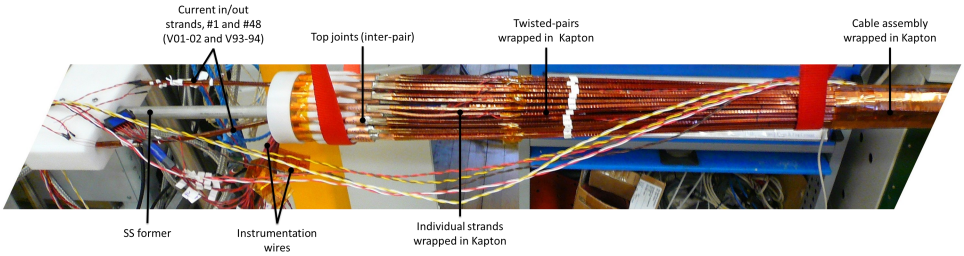

Figure 2.9: Top of 46-strand cable as set up for testing at the University of Southampton showing: current in/out strands; Kapton wrapping of strands, twisted-pairs and cable assembly; inter-pair joints; stainless steel former; instrumentation wires.

2.2.3.2 Joints

Joints between strands were made by soldering them together inside copper bars. The bars, of a diameter approximately twice the strand width, had a rectangular cutaway in which the strands were placed. This was then filled with solder and a flat copper strip or 'lid' was placed on top. The bars, and hence the joints, were approximately 200 mm long and were separated and electrically insulated from each other by a PTFE holder. A profile of a joint is shown in figure 2.10. Assembled joints for testing are shown in figure 2.11.

Joints between two strands which formed a twisted-pair or 'intra-pair joints' were located at the bottom end of the cable. Joints between twisted-pairs or 'inter-pair joints' were located at the top of the cable - note that this includes the joint between strands #4 and #7 which was made by the shorting out of damaged strands #5 and #6; strands #4 and #7 are clearly not a twisted-pair and this joint is located at the top. Figure 2.12 shows the cable assembly as tested at the University of Southampton.

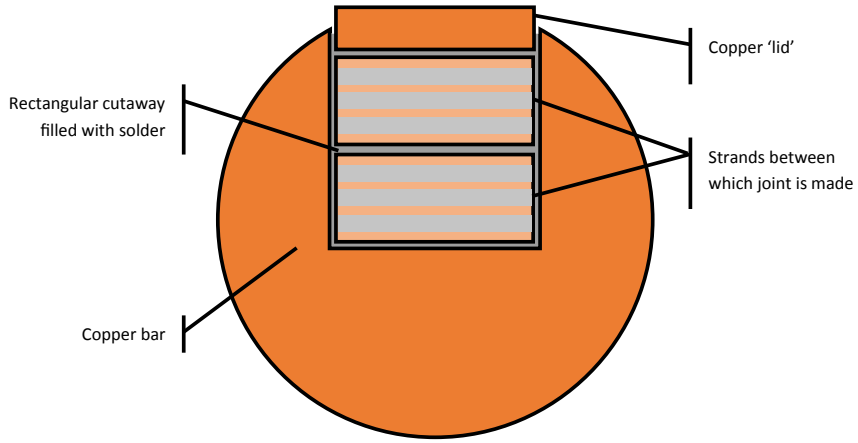

Figure 2.10: Profile of a joint between strands. The same configuration was used for both inter-pair and intra-pair joints.

Figure 2.11: Assembled intra-pair joints at the bottom of the cable. Notable features include copper joint lids and PTFE holder/separator.

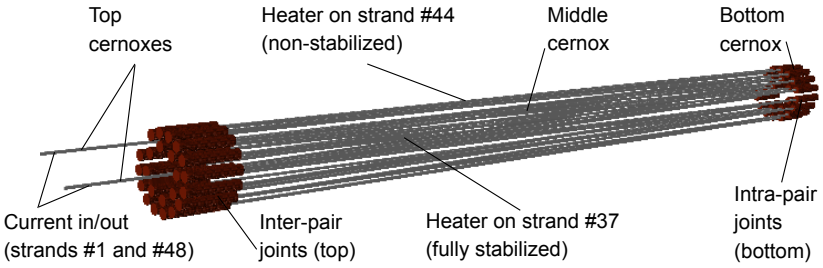

(a) Schematic of 46-strand cable including positions of cernox thermometers and heaters.

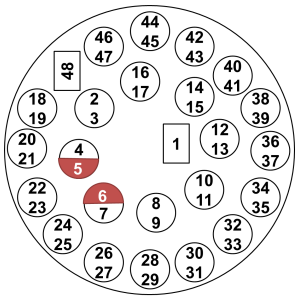

(b) Relative positions of strands (top view, inter-pair joints). Note that although there are 48 strands in the cable #5 and #6 were damaged and therefore had been shorted out (and a connection between strands #4 and #7 made), hence 46 strands were tested.

Figure 2.12: Schematics of 46-strand cable experimental set-up at the University of Southampton.

2.3 Preliminary 2 m Cable Tests: Research Questions

The 2 m-long sample cables used in the 2 m preliminary cable tests were monitored using v-taps which were attached to one of the superconducting tapes in each strand at CERN during the cable manufacturing process. For the tests of the Type-5 MgB_2-Cu cable in the 5 m cryostat, extra v-taps were soldered to each strand of the cable to increase the resolution of the voltage measurements. This was done by locally cutting and unwrapping the Kapton around the region where the new v-taps were to be placed and soldering to the edge of the tapes.

For the testing of the cryostat each strand was treated as a single conductor, assuming that the current was distributed evenly among the superconducting tapes and that a voltage was only measured when current entered the copper tapes because either I, B or T was above I_c, B_c or T_c i.e. it was assumed that which tapes within a strand the v-taps were attached to did not affect the voltage measurement. However, during the 2 m preliminary cable tests, it appeared that a negative voltage value was measured between certain v-tap pairs at the start of a quench or thermal runaway event. It was shown that this was not a reverse of polarity as the voltage value would eventually become positive. Perhaps it was the result of some inductive effect? But this did not explain why it was observed between certain v-tap pairs and not others.

It was ascertained that the negative voltage was only measured between pairs including one of the newly added v-taps. On closer inspection of these it appeared that where the new v-taps had been soldered to the strands, the solder had spread across the edges of multiple tapes and, furthermore, was not consistent in the tapes to which it had adhered; therefore measuring between a new v-tap and its neighbour did not measure the voltage across single tapes and, indeed, often measured between tapes. It was therefore deduced that the negative voltage measured was attributed to current transfer between tapes in the sandwich stack. It is from this observation that the two main research questions of this project were formed:

- What effect does the current transfer between the tapes within a strand, and the contact resistance between the tapes on which the current transfer is assumed to depend, have on cable behaviour?
- Can we observe and measure the current transfer between the tapes and therefore measure the contact resistance between them?

3

Quench Propagation and Detection in CERN 46-Strand Cable

3.1 Introduction

The 5 m-long demonstration cable described in the previous chapter, was built at CERN for testing at the University of Southampton in a purpose-built cryostat. As well as concept validation tests, showing that the cable could work within the design specification carrying 600 A at 25 K, stability tests were carried out to see how the cable behaved in response to disturbances. Investigations into the nature of quench propagation in this particular cable configuration were carried out, as well as experimentation to understand the most effective form of quench detection.

A key feature of the novel CERN cable design is the pressure-only contact between the superconductor and stabiliser layers, and it was unknown how this would effect current sharing and hence stabilising properties. Therefore, adjustments were made to the CERN demonstration cable at the University of Southampton so that the effect of increasing contact resistance between superconducting and stabilising layers could be investigated. The experimental set-up, results and analysis of these tests are discussed in this chapter.

3.2 Experimental Set-up

In order to study the quench properties of the cable, local heaters were used to apply point-like heat deposition to two strands, #37 and #44, which were chosen for their accessibility. Strand #37 was used as the fully stabilised or control case which, apart from the addition of a heater and extra thermometers and v-taps, was unchanged from the original CERN configuration. Strand #44 was used as the (partially) non-stabilised case in which the copper and superconducting tapes were separated by layers of Kapton, as described below. In this way, the effect of the contact resistance in the pressure-only contact between superconducting and stabilising layers could be investigated. In both cases, sections of the outer Kapton wrapping were removed locally to allow access for applying extra v-taps, heaters and thermometers. Great care was taken when applying additional instrumentation and techniques were developed to improve the accuracy of soldering the new instrumentation wires compared to those used in the 2 m preliminary cable tests.

The positions and nomenclature of the strand and joint v-taps attached at CERN are shown in figure 3.1; for strand numbering see figure 2.12b. For example, the voltage measured across strand #2 is that measured between v-taps V04 and V05, written VS04-05 (note the 'S' denotes a strand rather than a joint); for strand #3 the voltage measured is VS06-07; the joint between them, which is located at the top of the cryostat, since they do not form a twisted-pair, is that measured between v-taps V05 and V06, written V05-06.

3.2.1 Fully Stabilised Strand

In the fully stabilised case, two 47-Ω resistance heaters connected in series were applied to the strand, giving a total heater resistance of 94 Ω. Solder was applied across the revealed edge of the tapes, improving the thermal link between them and increasing the homogeneity of heating throughout the strand. The heaters were glued to a strip of copper which was then attached to the solder using GE varnish and insulated from it with a layer of paper. Where v-taps were added solder was also applied across the edges of all the tapes. The positions of the extra v-taps relative to the position of the heater are shown in figure 3.2 where v-taps VS70 and VS71 are those at the top and bottom of strand #37.

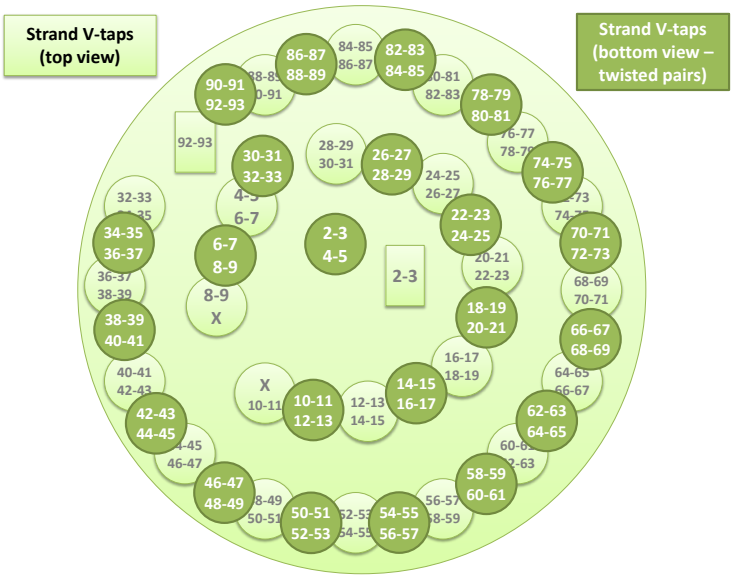

(a) Positions of strand v-tap pairs.

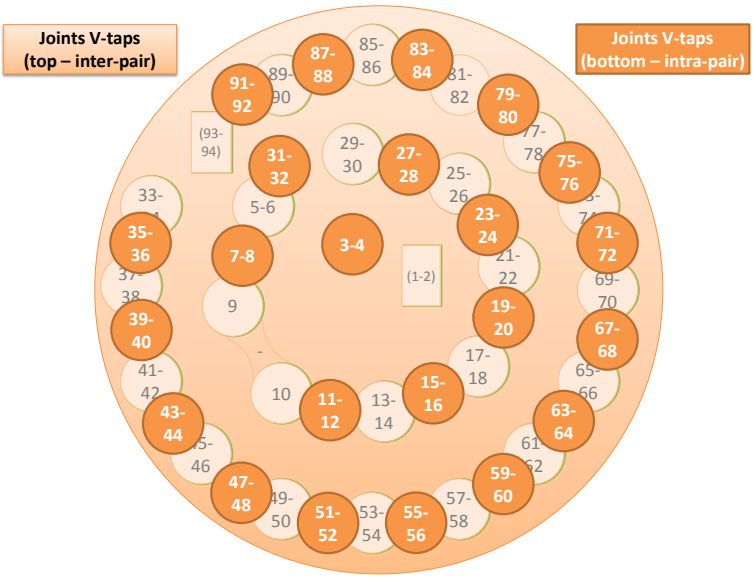

(b) Positions of joint v-tap pairs.

Figure 3.1: Strand and joint v-tap positions, 46-strand cable assembly. Note that V09 is on strand #4 and V10 is on strand #7 and that since damaged strands #5 and #6 have been shorted out, effectively forming a joint between strands #4 and #7, V09-10 measures the voltage across this inter-pair joint.

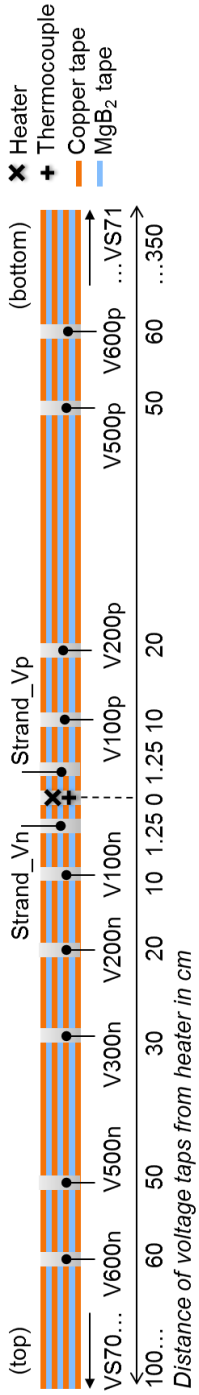

Figure 3.2: Relative positions of additional instrumentation and heater on fully stabilized strand #37.

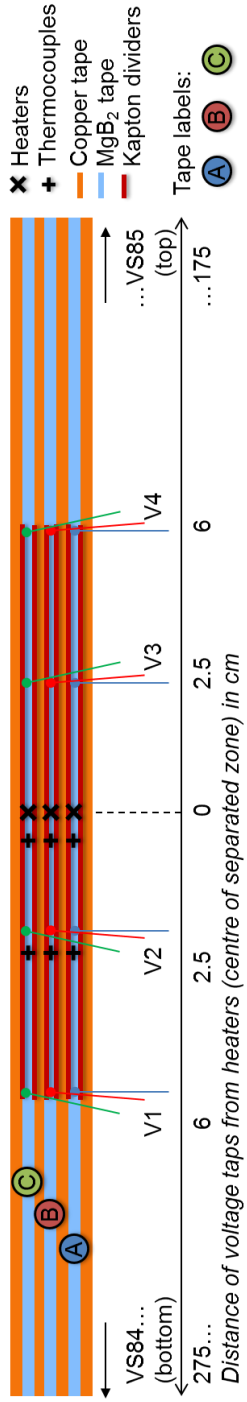

Figure 3.3: Relative positions of additional instrumentation and heaters on non-stabilized strand #44.

3.2.2 Non-Stabilised Strand

In comparison, an effectively infinite electrical contact resistance between the Cu and MgB_2 tapes was created in strand #44 by separating them with Kapton dividers, as shown in figures 3.4a and 3.4b. However, the thermal resistance of Kapton is not infinite and the thermal stabilisation effect of the Cu tapes was not completely removed. Therefore strand #44 may be referred to as the '(partially) non-stabilized' case.

The separated zone was approximately 12 cm long. 47-Ω resistance heaters were applied to each of the superconducting tapes, in the center of this zone, by gluing them to copper 'flags' which were soldered to the edge of the MgB_2 tapes (see figure 3.4c). The three heaters were connected in parallel, giving a total resistance of 15.7 Ω, and shared a common power source. The positions of the extra v-taps relative to the positions of the heaters are shown in figure 3.3 where v-taps VS84 and VS85 are those at the top at bottom of strand #44.

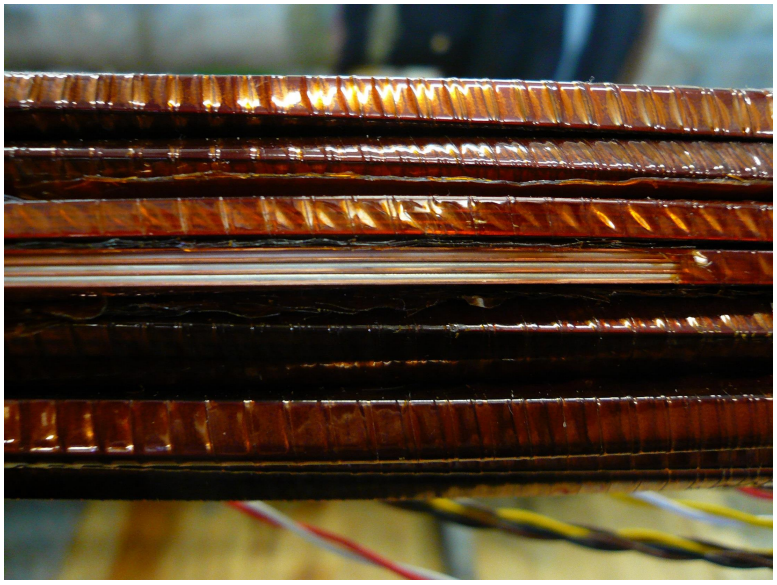

(a) Kapton layers removed to reveal approximately 12 cm of strand #44.

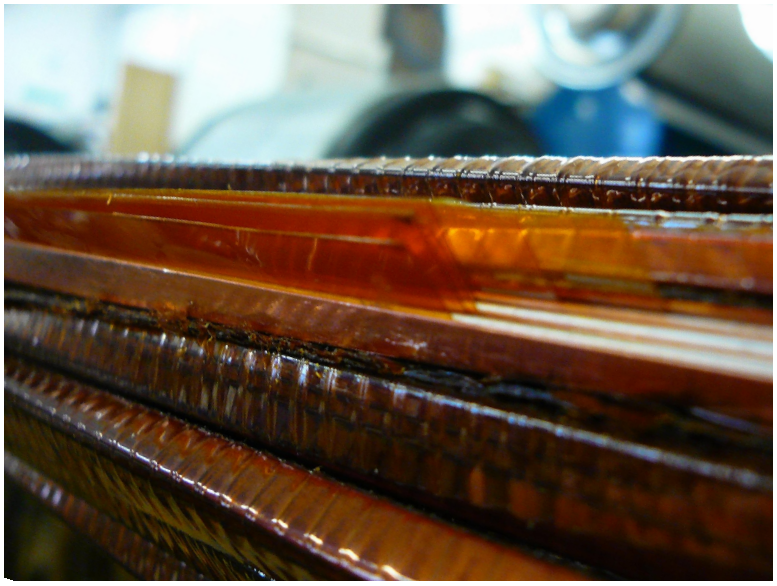

(b) Kapton dividers separating Cu and MgB_2 tapes in strand #44.

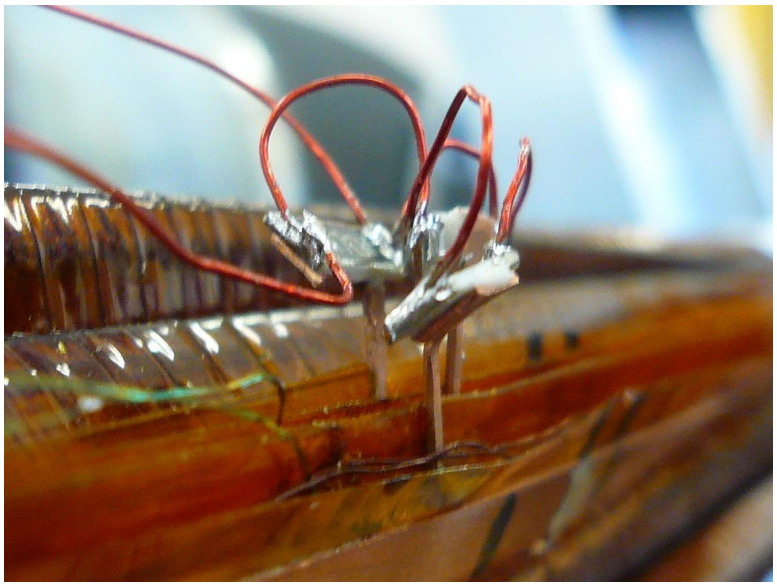

(c) Resistance heaters attached to copper 'flags'; a 'foot' of a flag is soldered to the edge of each of the three MgB_2 tapes in strand #44; heaters are connected in parallel to a single power supply.

Figure 3.4: Adding the Kapton dividers and tape heaters to non-stabilised strand #44, 46-strand cable at the University of Southampton.

3.3 Characterization of Thermal Stability

3.3.1 Minimum Quench Energy (MQE)

For both the stabilised and non-stabilised cases, the same method was used to estimate the Minimum Quench Energy (MQE). First, a constant, direct current was applied to the cable. Then a heat pulse of known duration and power was applied to the strand, from which the applied energy could be calculated. The local temperature increase due to the heat pulse was such that the applied (DC) current was greater than the I_c for the new, increased, local temperature but still below I_c for the rest of the cable.

At applied energies lower than the MQE, a voltage would be observed in the strand that would rise, peak and then decay - the strand would have recovered from the point disturbance. At energies above the MQE the strand would quench. For each given current and operating temperature, heater energies of increasing increments were applied. The MQE lay between the highest energy at which the strand recovered and the lowest energy at which it quenched. An example of such quench and recovery measurements plotted together is given in figure 3.5. Pauses were left between each measurement to allow for cooling before applying the next heat pulse. For temperatures between 22 K and 31 K a variety of current values were applied and the MQE measured for each one.

It is noted that, while every effort was made to insulate the heated region and maintain adiabatic heating of the superconducting tape within the strand, some of the energy will have been lost to the cooling helium gas. Furthermore, as mentioned previously, in the (partially) non-stabilised case, the thermal stabilisation effect of the copper was not completely removed. Both of these factors will have had an effect on the measured MQE values.

Figure 3.6a shows the range between the measured values of Maximum Recovery Energy (MRE) and MQE plotted against normalised current density, j. It is shown that the MQE is higher in the fully stabilised case (1.8 – 9.8 J) than in the non-stabilised case (0.2 – 7.9 J). In both cases the MQE values are higher than has been reported for MgB_2 tapes without additional Cu stabilisation i.e. which is less than 1 J per tape (less than 3 J for three tapes) [70–74].

To calculate j, I_c data taken from preliminary measurements with the cable assembly was used to calculate the approximate I_c value for a given nominal temperature, by

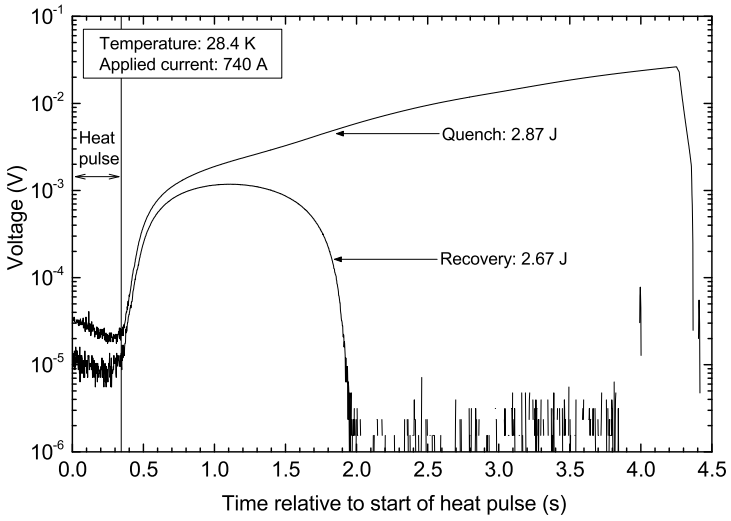

Figure 3.5: Example of quench and recovery measurements used to define MQE plotted together. Example shows V600n-p voltage trace taken from fully stabilized case (28.4 K, 740 A) at applied heater energies 2.67 J and 2.87 J (27 V and 28 V respectively across 94 Ω for 0.34 s).

linear extrapolation. Equation 3.1, from equation 1.2, where A is cross-sectional area, was then used:

$$j = \frac{J_{applied}}{J_C(T)} = \frac{I_{applied}}{A} \times \frac{A}{I_C(T)} = \frac{I_{applied}}{I_C(T)}. \tag{3.1}$$

In figure 3.6b, the MRE-MQE range is plotted against j. MRE is taken as the maximum applied energy which caused no voltage (and therefore transition to the resistive state) in the sample and MQE is taken as the minimum applied energy which caused a voltage in the sample. The range MRE-MQE is plotted using error bars, where the upper and lower bounds of the bars are MRE and MQE respectively, and the mean of the MRE and MQE values is the plotted point between them. Error bars are also used in the j axis where there were uncertainties in the overall temperature at the time the measurement was taken. Figure 3.6b shows that as critical current is approached, the MQE does not disappear, as predicted by the critical state model, but appears to approach a constant value, as predicted by the power law model. Both models predict that for a single MgB_2 tape, in the one-dimensional case, MQE has the following dependence on operational temperature, T_0:

$$\text{MQE} \propto \frac{c_p(T_0)}{J_e(T_0)} \times \sqrt{\frac{k(T_0)}{\rho(T_0)}} \times (T_C - T_0)^{\frac{3}{2}} \tag{3.2}$$

where c_p, J_e, k, ρ and T_C are the specific heat, engineering current density (see glossary entry for J_e), thermal conductivity, normal state resistivity and critical temperature of the MgB_2 tape respectively [6]. In the analysis that follows, physical properties of the MgB_2 tape have been taken from [75] and T_C is taken as 37.5 K.

In equation 3.2, the material properties solely dependent on temperature can be grouped together to form a constant of proportionality. Considering the non-stabilised case, and T_0 = 23 K and 31 K, constants of proportionality of 0.00429 and 0.00577 respectively are found. This suggests that the MQE at 23 K should be approximately 75 % of the MQE at 31 K. However, as figure 3.6a shows we have measured a *higher* MQE at 23 K than at 31 K and, indeed, a general trend for MQE to decrease as temperature increases; a trend which is also seen in [73] and [74]. Further study is required to explain this phenomenon.

3.3.2 Propagation of Resistive Zone

The measurement of the useful property 'normal zone propagation velocity' is less straightforward in materials with a smooth superconducting-to-non-superconducting transition (e.g. most HTS, MgB_2), than in those with a sharp transition (e.g. most LTS) [76, 77]. However, an approximation of a 'resistive zone propagation velocity', v_p, can be made.

Here, this was done by measuring the time between a resistive zone first appearing at one v-tap and at the next v-tap in the direction away from the disturbance source, then dividing by the distance between v-taps. The resistive zone was taken to have appeared at a v-tap when an electric field measuring 1 μV/cm was measured between it and the previous v-tap i.e. that closer to the disturbance source.

In the non-stabilised case velocities of up to 35 cm/s were measured, increasing with applied current and decreasing with temperature (see figure 3.7). Some variation in the three MgB_2 tapes was shown, particularly at higher currents. For the fully stabilised case the non-distinct nature of the initial resistive zone was particularly apparent and very few traces with clear propagations were captured. More data could be collected with improvements to the measurement method, for example, by applying more v-taps

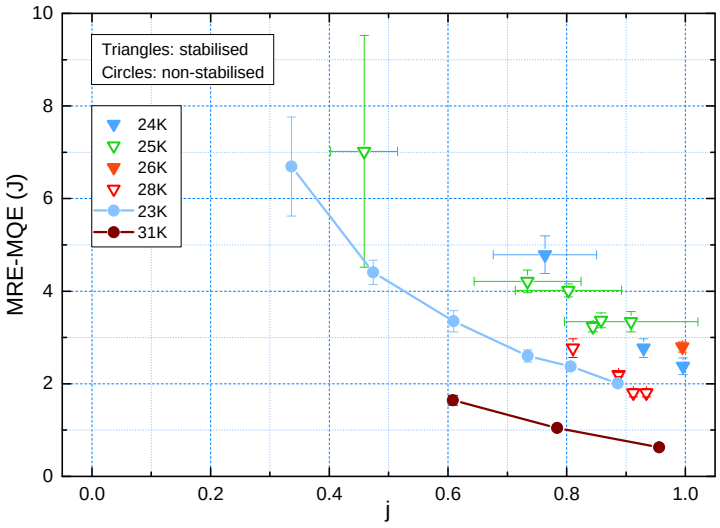

(a) MRE to MQE range as a function of normalised current density j; MQE and MRE values shown as upper and lower bounds of error bars respectively; plotted point value is MRE and MQE mean (j error due to uncertainties in local temperature measurement).

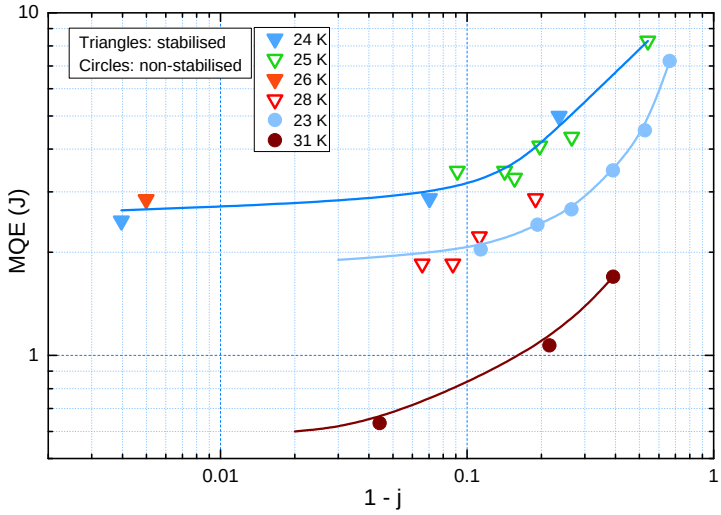

(b) MQE as a function of 1 —j, where j is normalised current density. Both stabilised and non-stabilised cases shown for various temperatures.

Figure 3.6: Minimum Quench Energy (MQE) and Maximum Recovery Energy (MRE) data as a function of (3.6a) j and (3.6b) 1 —j.

closer to the heated region/simulated point disturbance. However, early indications suggest that v_p is greater in the non-stabilised case, following the trend that an increase in MQE corresponds to a decrease in v_p. Not only has this trend been reported elsewhere [70–74] but it also follows from an analytical approach to investigating the properties MQE and v_p. The reasoning is as follows:

1. Adiabatic normal zone propagation velocity can be calculated using equation 3.3:

$$v_{p,adiabatic} = \frac{J}{C} \times \sqrt{\frac{\rho k}{T_{av} - T_0}} = j \times \frac{J_e}{c_p \gamma} \times \sqrt{\frac{\rho k}{T_{av} - T_0}} \tag{3.3}$$

   where J is the applied current density, C is the specific heat capacity and γ the density of the of the MgB_2 tape, taking $\gamma = 8000$ kg/m^3, T_{av} as calculated in equation (3.4):

$$T_{av} = \frac{T_0 + T_C}{2} \tag{3.4}$$

   and all other terms as defined in equation (3.2) [6].

2. Comparing equations 3.2 and 3.3 it can be seen that:

$$\text{MQE} \propto \frac{c_p \sqrt{k}}{J_e \sqrt{\rho}} \text{ while } v_p \propto \frac{J_e \sqrt{\rho k}}{c_p}. \tag{3.5}$$

3. It is therefore not unexpected that an increase in MQE generally corresponds to a decrease in v_p.

Figure 3.7b shows that although only a few data points in the fully stabilized case have been captured they show good agreement with the adiabatic propagation velocity as calculated in equation 3.3. In the (partially) non-stabilised case however, measured v_p values are less than half of those expected from equation 3.3.

3.3.3 'Hot Spot' Temperature

During the quenches in which the MQE and v_p measurements were made, temperature increases in the 'hot spots' or regions around the resistance heaters attached to the sample (see figures 3.2 and 3.3) of up to 63 K were observed (e.g. an increase from 24 K to 97 K). Under different conditions, it was also observed that a quench could be

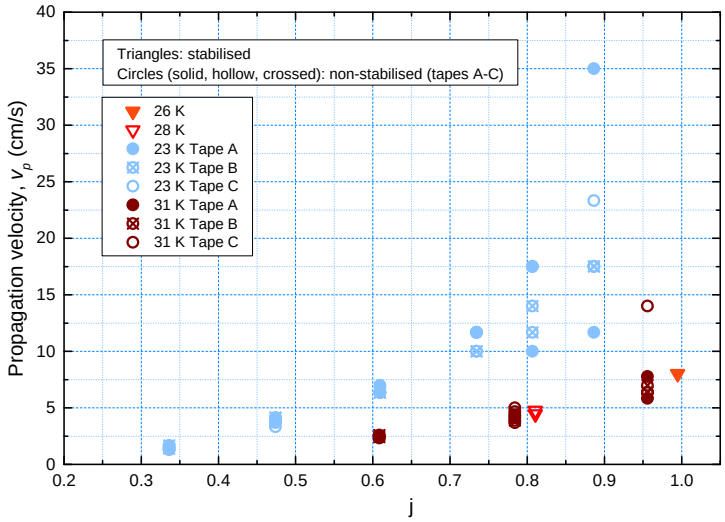

(a) Absolute values.

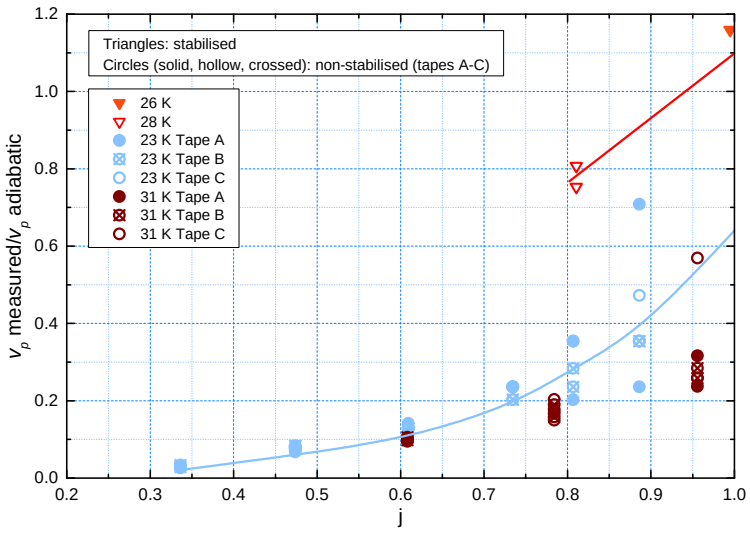

(b) As a proportion of the adiabatic propagation velocity.

Figure 3.7: Resistive zone propagation velocity, v_p, as a function of normalised current density, j, for stabilised and non-stabilised cases.

induced in the sample after an increase in local hot spot temperature of only 5 K, from 26 K to 31 K. The variation appears to be partially due to the ratio of the applied current to the critical current for the given nominal sample temperature, or j (see equation 3.1), where a lower j leads to a higher temperature increase. This could be explained by the fact that when $I_{applied}$ was much lower than I_c, a much higher energy needed to be applied to the sample heater in order to induce a quench, potentially leading to the greater local temperature increase.

Interestingly, the highest hot spot temperature increases were seen in the fully stabilised case, as can be seen in figure 3.8. In the (partially) non-stabilised case, temperature rises of up to 29 K (e.g. from 23 K to 52 K) were observed in the vicinity of the heater and increases of 26 K in the vicinity of v-tap 'V2', 2.5 cm away from the heater, as can be seen in figure 3.9. Note that the TCs across the three superconducting tapes were measured as one, with the overall signal measured being divided by three, so the temperatures measured here are an average of the three tapes in the strand.

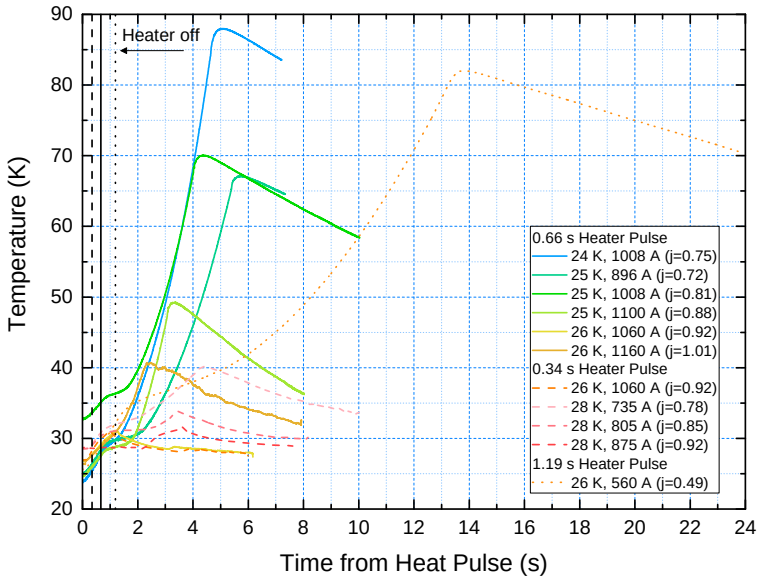

Figure 3.8: Local 'hot spot' temperature rise during quench in strand #37, fully stabilised case, for various applied currents and temperatures (i.e. various j values), and various heater pulse lengths.

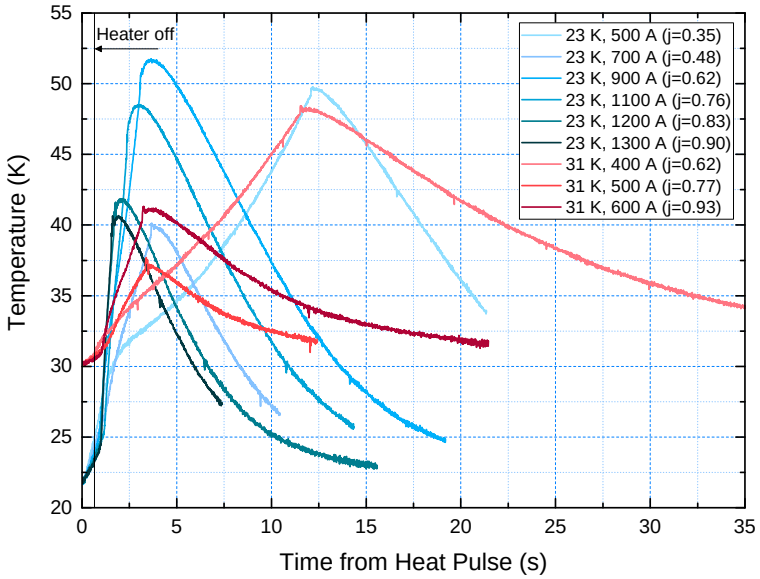

(a) In the vicinity of the sample heater.

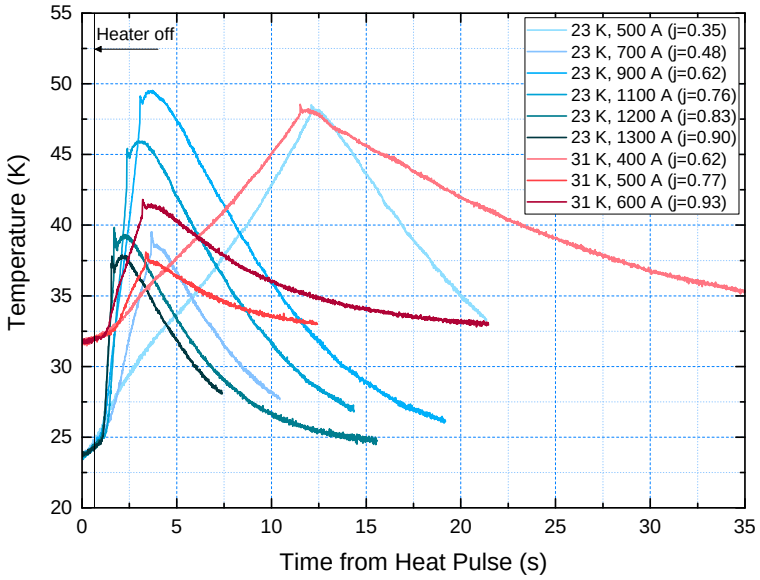

(b) In the vicinity of v-tap V2, 2.5 cm away from the sample heater (see figure 3.3).

Figure 3.9: Local 'hot spot' temperature rises during quench in strand #44, (partially) non-stabilised case, for various applied currents and temperatures (i.e. various j values).

3.3.4 Quench Detection

Quench detection is a vital part of any superconducting component design as discussed in previous chapters. Conventional quench detection relies on voltage measurements. For large-scale/long-length applications such as the CERN HL-LHC proposed superconducting link, a quench or thermal runaway event must generate a high voltage in order to be detectable above the high signal noise. Although the sandwich design increases the thermal stability of the system by increasing the MQE, the time constant before such a detectable voltage is reached, and, therefore, before a quench becomes detectable, is also increased. This is the result of the decreased v_p and the temperature-homogenizing properties of the added Cu tapes.

For example, in the stabilised strand, as shown in figure 3.10, the point at which the quench has most likely propagated 1.25 cm away from the heater to v-taps Strand_Vn and Strand_Vp lies between points I and II. The overall voltage measured across the strand at this point is between 2 and 7 mV. Almost a second later at point III, when the quench has reached v-taps V_100n and V_100p 10 cm away, the overall voltage is 20 mV.

By increasing the contact resistance over a short length, as in the (partially) non-stabilised case, this voltage noticeably increases as shown in figure 3.11. At point I, where the quench has propagated to v-taps V2 and V3, 2.5 cm away from the heater, the overall voltage is 21 mV; this is potentially between 3 and 10 times as large as the voltage in the stabilised strand at a similar point of propagation. Less than half a second later at point II, where the quench has propagated 6 cm away from the heater to v-taps V1 and V4, the overall voltage is 31 mV, an increase of at least 1.5 compared to the stabilised case at a similar point of propagation. The cable remains sufficiently stable or 'recoverable' as in the fully stabilised case.

3.4 Conclusions

3.4.1 Design Specification and Thermal Stability

Design specification and thermal stability tests were carried out on a 5 m-long, 24 × twisted-pair, MgB_2-Cu sandwich cable designed by CERN as part of the LHC HiLumi

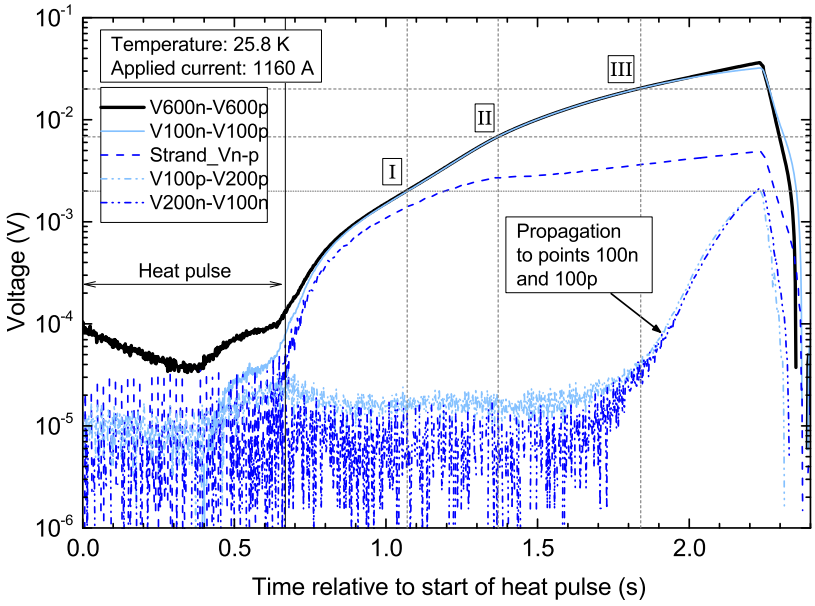

Figure 3.10: Stabilised strand #37. Point I: Overall strand trace V600n-p starts to deviate from Strand_Vn-p; Point II: Change in slope in Strand_Vn-p; possible points of propagation past v-taps Strand_Vn and Strand_Vp. Point III: V600n-p deviates from V100n-p, appearance of quench in V100-200p and V200-100n; quench has propagated past v-taps V100n and V100p.

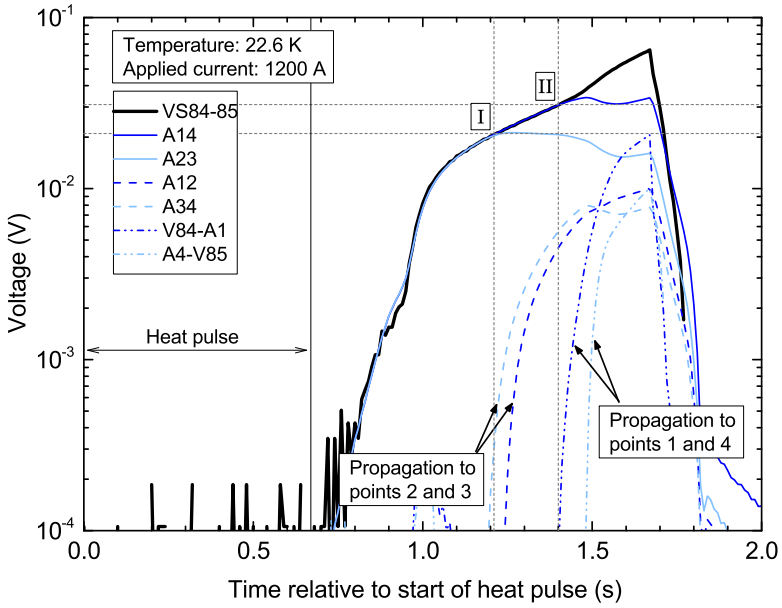

Figure 3.11: Non-stabilised strand #44. Point I: Overall strand trace VS84-85 deviates from A23, appearance of quench in A12 and A34; quench has propagated past v-taps A2 and A3. Point II: VS84-85 deviates from A14, appearance of quench in V84-A1 and A4-V85; quench has propagated past v-taps A1 and A4. Note: Only tape A is shown for clarity; tapes B and C show comparable propagation.

project. The cable design has been tested within the given working specification of 600 A at 25 K and it has been shown that this is well within the capabilities of the cable.

By attaching resistance heaters to individual strands within the test cable it has been possible to apply point-like heat deposition and simulate point disturbances such as those which the cable may experience when in use. Properties such as minimum quench energy (MQE) and resistive zone propagation velocity (v_p) have been measured under a number of conditions by varying operating temperature, current applied and contact resistance between MgB_2 and copper tapes within the strand. It has been shown that the addition of the copper tapes increases the MQE, meaning that the cable is more robust than it would be without the additional copper and able to withstand greater disturbances before a quench occurs.

However, this comes at the cost of reduced v_p so that, should a sufficient disturbance occur and the cable quench, the heated zone would remain localised and an undesirably steep temperature gradient would be produced. Furthermore, the voltage read across the heated strand at this time remains low as only small portions of the strand have started the transition from the superconducting state (where no voltage is measured) to the resistive state. Since the majority of quench detection systems currently rely on voltage measurement, and given the large signal noise expected due to the size of the cable, an increase in voltage measured during a quench is desirable.

These results suggest an optimisation of the cable design. It is hypothesised that by adjusting the parameter MgB_2-Cu tape contact resistance, a cable can be designed that is optimised for both thermal stability (or resistance to quench) and detectability of quench should it occur.

3.4.2 Current Transfer and Contact Resistance

In order to further understand and investigate such an optimisation, more information about the nature of the transfer and distribution of current between superconducting and stabilising layers, as well as how this is affected by contact resistance, is required. During the 2 m preliminary cable tests, it was found that it was possible to measure current transfer between layers within a strand and that the direction of transfer was indicated by the polarity of the voltage measured.

In these tests, as well as the v-taps attached at CERN during the manufacture and assembly of the cable, additional v-taps were added at the University of Southampton.

As described as part of the experimental set-up in section 3.2, the process of attaching new instrumentation wires to the test cable was not simple once the cable had been mounted in the cryostat. The strands within the cable were not easily accessible. This was due to both:

- **The outer Kapton wrapping** — which had to be removed around the area to be worked on, and
- **Limited workspace around the cable** — since the cable needed supporting along its entire length to avoid stresses on the cable-cryostat joints.

To compliment the tests on the 5 m-long demonstration cable, therefore, a bespoke test rig was designed to investigate the current transfer in a single MgB_2-Cu sandwich under various contact resistance configurations.

4

A New Method for Measuring Current Transfer and Contact Resistance

4.1 Introduction

From the cable tests described in the previous chapter, contact resistance between the superconducting and stabilising tapes has been identified as an important variable in understanding the behaviour of the CERN sandwich stack cable design.

4.1.1 Standard Conductor Contact Resistance Measurements

Methods for measuring contact resistance between standard conductors have long been established. Two solid surfaces are held in contact while one conductor is connected to the positive terminal of a current supply and the other to the negative terminal. A v-tap is also connected to each conductor, a current is passed between them and the voltage measured divided by the current applied gives the resistance of the connection [78, 79]. There are many variations in contact forms and holding configurations but the principle of measurement remains the same.

As with all electrical resistance, the greater the surface area of the conductor - or, in this case, the contact area between the two conductors - the smaller the electrical resistance. For a standard conductor this is shown by equation 4.1:

$$R = \frac{\rho \times l}{A} \tag{4.1}$$

where ρ is the electrical resistivity of the conductor, a material property dependent on temperature, l is the conductor length and A is the conductor cross-sectional area.

When looking at the resistance caused by the contact between two conductors, the length of the contact is on the microscale and generally not measurable. The contact area, however, remains an important variable, especially when designing an electrical connection. In the design process it is, in fact, more useful to know the contact resistance in units of $\Omega \times$ unit area for a given pair of materials in a given contact configuration than to know the resistance in Ω of a specific conductor pair set up. For example, if it is known that the contact resistance of a particular electrical joint configuration is 10 Ωcm^2 then, if the design requirement is a resistance of 2 Ω, a joint of 5 cm^2 is required; but, equally, if the design is restricted to an area of 2 cm^2, then the resistance will be known to be 5 Ω.

When talking about contact area between two conductors with reference to the contact resistance between them, what is actually being discussed is generally 'apparent contact area' or the common surface area of the two conductors. Even the most polished surfaces are uneven on the microscale and the actual points of contact are determined by surface asperities or roughness. Only the peaks of the asperities will make contact with each other and these points of contact form 'a-spots', as depicted in figure 4.1a, the combined area of which makes the actual contact surface area, which is generally only a fraction of the apparent surface area, as visualised in figure 4.1b.

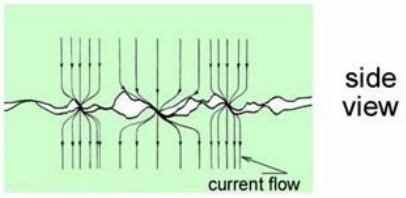

(a) Electrical contact occurs only at peaks of surface asperities.

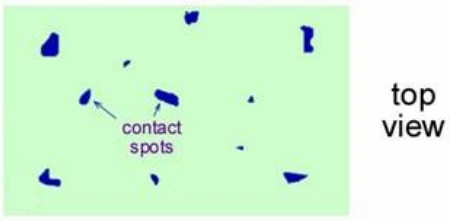

(b) Actual contact surface area (blue) is only a fraction of the apparent contact surface area (light green).

Figure 4.1: Schematics of an electrical contact as seen from: (4.1a) the side, showing the surface roughness of the electrical conductors and the restricted current flow between them; and (4.1b) the top, showing the area of actual contact or 'a-spot' area [80].

For the majority of materials and contact configurations, the actual contact area increases with pressure, as shown in figure 4.2. This is because as the conductor surfaces are forced together under pressure, the a-spots deform, widening and flattening, and the actual contact surface area increases. How readily the a-spots deform depends on the hardness of the conductor materials.

4.1.2 Contact Resistance Measurements Involving Superconductors

Unlike in standard conductor contact resistance measurements, temperature is a very important factor in contact resistance measurements involving superconductors. Due to the high currents applied, the heat transfer both between and within components and due to the cooling system, and the strong dependencies of material properties such as electrical resistivity and heat capacity on temperature, particularly at cryogenic temperatures, the electrical and thermal properties of the system form strong and dynamic co-dependencies which are not seen in standard conductor systems. Note that a superconducting system above its critical temperature, T_c, can generally be treated as a standard conductor system with a severely reduced current-carrying capacity.

Tests have so far been carried out to measure the joint resistances of joints between two superconducting components [81–85] and between superconducting and resistive components [86, 87] using much the same experimental set-ups as those used for standard conductor contact resistance measurements such as those described in [78, 79]. Investigations into determining the Current Transfer Length (CTL), the length over which current transfers from the normal metal matrix to the superconducting filament within a superconducting component, both theoretically and experimentally, have also been carried out [88, 89].

4.1.3 Superconductor-Stabiliser Contact Resistance Over a Significant, Un-Soldered Length

However, no evidence of measurement of contact resistance along a significant length of un-soldered superconductor-stabiliser contact has been found. Nor has any comprehensive study of the current distribution between superconducting and stabilising components or layers.

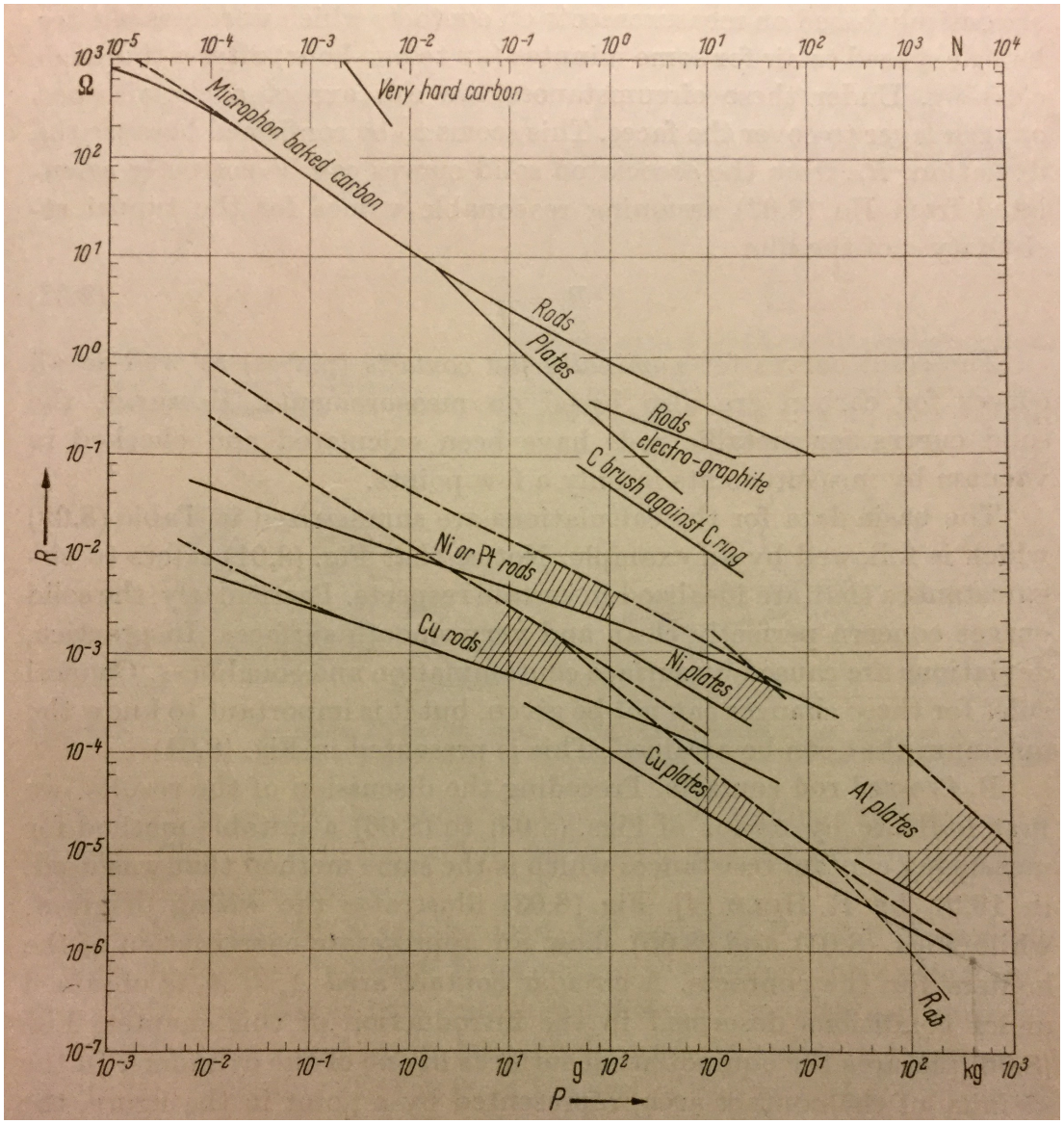

Figure 4.2: Contact resistance, R, for various common conductor materials and contact styles ('rods' which are crossed rod contacts and 'plates' which are nominally flat contacts), plotted against contact load, P, where: solid lines show clean contacts; dashed lines show materials in air (which have therefore become covered by a monolayer of oxygen); and associated solid and dashed lines are shown by shading between lines [78].

To this end, bespoke experimental facilities were designed and built to simultaneously test the contact resistance and map the current distribution between superconducting and stabilising tapes of up to 200 mm in length, in a temperature range of approximately 30-40 K, in the small-sample cryogenic testing facilities at the University of Southampton. For the superconducting layer, MgB_2 tapes in a nickel matrix from the same manufacturing batch as those used in the CERN prototype cable described in chapter 3 were used. For the stabilising layer, copper tapes of the same specification and dimensions as those in the CERN cable were used. This chapter describes the testing facilities, the experimental and sample set-ups and experimental methods, and the contact resistance calculation methods. The results and conclusions are discussed in chapter 5.

4.2 Test Facilities

4.2.1 The Cryostat

A double-walled, vacuum-insulated stainless steel vessel was used to contain samples in a cryogenic environment. Samples were brought to cryogenic temperatures by use of a cryocooler. The thermal connection to the cold head of the cryocooler was provided by copper bars which were soldered to the cryostat-sample interface (or 'platform' - see section 4.2.2) and soldered and bolted to a copper flange which was in turn connected to (but electrically insulated from) the second stage of the cryocooler.

The electrical connection to an external current supply was provided via HTS current leads which were cooled by liquid nitrogen. These provided a thermal break in the system between the sample at very low temperatures and the external environment at room temperature, thus increasing the system efficiency. The cryostat also featured sealed exit ports for instrumentation and control connections. Figure 4.3 shows the internal features and connections of the cryostat including a sample mounted on the sample-cryostat interface or 'platform'.

4.2.2 The Cryostat-Sample Interface (Platform)

The cryostat was designed for use with multiple samples. To allow samples to be changed easily a cryostat-sample interface or 'platform' was used. The platform con-

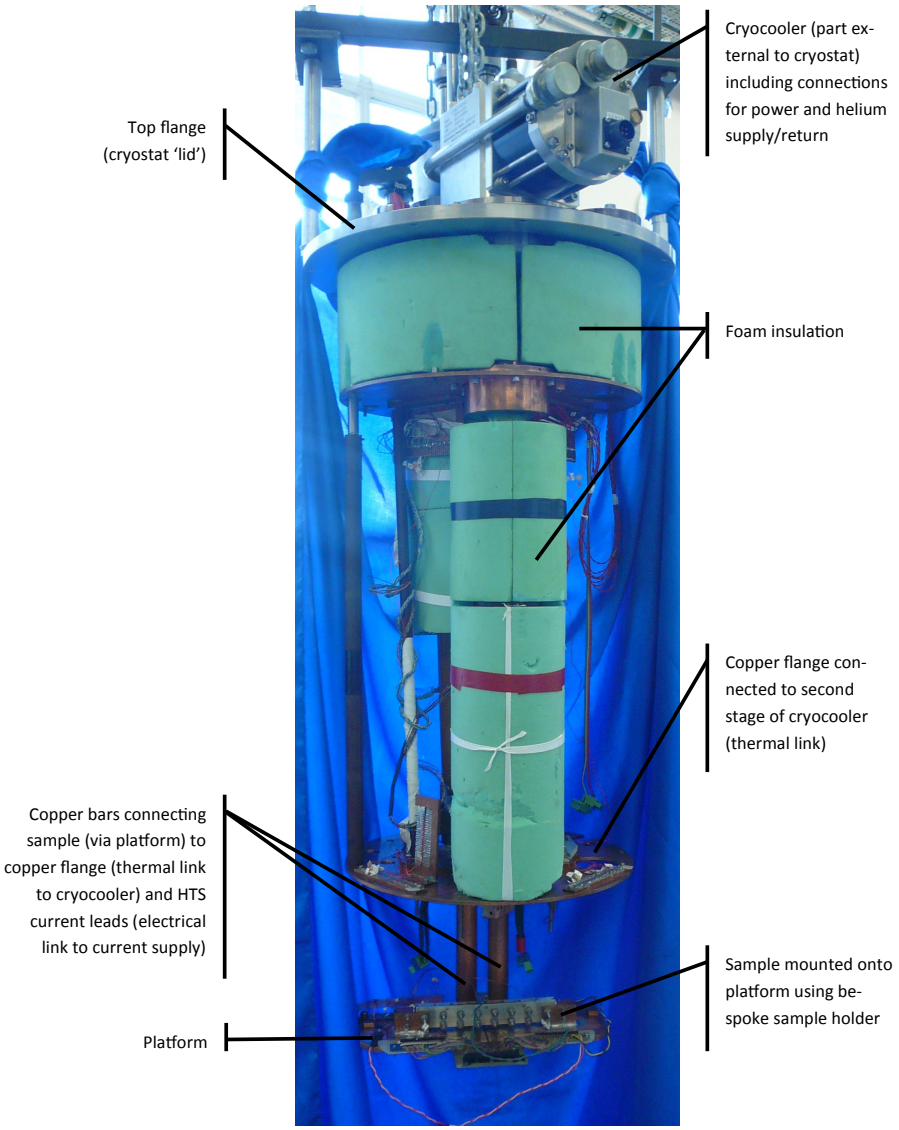

Figure 4.3: Experimental set-up for current transfer and contact resistance measurements: inside the cryostat, with sample-platform-cryocooler-cryostat connections highlighted, at the University of Southampton.

sisted of two copper plates mounted on and electrically insulated from each other by a G-10 holder.

A copper bar was soldered to each of the plates. These bars provided both the electrical connection to the external current supply (via HTS current leads) and the thermal connection to the cryocooler via the copper flange connected to the second stage of the cryocooler.

The platform temperature was monitored using cernox thermometers. Cernoxes in their protective housing were coated in grease for better contact and fitted inside small copper blocks which were glued to each side of the platform with GE varnish. A resistance heater with a layer of grease was bolted to each side of the platform. Using a PID controller to adjust the power to the heaters, the temperature of each side of the platform could be controlled. The PID had two input and two output channels so the heater-cernox pair on each side of the platform could be controlled independently. Samples, either directly or in bespoke sample holders, could then be mounted on the platform with one end soldered to each copper plate.

The platform also featured capacity for connections for instrumentation. A piece of stripboard attached to the 'left' side of the platform provided a thermal reference point for TCs. This was covered by a copper strip which provided a thermal shield from the crycooler cold head above it.

Figure 4.4 shows the platform away from the cryostat with a sample mounted using the bespoke sample holder used for the contact resistance measurements. Figure 4.5 shows the platform layout.

4.3 Experimental and Sample Set-Up

4.3.1 Experimental Set-up: Simple Clamp Sample Holder

For a series of preliminary tests to validate the concept of measuring contact resistance between superconducting and stabilising tapes over a significant, un-soldered length, a prototype experimental set-up was designed and built, known as the 'simple clamp sample holder'.

The clamp consisted of two pieces of copper bar each glued to a rectangular strip of G-10. Helicoils were inserted into one G-10 strip and clearance holes were drilled in the other so that the two sides of the clamp could be bolted together. The sandwich tapes

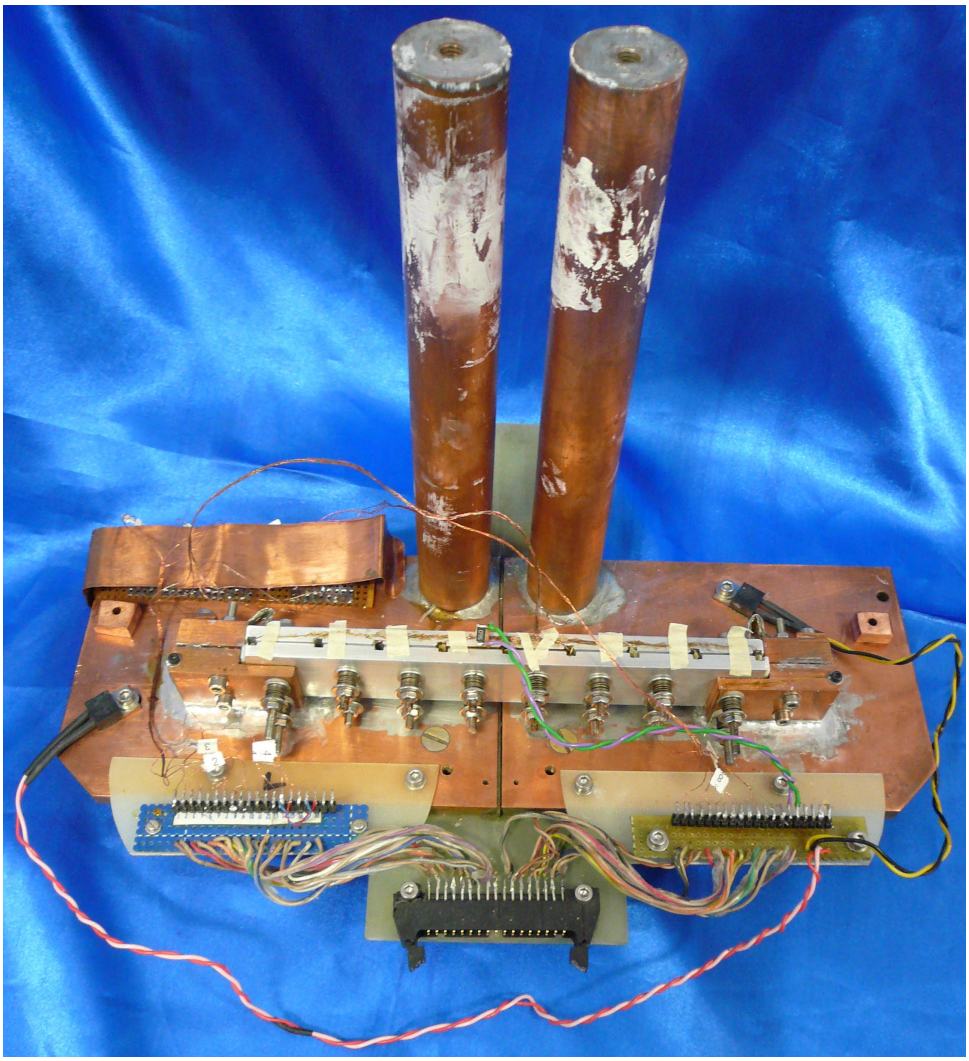

Figure 4.4: Experimental set-up for current transfer and contact resistance measurements: cryostat-sample interface or 'platform' with sample mounted using bespoke adjustable clamp sample holder, at the University of Southampton.

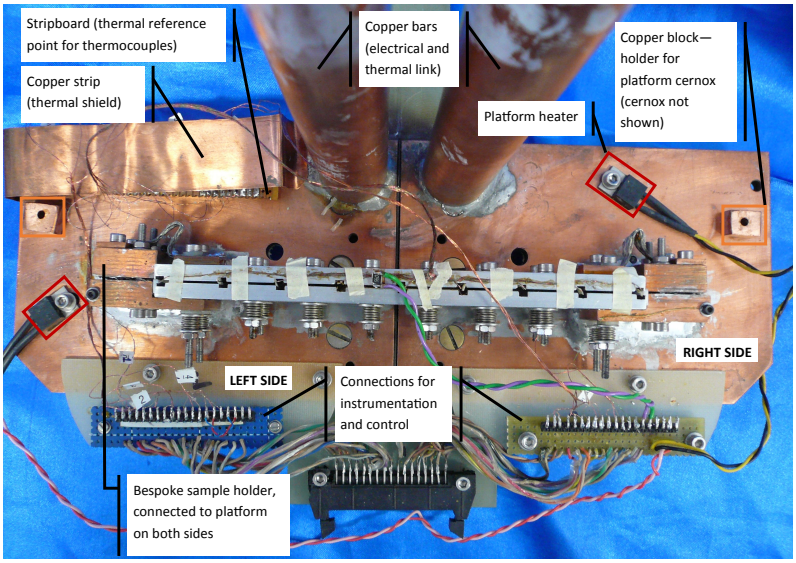

(a) Platform with sample mounted: top view, labelled.

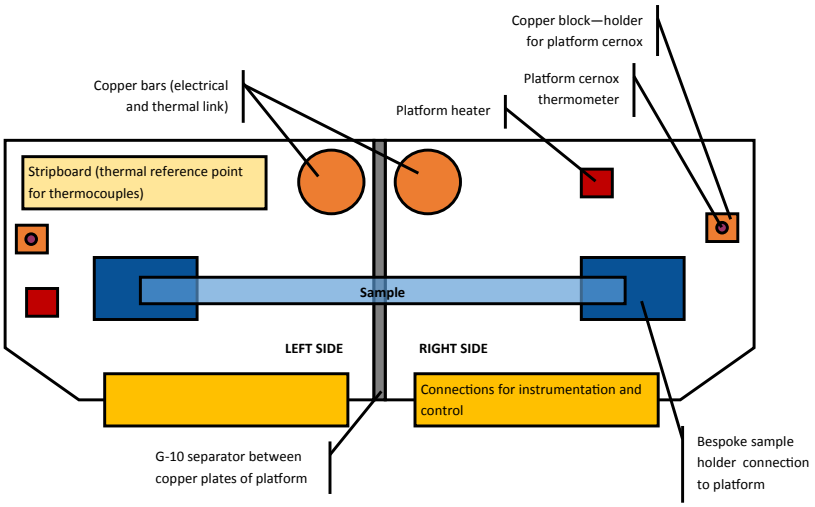

(b) Schematic of figure 4.5a.

Figure 4.5: Experimental set-up for current transfer contact resistance measurements: layout of platform components including sample mounted using bespoke sample holder, at the University of Southampton. Note: For unlabelled components on left side of platform see equivalent components on right side.

were clamped between the copper bars which were covered in adhesive Kapton tape to electrically insulate them from the sample. The purpose of the copper bars was to homogenise the temperature along the length of the sample. The clamp simulated the pressure contact made by the non-adhesive Kapton wrapping in the CERN sandwich strand design.

The G-10 pieces were shorter than the sample to be tested. The protruding ends of the sample were soldered between small copper blocks which in turn were soldered to the platform, providing the electrical and thermal link to the current supply and cooling system.

The tests carried out using this clamping system validated the concept of contact resistance and current transfer measurements within a sandwich stack over a significant length (up to 200 mm).

4.3.2 Experimental Set-up: Adjustable Clamp Sample Holder

To further the investigations, an adjustable clamping system was constructed which gave greater control over the pressure under which the sample was held, allowing measurements to be taken under multiple pressure configurations and therefore tape behaviour under different contact resistances to be observed.

4.3.2.1 Clamp Pieces

The clamp consisted of two pieces of aluminium each 164 mm long, 25 mm wide and 5 mm thick. In one of the clamp pieces pairs of 3 mm clearance holes were drilled at 20 mm intervals; these were mirrored by pairs of 3 mm tapped holes in the other clamp piece. In between each pair of holes on each clamp piece were 3 mm-wide and 1.5 mm-deep grooves to run instrumentation wires in and to account for the thickness of the solder attaching the instrumentation wires to the sample. Adhesive Kapton tape was used to electrically insulate the clamps from the sample. G-10 runners were glued to one of the clamp pieces to keep the sample in position. The aluminium clamp pieces are shown in figure 4.6. Note that the end holes were of a larger diameter to allow for fixings to the copper blocks which provided the electrical and thermal link to the platform.

Aluminium was used, like the copper bars in the preliminary sample holder, to homogenise the temperature along the length of the sample. Although aluminium

has a lower thermal conductivity than copper and would therefore be less effective a material at temperature homogenisation, it has the benefit of being easier to machine. By clamping directly with the homogenising material rather than via a bar of it attached to a clamp, more control was given over the pressure applied.

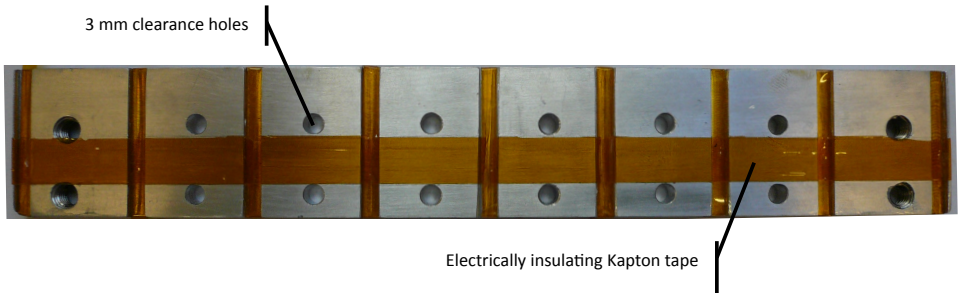

(a) Front clamp piece.

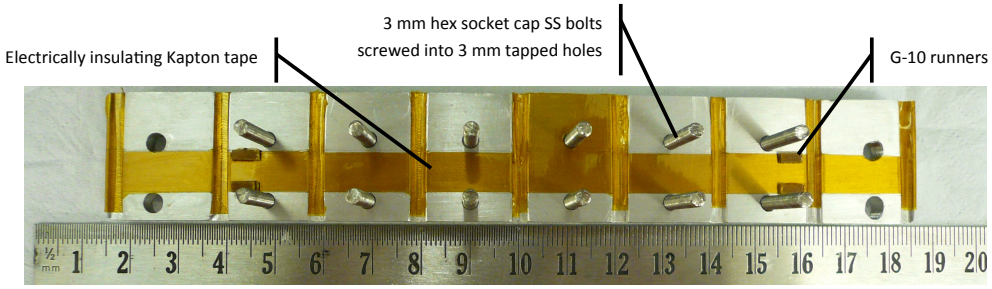

(b) Back clamp piece.

Figure 4.6: Adjustable aluminium clamp, made at the University of Southampton.

4.3.2.2 Controlling Clamping Pressure

The clamping pressure was adjusted using 3 mm SS bolts and Belleville washers. Belleville washers or disc springs are frusto-conical shaped washers which behave like a spring in that they deflect a known amount under a given force. In this instance washers of 6 mm external diameter, D_e, were used which had a maximum deflection,

$s_max.$, of 0.15 mm per washer under a force of 109.9 N. A schematic of a Belleville washer is shown in figure 4.7.

In order to increase the deflection per unit force so that it is easier to measure, it is possible to stack Belleville washers in parallel. In this instance a stack of 12 washers was used on each bolt so that the maximum deflection was 12×0.15 mm = 1.8 mm. A schematic of a 12-washer parallel stack is shown in figure 4.8a.

Note that by stacking washers in series, the amount of force required to produce the same deflection would increase; for example, figure 4.8b shows a 12-washer series stack which, if made of the same washers used here, would deflect 0.15 mm under 12×109.9 N = $1,318.8$ N. However, this technique was not used in this instance.

By measuring the deflection of the washer stacks it was therefore possible to estimate the force being applied under each stack. Each full turn of the bolt head whilst tightening corresponded to a deflection equal to the pitch of the bolt thread, in this instance 0.5 mm. A tightening regime was instigated to minimise buckling and bending of the sample whilst applying pressure homogeneously: bolts were tightened half a turn at a time (0.25 mm deflection) starting from the bolts in the middle of the clamps and working outwards. Washer stack height was monitored while applying pressure by counting the number of turns the bolts were tightened, and then measured with digital vernier calipers to confirm homogeneous final deflection, s. s was calculated from the stack height using equation 4.2,

$$s = h_{0,stack} - h_{final,measured} \tag{4.2}$$

where $h_{final,measured}$ is the final, measured washer stack height and $h_{0,stack}$ can be found using equation 4.3,

$$h_{0,stack} = h_{0,singlewasher} \times n_{washers} \tag{4.3}$$

where $h_{0,singlewasher}$ is the undeflected height of a single washer and $n_{washers}$ is the number of washers in the stack. In this instance $h_{0,singlewasher} = 0.45$ mm and $n_{washers} = 12$ so $h_{0,stack} = 5.4$ mm.

Note that equation 4.3 is valid since the Belleville washers were stacked in parallel. If the washers were stacked in series, $I_{0,stack}$ would be found using equation 4.4,

$$h_{0,stack} = h_{0,singlewasher} + (n_{washers} - 1) \times t \tag{4.4}$$

where t is washer thickness.

Using the measured final deflection, the force applied under each washer stack could therefore be interpolated from the force-deflection data in [90], reproduced in figure 4.9 as a function of both measured deflection and no. of turns (where one turn corresponds to 0.5 mm deflection). As 12-washer stacks were used under each of the 16 bolts in the adjustable clamp sample holder (including those which also provided fixings to the copper blocks described in section 4.3.2.3), the total force applied would be 16 × this value.

In order to calculate the pressure under which the sample was measured, this force must be divided by the sample area. During initial tests pressure-sensing film was used to monitor the local pressure and confirm the homogeneity of the pressure applied. During these tests it was noticed that the area under the grooves in the clamps was under little or no pressure. Therefore the area of sample under pressure, $A_{underpressure}$, is the difference between the total clamped area and the area under the grooves, as in equation 4.5:

$$A_{underpressure} = w_{sample} \times (l_{sample,clamped} - l_{grooves,total}). \tag{4.5}$$

The sample width, w_{sample}, in this case refers to that of the Cu tape which is 3 mm. The SC tape was wider at 3.5 mm but only the part of the SC tape in contact with the Cu tape was under pressure. The length of sample which was clamped, $l_{sample,clamped}$, is also that of the Cu tape which is approximately 1 mm shorter than the length of the clamps at each end or 164 mm - (2 × 1 mm) = 162 mm. Since each of the grooves are 3 mm wide and there are 9 grooves in total, the total length of sample under the grooves is 9 × 3 mm = 27 mm. Therefore the area of sample under pressure is 3 mm × (162 mm - 27 mm) = 3 mm × 135 mm = 405 mm^2 or 4.05×10^{-4} m^2. The sample pressure applied as a function of both measured deflection and no. of turns (where one turn corresponds to 0.5 mm deflection) is shown in figure 4.10.

4.3.2.3 Connection to Platform

As with the simple clamp, the sample was connected to the platform via copper blocks. On one side (the front) the blocks were L-shaped so that the clamps could rest on them and be suspended above the platform. The clamps were electrically insulated from the

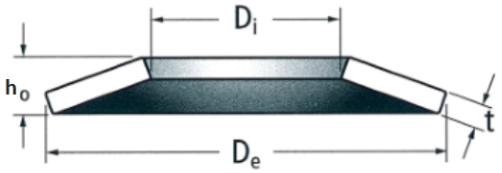

Figure 4.7: Schematic of a Belleville washer. D_e is external diameter, D_i is internal diameter, h_0 is un-compressed washer height (0 mm deflection) and t is thickness, [90].

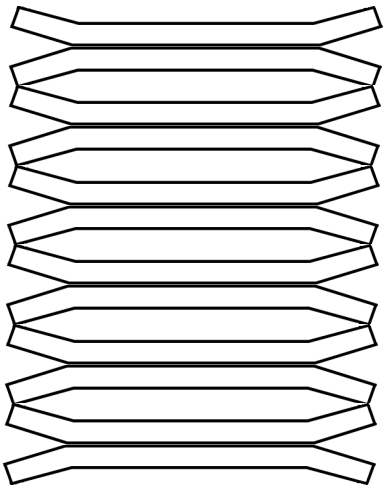

(a) 12-washer parallel stack as used in the adjustable clamp sample holder; deflection of stack is 12 × deflection of a single washer under a given force.

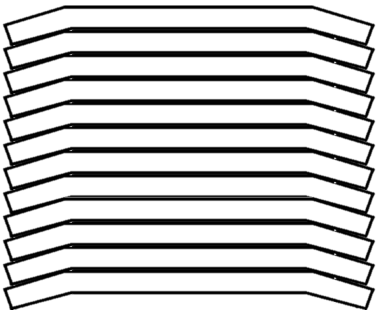

(b) 12-washer series stack (example, not used here); deflection of stack is the same as the deflection of a single washer under 12 × the force.

Figure 4.8: Schematics of Belleville washer stacks.

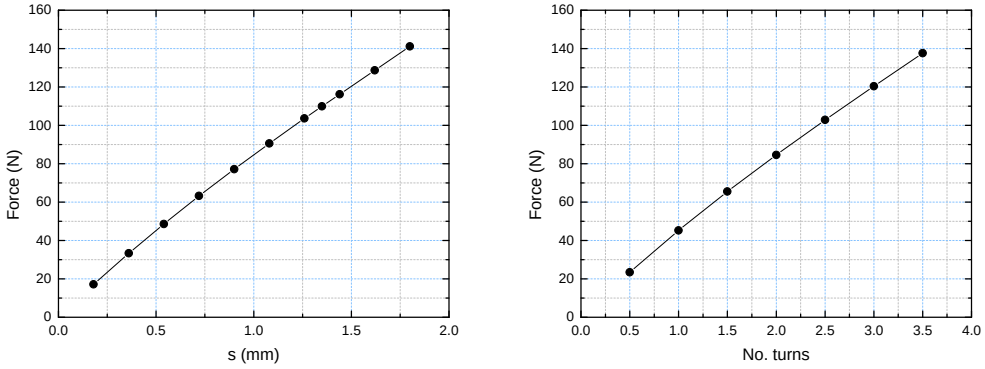

(a) Force vs deflection, s.

(b) Force vs no. turns.

Figure 4.9: Force applied as a function of (4.9a) Belleville washer deflection and (4.9b) no. of bolt head turns (where one turn corresponds to 0.5 mm deflection) for a 12-washer parallel stack. Adapted from [90].

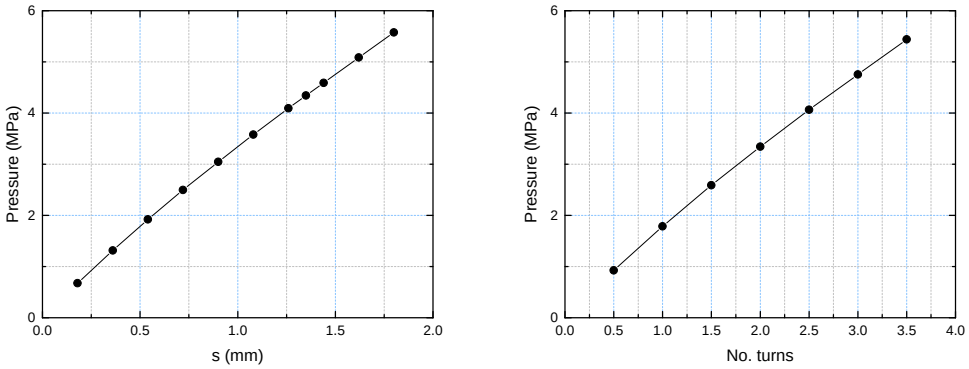

(a) Pressure vs deflection, s.

(b) Pressure vs no. turns.

Figure 4.10: Pressure applied to sample as a function of (4.10a) Belleville washer deflection and (4.10b) no. of bolt head turns (where one turn corresponds to 0.5 mm deflection) for 16 $\times$ 12-washer parallel stacks over a sample surface area of 4.05×10^{-4} m^2. Adapted from [90].

blocks by both adhesive Kapton tape and L-shaped pieces of PTFE, as seen in figure 4.11.

On the other side (the back) the copper blocks were in two pieces: the main block which was connected to the platform and to which the sample was soldered (figure 4.12); and a flexible extension of the main block in the form of a pair of copper tabs attached to either end of a piece of copper braid, with one tab bolted to the main block and the other to the back clamp (and electrically insulated from it by adhesive Kapton tape). A sample in the adjustable clamp sample holder with both front and back copper blocks highlighted is shown in figure 4.13.

The original design used L-shaped copper blocks supporting both the front and back clamps. However, this did not leave any flexibility to account for differential thermal contraction of the various materials in the system. Furthermore, should all of the parts not have lined up perfectly due to any imperfections in their manufacturing, the sample could have ended up under potentially damaging strain. The contact between the SC tape, the Cu tape, the clamps and copper blocks could also have differed significantly from one end of the sample to the other creating inhomogeneities in the temperature and current sharing. The back blocks were therefore adapted to the block-and-tab design described above. This added a degree of flexibility to the system whilst maintaining thermal contact between the back aluminium clamp piece and the platform.

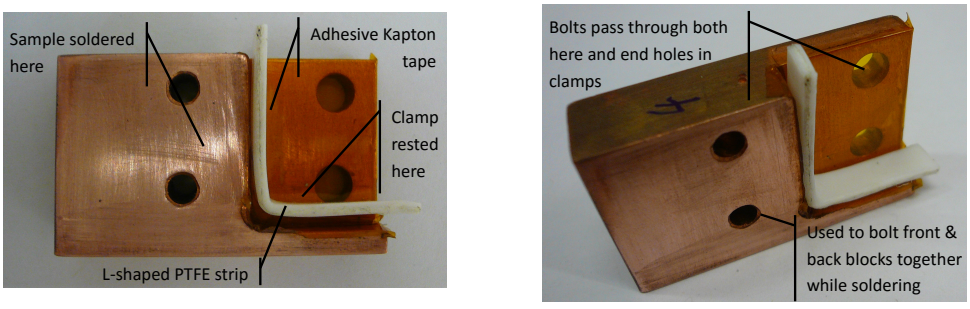

(a) Inner face. **(b)** Top view.

Figure 4.11: One of two front copper L-shaped blocks used as the thermal and electrical link from the sample in the sample holder to the platform; shown from two different angles; including Kapton tape and L-shaped PTFE strip used to electrically insulate blocks from clamps.

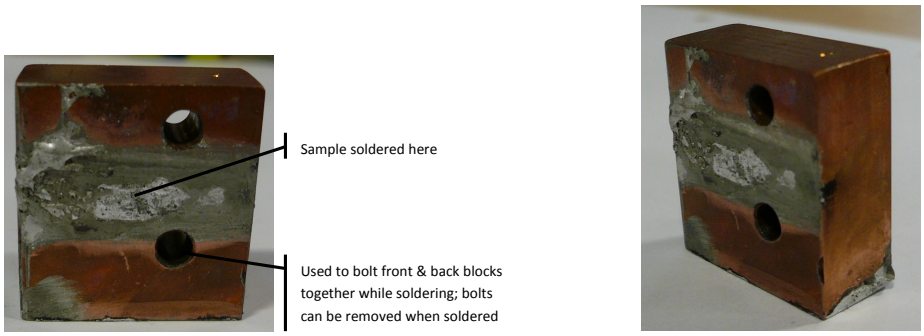

(a) Inner face. **(b)** Side view.

Figure 4.12: One of two back copper blocks used as the thermal and electrical link from the sample in the sample holder to the platform; shown from two different angles.

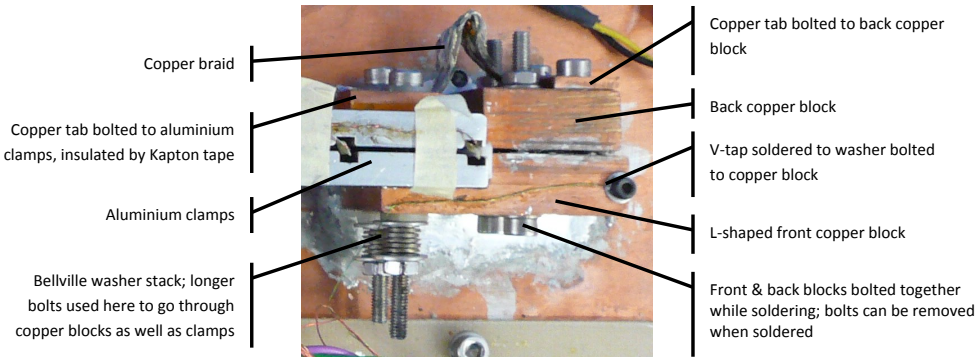

Figure 4.13: Front and back copper blocks, including copper tabs joined by copper braid, assembled with the aluminium clamps and soldered to the platform; top view.

4.3.3 Preliminary Sample Set-up: Single Sandwich in Simple Clamp Sample Holder

The preliminary tests in the simple clamp sample holder were carried out on a 'single-sandwich' consisting of one MgB_2 tape in the middle of two Cu tapes. After clamping in place between the aluminium clamp pieces, the ends of the tapes were soldered together and then soldered to and bolted between the small copper blocks which provided the electrical and thermal link to the platform. Current injection was therefore to all three tapes simultaneously. However, it is known that copper forms a better electrical contact with the commonly used tin-based solder than the nickel metal matrix of the MgB_2 tape. Therefore it can be assumed that some or all of the current initially injected into the Cu tapes and transferred into the SC tapes over a length comparable to the CTL within a superconductor.

A resistance heater was installed in the centre of the sandwich to give greater control over thermal runaway occurrences and current transfer between layers. For example, current transfer from the SC to the Cu tapes could be induced by using the tape heater to create a temperature gradient along the length of the sandwich and applying a current that was below I_c for the ends of the tape where the temperature was lower but above I_c for the heated section of the tape; therefore current would flow in the SC tape at the ends where it offered the least resistive path and then be forced to transfer into the Cu tapes around the heated section.

Voltage taps were placed at seven points along the SC tape and one of the Cu tapes. Voltage was measured along each tape and between the SC and Cu tapes at each point. It was noted that, as observed in the negative voltage seen in the 2 m preliminary cable tests, the polarity of the SC-Cu voltage measurements changed depending on the direction of current transfer. For example, when the tape heater was used and current was diverting into the copper tapes around the heated section, SC-Cu voltage on one side of the heated section was positive (suggesting SC-to-Cu current transfer) and negative (suggesting Cu-to-SC current transfer) on the other side.

4.3.4 Intermediate Sample Set-up: Single Sandwich in Adjustable Clamp Sample Holder

Originally, the same single-sandwich configuration of one MgB_2 tape and two Cu tapes was tested in the improved experimental set-up of the adjustable clamp sample holder, with v-taps on the superconducting tape and on one of the stabiliser tapes, and a tape heater in the middle to induce temperature gradients along the tape length. As with the preliminary set-up, it was shown that current transfer could be observed and that the direction of the transfer was indicated by the polarity of the voltage measured between Cu and SC tapes. However, it became clear that, with the single-sandwich configuration, it was not possible to accurately ascertain or measure the magnitude of current transferring as the following factors were unknown:

- The CTL of the current injection into the SC tape,
- How much current the SC tape was carrying either side of the heated section,
- Any information about the unmeasured Cu tape.

With regards to the second, unmeasured Cu tape, it was originally assumed that the unmeasured tape would behave similarly enough to the measured tape that the two Cu tapes could be considered symmetric. However, it became apparent that this was an invalid assumption. For example, at one stage during test development, the non-measured Cu tape was replaced when the measured Cu tape was not. Contamination and oxidation of the old, measured Cu tape meant that the SC-Cu contact was much worse on the measured side than the non-measured side where no such degradation had yet occurred to the new tape. This yielded strongly asymmetric current transfer between the SC tape and the two Cu tapes and, consequently, the results were very difficult to interpret.

4.3.5 Final Sample Set-up: Half-Sandwich in Adjustable Clamp Sample Holder

The final sample, described as a 'half-sandwich', consisted of a single SC tape and a single Cu tape. As in the previous sample set-ups, the tapes were held together by compressive forces only to simulate the conditions of the CERN sandwich strand

design. The half-sandwich configuration using a single Cu tape, as opposed to a SC tape sandwiched between two Cu tapes trialled in previous set-ups, had multiple advantages.

With only two tapes in the sample, all tapes could be measured where it would not have been possible to measure three tapes to the same resolution without significant adjustments to the small-sample cryostat. This vastly simplified the required interpretation of the measurements and ensured that the current distribution of the entire sample could be measured throughout the tests.

Another of the problems in interpreting the results was that the current was injected into all three tapes at once and, due to the superior solder contact of the Cu tapes, it was very likely that the current injected preferentially to the Cu tapes rather than the SC tape. To overcome this issue, the final sample set-up was designed so that the SC tape was longer than the Cu tape. Only the SC tape was soldered to the copper blocks and the Cu tape was shorter than the clamp pieces so that the current injected fully into the SC tape.

This set-up meant that all the current applied could only be flowing in the SC tape at the ends of the sample and if it was forced to share with the single Cu tape this could only happen within the measured section so that a complete current transfer journey could be mapped.

4.3.5.1 Tape Heater

As in the preliminary and intermediate tests, a resistance heater was applied to the centre of the sample to give greater control over local thermal runaway current and current transfer between the SC and Cu tapes. However, in this case, the control it gave served a slightly different purpose, since the current was injected only into the SC tape and there were only two possible current paths - the SC and Cu tapes - which already gave more control over the current transfer than previously.

Due to the almost symmetrical nature of the current transfer from SC to Cu on the LHS and from Cu to SC on the RHS, R_C measurements in the centre where the direction of transfer changed and very little current transferred, were often inaccurate. By using the tape heater to create a temperature gradient along the sample and, therefore, force more current to transfer in the central regions, R_C values closer to the centre of the sample - or, more accurately, the point of the change of direction in the current transfer as this was observed not to be in the very centre of the sample - could be obtained.

Similarly, the reduced current transfer at the ends of the tapes in the heated cases meant that the measured R_C values here were less reliable and so non-heated cases were still investigated to ensure a full range of R_C values could be calculated.

The tape heater was attached to the SC tape using the 'flag' method described in the large cable tests in section 3.2.2 and figure 3.4c: a resistance heater was glued to a copper 'flag', the 'foot' of which was soldered to the edge of the SC tape. An example of such flags are shown in figure 4.14. Note that the sample shown in figure 4.14a still used the method of laying instrumentation wires along the sample edge and securing them with GE varnish which was not used in the final experimental method (discussed in the following sections). Figure 4.14b shows the tape heater in the final sample set-up with current in/out wiring attached. In order to prevent a short circuit between the copper flag and the aluminium clamp pieces, extra Kapton tape was used, as shown in figure 4.15.

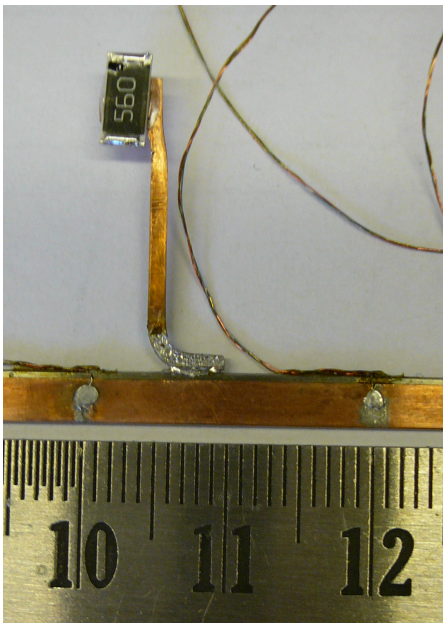

(a) Tape heater attached to SC tape of sample using copper 'flag' method; note that the method of attaching other instrumentation shown here is not the final method used.

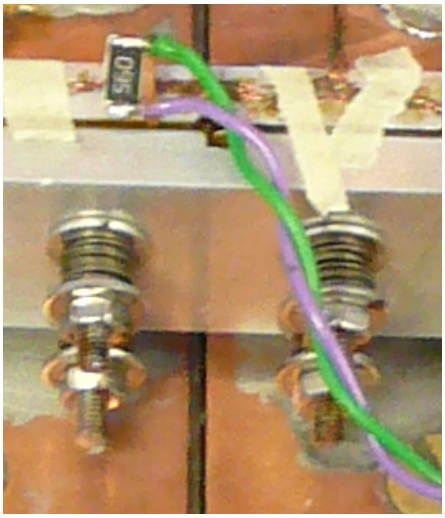

(b) Tape heater in final sample set-up with current in/out wires attached.

Figure 4.14: Tape heater used to improve range of R_C values available.

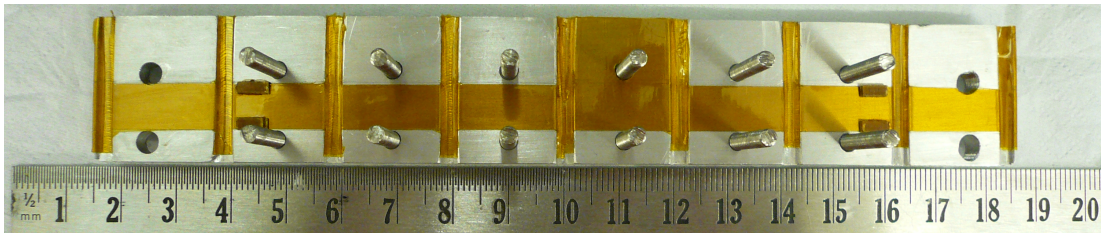

Figure 4.15: Aluminium clamp piece with electrically insulating Kapton tape including extra coverage in middle to avoid short circuit between the tape heater flag and the clamp piece. The SC tape would lie from 0 cm to 20 cm on the steel rule shown in the figure.

4.3.5.2 Voltage Measurement

V-taps which, on the SC tape, doubled as TCs (see the following section 4.3.5.3), were soldered to the tapes at nine positions at 20 mm intervals, as shown in the schematic in figure 4.16. V-taps were labelled 1 to 9 from left to right, consistent with the left and right sides of the platform as shown in figure 4.5.

Another advantage of the half-sandwich configuration was the ability to solder voltage taps to the sides of the SC and Cu tapes (of widths 3.5 mm and 3 mm respectively), rather than the edges of the tapes (of thicknesses 0.65 mm and 0.2 mm respectively). Whilst developing the test method, with wires soldered to the edges of the tapes, the twisted instrumentation wires were drawn along the edges of the tapes and secured with GE varnish to minimise wire bending and potential for wires to break or become disconnected from the sample. However, it was discovered that the GE varnish penetrated between the SC and Cu tapes significantly increasing the contact resistance. In the half-sandwich set-up with the wires soldered to the sides of the tapes it was possible to securely bring the wires vertically away from the tapes and out of the clamps, without any need for GE varnish inside the clamps.

4.3.5.3 Temperature Measurement

Temperature measurement of the sample was carried out using TCs. By twisting in a constantan wire with the copper v-taps and soldering the copper-constantan joint to the sample, temperature could be measured at the same points as voltage without a high increase in instrumentation demand. The copper-constantan junction formed part

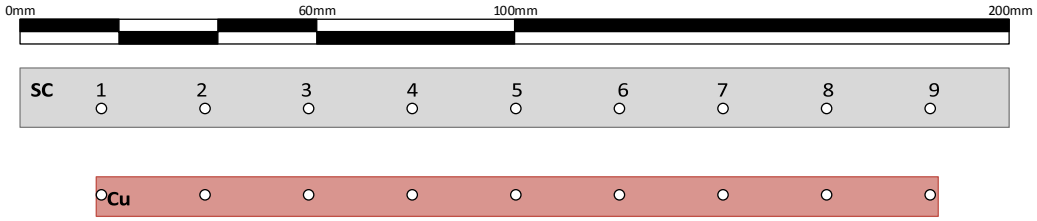

Figure 4.16: Schematic showing positions of v-taps and TCs on SC and Cu tapes in half-sandwich sample, labelled 1 to 9 from left to right, at 20 mm intervals.

of a differential Type T TC. Type T is a common choice of TC for cryogenic functions due to its ability to measure at very low temperatures.

Using differential TCs, a reference point was required and in this case the platform was used. The copper-constantan wires were brought to and soldered to the stripboard which was glued and bolted to the LHS of the platform. From the stripboard copper wires brought the signals out of the cryostat (see figures 4.4 and 4.5). The constantan-copper joint via the stripboard acted as the differential joint at the reference temperature. It was assumed that all the joints on the stripboard were at the temperature of the platform, which was taken to be the nominal set temperature measured by the platform cernoxes. It was also assumed that, along with the homogenising properties of the aluminium clamps, the contact between the Cu and SC tapes was good enough that there was little or no temperature difference between them; therefore only the temperature of the SC tape was measured.

The voltage difference measured across the copper-constantan junction on the sample was relative to the temperature difference between that junction and the reference junction on the stripboard or the measured point on the sample and the nominal or platform temperature. The temperature of the sample could therefore be interpolated using the nominal temperature and Type T TC voltage difference-temperature data.

4.3.5.4 Other Instrumentation Configuration

At each position along the sample the Cu wire on the Cu tape (v-tap) and the Cu and constantan wires on the SC tape (v-tap and TC) were gently twisted together by hand before the sample was placed in the clamp, to form a 'twisted-triplet'. Faster twisting methods which resulted in a smaller twist-pitch such as using an electric hand drill were experimented with (twisting wires together before soldering to the tapes); however, the extra stresses caused by this method on the wires led to them breaking very easily, sometimes causing short circuits between the sample and the aluminium clamps.

The twisted-triplets of instrumentation wires from each point were then brought along the edge of one of the clamp pieces to the centre (around point 5), being secured to the outer edge of the clamps by GE varnish. This minimised the induction loops in the measured signals which would be significant given the large current that would be flowing in the tapes. It also made the system more robust as the wires were less likely to be disturbed, tugged, caught or broken when manoeuvring the sample holder. The bundle of 27 wires was then coated in GE varnish and brought to the stripboard where the individual wires were connected (as seen in figure 4.5 and discussed in previous sections).

As mentioned previously, the stripboard, which was glued (also using GE varnish) to the platform was used as the thermal reference point for the TCs. It was also the point of connection for the instrumentation wires soldered directly to the sample and the instrumentation wires that would carry these signals to the instrumentation ports of the cryostat. This connection also increased the robustness of the system by further protecting the fragile instrumentation wires from any buffeting during experimental set-up as well as making it easier to load and unload multiple samples using the platform.

The measuring configuration was designed so that real-time voltage-time data was acquired and displayed for the following:

- $V_{SC}x - y$ — Voltage drops between neighbouring sections along the SC tape,
- $V_{Cu}x - y$ — Voltage drops between neighbouring sections along the Cu tape,
- $V_{SC-Cu}x$ — Voltage drops between SC and Cu tapes at each position,

- $V_{TC}x$ — TC voltage measurements on the SC tape at each position, which were later converted to the temperature difference between the sample and the platform in K (and, consequently, the temperature of the sampe).

Note that in this instance 'x' refers to the position of a given v-tap (labelled 1-9 as in figure 4.16) along the tapes and 'y' to the neighbouring position where $y = x + 1$.

4.4 Measurement Method

The following is a description of the test procedure of the final sample and experimental set-up, a half-sandwich in the adjustable clamp sample holder. This procedure was derived from the concept validation tests using a single sandwich in the simple clamp sample holder and the set-up finalisation tests using a single sandwich in the adjustable clamp sample holder.

Measurements were carried out at various temperatures and applied currents for two pressure contact scenarios, both with and without use of the tape heater. Both steady state and transient conditions were investigated. The final measurement methods and scenarios investigated are described below.

4.4.1 Pressure Contact Between SC and Cu Tapes

The two contact scenarios tested were as follows:

- **'Bolts Tightened'** — In the Bolts Tightened (BT) scenario, the bolts of the adjustable clamp were tightened to full Belleville washer compression, a total washer deflection of 1.8 mm. From the data in figure 4.10a this equates to a tape contact pressure of approximately 5.6 MPa. This is the best contact or lowest R_C achievable with this particular experimental set-up.

- **'Bolts Loosened'** — In the Bolts Loosened (BL) scenario, the bolts of the adjustable clamp were loosened so that the total Belleville washer compression was 0.6 mm. From the data in figure 4.10a this equates to a tape contact pressure of approximately 2.1 MPa and therefore provided a higher R_C case to compare with the BT scenario.

4.4.2 Applied Current

At temperatures below T_c, steps of increasing current were applied until the critical current, I_c and, then, the quench or thermal runaway current, I_{quench} were reached. The criteria used to define these characteristic current values for the sample were as follows:

- **'Critical current',** I_c — The current at which 10 μV was measured across a given section, i.e. 5 μVcm^{-1} since each section was 2 cm long. This was the most reliable voltage measurement resolution possible for the observed signal noise, after filtering (smoothing).

- **Quench current,** I_{quench} — The current at which both an exponentially increasing voltage and sample heating were observed.

Thermal runaway current data gathered in the preliminary sample and experimental set-up tests were used was used to estimate the I_c region of the sample at each temperature. This is shown in the results and discussion chapter in figure 5.1.

The current was applied in two steps, each lasting one second, where the first step was a 'sacrificial' current step: the large change in current from 0 A to the applied current induced voltages in the system seen as a 'spike' in the voltage-time trace; to avoid this spike interfering with the data or unintentionally causing a quench, the first current step was always lower than I_c so that after the spike no voltage was seen due to flow of current in the sample; the first step was long enough (one second) that the induced voltages had settled (the voltage traces had returned to their zero values after the spike); and the difference in current between the first, 'sacrificial' step and the measurement step was small enough that the induced voltages due to this change in current were minimal. Thus, the effect of 'inductive voltage spikes' on the useful measurement data caused by the step application of current to the sample was minimised.

At temperatures above T_c where low currents were used, the inductive voltage spikes were negligible and single current steps of 5, 10 and 15 A were applied, each one second long.

4.4.3 Nominal Temperature and Forced Temperature Gradients

Each scenario was investigated at temperatures above and below the T_c of MgB_2 which is between 37.5 K and 38 K. The temperatures investigated were: 40 K, 37.5 K, 37 K, 36 K, 35 K, 34 K, 33 K. Measurements were also attempted at 31 K but this was at the limit of the capability of this experimental set-up due to the high I_c at this temperature; and at 38 K and 39 K but they were not significantly different from the 40 K measurements.

As described previously in section 4.3.5, a tape heater was used to create temperature gradients along the sample length and allow a wider range of R_C values to be calculated. Unlike the large-scale tests described in chapter 3, in which a constant current was applied and then a pulse of power applied to the heater, in this instance a steady temperature gradient was set up by applying a constant power to the tape heater and waiting for the temperature gradient to settle. Then the current steps (two steps, each one second long) were applied as in the non-heated scenarios. Measurements were taken with three different heater powers creating three different temperature gradients, as shown in table 4.1. When post-processing the data it was observed that the '3 V' scenario provided a practical compromise between sufficiently measurable forced current transfer (unlike the '2 V' scenario) and minimised overheating (unlike the '4 V' scenario). The 'heated' scenarios used in the analysis that follows therefore refer to the 3 V measurements unless otherwise stated.

Heating Scenario - voltage across heater (V)	**Heater Power (mW)**	**Local Temp. Increase (K)**
2	64	0.2
3	144	0.4
4	257	0.8

Table 4.1: Heating scenarios tested using tape heater to create temperature gradients along sample length. Note: 'Local Temp. Increase' estimated using average difference between TC readings at point 5 (heated region) and nominal sample temperature with no current applied.

4.4.4 Steady State and Transient Cases

At temperatures at and around T_c the current distribution was constant with time or 'steady state'. For analysis purposes, an average value of the measured voltages was used in these scenarios. It is noted that although a small amount of Joule heating was exhibited, the cooling was sufficient that the effects of this on the system were negligible.

In the majority of cases, however, the response investigated was transient. For a given applied contact, current and nominal temperature, current would redistribute within the measured one second step, as signified by the measured voltage-time traces. In order to analyse these cases, data was extracted for given instances in time or 'time slices'. The times at which data was extracted were generally those at which the highest voltages were reached before the effect of heating on the resistivities of the Cu and SC tapes became dominant. Where multiple 'phases' of current distribution (as discussed in the following results section) were observed, multiple time slices which demonstrated an example of each phase were investigated where possible.

4.5 R_C Calculation Method

As discussed previously, the measurement of contact resistance between a superconducting and normal metal tape, over the length of the tape, at cryogenic temperatures and, in particular, at a nominal temperature below the T_c of the superconducting material, is not a simple process. The method described in this body of work underwent many iterations during its development. Of these, two key iterations which function as independent methods are described in this section:

- A *preliminary method* which was first used to approximate R_C values and validate the concept, and,
- The *final method* from which the analyses that follow are derived.

In the following method descriptions, the examples shown are from a series of tests taken at 40 K i.e. above the T_c of the sample but still at a low temperature. This is because without the added heat and current transfer complexities seen when the sample is the superconducting state - that is, treating the tapes as two normal conductors of

varying resistivity values - gives the clearest picture of the R_C calculation methods. Results from tests carried out at temperatures below the T_c of the sample are discussed in the analyses that follow.

4.5.1 Preliminary Method: Discrete Resistors Model

The simplest way to interpret the voltage measurements was to model the tapes as a series of discrete resistors, as shown in figure 4.17.

First, the temperature of each resistor was estimated by taking the mean of the TC readings either side of it. For example, for the resistor modelling a tape section between v-tap 1 and 2, the temperature of that section, T_{1-2} was given by,

$$T_{1-2} = \frac{T_1 + T_2}{2}. \tag{4.6}$$

Equation 4.6 can be written more generally as:

$$T_{n-(n+1)} = \frac{T_n + T_{(n+1)}}{2} \tag{4.7}$$

where n is the v-tap number.

Using the temperature for a given section of Cu tape modelled as a single, discrete resistor, its resistivity could be interpolated from the resistivity of copper as a function of temperature. Two copper resistivity data sources were considered:

- Resistivity of a sample of the Cu tape used, calculated at the University of Southampton using a PPMS, and,
- Reference data for copper with a RRR of approximately 400, available from the CDA [91].

As can be seen from figure 4.18, for temperatures down to approximately 30 K, the measured resistivity of the Cu tape is highly comparable to the CDA reference data although, at temperatures below 30 K, it is clear that the residual resistivity of the measured sample is higher than that of the reference data. However, as all tests were carried out at temperatures above 30 K and the reference data contained more data points, a linear interpolation of the CDA reference data was used to calculate copper resistivity.

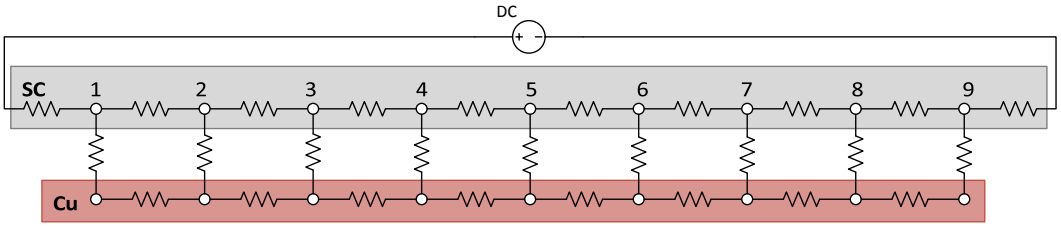

Figure 4.17: Schematic of discrete resistors model of 'half-sandwich' tapes including voltage tap numbers. Note that current injection is via the SC tape only.

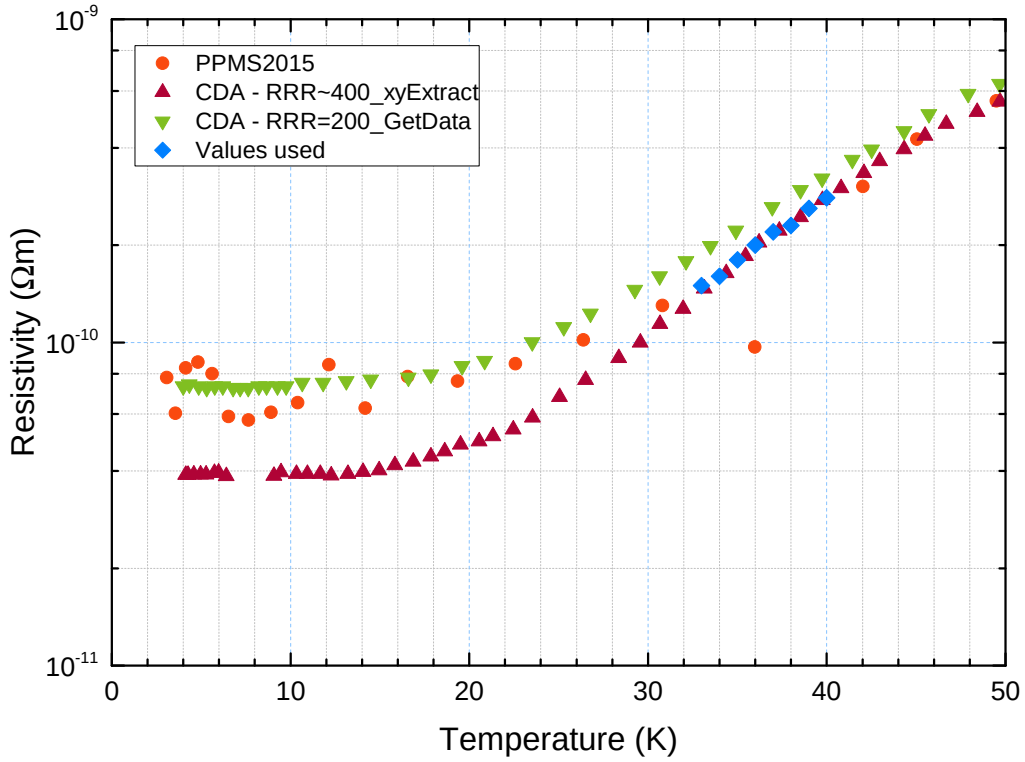

Figure 4.18: Copper resistivity as a function of temperature: PPMS2015 - from a sample of the Cu tape used, as measured at the University of Southampton in a PPMS; CDA - RRR∼400 - reference data for copper with a RRR of approximately 400 [91]; CDA - RRR = 200 - reference data for copper with a RRR of 200 [91]; Values used - resistivity values used in calculations that follow.

The resistance of a given section of Cu tape, at a given temperature, could then be calculated using equation 4.1 and the Cu tape dimensions, as shown in equation 4.8:

$$R_{Cusection} = \frac{\rho_{Cu}(T) \times l_{section}}{A_{section}} \tag{4.8}$$

where $l_{section}$, the length of the tape section modelled as a resistor, is the distance between two v-taps, in this case 20 mm or 2×10^{-2} m; and $A_{section}$, the cross-sectional area, is that of the Cu tape, in this case 3 mm $\times$ 0.2 mm or 6×10^{-7} m^2.

The current carried by each section of Cu tape, $I_{Cu,n-(n+1)}$, could therefore be calculated simply using Ohm's law, equation 1.1, interpreted in this case as:

$$I_{Cu,n-(n+1)} = \frac{V_{Cu,n-(n+1)}}{R_{Cu,n-(n+1)}} \tag{4.9}$$

where $V_{Cu,n-(n+1)}$ is the measured voltage drop across a section and $R_{Cu,n-(n+1)}$ is the resistance of a section as calculated in equation 4.8.

As current must be conserved, any difference in current between neighbouring Cu tape sections must be attributed to current transferring between the Cu and SC tapes. For example, working from left to right, if $I_{Cu,1-2}$ was less than $I_{Cu,2-3}$ then current would have transferred into the Cu tape, from the SC tape, between voltage taps 1 and 3. In the discrete resistors model it was assumed that this current transfer happened at point 2 and that the vertical resistor shown there between the SC and Cu tapes represents the contact resistance at that point (as shown in figure 4.17).

This simplifies the calculation so that to calculate the contact resistance at point 2, the voltage measured between the SC and Cu tapes at point 2, $V_{SC-Cu,2}$ would be divided by the estimated current transferred between sections 1-2 and 2-3, namely $I_{Cu,2-3} - I_{Cu,1-2}$. This can be written more generally as is shown in equation 4.10, the contact resistance equation used for the discrete resistors model:

$$R_{C(DR),m} = \frac{V_{SC-Cu,m}}{I_{Cu,m-(m+1)} - I_{Cu,(m-1)-m}} \tag{4.10}$$

where m is the v-tap number such that, from previous equations, $m = n + 1$. An example of a contact resistance profile as calculated using this method is shown in figure 4.19.

It is important to note that this model results in a contact resistance with the units of Ω as it represents a particular resistance to the current flow between two particular

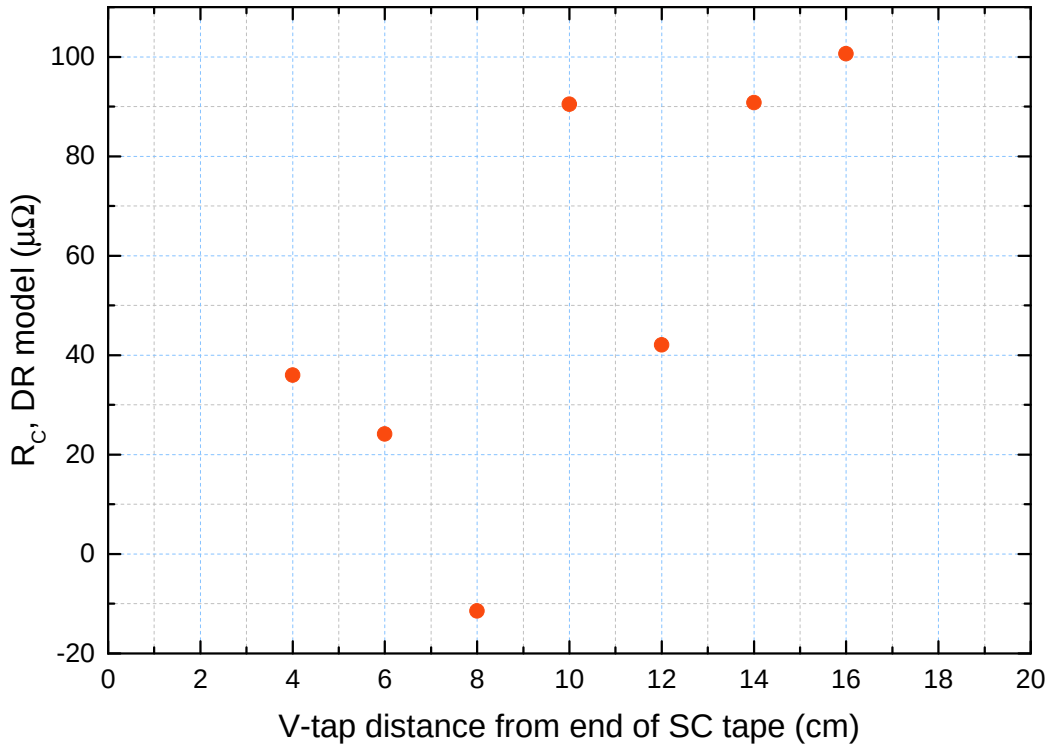

Figure 4.19: An example of contact resistance approximation along tape length as calculated using the discrete resistors model; 40 K, no tape heater, 15 A applied, bolts tightened. Note that the negative value at 8 cm has no practical sense and is an artefact of the misalignment of the measured SC-Cu voltage and the assumed point at which the estimated change in direction of current transfer takes place. Note also that this method is limited in the x-range i.e. it does not estimate R_C values for the full length of the Cu tape (2-18 cm from the end of the SC tape).

conductors in contact and does not, therefore, give contact resistance information as would be useful in the design process, as was discussed in introductory section 4.1.1.

It is clear that since the tapes are in continuous contact along their length, the current transfer did not take place at discrete, arbitrary points denoted by the position of the v-taps. Since we are looking at the cases in which it was preferable for current to share with the Cu tape and since current was only injected in/out of the sample via the SC tape, the current transfer can be assumed in a steady state case to change homogeneously with length or position along the sample such that it is: large and positive (SC-to-Cu) on the current-in side/LHS; staying positive but decreasing in magnitude as you move left-to-right along the sample; zero at some point near the middle; becoming negative (Cu-to-SC) and increasing in magnitude as you continue to move left-to-right; and negative and large on the current-out side/RHS.

Assuming this homogeneity of current transfer as a function of position along tape length from left-to-right/current-in-to-current-out, then the current transfer calculated as the difference between two neighbouring sections could therefore be taken to be an average value, corresponding to the actual estimated value at the central position between extreme voltage taps; for example, in the case above, between voltage taps 1 and 3, the position of the average current transfer would be at point 2. Under this assumption the calculation of R_C using equation 4.10 is still valid.

However, it is still clear that the fact that the model does not take into account the continuous nature of the current transfer along the length of the tapes remains a key limitation. The voltage measurements attributed to driving said current transfer are likely to be done so wrongly, yielding inaccurate contact resistance results. An example of this is the contact resistance value calculated at point 4, 8 cm from the end of the SC tape, in the 40 K, 15 A example shown in figure 4.19, which is negative. A negative contact resistance has no practical sense and this is the result of a misalignment between the voltage attributed to current transfer at this point and the estimated current transfer direction. In this case, the current difference estimated between $I_{Cu,3-4}$ and $I_{Cu,4-5}$ was estimated to be -0.1 A, whereas the voltage measured $V_{SC-Cu,4}$ was small ($\sim$ 1 μV) but positive. The assumption that the estimated current transfer took place at point 4 was not reflected by the measured voltage difference there.

Furthermore, this method does not estimate R_C values for the full length of the Cu tape. It is for these reasons that the method was further developed.

4.5.2 Final Method: SLM Spline Model

A new method was developed for estimating the transfer current between the tapes and, from this, a method to calculate contact resistance, R_C, in units of Ωcm^2. The MATLAB® code referred to throughout the method description is given in the appendix, chapter 7.

In order to compare this method with the preliminary, discrete resistors method, the same dataset (40 K, 15 A, bolts tightened) has been used to generate exemplar plots. However, to describe certain aspects of the final, SLM spline method, a lower temperature example has been used (35 K, 198 A, bolts loosened, no tape heater, snapshot 2.03 s from measurement start).

4.5.2.1 Creating a Continuous $\mathbf{V}_{Cu}(x)$ Function

Firstly, the cumulative voltage drop across both SC and Cu tapes as a function of continuous position along tape length, x, is plotted by summing the individual voltage drops between points and finding the difference between the cumulative values and the total voltage drop. An example is shown in figure 4.20a.

A continuous approximation of the cumulative voltage drop in the Cu tape is then made using the MATLAB® SLM function. The SLM function creates a spline approximation using the cumulative voltage data points given to it and, unlike other spline approximation methods and functions, allows for control of the shape of the spline where desired, appreciating that a known pattern or physical factor can be adjusted for by visual inspection. An example of an SLM spline approximation of a cumulative voltage drop seen in the Cu tape is shown in figure 4.20b.

The shape adjustments applied to the SLM spline approximations of cumulative voltage drops seen in the Cu tape in this method are:

- **Boundary conditions** — As the Cu tape was shorter than the SC tape, current transfer could not take place either side of the ends of the Cu tape; therefore the change in V_{Cu} with x at these points (taken to be 2 cm and 18 cm from the end of the SC tape), or the first derivative of $V_{Cu}(x)$ with respect to x, was set to zero here.

- **Numbers and positions of spline knots** — The knots are fixed points in the approximated curve or the points between which the curve generated can be

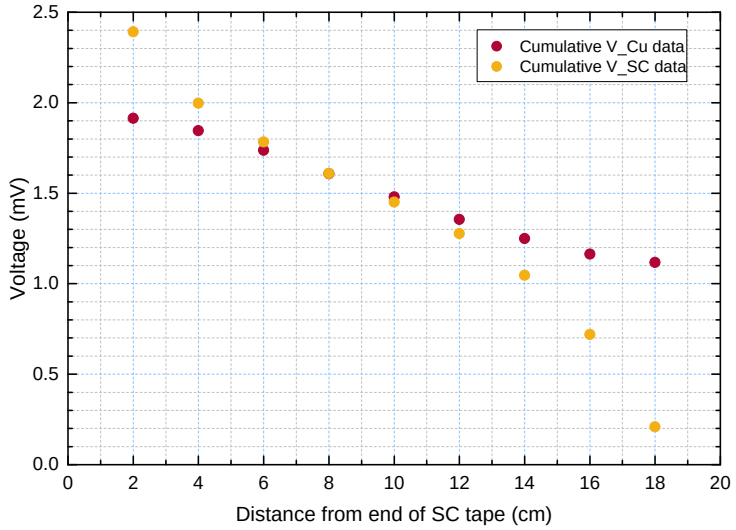

(a) Cumulative voltage drop plots for SC and Cu tapes.

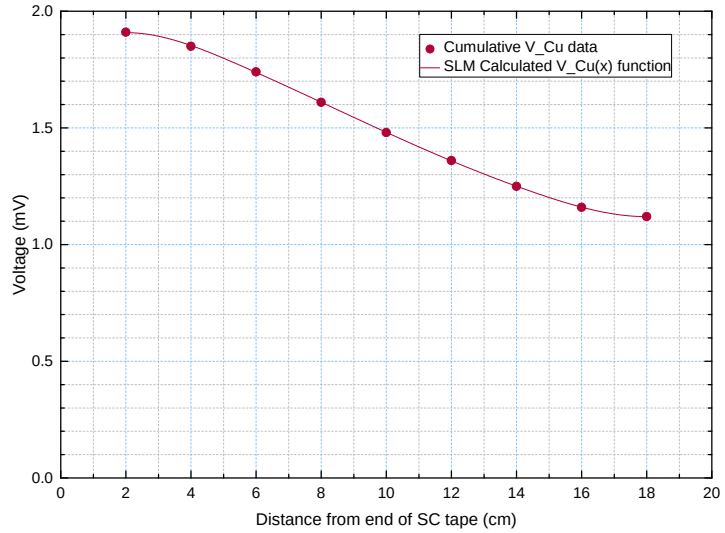

(b) Cumulative voltage drop plot for Cu tape with spline approximation of voltage drop as continuous function of position along tape length, produced using MATLAB® SLM function with 6 evenly spaced knots.

Figure 4.20: Examples of SC and Cu cumulative voltage drops (measured point data and, for Cu, approximated continuous function) as a function of position along the tapes: points correspond to v-taps 1-9 from left to right where v-tap 1 is at 2 cm from the end of the SC tape etc.; 40 K, no tape heater, 15 A applied, bolts tightened.

described using separate, independent functions; spline curve data is generated such that there is as smooth as possible a continuation from one section to the next at the knots.

The adjustments were added using the 'slmengine' input to the SLM function in MATLAB® as seen in line 56 of the function 'slmfilenameknotsplotall' found in the appendix, chapter 7.

It is noted that the ends of the Cu tape are in fact approximately 1-2 mm either side of the first and last voltage taps or approximately at positions $x \cong$ 1.8-1.9 cm and $x \cong$ 18.1-18.2 cm. This has been primarily treated as an x-error since it is already known that due to the nature of the method of soldering the v-taps to the tapes it is possible that x position discrepancies of up to half a groove width or 1.5 mm occurred in any or all of the v-tap positions. It is therefore reasonable to take it that both the measurements at v-taps 1 and 9 and the ends of the Cu tape were positioned 2 cm and 18 cm from the end of the SC tape respectively.

4.5.2.2 Knot Value Choices: Numbers of and Positions of Knots

The choice of knot values (numbers and positions of knots) affect not only the shape of the generated $V_{Cu}(x)$ curve but also that of the $I_{Cu}(x)$ curve that it is later used to calculate as part of this method. As this method was developed iteratively, the methods for calculating $I_{Cu}(x)$ and, consequently, R_C, were already known at the stage in which the refinement of knot values choices was taking place. In order to present the full method in the order in which it was applied to generate the data used in the analysis which follows, the explanation of this choice of knot values, which relies on observation of the effects of changing them on the resultant $I_{Cu}(x)$ curves, is shown here; and the methods for generating the $I_{Cu}(x)$ curves are given in the following sections.

The criteria for knot selection were that:

1. Little or no negative (and therefore meaningless) R_C values were generated,

2. Minimal $I_{Cu}(x)$ curve features were produced,

3. Any $I_{Cu}(x)$ curve features produced were supported by $V_{SC-Cu}(x)$ data.

In the development phase of this method, the MATLAB® function 'slmcomparercknotrange' (see appendix, chapter 7) was used to aid decisions on knot values by generating data using evenly spaced knots. This gave an overview of the effects of different numbers of knots at various positions. Initially R_C plots were generated directly in MATLAB® so that, in the first case, knot configurations could be judged on whether or not they generated meaningful R_C data. However, it was observed that the negative values of R_C generated were an artefact of a misalignment of curve features, in particular, features in curves resulting from the $I_{Cu}(x)$ curve and the $V_{SC-Cu}(x)$ data. Therefore a visual inspection of the $I_{Cu}(x)$ curve became the primary method for knot choice. An example of continuous $V_{Cu}(x)$ curves generated using between three and nine evenly spaced knots and the resultant $I_{Cu}(x)$ curves are shown in figure 4.21.

The measured $V_{SC-Cu}(x)$ and cumulative voltage data was then inspected to ascertain the expected features in the $I_{Cu}(x)$ curve, which could be compared to the $I_{Cu}(x)$ curves generated using 'slmcomparercknotrange'. The polarity of the $V_{SC-Cu}(x)$ data showed whether the current in the Cu tape was increasing or decreasing while looking from left to right along the tape length i.e. the shape of the $I_{Cu}(x)$ curve. The magnitude of the $V_{SC-Cu}(x)$ values showed the rate at which the current in the Cu tape was increasing or decreasing i.e. the slope of the $I_{Cu}(x)$ curve. The $V_{SC-Cu}(x)$ and cumulative voltage data for the example in figure 4.21 are shown in figure 4.22a. From this, the expected features in the $I_{Cu}(x)$ curve of the example scenario are: a steep increase in I_{Cu} between 2 and 4 cm, a peak between 4 and 5 cm, and a much less steep decrease in I_{Cu} between 5 and 18 cm. By comparing with the $I_{Cu}(x)$ curves in figure 4.21, it is possible to start identifying which knot positions may lead to the best fit, with minimum curve features.

Using this information, the position of knots in areas where the $I_{Cu}(x)$ curve deviated from these expectations could be experimented with. Continuing with the example in figure 4.21, the results of such experimentation, with the expected features and the selected knot choice highlighted, are shown in figure 4.22b.

Through this experimentation it was discovered that overall four, five or six knots worked best. It was also identified that for the range of data collected the $I_{Cu}(x)$ curves, supported by the measured $V_{SC-Cu}(x)$ data, took one of five shapes; and that using five unique knot values configurations, one for each characteristic Cu tape current profile, consistently gave the best fit $I_{Cu}(x)$ curves and consequent R_C values. As the $I_{Cu}(x)$

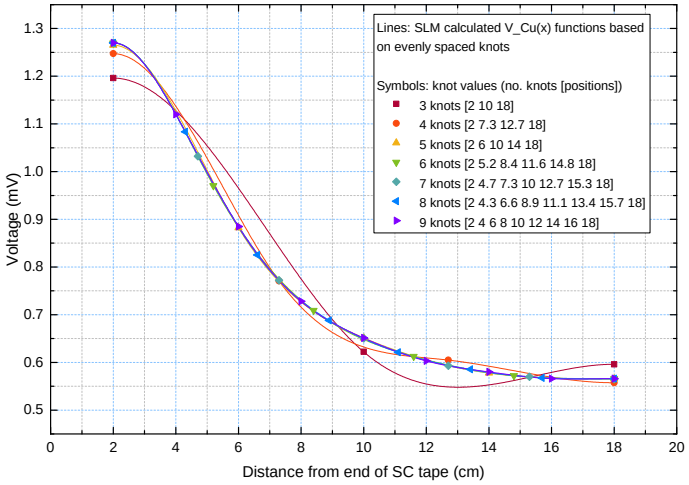

(a) SLM spline approximations of a continuous $V_{Cu}(x)$ function using various numbers of evenly spaced knots, with knot positions shown. Zoomed scale so that curve shapes can be seen more easily.

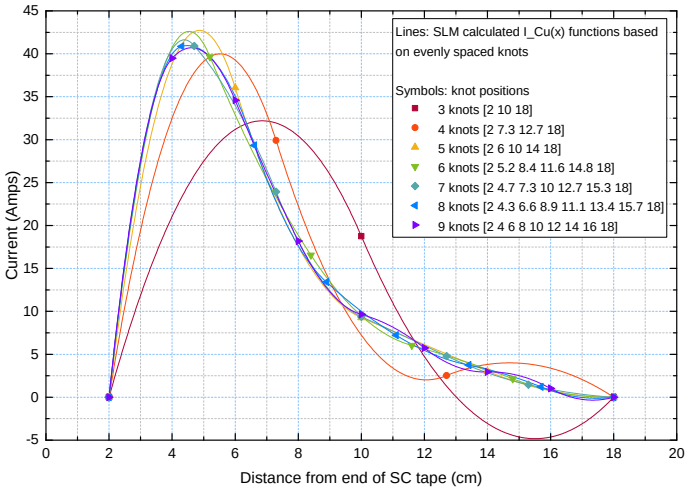

(b) $I_{Cu}(x)$ curves generated using the SLM spline approximations of a continuous $V_{Cu}(x)$ function shown in figure 4.21a.

Figure 4.21: Examples of approximated continuous Cu cumulative voltage drop functions and resultant curves representing current carried by Cu tape, both as a function of position along the tapes; using evenly spaced knots in the knot configuration investigation process; 35 K, no tape heater, 198 A applied, bolts loosened, snapshot taken at 2.03 s from measurement start.

represents the profile of the current in the Cu tape which in turn is representative of the current sharing between the Cu and SC tapes, these characteristic shapes were referred to as 'current-sharing phases'. The five current-sharing phases identified were:

- Left or L-Phase,
- Right or R-Phase,
- Unsettled sharing or US-Phase,
- Settled sharing or SS-Phase,
- Heater or H-Phase.

The current sharing phases are described in more detail in the following chapter, with their characteristic plots shown in figures 5.3 to 5.7. Through the experimentation with knot values described above, reliable knot value configurations for each phase were found and are given in table 4.2. These are the knot value configurations that were used in all the calculations which follow.

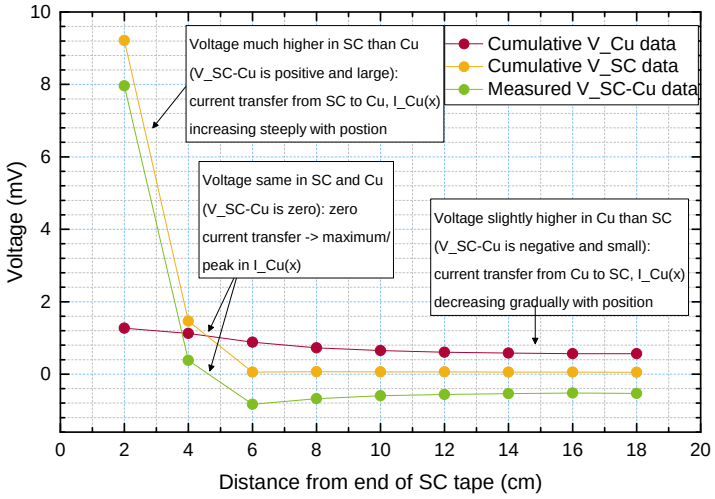

(a) SC and Cu cumulative voltage drops and voltage between the SC and Cu tapes (measured point data); features expected in $I_{Cu}(x)$ curve highlighted.

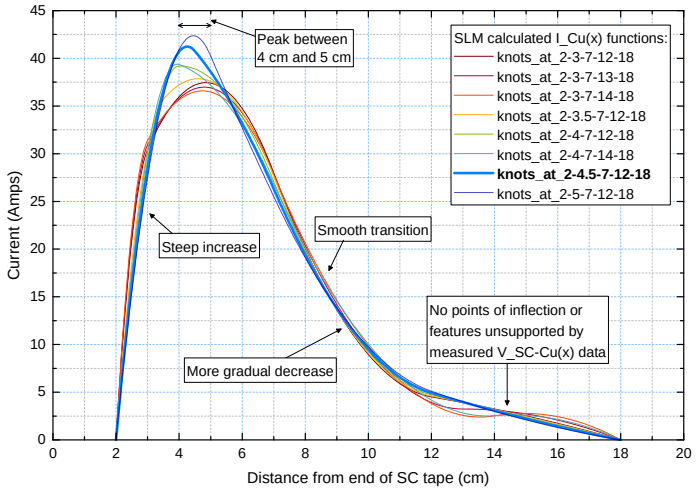

(b) $I_{Cu}(x)$ curves generated using the SLM spline approximations generated using various knot configurations; expected features and selected knot configuration highlighted.

Figure 4.22: Examples of refining the knot values configuration by adjusting knot values following results in figure 4.21; 35 K, no tape heater, 198 A applied, bolts loosened, snapshot taken at 2.03 s from measurement start.

Current-Sharing Phase	**Current Sharing Characteristics**	**When in Quench Process Observed**	**Knot Positions (cm from end of SC tape)**
Left (L-Phase)	Mostly on LHS	Initial sharing/beginning of quench	[2 4.5 7 12 18]
Right (R-Phase)	Mostly on RHS	Initial sharing/beginning of quench	[2 9 15 18]
Unsettled Sharing (US-Phase)	Mostly at ends with some fluctuation in the middle	Later sharing	[2 4 7 14 18]
Settled Sharing (SS-Phase)	Mostly at ends	Later sharing, when approaching steady-state/Joule heating only	[2 5.2 8.4 11.6 14.8 18] (6 evenly spaced knots)
Heater (H-Phase)	Mostly in middle	When heater applied	[2 8 10 12 18]

Table 4.2: Current-sharing phases observed in contact resistance measurements including characteristic/identifiable features and best-fit knot positions for SLM spline approximation of $V_{Cu}(x)$ curves.

4.5.2.3 Creating a Continuous $I_{Cu}(x)$ Function

As all current injection occurred directly to the SC tape, there could only be current in the Cu tape if current had transferred there from the SC tape. An increase in current transfer from the SC tape to the Cu tape was therefore also signified by an increase in the current being carried by the Cu tape shown by an increase in the function $V_{Cu}(x)$ with x; and it follows that a decrease in the function $V_{Cu}(x)$ with x signifies a decrease in the current being carried by the Cu tape similarly due to a decrease in or reverse of direction of current transfer. Therefore the 'rate' of change of $V_{Cu}(x)$ with x, or the first derivative of the function $V_{Cu}(x)$ with respect to x, shows the electric field in the Cu tape due to the current flow within it. Note that in this case 'rate' does not refer to the function changing with time but with position along the sample length or with increasing x. For both methods presented in this chapter either an instant in time is considered or a steady state scenario. As $V_{Cu}(x)$ has been plotted as an electrical potential drop, decreasing with increasing x, the electric field itself, $E_{Cu}(x)$ is given by:

$$E_{Cu}(x) = -\frac{dV_{Cu}(x)}{dx}. \tag{4.11}$$

Equation 4.12 below is an alternative form of Ohm's Law (equation 1.1):

$$E = \rho \times J \tag{4.12}$$

where E is the electric field, ρ is the resistivity and J is the current density (see equation 1.2). Using equation 4.12, the current density of the Cu tape as a function of position along tape length, $J_{Cu}(x)$, can be calculated using the calculated $E_{Cu}(x)$ and the resistivity of the Cu tape, ρ_{Cu}.

Assuming homogeneity of the Cu tape, the resistivity is only a function of tape length insomuch as the temperature of the tape is a function of tape length and the resistivity is a function of temperature. However, in most of the tested cases, differences in ρ_{Cu} values with position due to local temperature differences were negligible at the times looked at and a constant ρ_{Cu} value taken from the curve in figure 4.18 based on the nominal sample temperature was used. The function $J_{Cu}(x)$ was then calculated using this ρ_{Cu} value and the function $E_{Cu}(x)$ from equation 4.11.

A more accurate model would take into account the dependence of ρ_{Cu} on temperature and is recommended as further work for this project as it would allow analysis of

the data after the point at which the effect of local heating on ρ becomes a dominant factor, which would be useful as the voltage differences measured here are typically much larger and would therefore lend themselves to easier interpretation and less error in R_C calculations.

The current carried by the Cu tape as a function of position along tape length can therefore be calculated using the tape dimensions since:

$$I_{Cu}(x) = J_{Cu}(x) \times A_{Cu} \tag{4.13}$$

where A_{Cu} is the cross-sectional area of the Cu tape which here is 3 mm $\times$ 0.2 mm or 6×10^{-3} cm^2, as used in equation 4.8. An example of the function $I_{Cu}(x)$ plotted with the discrete current values calculated in the discrete resistors method is shown in figure 4.23.

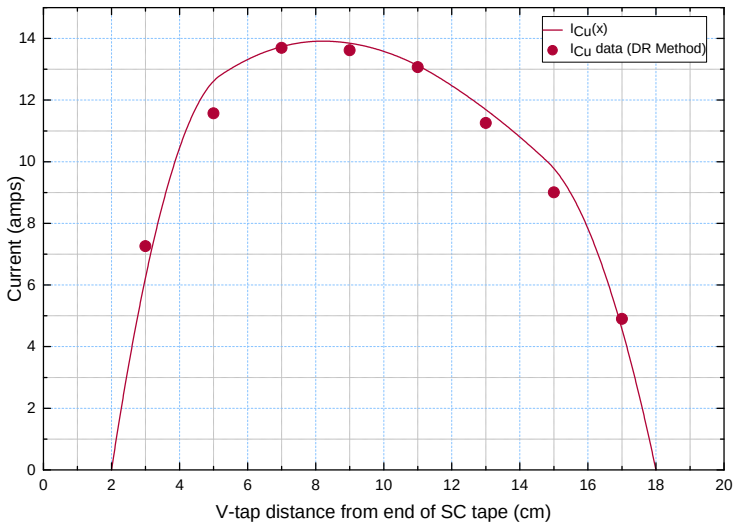

Figure 4.23: Current carried by Cu tape as a function of position along tape length: symbols - calculated using discrete resistors method, symbol is plotted in centre of section modelled by resistor i.e. between two v-taps; curve - approximated continuous function with 6 evenly spaced knots, as part of the SLM spline approximation method; 40 K, no tape heater, 15 A applied, bolts tightened.

Recalling that the end of the Cu tape is approximately at $x = 2$ cm and 18 cm, it is logical that $I_{Cu} = 0$ A at $x \leq 2$ cm and $x \geq 18$ cm. Combining equations 4.11, 4.12 and 4.13, it is seen that this is achieved by setting the first derivative of $V_{Cu}(x)$ with

respect to x to zero at $x = 2$ cm and $x = 18$ cm:

$$I_{Cu}(x) = A_{Cu} \times J_{Cu}(x) = A_{Cu} \times \frac{E_{Cu}(x)}{\rho_{Cu}} = \frac{A_{Cu}}{\rho_{Cu}} \times -\frac{dV_{Cu}(x)}{dx}. \tag{4.14}$$

This is the other shape adjustment applied to the SLM spline model of the continuous $V_{Cu}(x)$ function described previously (the first being the selection of knot values).

Calculating the $I_{Cu}(x)$ function is useful both for visualising the current distribution and, in combination with the V_{SC-Cu} data measured, assessing the validity of the spline knot numbers and positions, as described previously. However, for the R_C calculation, it is the derivative of $I_{Cu}(x)$ or, in fact, the second derivative of $V_{Cu}(x)$ that is required.

4.5.2.4 Calculating R_C for Given Values of x

As any increase or decrease in current in the Cu tape, as signified by the function $I_{Cu}(x)$, must be due to current transfer to and from the SC tape, we can therefore use $I_{Cu}(x)$ to quantify current transfer as a function of position along tape length x. The derivative of the function $I_{Cu}(x)$ with respect to x therefore shows the rate of change of current in the Cu tape or the rate of current transfer. Note that here, again, the term 'rate' is not referring to how the current transfer changes with time, rather with position along tape length.

It is assumed that the current transfer is homogeneous with the width of the Cu tape, w_{Cu}. Note that while the SC tape is 0.5 mm wider than the Cu tape, transfer can only occur where the tapes are in contact and hence the width of the Cu tape is used. The rate of change in current transfer per unit width, $\sigma(x)$, with x is therefore given by:

$$\frac{d\sigma_{Cu}(x)}{dx} = \frac{1}{w_{Cu}} \times \frac{dI(x)}{dx}. \tag{4.15}$$

Combining equations 4.14 and 4.15 gives the derivative of current transfer per unit width with respect to position along tape length:

$$\frac{d\sigma_{Cu}(x)}{dx} = \frac{A_{Cu}}{\rho_{Cu} w_{Cu}} \times -\frac{d^2V_{Cu}}{dx^2} = \frac{t_{Cu}}{\rho_{Cu}} \times -\frac{d^2V_{Cu}}{dx^2} \tag{4.16}$$

where the cross-sectional area of the Cu tape, A_{Cu}, is the product of the tape width, w_{Cu}, and thickness, t_{Cu}.

With this method of estimating current transfer between tapes, the contact resistance can be calculated using equation 4.17:

$$R_C = \frac{V_{SC-Cu}(x)}{\frac{d\sigma_{Cu}(x)}{dx}}. \tag{4.17}$$

This model results in a contact resistance the unit of which is $\Omega \times$ unit area e.g. $\Omega-\text{cm}^2$.

An example of a contact resistance profile as calculated using this method is shown in figure 4.24. As can be seen, a greater contact resistance on the RHS, observed using the preliminary R_C calculation method, is also seen here.

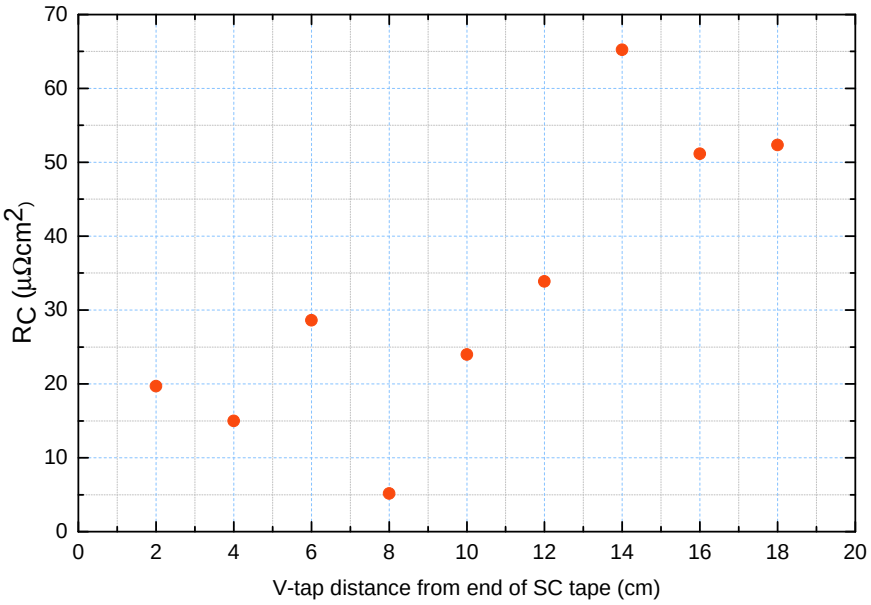

Figure 4.24: Contact resistance approximation along tape length as calculated using the SLM spline model; 40 K, no tape heater, 15 A applied, bolts tightened.

5

Current Transfer and Contact Resistance in an MgB_2-Cu Half-Sandwich

This chapter presents the results generated using the methods described in chapter 4 and their discussion.

5.1 Preliminary and Intermediate Experimental and Sample Set-up: Thermal Runaway Current Measurement

The results using the preliminary sample holder validated the concept of measuring current transfer within a SC-Cu sandwich but an improved experimental set-up was required to produce results which could be interpreted meaningfully enough to understand the current transfer mechanisms and estimate contact resistance.

The preliminary set-up was not designed to measure I_c and the signal noise was such that the standard 1 μVcm^{-1} criteria measurements were not possible. However, the opportunity was taken to measure thermal runaway current of the sample both stabilised (with the Cu tapes) and un-stabilised (the SC tape on its own) as a function of temperature. This information allowed us to become familiar with the behaviour of this particular batch of SC tape and was useful in consequent experiments. The results are shown in figure 5.1. The use of the tape heater has been accounted for by adding 0.25 K to the nominal tape temperature for every 20 mA applied to the heater.

Figure 5.1 was used as a guide to estimate the I_{quench} region for a given temperature in the intermediate 200 mm single-sandwich tests, the final 200 mm half-sandwich tests, and the 5 m multi-strand cable tests. With a single superconducting tape the I_{quench} values could be read directly from figure 5.1 for a given temperature; for the 5 m multi-strand cable tests the I_{quench} values in figure 5.1 had to be multiplied by the number of superconducting tapes in the sample cable to be tested i.e. three.

Although measurements were taken using the intermediate set-up (a single-sandwich in the adjustable clamp sample holder), as discussed in the previous chapter, these proved difficult to usefully interpret. This led to the development of the final experimental and sample set-up.

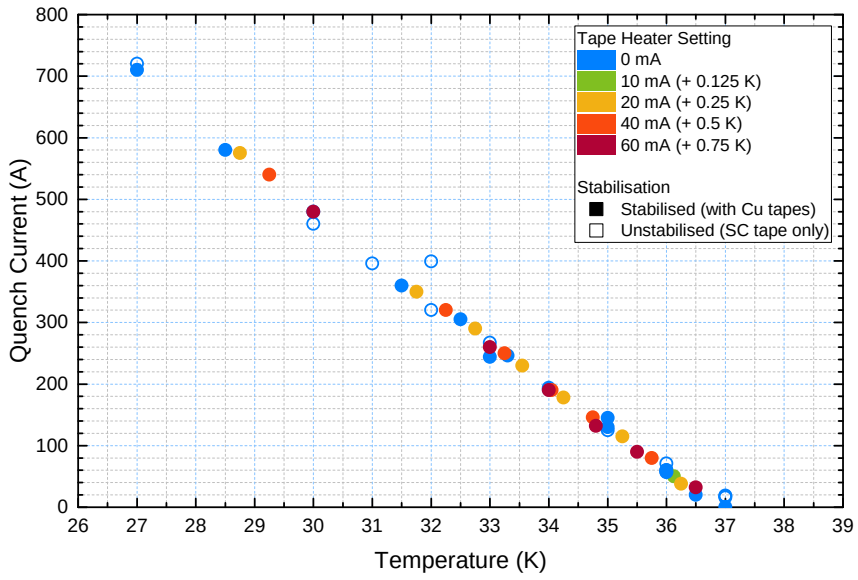

Figure 5.1: Thermal runaway or quench current as a function of temperature for MgB_2 tape (stabilised: sandwiched between two copper tapes; unstabilised: without any copper tapes) tested in preliminary sample holder mounted on platform of multi-purpose cryostat, at the University of Southampton.

5.2 Final Experimental and Sample Set-up

For each sample set-up, a new MgB_2 tape was used. For all experiments discussed in this body of work, the MgB2 tapes used were from the same manufacturing batch.

Recall from section 4.4.1, the two contact scenarios tested in the final experimental and sample set-up were as follows:

- **'Bolts Tightened'** — In the BT scenario, the bolts of the adjustable clamp were tightened to full Belleville washer compression, a total washer deflection of 1.8 mm. From the data in figure 4.10a this equates to a tape contact pressure of approximately 5.6 MPa. This is the best contact or lowest R_C achievable with this particular experimental set-up.

- **'Bolts Loosened'** — In the BL scenario, the bolts of the adjustable clamp were loosened so that the total Belleville washer compression was 0.6 mm. From the data in figure 4.10a this equates to a tape contact pressure of approximately 2.1 MPa and therefore provided a higher R_C case to compare with the BT scenario.

It is noted that for the profile figures described here and all those that follow, where individual points are plotted (as opposed to continuous curves), points correspond to v-taps 1-9 from left to right where v-tap 1 is at 2 cm from the end of the SC tape etc. - see also figure 4.16 for reference. This is consistent with all profile plots in both this chapter and chapter 4.

5.2.1 Data Selection

In order to calculate R_C, as described previously, tape profiles were investigated. This could be done at a given instance in time or, for a steady state scenario, an average over a length of time could be taken. For dynamic scenarios, profiles were studied for a range of time 'slices' to see if there was any significant change in the calculated values of R_C as the voltage signals changed with time. Generally, five to six time slices were used, each 10 ms apart which, at the recording frequency of 200 Hz, equated to two datapoints apart.

A 4-point adjacent averaging smoothing function was applied to the measured voltage-time signals to reduce the signal noise. After some experimentation, this was the smoothing method deemed to offer the best compromise between mitigating the effects of signal noise and losing the least signal information.

Selection of the time slices was based on two criteria:

1. The voltage signal was greater than 10 μV so that the signal was sufficiently distinctive from the signal noise (which was seen to have an amplitude of up to 10 μV after smoothing);

2. The effect of heating on the resistivity of the Cu tape was not dominant.

The second criterion was necessary because the current method for calculating R_C uses a constant value of Cu resistivity. A method to adapt the model to take into account the change in Cu resistivity with temperature based on the data in figure 4.18 has been investigated and is discussed as potential future work in section 5.4.

It is also noted that R_C can only be calculated in scenarios where the superconducting tape was undergoing the transition to the resistive state and therefore was a) sharing the current with the copper tape and b) producing a measurable electric field which is, of course, not the case when in the superconducting (non-resistive) state.

During the experimentation process, current steps of increasing magnitude, at coarse intervals when below the I_{quench} region and then at fine intervals of 1 A when approaching the I_{quench} region, were applied until a transition to the resistive state had begun and current sharing between the tapes was observed. In some situations, particularly in the lower pressure or BL scenarios, there was a very distinct transition with no voltage measured above signal noise at x A and clear, exponential voltage signals showing the characteristic positive feedback loop due the interdependent heating and resistivity of a quench at $x+1$ A. In other cases, almost solely in the higher pressure or BT scenarios, there were a range of currents over which the beginning of a quench could be observed through to the clear exponential voltage signal appearing. Therefore, for the R_C calculations, where interesting, more than one applied current was investigated at a given temperature and heater set-up.

As described previously, measurements were taken both with and without use of a resistance heater in the centre of the tape (the 'tape heater') giving additional control over the current sharing between the tapes during a quench. The difference in results found with and without the heater are discussed in the sections which follow.

The final scenarios for which the R_C profile was calculated based on the above selection criteria are summarised in table 5.1.

Contact	Nominal Temp. (K)	Tape Heater	Applied Current (A)
Bolts Tightened (BT)	33	off	354
		on	319
	34	off	270
		on	238
	35	off	194
			195
		on	166
	36	off	110
		on	84
	37	off	40
	37.5	off	20
	40	off	15
Bolts Loosened (BL)	33	off	351
		on	333
	34	off	270
		on	248
	35	off	198
		on	174
	36	off	115
		on	100
	37	off	55
	37.5	off	20
	40	off	15

Table 5.1: Summary of tested scenarios for MgB_2-Cu half-sandwich sample for which R_C profiles were calculated and current transfer investigated.

5.2.2 Characteristic Currents

Although this experimental set-up was not specifically designed for critical current measurements, some characteristic current data was collected to aid experimentation, using the criteria below, also discussed in section 4.4.2:

- **'Critical current',** I_c — The current at which 10 μV was measured across a given section, i.e. 5 μVcm^{-1} since each section was 2 cm long. This was the most reliable voltage measurement resolution possible for the observed signal noise, after filtering (smoothing).

- **Quench current,** I_{quench} — The current at which both an exponentially increasing voltage and sample heating were observed.

Figure 5.2a plots both the measured I_c and I_{quench} values together. For all values in figure 5.2a the effect of the use of the tape heater has been compensated for by adding 0.4 K to the nominal temperature. This value was that estimated as the local temperature increase due to applying 3 V to the tape heater, as shown in table 4.1.

Figure 5.2b shows the characteristic currents measured in the adjustable clamp sample holder described above and in figure 5.2a plotted alongside the I_{quench} values measured using the preliminary sample holder as described in figure 5.1. It can be seen that higher characteristic current values were measured in the tape used in the later tests. These differences are likely due to the fact that for each sample set-up, a new MgB_2 tape was used. Although the MgB2 tapes used were from the same manufacturing batch, inhomogeneities in characteristic current values are still possible.

All following results and discussion refer to the tape for which the measured characteristic current values are shown in figure 5.2a.

5.2.3 Current Sharing Phases

Without the tape heater, the current transfer that occurred when the tape was forced into the resistive state (by applying a current greater than the I_c for the tape temperature) took the form of one of four 'phases' as described in section 4.5.2.1 and table 4.2. When the tape heater was applied, the current transfer took the form of a fifth phase, also described in section 4.5.2.1 and table 4.2.

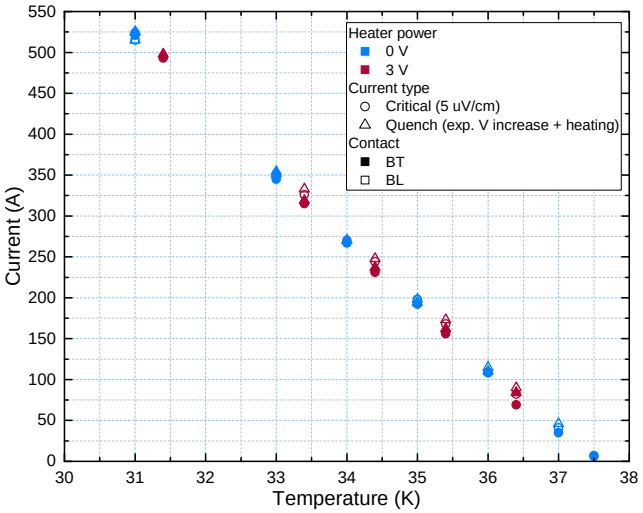

(a) Characteristic current values from the final sample set-up as a function of temperature: Circles - Critical current, I_c; Triangles - Quench current, I_{quench}. Use of tape heater was accounted for by adding 0.4 K to the nominal temperature.

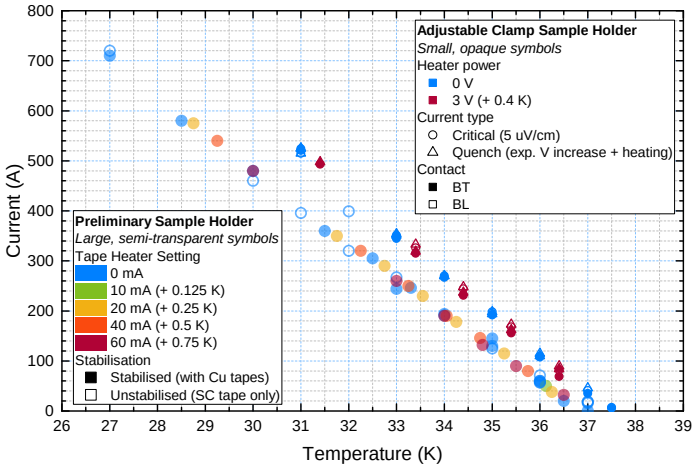

(b) Comparison of preliminary and final sample set-up characteristic current values from figures 5.2a and 5.1.

Figure 5.2: Characteristic current values as a function of sample temperature with the criteria: I_C - current at which 5 μVcm^{-1} was measured; I_{quench} - current at which both exponentially increasing voltage and sample heating were observed. Different MgB_2 tapes from the same manufacturing batch were used for each set-up.

The current-sharing phase occurring at a given point in time could be identified from the SC and Cu cumulative voltage drops using the following:

- Where V_{SC} was greater than V_{Cu}, current was transferring from the SC tape to the Cu tape,
- Where V_{Cu} was greater than V_{SC}, current was transferring from the Cu tape to the SC tape,
- Where the $V_{SC}(x)$ and $V_{Cu}(x)$ crossed or $V_{SC} \simeq V_{Cu}$, little or no current was transferring and it was at this point along the tape length where the current transfer was changing direction; this is hence referred to as the 'zero-point' as it represents zero current transfer.

Figure 5.3, taken from the same scenario as that in figure 4.20a (40 K, no tape heater, 15 A applied, step average, BT), shows the above current sharing identification characteristics of the SC and Cu cumulative voltage drops and the resultant $I_{Cu}(x)$ profile. This is an example of 'settled-sharing' or SS-Phase current sharing which was generally observed in the scenarios at temperatures at and around T_c and later in the quench process in other scenarios.

In this current sharing phase, the majority of the current would transfer from the SC tape to the Cu tape within a relatively short length of the sample, with the amount of current transferring decreasing as approaching the tape centre. Then the current would return from the Cu tape to the SC tape, with current transfer increasing in magnitude as approaching the tape end, again with the majority of current transferring within a relatively short length of the sample. In SS-Phase current sharing, current would be carried preferentially by the Cu tape rather than the SC tape, for as much of the tape length as possible.

Generally, as in figure 5.3, there would be a single zero-point with current transferring from the SC to the Cu tape on the left of it and from the Cu tape back to the SC tape on the right of it. During an SS-Phase, the single zero-point would be generally close to the centre but it was observed to move with time, even within a given applied current, temperature and tape pressure contact scenario. In other phases it was seen to be positioned more extremely to the left or right of centre, as in the L-Phase and R-Phase current sharing.

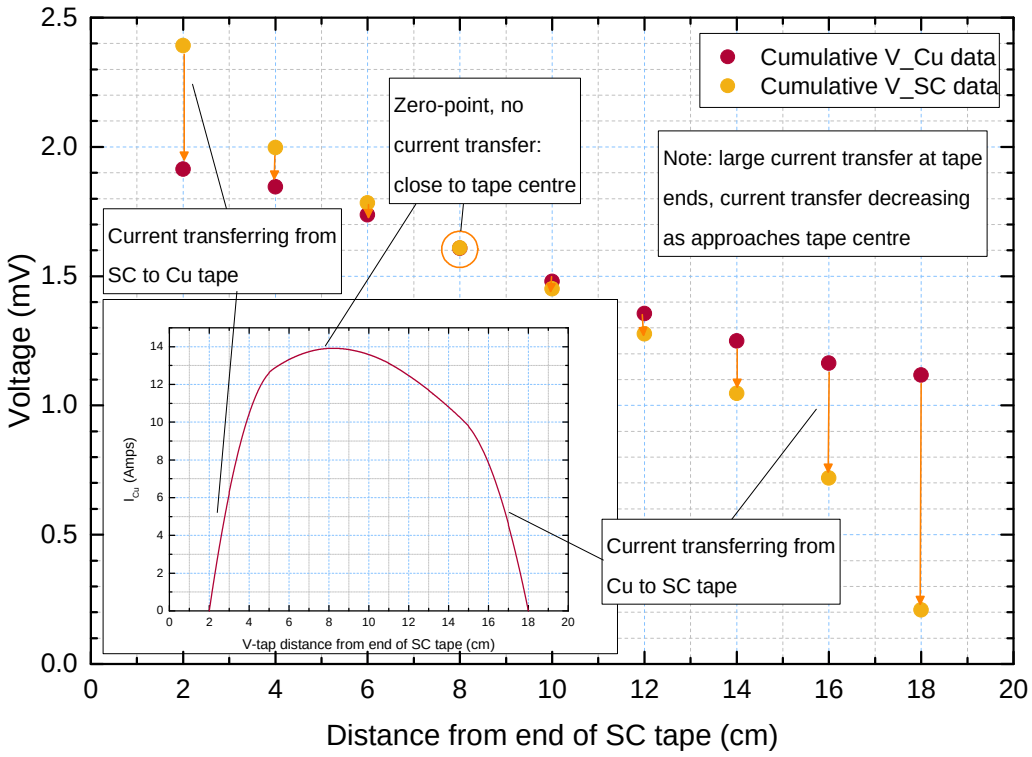

Figure 5.3: Main figure: SC and Cu cumulative voltage drops as a function of position along the tapes: points correspond to v-taps 1-9 from left to right where v-tap 1 is at 2 cm from the end of the SC tape etc.; Inset: Current carried by Cu tape as a function of position along tape length; Both annotated to show an example of how current sharing phase and features of $I_{Cu}(x)$ profile can be deduced from cumulative voltage drops; SS-Phase current sharing, 40 K, no tape heater, 15 A applied, step average, bolts tightened.

In an L-Phase current sharing phase, the zero-point was to the left of the tape centre and the majority of current transferred from the SC tape to the Cu tape over a short length on the LHS, then returned to the SC tape over the remaining longer length of the tape. Figure 5.4 shows an example of both SC and Cu cumulative voltage drops and the resultant $I_{Cu}(x)$ profile in a scenario in which L-Phase current sharing was observed for the selected time slice. Unlike SS-Phase sharing, current appeared to be only carried by the Cu tape locally.

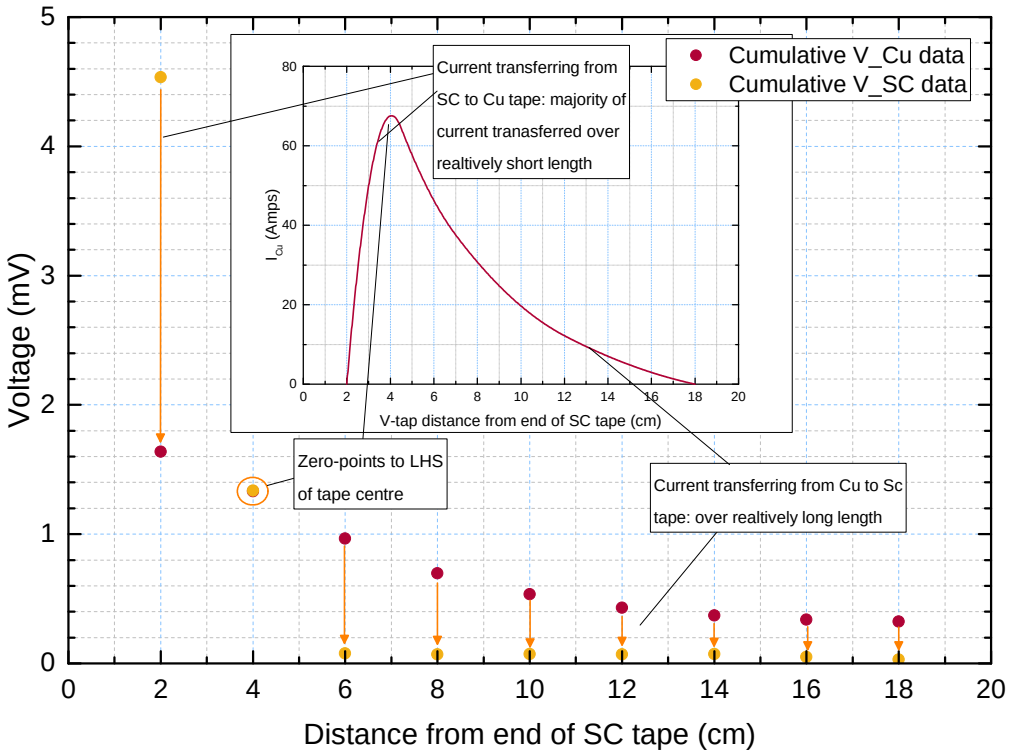

Figure 5.4: Main figure: SC and Cu cumulative voltage drops as a function of position along the tapes: points correspond to v-taps 1-9 from left to right where v-tap 1 is at 2 cm from the end of the SC tape etc.; Inset: Current carried by Cu tape as a function of position along tape length; Both annotated to show an example of how current sharing phase and features of $I_{Cu}(x)$ profile can be deduced from cumulative voltage drops; L-Phase current sharing, 36 K, no tape heater, 110 A applied, time slice 2.24 s, bolts tightened.

Likewise, in an R-Phase current sharing phase, the zero-point was to the right of the tape centre. The current transferred from the SC tape to the Cu tape over a length greater than half of the tape length and the majority of current sharing from

the Cu tape back to the SC tape occurred on the RHS of the tape. Figure 5.5 shows an example of both SC and Cu cumulative voltage drops and the resultant $I_{Cu}(x)$ profile in a scenario in which R-Phase current sharing was observed for the selected time slice.

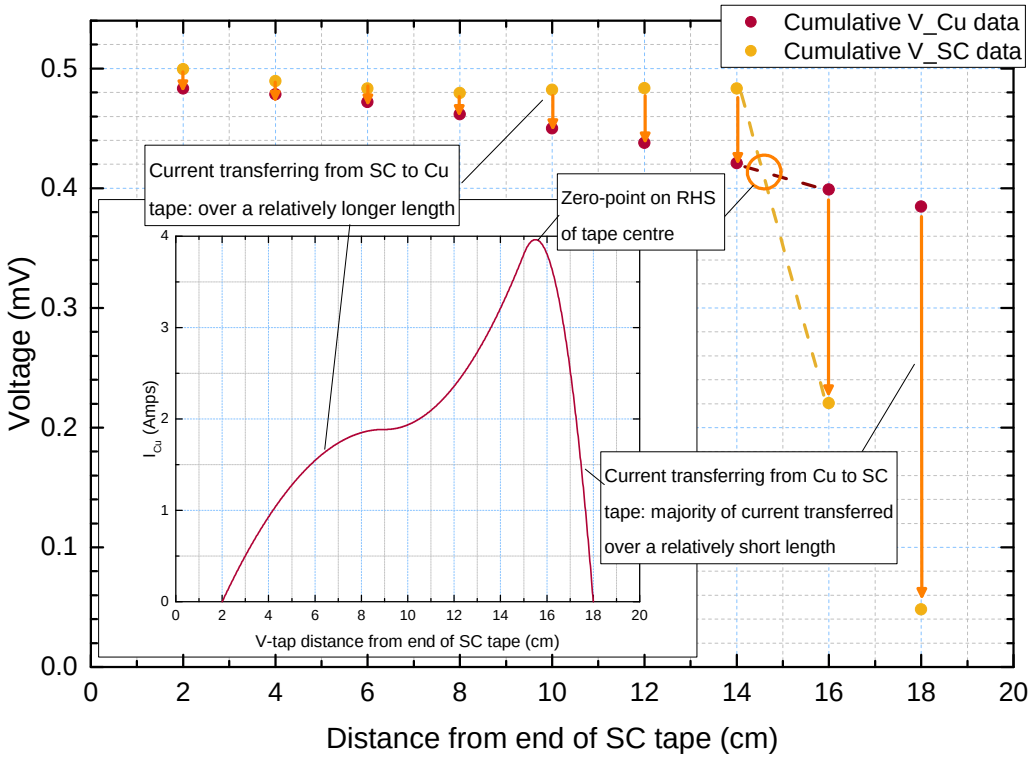

Figure 5.5: Main figure: SC and Cu cumulative voltage drops as a function of position along the tapes: points correspond to v-taps 1-9 from left to right where v-tap 1 is at 2 cm from the end of the SC tape etc.; Inset: Current carried by Cu tape as a function of position along tape length; Both annotated to show an example of how current sharing phase and features of $I_{Cu}(x)$ profile can be deduced from cumulative voltage drops; R-Phase current sharing, 35 K, no tape heater, 194 A applied, time slice 2.265 s, bolts tightened.

The majority of current-sharing scenarios started in either an L-Phase or an R-Phase. Sharing would often then shift to a state of unsettled sharing or a US-Phase with three zero-points and current transferring (from left to right): from the SC tape to the Cu tape, back to the SC tape, back to the Cu tape and finally back to the SC tape. Figure 5.6 shows an example of both SC and Cu cumulative voltage drops and the resultant $I_{Cu}(x)$ profile in a scenario in which US-Phase current sharing was observed for the selected time slice.

The US-Phase was the hardest to model and led to the most unreliable R_C values with no knot values found which led to no negative R_C values being generated 100 % of the time. The final knot positions used were those which led to the most consistent R_C values.

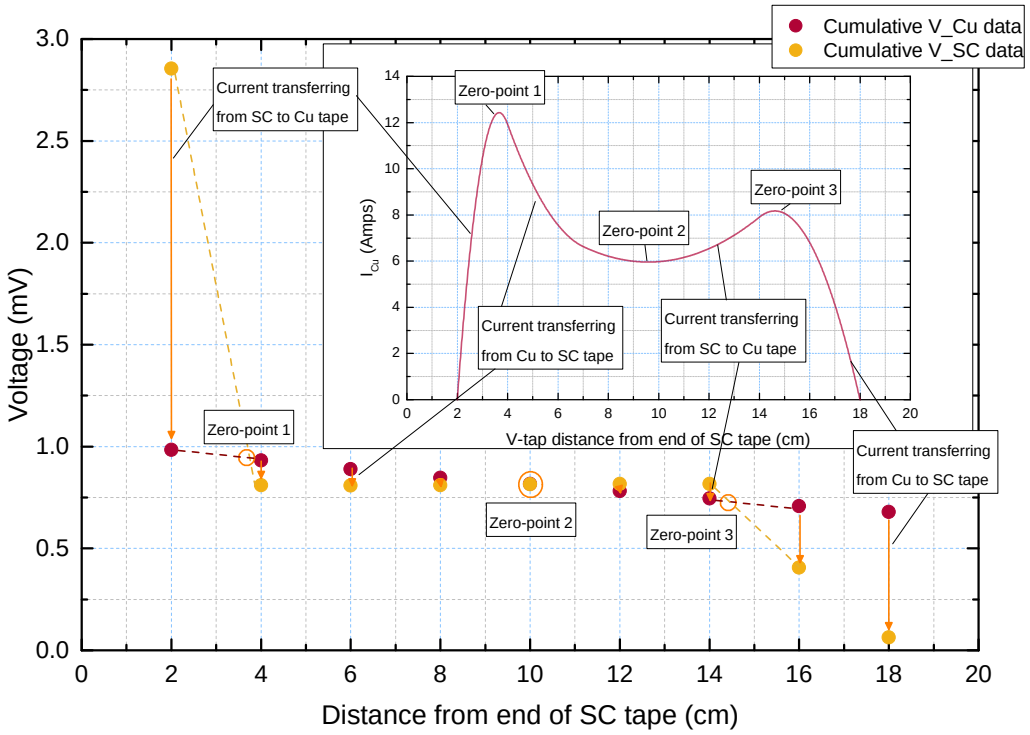

Figure 5.6: Main figure: SC and Cu cumulative voltage drops as a function of position along the tapes: points correspond to v-taps 1-9 from left to right where v-tap 1 is at 2 cm from the end of the SC tape etc.; Inset: Current carried by Cu tape as a function of position along tape length; Both annotated to show an example of how current sharing phase and features of $I_{Cu}(x)$ profile can be deduced from cumulative voltage drops; US-Phase current sharing, 34 K, no tape heater, 270 A applied, time slice 2.165 s, bolts tightened.

Eventually in most scenarios a settled sharing phase or SS-Phase would be established. It was possible to regard all of these phases in most of the non-heated scenarios investigated by observation of the SC and Cu cumulative voltage drops for various time slices. However, by the time SS-Phase sharing occurred, the effect of heating on the Cu tape resistivity had usually become dominant and so $I_{Cu}(x)$ and R_C profiles have only been calculated for this phase at temperatures greater than or in the region of T_c,

where applied currents were very low and so the effect of heating was minimal.

A fifth current sharing phase was observed when the tape heater was used. Instead of 'escaping' to (and from) the Cu tape over as short a length of tape as possible so that as much current as possible was shared with the Cu tape, as in the SS-Phase, in the H-Phase or heated phase current would remain in the SC tape as much as possible, transferring to and from the Cu mostly around the heated section. Figure 5.7 shows an example of both SC and Cu cumulative voltage drops and the resultant $I_{Cu}(x)$ profile in a scenario in which H-Phase current sharing was observed for the selected time slice.

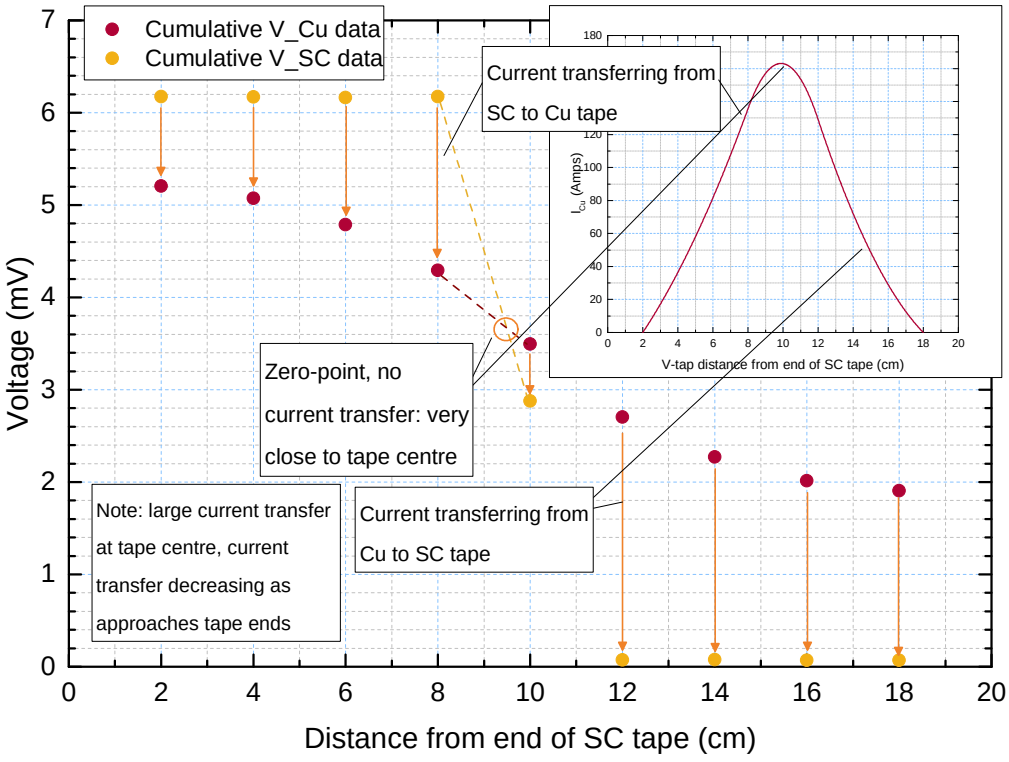

Figure 5.7: Main figure: SC and Cu cumulative voltage drops as a function of position along the tapes: points correspond to v-taps 1-9 from left to right where v-tap 1 is at 2 cm from the end of the SC tape etc.; Inset: Current carried by Cu tape as a function of position along tape length; Both annotated to show an example of how current sharing phase and features of $I_{Cu}(x)$ profile can be deduced from cumulative voltage drops; H-Phase current sharing, 33 K, 3 V tape heater setting, 319 A applied, time slice 2.26 s, bolts tightened.

5.2.4 Results with No Tape Heater, At and Around T_C

At 40 K, in the cold but resistive state, without use of the tape heater, in both the BT and BL or 'good' and 'bad' contact scenarios, SS-Phase current sharing was observed. In figures 5.8a (BT) and 5.10a (BL) it can be seen that the voltage measured in the Cu tape was constant with time in both cases. Being in the resistive state, ohmic or Joule heating would have been occurring but the cooling was sufficient that this did not lead to an increase in the voltages measured. By observing the cumulative voltage drops in figures 5.8b (BT) and 5.10b (BL) and the $I_{Cu}(x)$ profiles in figures 5.9a (BT) and 5.11a (BL) it is seen that current sharing is almost symmetrical, entering the Cu tape on the LHS and leaving at a similar 'rate' on the RHS with the $I_{Cu}(x)$ maximum slightly to the left of the tape centre.

It is also clear that the increased R_C in the BL scenario has decreased the amount of current that can be shared with the Cu tape over the tape length, from the following observations in figures 5.9a and 5.11a:

- In the BT scenario, most of the current that transferred to and from the Cu tape did so in approximately the first and last 2 cm at either end of the tape contact length and the Cu tape is seen to have carried the majority of the current, approximately 14 A out of the 15 A applied at its maximum,
- In the BL scenario, however, practically half the length of the tape contact was required to transfer current to and from the Cu tape and not only was the maximum current shared less, being approximately 13 A out of the 15 A applied, but it carried this maximum percentage of the applied current over a shorter distance, due to the greater transfer lengths (CTLs).

Looking at the R_C values calculated, in figures 5.9b (BT) and 5.11b (BL), we can see that the BL scenario does indeed have an increased contact resistance compared to the BT scenario; but also that, in both contact cases, there appears to be a higher R_C on the RHS of the sample than that on the LHS. This phenomenon is observed consistently throughout the results and discussed in section 5.2.8.

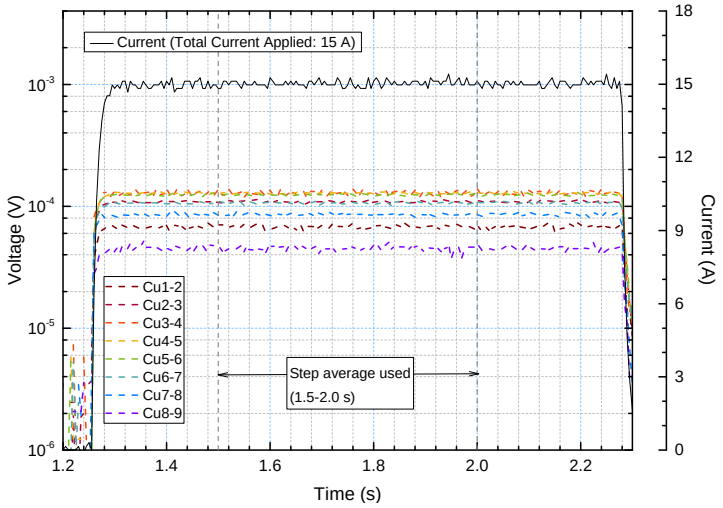

(a) Voltage-time traces for sections of Cu tape indicating time slice(s)/step average investigated.

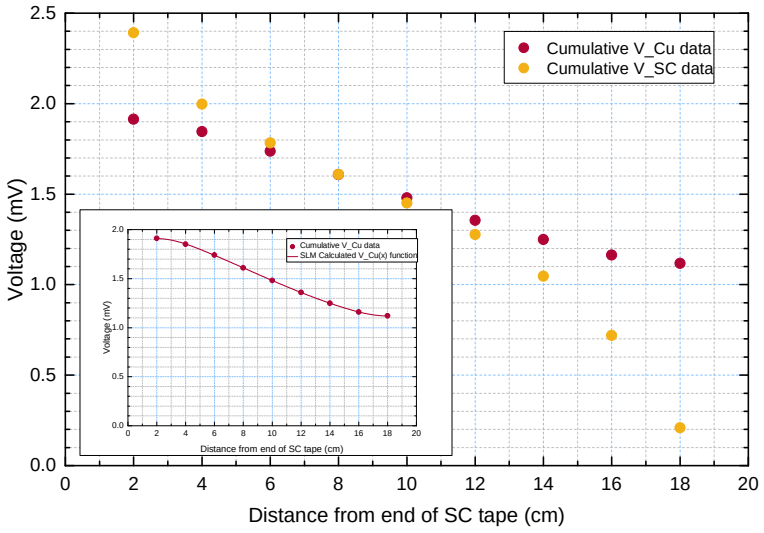

(b) Main figure: Measured cumulative voltage drop profiles for SC and Cu tapes; Inset: Measured cumulative voltage drop profile and continuous SLM spline approximation for Cu tape.

Figure 5.8: Plots for 40 K, no tape heater, 15 A applied, bolts tightened scenario; SS-Phase current sharing (continued in figure 5.9).

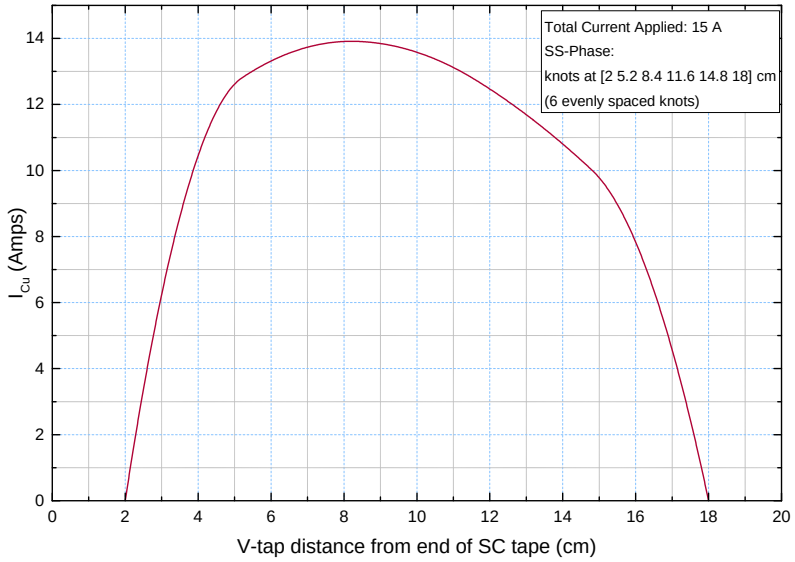

(a) Current carried by the Cu tape as a function of position along tape length, continuous function derived from differentiation of SLM curve in figure 5.8b (Inset).

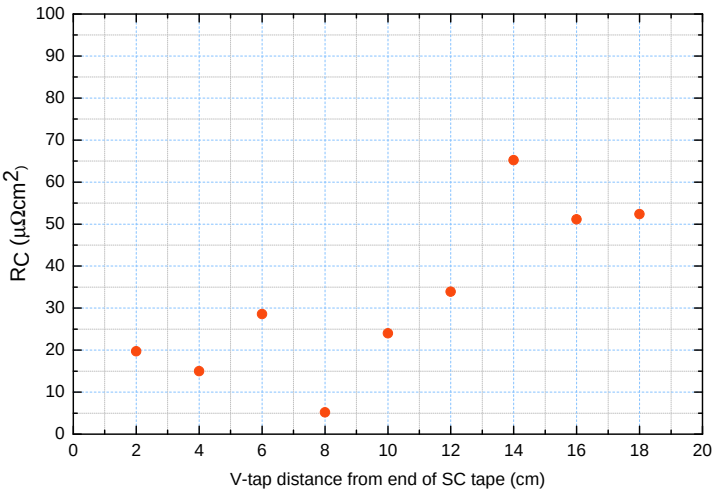

(b) Contact resistance approximation along tape length as calculated using the SLM spline method.

Figure 5.9: Continued plots for 40 K, no tape heater, 15 A applied, bolts tightened scenario; SS-Phase current sharing.

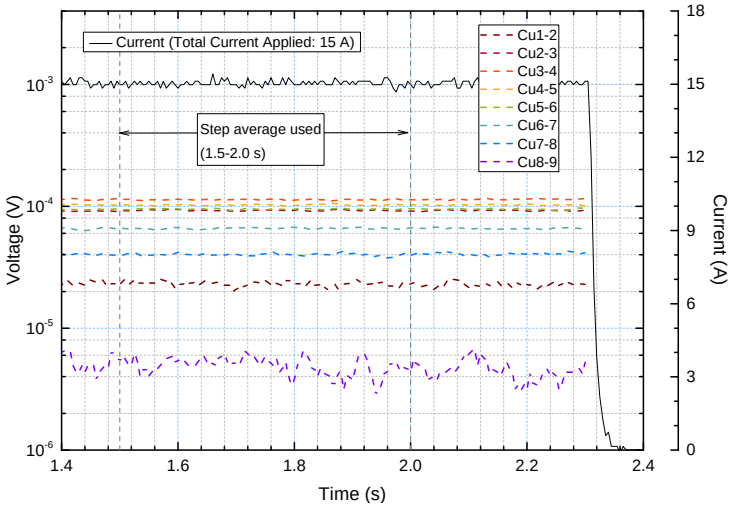

(a) Voltage-time traces for sections of Cu tape indicating time slice(s)/step average investigated.

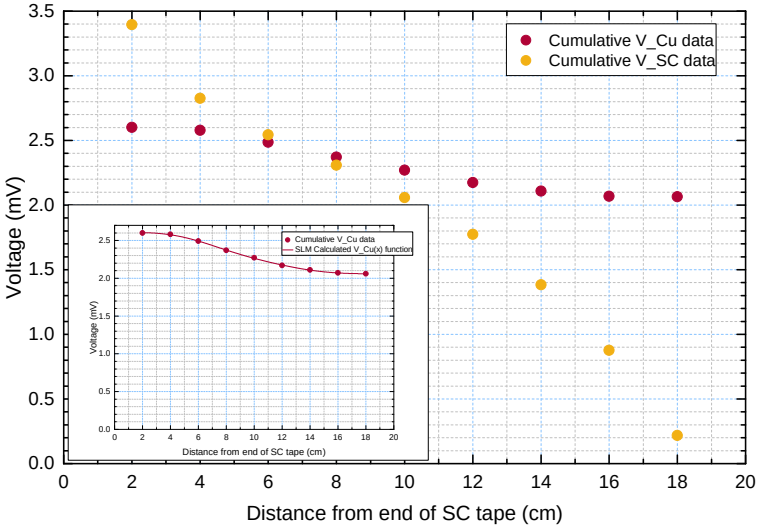

(b) Main figure: Measured cumulative voltage drop profiles for SC and Cu tapes; Inset: Measured cumulative voltage drop profile and continuous SLM spline approximation for Cu tape.

Figure 5.10: Plots for 40 K, no tape heater, 15 A applied, bolts loosened scenario; SS-Phase current sharing (continued in figure 5.11).

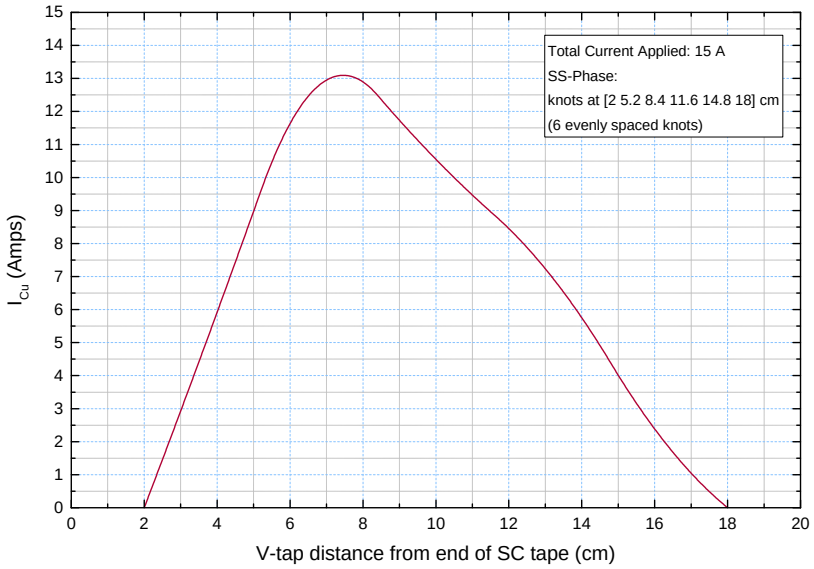

(a) Current carried by the Cu tape as a function of position along tape length, continuous function derived from differentiation of SLM curve in figure 5.10b (Inset).

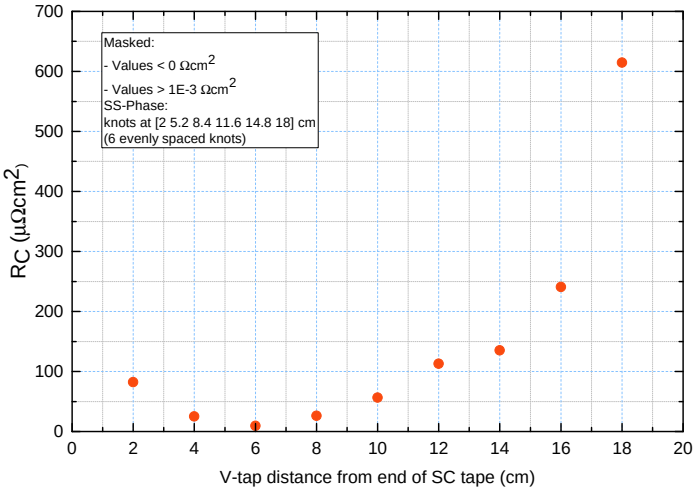

(b) Contact resistance approximation along tape length as calculated using the SLM spline method.

Figure 5.11: Continued plots for 40 K, no tape heater, 15 A applied, bolts loosened scenario; SS-Phase current sharing.

At 37.5 K, which is approximately the T_c of the SC tape, we see also a steady state, SS-Phase current sharing regime occurring in both BT and BL scenarios, with less current being shared in the BL scenario (maximum 9 A of the total applied 20 A, figure 5.15a) than the BT scenario (12 A of the total applied 20 A, 5.13a). In both cases less current is shared than at 40 K, suggesting that the SC tape is partially in the superconducting state, sharing only the excess current above I_c with the Cu tape. The effects of decreasing the contact pressure between the BT and BL scenarios, as observed at 40 K, are repeated in the $I_{Cu}(x)$ profiles and calculated R_C values at 37.5 K; as is the observed higher R_C on the RHS than on the LHS. Furthermore, R_C values calculated at 37.5 K are of the same order of magnitude as those calculated at 40 K (see figures 5.13b and 5.15b).

Just below the T_c of the SC tape, at 37 K, we observe a further effect of the contact pressure on the current sharing behaviour. In the BT scenario, steady state sharing is still just about observed, with some signs of increasing voltage due to ohmic or Joule heating (see figure 5.16a). However, the current sharing regime is US-Phase, with current transferring to and from, and to and from, the Cu tape (see figures 5.16b and 5.17a). This suggests that although an equilibrium in time was reached, the mechanisms driving the current sharing between the SC and Cu tapes, may not have been wholly dominated by R_C; for example, local I_c inhomogeneities in the SC tape may exist. It is interesting to note that, at all other temperatures where US-Phase sharing was observed it would, after time, resolve to SS-Phase sharing - whereas here it appeared a stable (with time) current sharing phase. Current was still being carried in the superconducting state so that less than 6 A of the 40 A applied was carried by the Cu tape at its maximum.

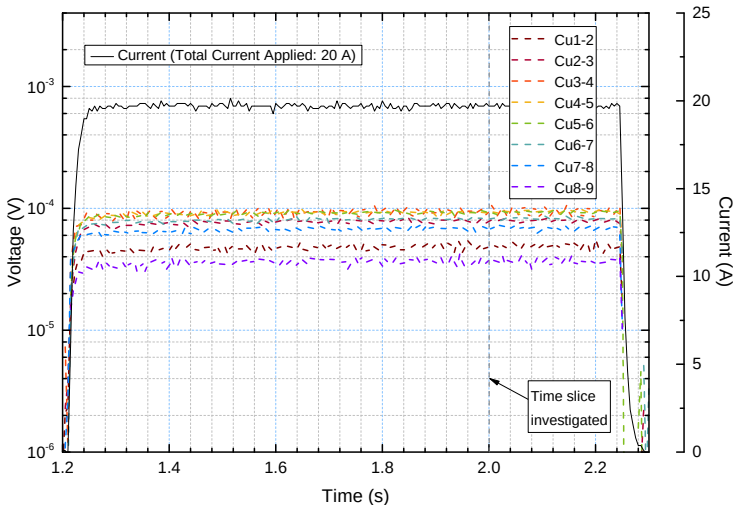

(a) Voltage-time traces for sections of Cu tape indicating time slice(s)/step average investigated.

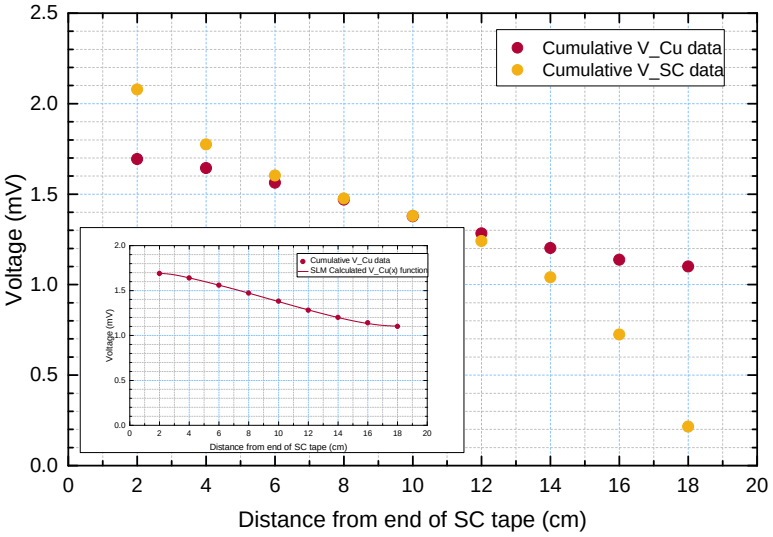

(b) Main figure: Measured cumulative voltage drop profiles for SC and Cu tapes; Inset: Measured cumulative voltage drop profile and continuous SLM spline approximation for Cu tape.

Figure 5.12: Plots for 37.5 K, no tape heater, 20 A applied, bolts tightened scenario; SS-Phase current sharing (continued in figure 5.13).

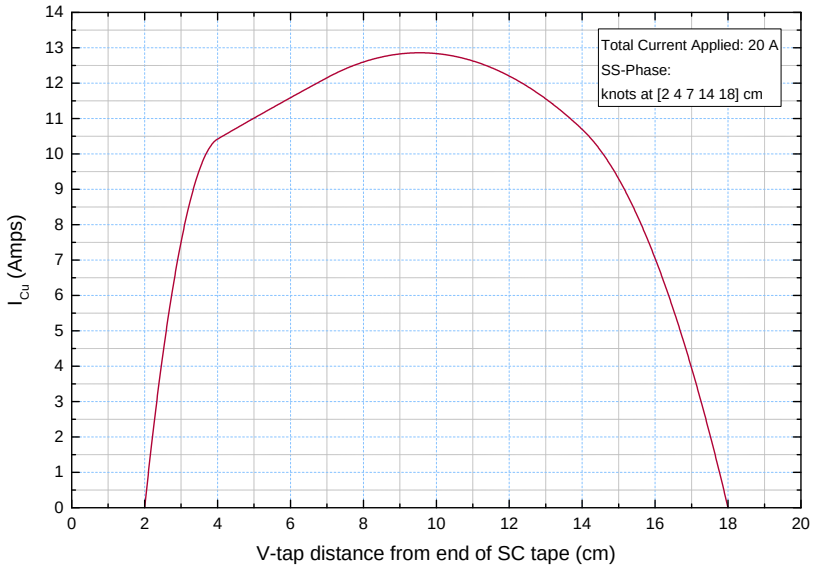

(a) Current carried by the Cu tape as a function of position along tape length, continuous function derived from differentiation of SLM curve in figure 5.12b (Inset).

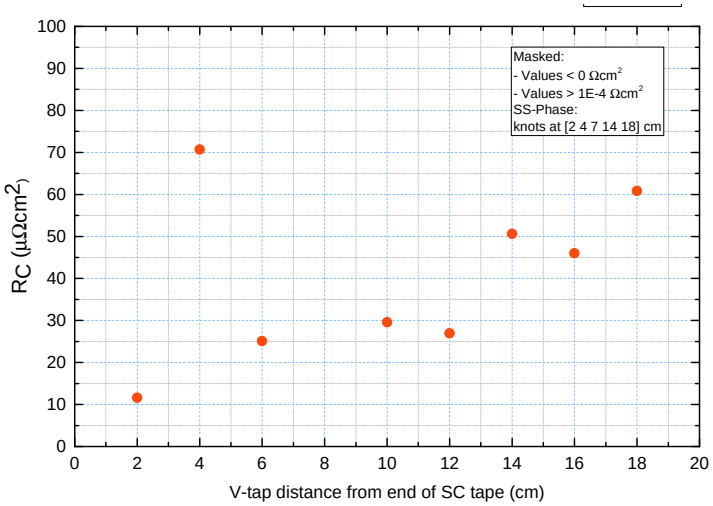

(b) Contact resistance approximation along tape length as calculated using the SLM spline method.

Figure 5.13: Continued plots for 37.5 K, no tape heater, 20 A applied, bolts tightened scenario; SS-Phase current sharing.

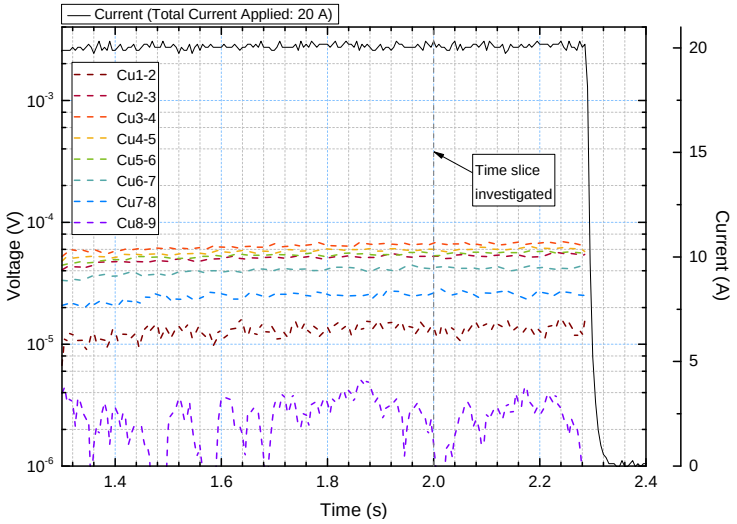

(a) Voltage-time traces for sections of Cu tape indicating time slice(s)/step average investigated.

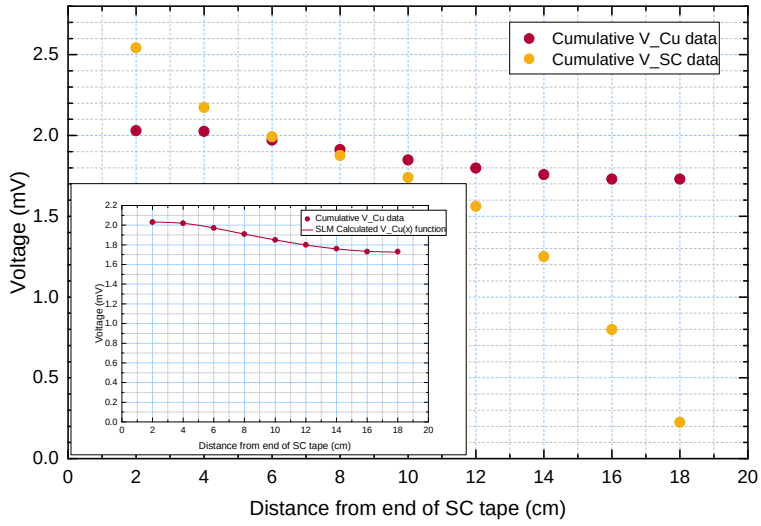

(b) Main figure: Measured cumulative voltage drop profiles for SC and Cu tapes; Inset: Measured cumulative voltage drop profile and continuous SLM spline approximation for Cu tape.

Figure 5.14: Plots for 37.5 K, no tape heater, 20 A applied, bolts loosened scenario; SS-Phase current sharing (continued in figure 5.15).

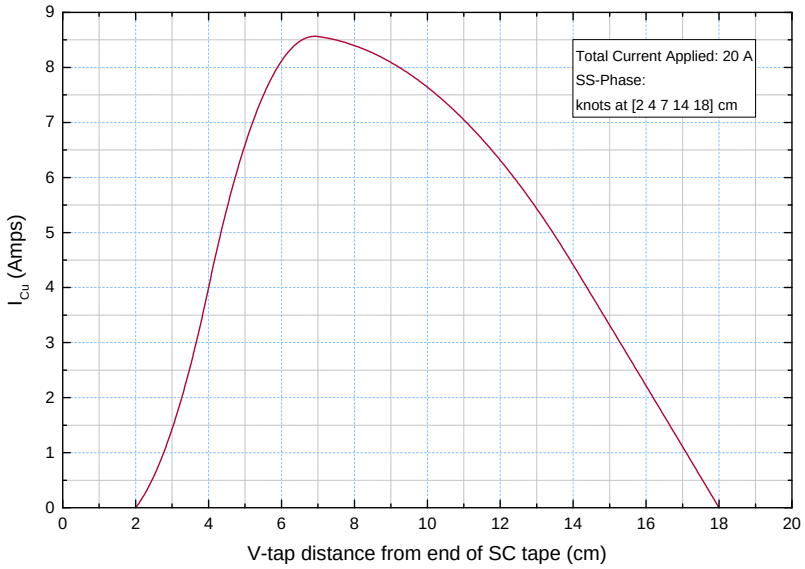

(a) Current carried by the Cu tape as a function of position along tape length, continuous function derived from differentiation of SLM curve in figure 5.14b (Inset).

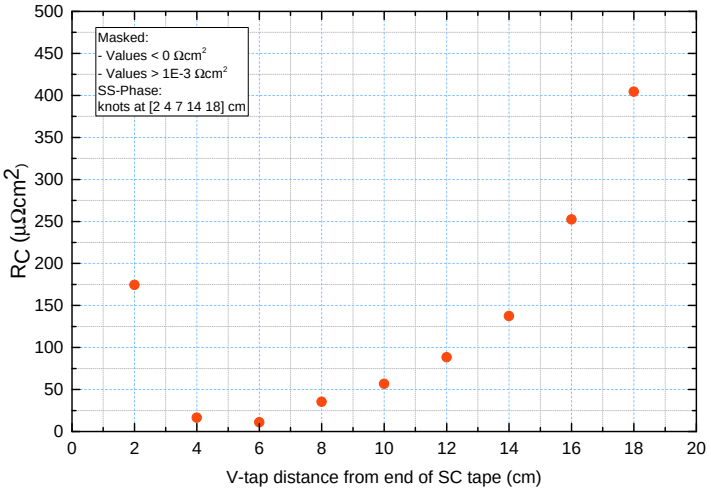

(b) Contact resistance approximation along tape length as calculated using the SLM spline method.

Figure 5.15: Continued plots for 37.5 K, no tape heater, 20 A applied, bolts loosened scenario; SS-Phase current sharing.

Figure 5.18a shows that, in the BL scenario, the voltages measured are no longer constant with time, unlike the BT equivalent, and so a time slice at the end of the current step, with the highest measured voltages, is observed, in figures 5.18 and 5.19. Also unlike the BT scenario, in the equivalent BL scenario, SS-Phase current sharing is still observed (see figures 5.18b and 5.19a). However, much more current is shared with the copper tape than both the the equivalent BT and the higher temperature BL scenarios, with up to a maximum of 35 A in the Cu tape of the 55 A applied; the system had become unstable with a positive feedback heating loop preventing a steady state equilibrium being reached.

A further difference between the different contact scenarios, not seen at higher temperatures, is that, unexpectedly, higher currents are required to start a thermal runaway in the BL than in the BT scenario. This is also observed at some lower temperatures, as shown by the differences in I_{quench} in figure 5.2a, and possible explanations of this are discussed in section 5.2.6.1.

As observed at 40 K and 37.5 K, the difference between the BT and BL $I_{Cu}(x)$ profiles and calculated R_C values is also present at 37 K; as is the observed higher R_C on the RHS than on the LHS. The R_C values calculated also show consistency across all three temperatures, with BT values being around 10 to 70 $\mu\Omega\text{cm}^2$ and BL values around 50 to 500 $\mu\Omega\text{cm}^2$, with the variation being with position along tape length rather than between the different temperatures. R_C results at positions around that of the zero-points or maximums in the $I_{Cu}(x)$ curves appear somewhat unreliable, a trend which is observed at all temperatures measured and which is discussed in section 5.2.6.2.

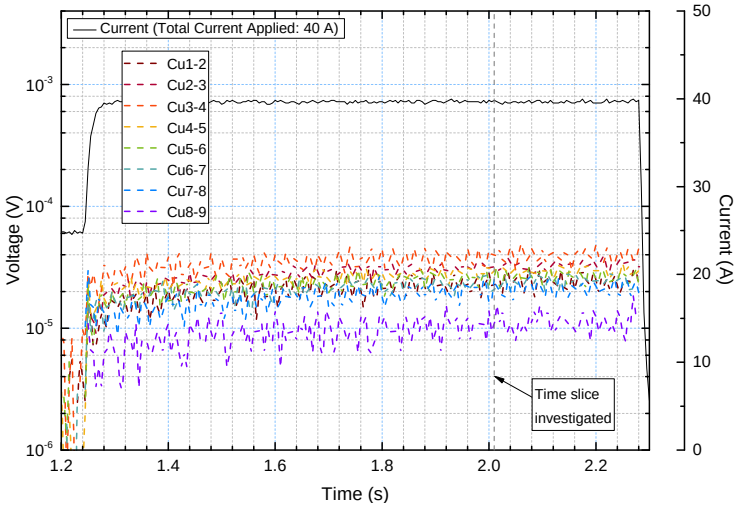

(a) Voltage-time traces for sections of Cu tape indicating time slice(s)/step average investigated.

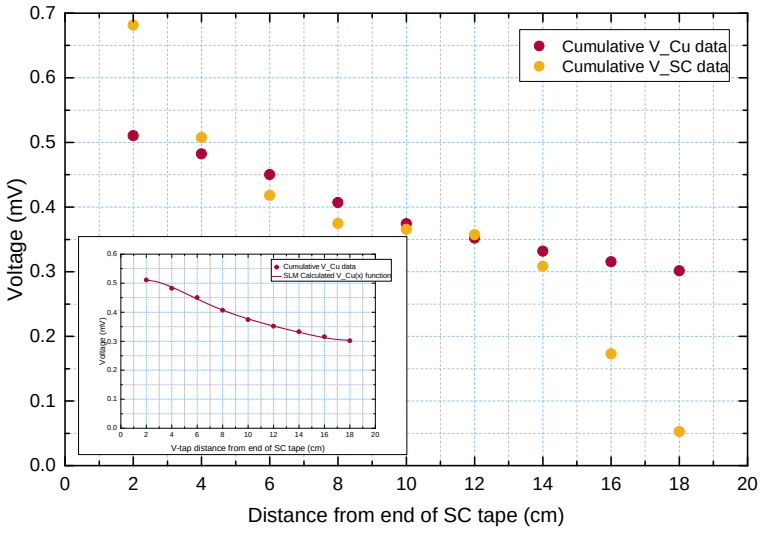

(b) Main figure: Measured cumulative voltage drop profiles for SC and Cu tapes; Inset: Measured cumulative voltage drop profile and continuous SLM spline approximation for Cu tape.

Figure 5.16: Plots for 37 K, no tape heater, 40 A applied, bolts tightened scenario; US-Phase current sharing (continued in figure 5.17).

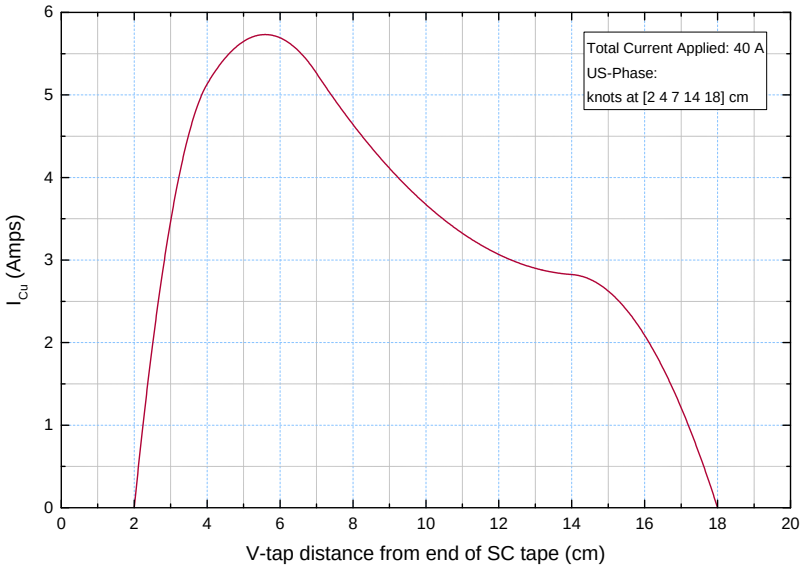

(a) Current carried by the Cu tape as a function of position along tape length, continuous function derived from differentiation of SLM curve in figure 5.16b (Inset).

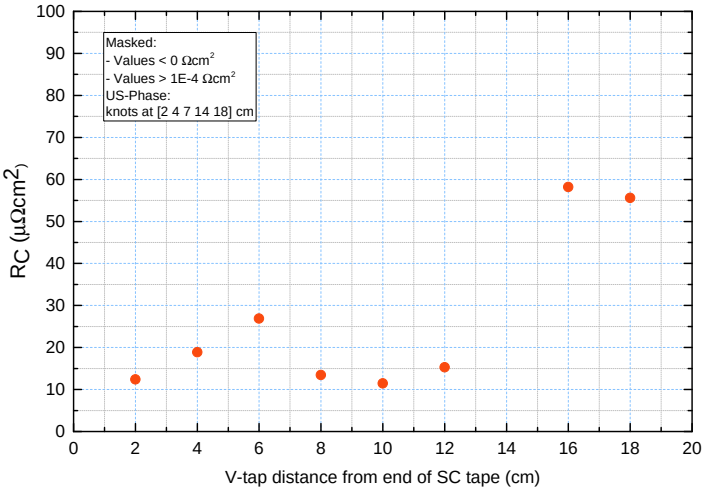

(b) Contact resistance approximation along tape length as calculated using the SLM spline method.

Figure 5.17: Continued plots for 37 K, no tape heater, 40 A applied, bolts tightened scenario; US-Phase current sharing.

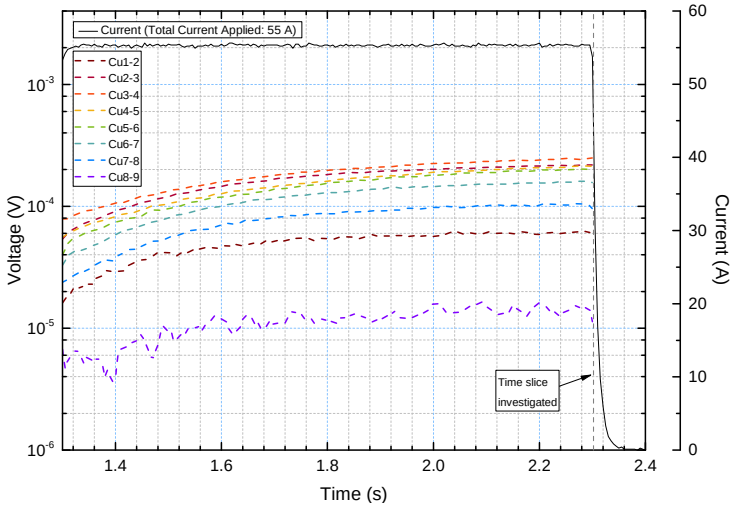

(a) Voltage-time traces for sections of Cu tape indicating time slice(s)/step average investigated.

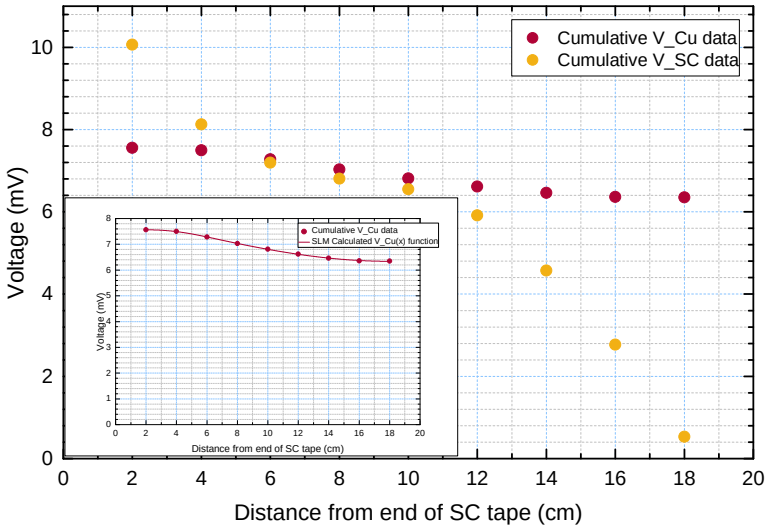

(b) Main figure: Measured cumulative voltage drop profiles for SC and Cu tapes; Inset: Measured cumulative voltage drop profile and continuous SLM spline approximation for Cu tape.

Figure 5.18: Plots for 37 K, no tape heater, 55 A applied, bolts loosened scenario; SS-Phase current sharing (continued in figure 5.19).

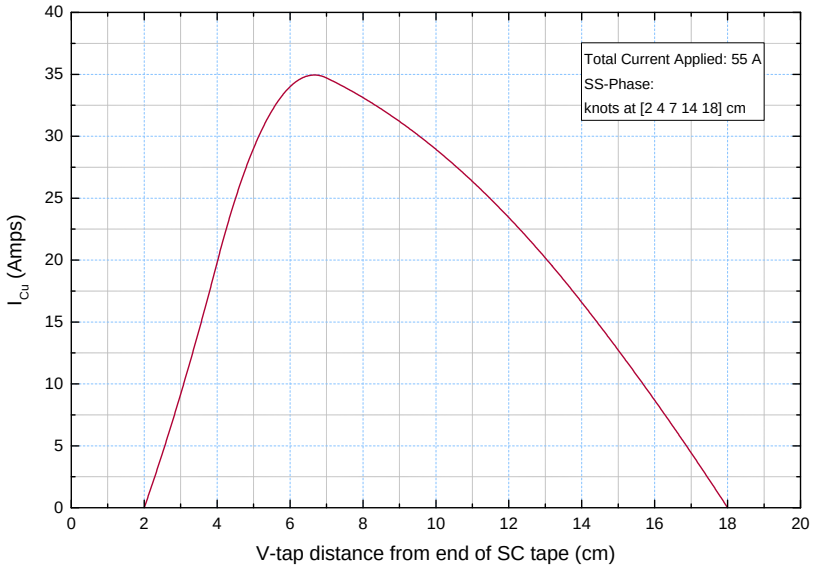

(a) Current carried by the Cu tape as a function of position along tape length, continuous function derived from differentiation of SLM curve in figure 5.18b (Inset).

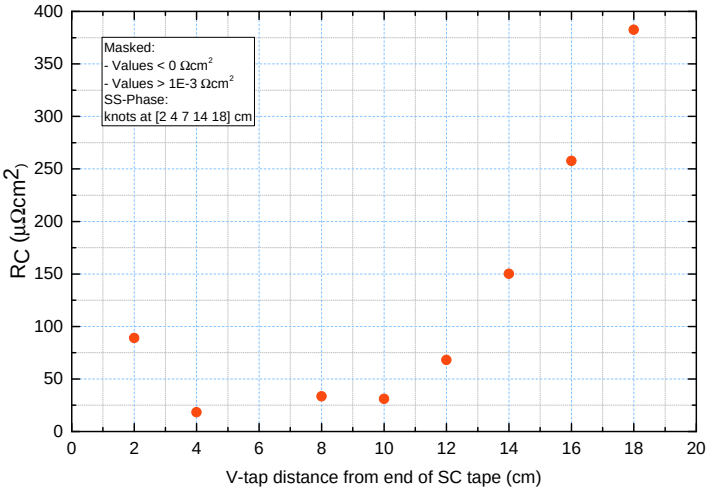

(b) Contact resistance approximation along tape length as calculated using the SLM spline method.

Figure 5.19: Continued plots for 37 K, no tape heater, 55 A applied, bolts loosened scenario; SS-Phase current sharing.

The most stable current sharing regime at and around the sample T_c has been shown to be for the majority of the current to be carried by the Cu tape as the resistivity of Cu is lower than that of the SC tape in the resistive state, which is mainly dependent on that of its nickel alloy sheath. The nature of the contact between the tapes determines the CTL and the total current shared: the better the contact (the higher the contact pressure and the lower the contact resistance), the shorter the CTL and, over a finite length, the more current was shared. How the current was distributed, however, was not solely reliant on R_C, as will be seen in the following lower temperature results.

5.2.5 Results with No Tape Heater, Below T_C

At 36 K, L-Phase current sharing can be observed in both the BT and BL scenarios, as shown in figures 5.20b and 5.21a (BT) and 5.22b and 5.23a (BL). Higher R_C values are once again calculated on the RHS in both cases (figures 5.21b [BT] and 5.23b [BL]). It appears that in these scenarios, the higher R_C on the RHS is the dominant mechanism in driving the current transfer regime, forcing current to share with the Cu tape predominantly on the LHS of the sample. It is worth noting the different $I_{Cu}(x)$ shapes in the BT and BL scenarios, with more current shared in the BT scenario, both over the length of the tapes and with a higher maximum (71 A of the applied 110 A compared to 41 A of the applied 115 A in the BL case). Higher R_C values are seen in the BL scenario overall, and all R_C values are of a similar order of magnitude to those calculated at higher temperatures.

Note that in figure 5.23b, R_C values calculated at $x = 12$ cm are not reliable values. This has been observed for R_C values estimated around the zero-points and is discussed in section 5.2.6.2.

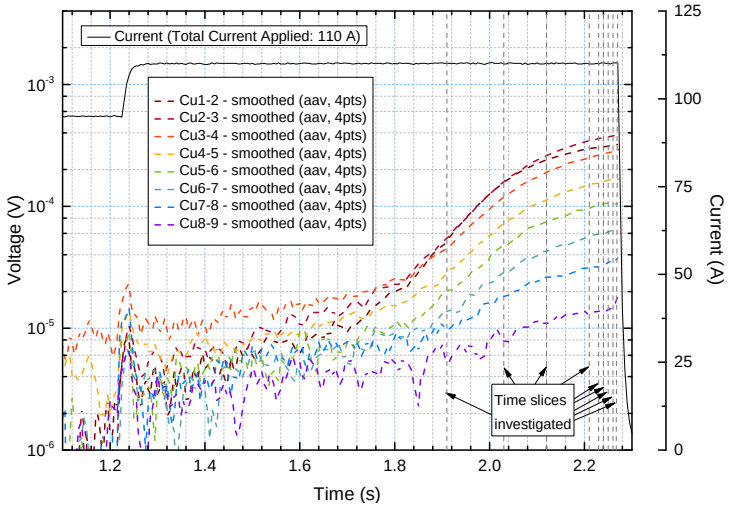

(a) Voltage-time traces for sections of Cu tape indicating time slice(s)/step average investigated.

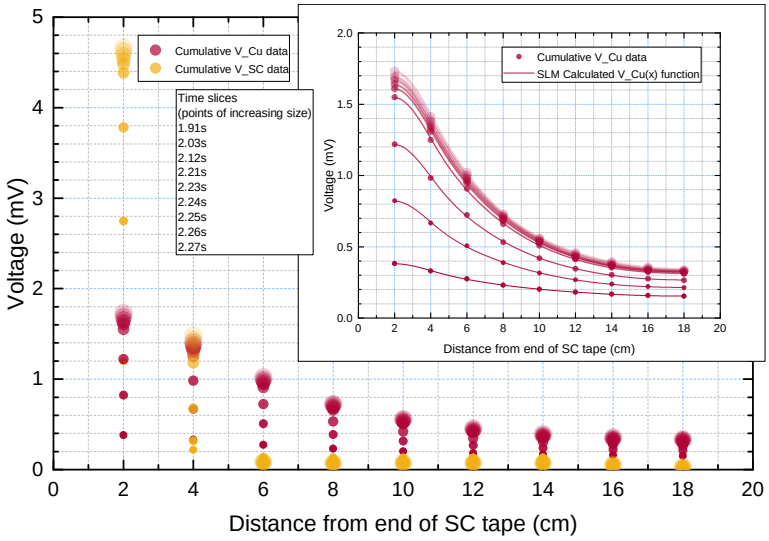

(b) Main figure: Measured cumulative voltage drop profiles for SC and Cu tapes; Inset: Measured cumulative voltage drop profile and continuous SLM spline approximation for Cu tape.

Figure 5.20: Plots for 36 K, no tape heater, 110 A applied, bolts tightened scenario; L-Phase current sharing (continued in figure 5.21).

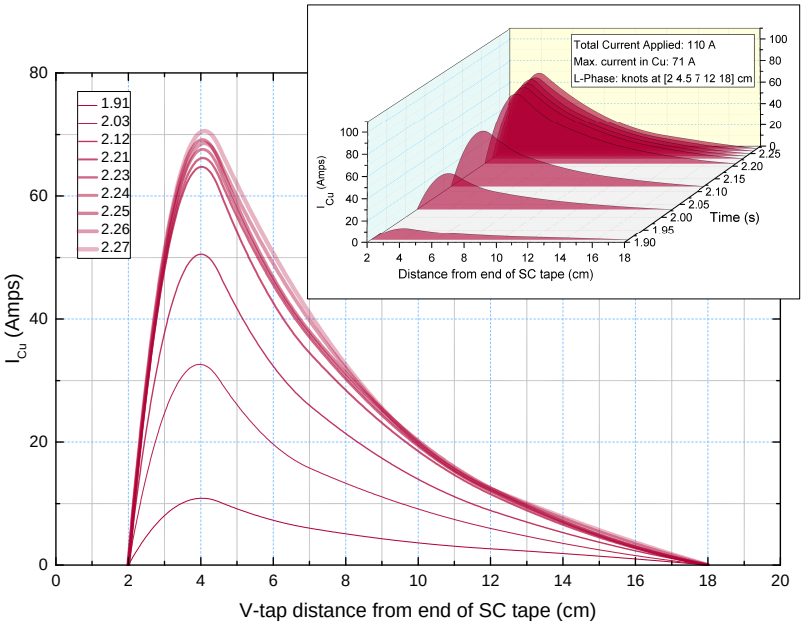

(a) Current carried by the Cu tape as a function of position along tape length, continuous function derived from differentiation of SLM curves in figure 5.20b (Inset) - Main figure: 2D plot, zoomed scale; Inset: 3D plot showing evolution with time, scale reflects total applied current.

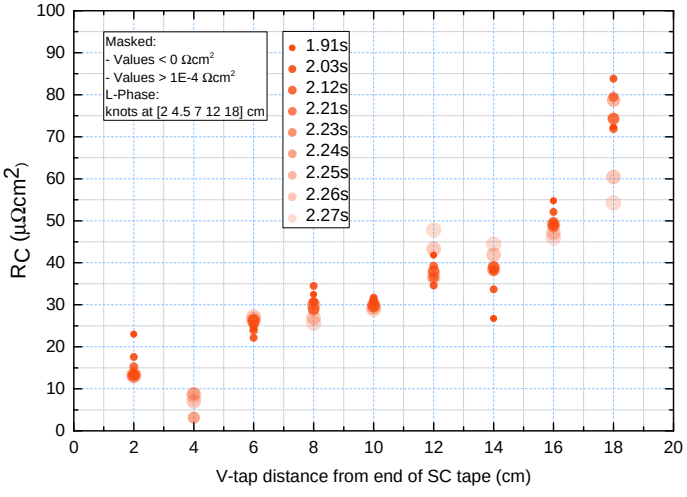

(b) Contact resistance approximation along tape length as calculated using the SLM spline method.

Figure 5.21: Continued plots for 36 K, no tape heater, 110 A applied, bolts tightened scenario; L-Phase current sharing.

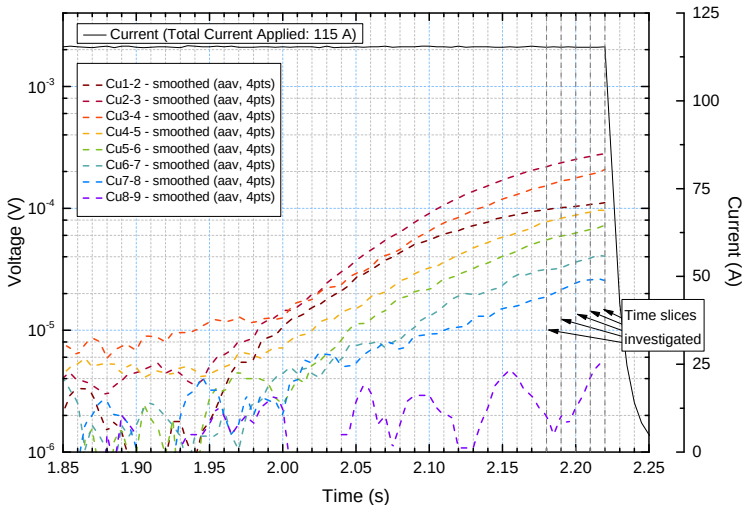

(a) Voltage-time traces for sections of Cu tape indicating time slice(s)/step average investigated.

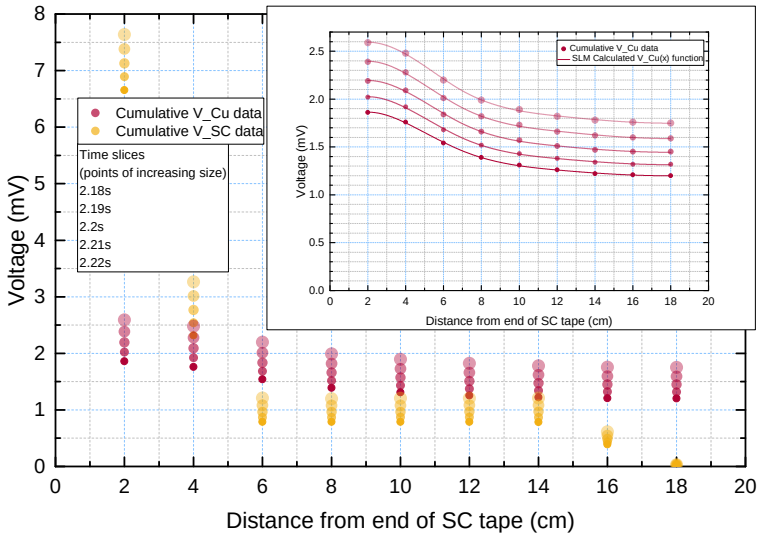

(b) Main figure: Measured cumulative voltage drop profiles for SC and Cu tapes; Inset: Measured cumulative voltage drop profile and continuous SLM spline approximation for Cu tape.

Figure 5.22: Plots for 36 K, no tape heater, 115 A applied, bolts loosened scenario; L-Phase current sharing (continued in figure 5.23).

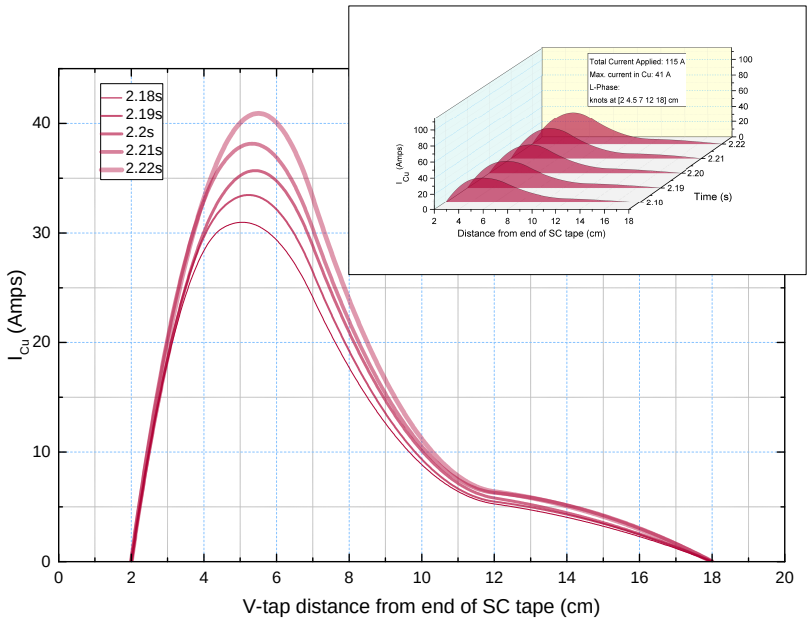

(a) Current carried by the Cu tape as a function of position along tape length, continuous function derived from differentiation of SLM curves in figure 5.22b (Inset) - Main figure: 2D plot, zoomed scale; Inset: 3D plot showing evolution with time, scale reflects total applied current.

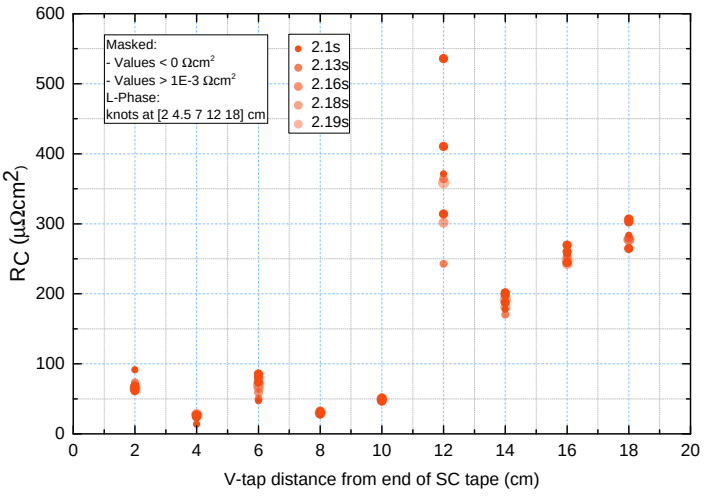

(b) Contact resistance approximation along tape length as calculated using the SLM spline method.

Figure 5.23: Continued plots for 36 K, no tape heater, 115 A applied, bolts loosened scenario; L-Phase current sharing.

As shown in figure 5.2a, at temperatures below 36 K, in the BL scenarios I_c was equal to I_{quench} whereas in the BT scenarios I_{quench} remained between 2 A and 9 A higher than I_c. In the case of the 35 K BT scenario, under the definition for I_{quench} given in section 5.2.2, the first exponential voltage increase with sample heating was measured at 194 A - however, this temperature increase was only seen in the far right of the SC tape. The 195 A scenario is therefore also shown here.

This has led to an interesting observation. As figures 5.24 and 5.25 show, in the BT 194 A scenario, current sharing was only just beginning, with a maximum of 4 A estimated to be carried by the Cu tape. However, this current was shared predominantly on the RHS of the sample, which is contrary to what was observed at 36 K, and what is seen in the BL 35 K scenario, in which L-Phase current sharing was observed (see figures 5.28 and 5.29). Despite the higher R_C on the RHS side of the sample, which was still observed at 35 K (figures 5.25b [BT 194 A], 5.27b [BT 195 A] and 5.29b [BL]), current, albeit a relatively small amount, was transferring to the Cu tape preferentially on the RHS than on the LHS where R_C was shown to be lower. This suggests, as with the US-Phase scenarios, that a mechanism other than the higher R_C on the RHS was determining the current transfer regime.

In the BT 35 K, 195 A scenario, US-Phase current transfer is observed (figures 5.26 and 5.27). It is believed that this increase in current transfer on the LHS, with a secondary peak in the $I_{Cu}(x)$ curve on the RHS, occurs as the higher R_C on the RHS becomes more dominant in driving current transfer than any other mechanism, for example, potentially lower local I_c on the RHS. Figures 5.28 and 5.29 show the results of the 35 K BL scenario, once again with L-Phase current sharing.

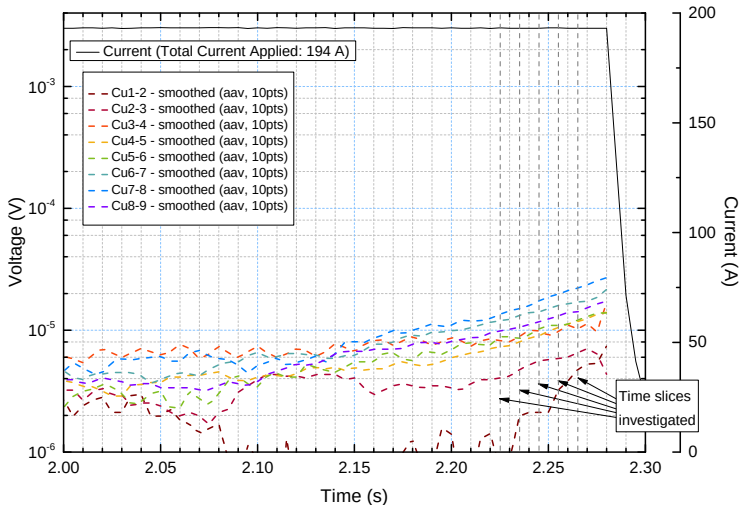

(a) Voltage-time traces for sections of Cu tape indicating time slice(s)/step average investigated.

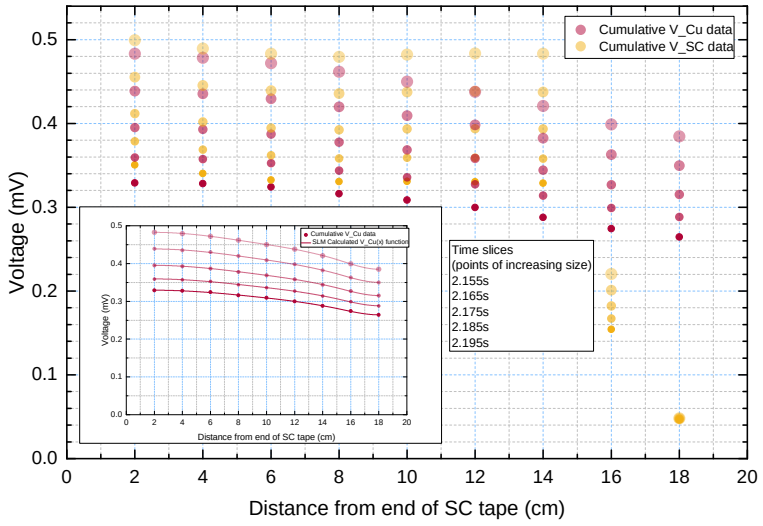

(b) Main figure: Measured cumulative voltage drop profiles for SC and Cu tapes; Inset: Measured cumulative voltage drop profile and continuous SLM spline approximation for Cu tape.

Figure 5.24: Plots for 35 K, no tape heater, 194 A applied, bolts tightened scenario; R-Phase current sharing (continued in figure 5.25).

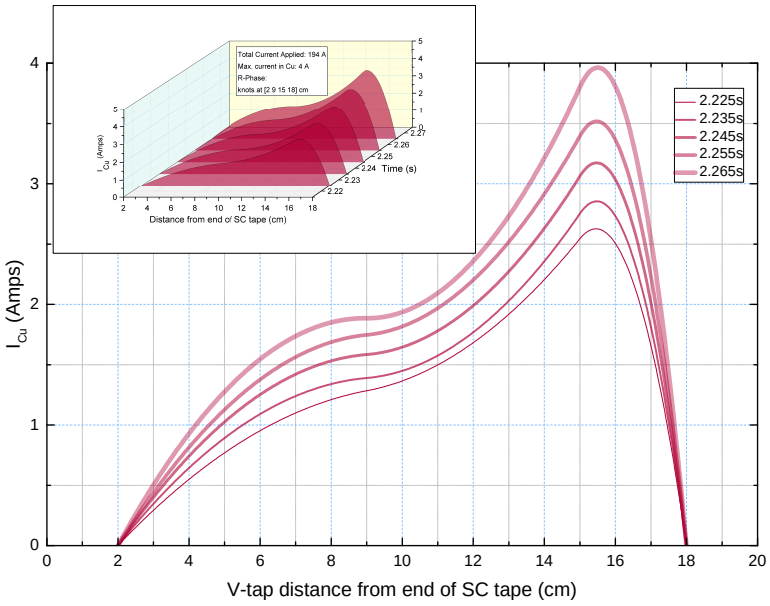

(a) Current carried by the Cu tape as a function of position along tape length, continuous function derived from differentiation of SLM curves in figure 5.24b (Inset) - Main figure: 2D plot, zoomed scale; Inset: 3D plot showing evolution with time, zoomed scale.

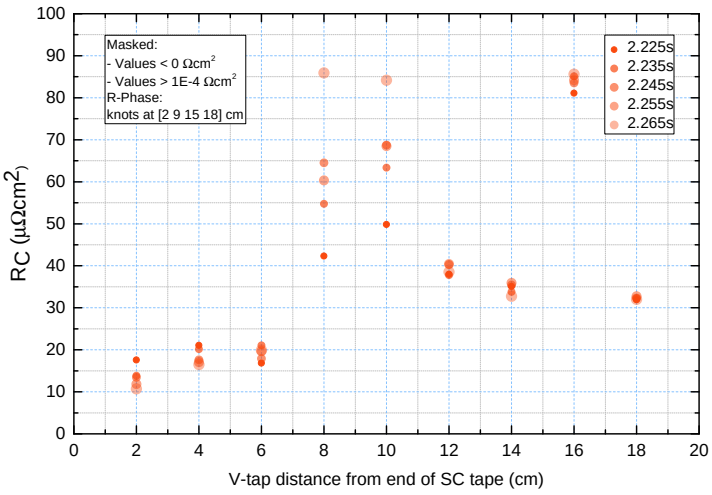

(b) Contact resistance approximation along tape length as calculated using the SLM spline method.

Figure 5.25: Continued plots for 35 K, no tape heater, 194 A applied, bolts tightened scenario; R-Phase current sharing.

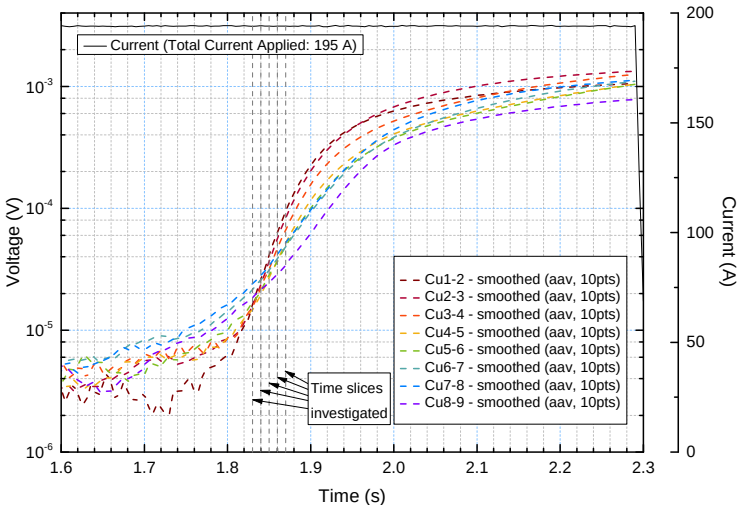

(a) Voltage-time traces for sections of Cu tape indicating time slice(s)/step average investigated.

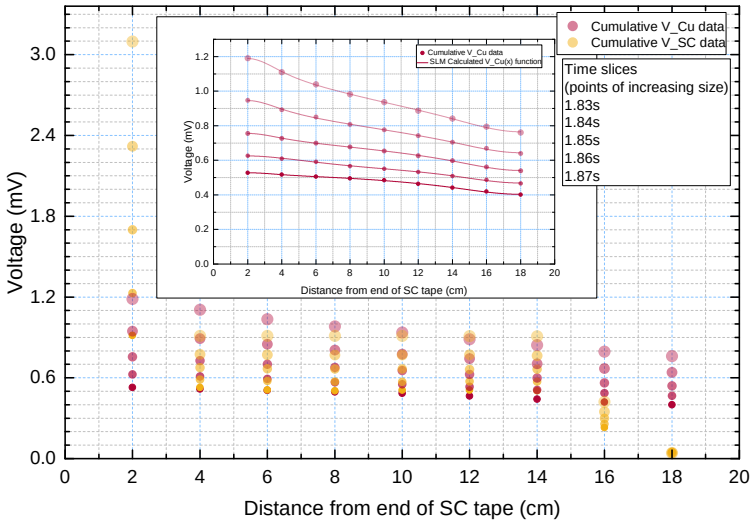

(b) Main figure: Measured cumulative voltage drop profiles for SC and Cu tapes; Inset: Measured cumulative voltage drop profile and continuous SLM spline approximation for Cu tape.

Figure 5.26: Plots for 35 K, no tape heater, 195 A applied, bolts tightened scenario; US-Phase current sharing (continued in figure 5.27).

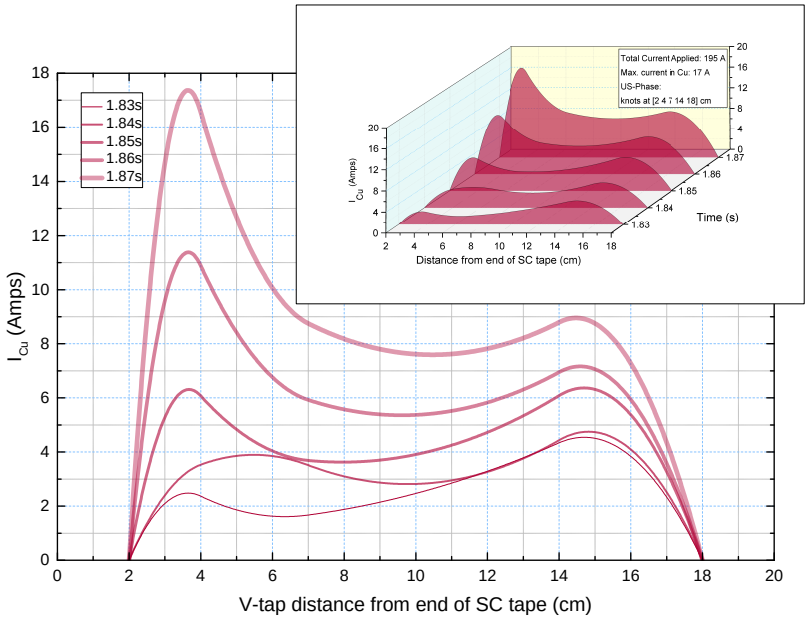

(a) Current carried by the Cu tape as a function of position along tape length, continuous function derived from differentiation of SLM curves in figure 5.26b (Inset) - Main figure: 2D plot, zoomed scale; Inset: 3D plot showing evolution with time, zoomed scale.

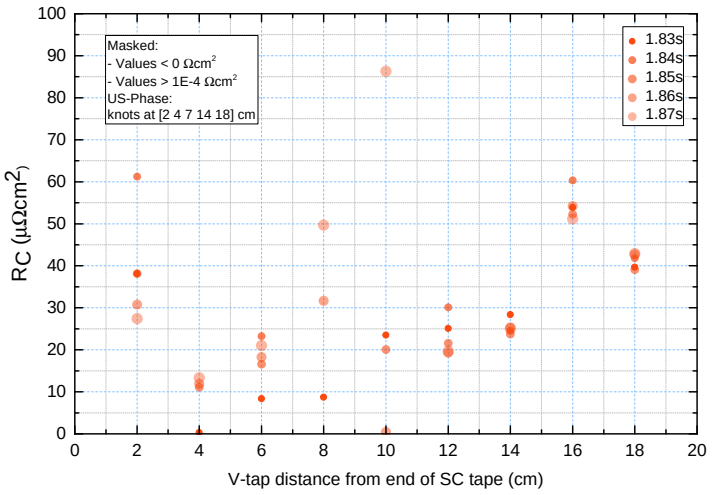

(b) Contact resistance approximation along tape length as calculated using the SLM spline method.

Figure 5.27: Continued plots for 35 K, no tape heater, 195 A applied, bolts tightened scenario; US-Phase current sharing.

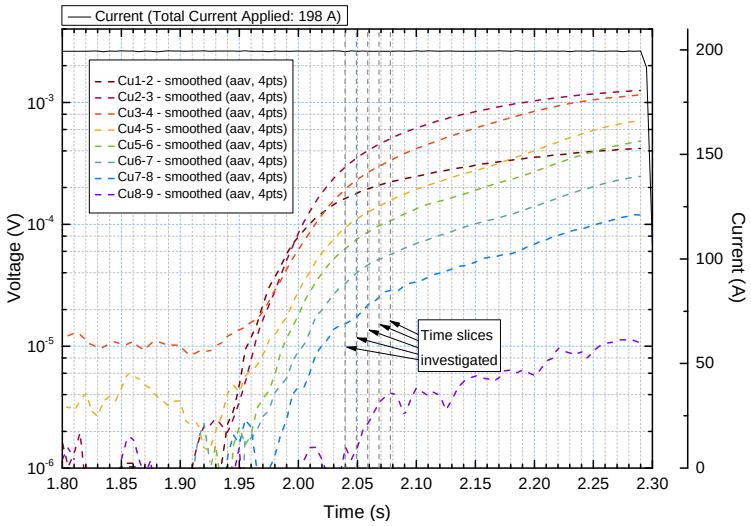

(a) Voltage-time traces for sections of Cu tape indicating time slice(s)/step average investigated.

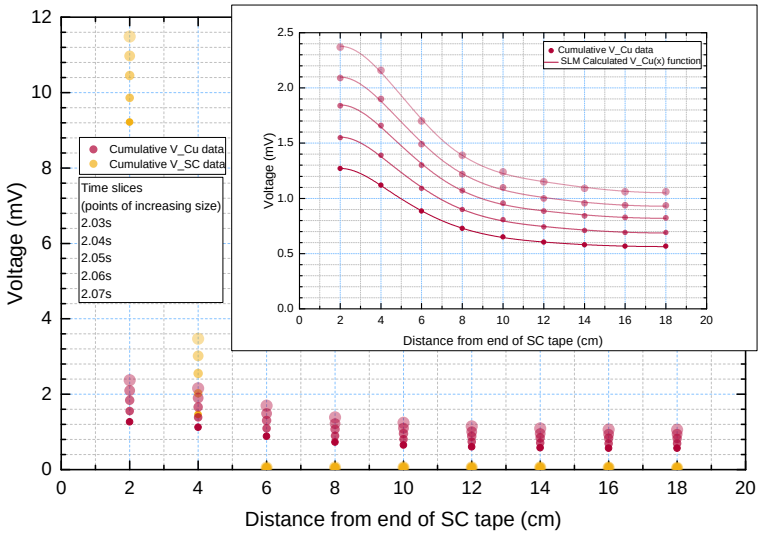

(b) Main figure: Measured cumulative voltage drop profiles for SC and Cu tapes; Inset: Measured cumulative voltage drop profile and continuous SLM spline approximation for Cu tape.

Figure 5.28: Plots for 35 K, no tape heater, 198 A applied, bolts loosened scenario; L-Phase current sharing (continued in figure 5.29).

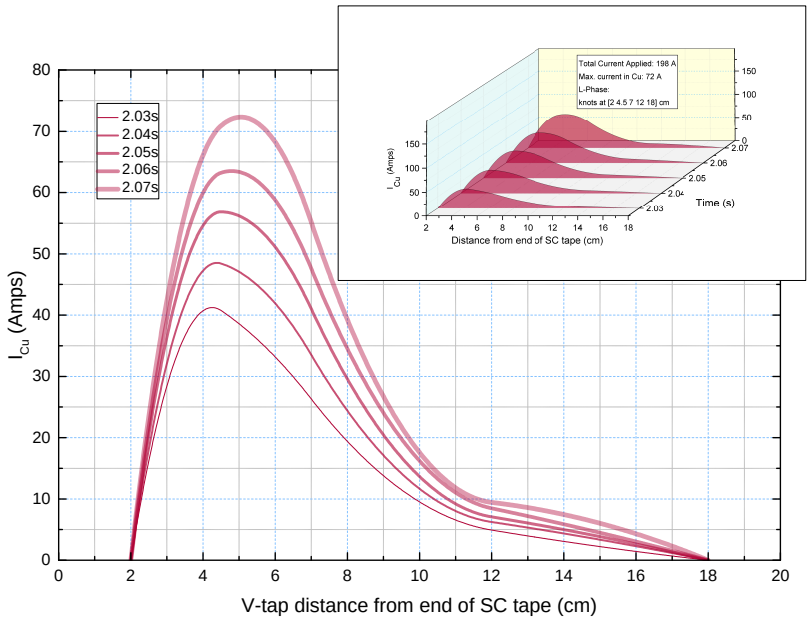

(a) Current carried by the Cu tape as a function of position along tape length, continuous function derived from differentiation of SLM curves in figure 5.28b (Inset) - Main figure: 2D plot, zoomed scale; Inset: 3D plot showing evolution with time, scale reflects total applied current.

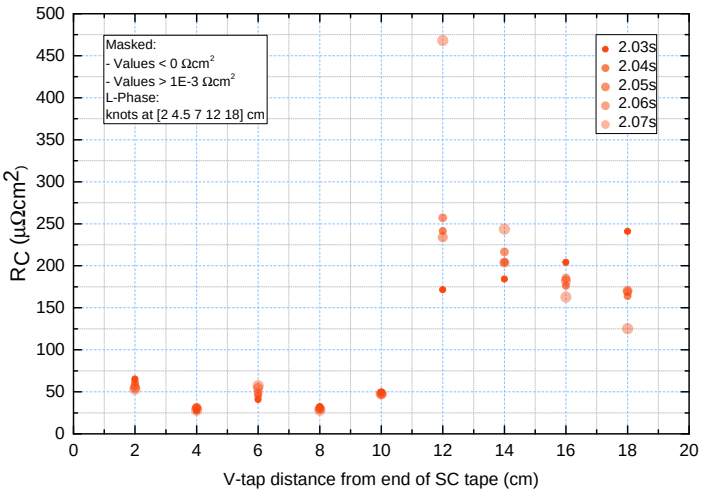

(b) Contact resistance approximation along tape length as calculated using the SLM spline method.

Figure 5.29: Continued plots for 35 K, no tape heater, 198 A applied, bolts loosened scenario; L-Phase current sharing.

At 34 K, US-Phase current sharing is observed in the BT scenario and L-Phase in the BL scenario (see figures 5.30 to 5.33). Unlike at all other temperatures measured, I_{quench} was the same in both the BT and BL scenarios at 34 K.

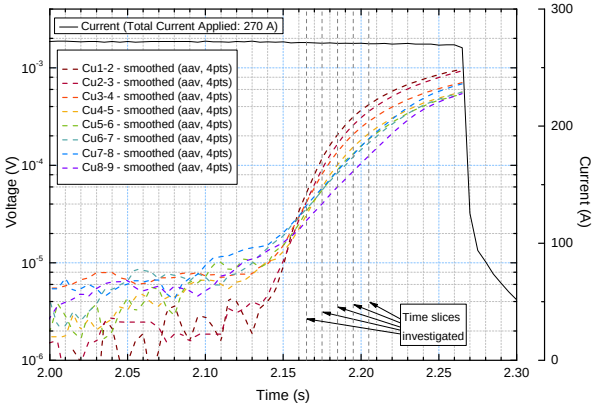

(a) Voltage-time traces for sections of Cu tape indicating time slice(s)/step average investigated.

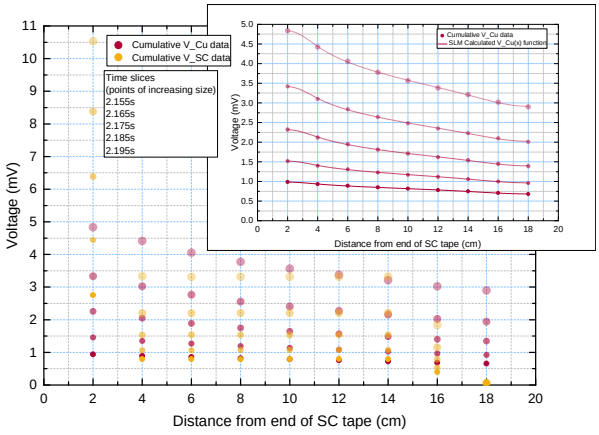

(b) Main figure: Measured cumulative voltage drop profiles for SC and Cu tapes; Inset: Measured cumulative voltage drop profile and continuous SLM spline approximation for Cu tape.

Figure 5.30: Plots for 34 K, no tape heater, 270 A applied, bolts tightened scenario; US-Phase current sharing (continued in figure 5.31).

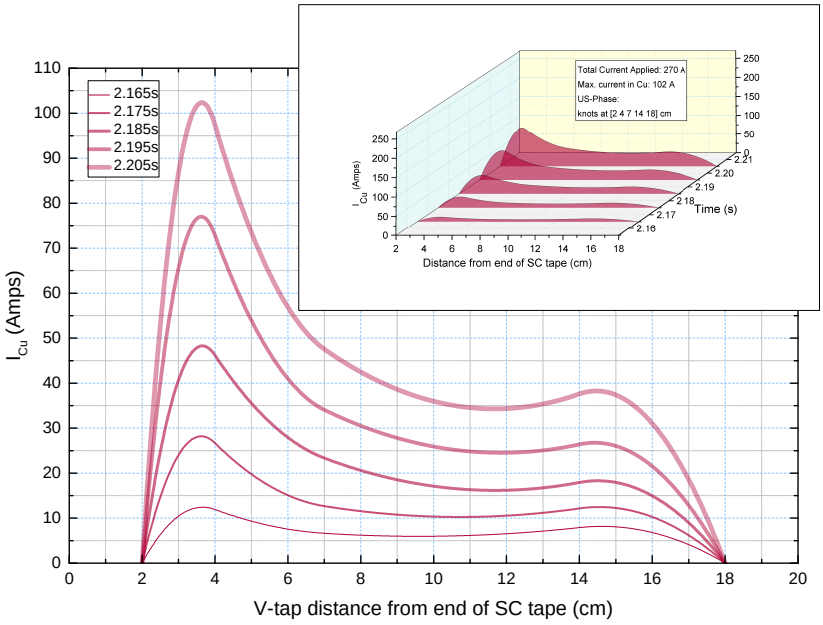

(a) Current carried by the Cu tape as a function of position along tape length, continuous function derived from differentiation of SLM curves in figure 5.30b (Inset) - Main figure: 2D plot, zoomed scale; Inset: 3D plot showing evolution with time, scale reflects total applied current.

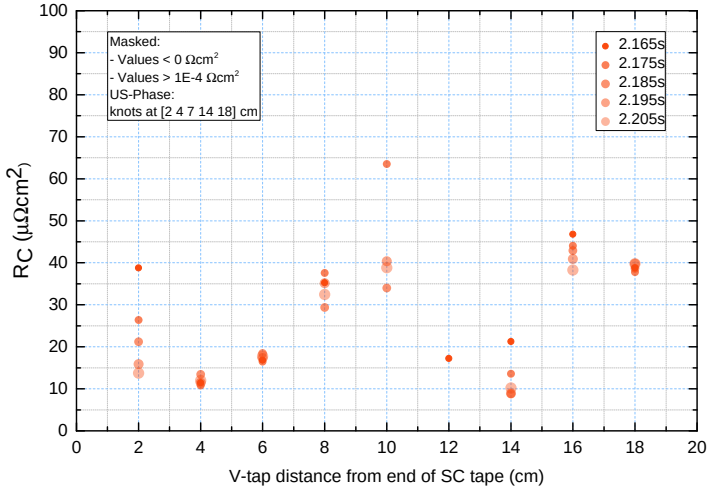

(b) Contact resistance approximation along tape length as calculated using the SLM spline method.

Figure 5.31: Continued plots for 34 K, no tape heater, 270 A applied, bolts tightened scenario; US-Phase current sharing.

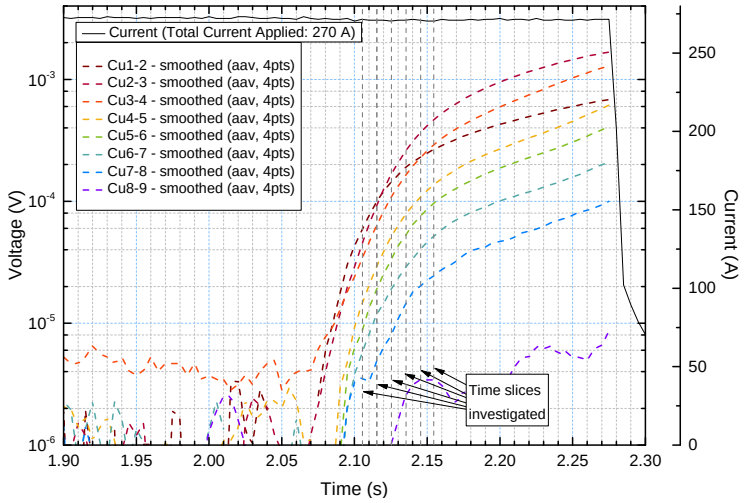

(a) Voltage-time traces for sections of Cu tape indicating time slice(s)/step average investigated.

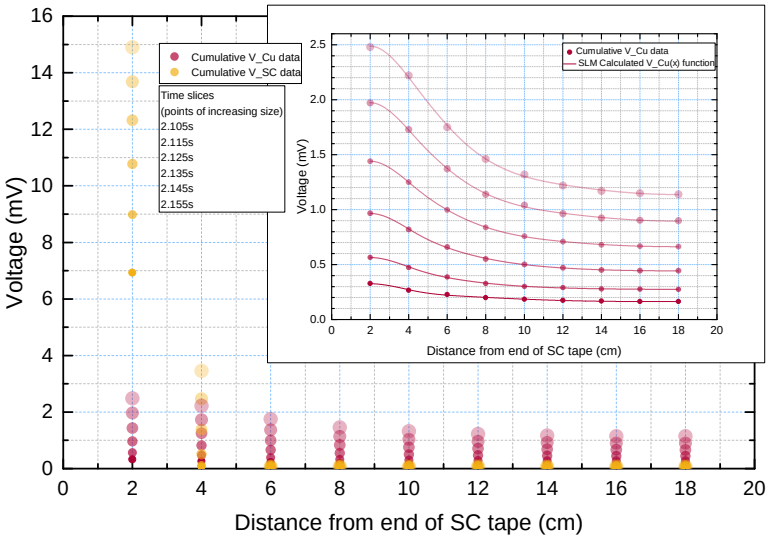

(b) Main figure: Measured cumulative voltage drop profiles for SC and Cu tapes; Inset: Measured cumulative voltage drop profile and continuous SLM spline approximation for Cu tape.

Figure 5.32: Plots for 34 K, no tape heater, 270 A applied, bolts loosened scenario; L-Phase current sharing (continued in figure 5.33).

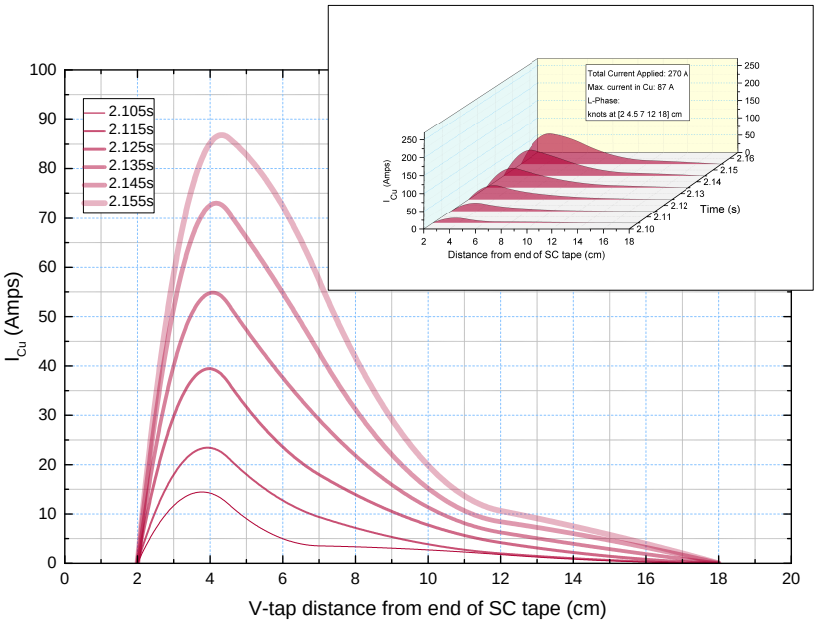

(a) Current carried by the Cu tape as a function of position along tape length, continuous function derived from differentiation of SLM curves in figure 5.32b (Inset) - Main figure: 2D plot, zoomed scale; Inset: 3D plot showing evolution with time, scale reflects total applied current.

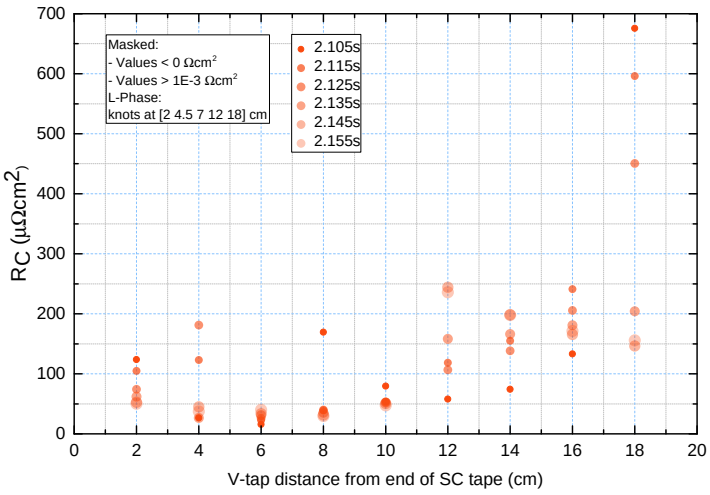

(b) Contact resistance approximation along tape length as calculated using the SLM spline method.

Figure 5.33: Continued plots for 34 K, no tape heater, 270 A applied, bolts loosened scenario; L-Phase current sharing.

At 33 K, we see R-Phase sharing once more in the BT scenario, although unlike at 35 K, it is far more substantial, with a maximum of 190 A of the 354 A applied. L-Phase is continued to be observed in the BL scenario. (See figures 5.34 to 5.37.)

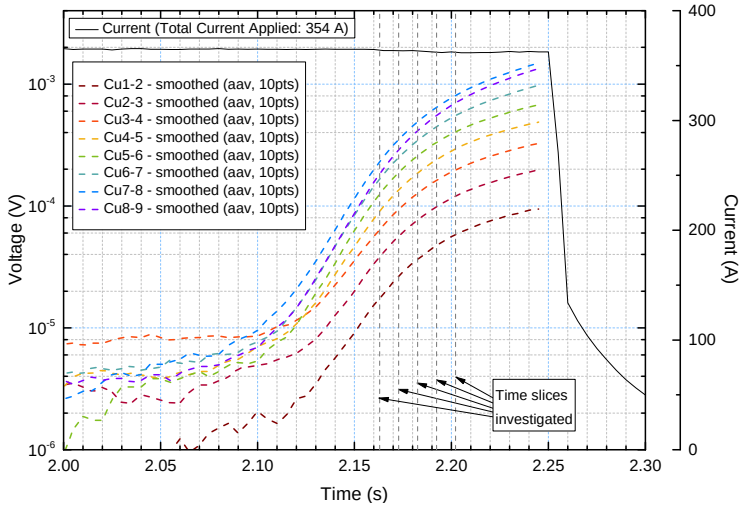

(a) Voltage-time traces for sections of Cu tape indicating time slice(s)/step average investigated.

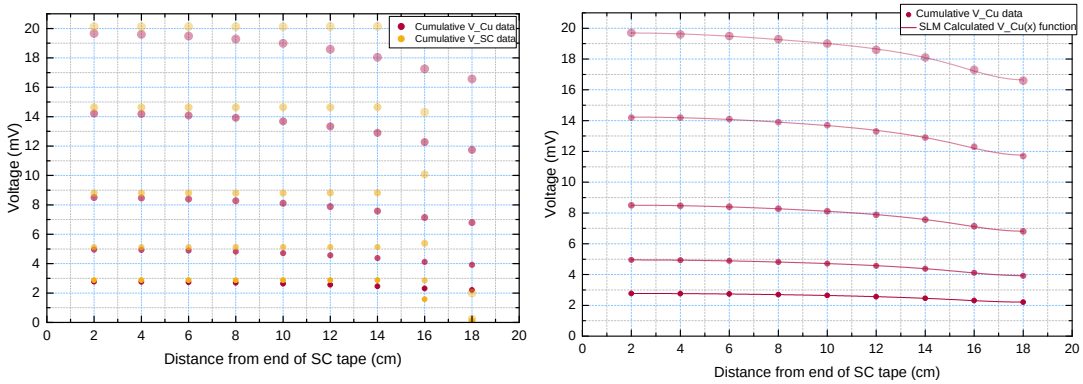

(b) Left: Measured cumulative voltage drop profiles for SC and Cu tapes; Right: Measured cumulative voltage drop profile and continuous SLM spline approximation for Cu tape.

Figure 5.34: Plots for 33 K, no tape heater, 354 A applied, bolts tightened scenario; R-Phase current sharing (continued in figure 5.35).

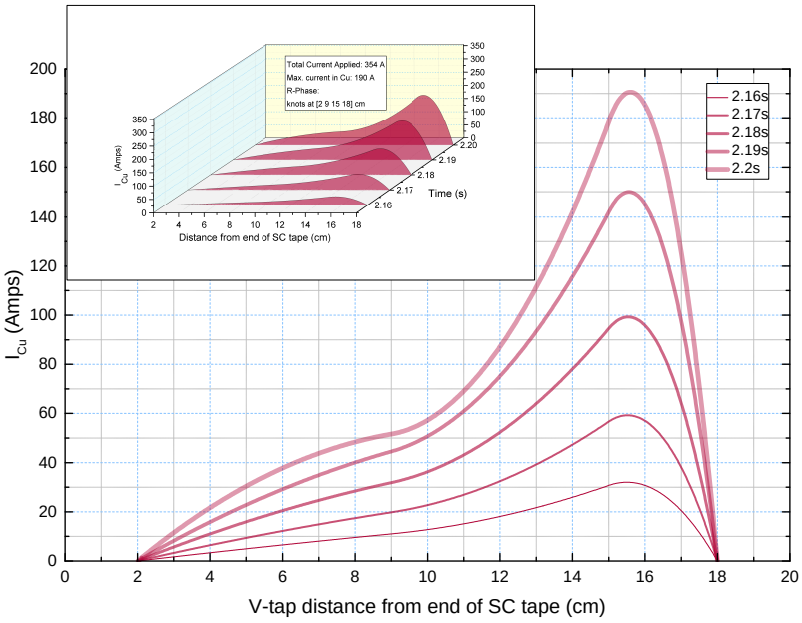

(a) Current carried by the Cu tape as a function of position along tape length, continuous function derived from differentiation of SLM curves in figure 5.34b (Inset) - Main figure: 2D plot, zoomed scale; Inset: 3D plot showing evolution with time, scale reflects total applied current.

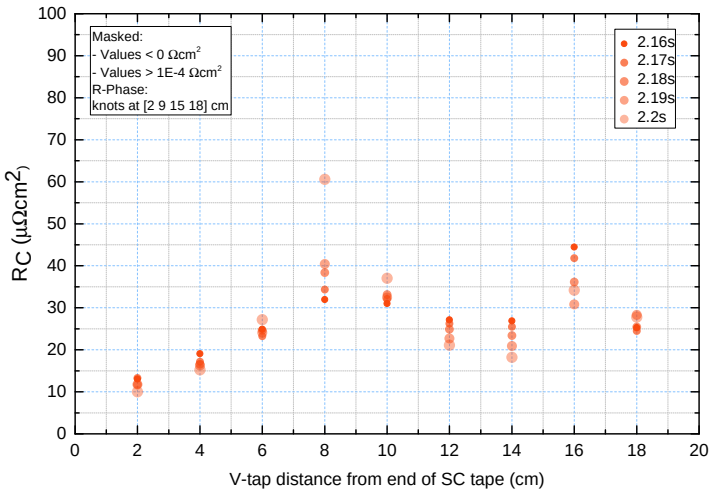

(b) Contact resistance approximation along tape length as calculated using the SLM spline method.

Figure 5.35: Continued plots for 33 K, no tape heater, 354 A applied, bolts tightened scenario; R-Phase current sharing.

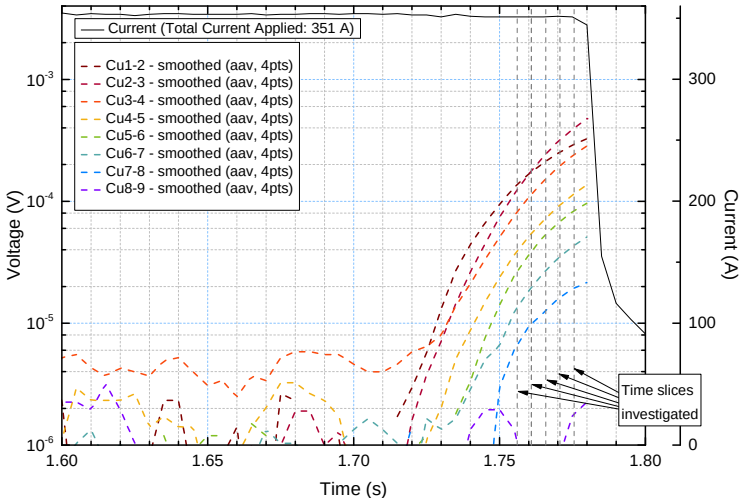

(a) Voltage-time traces for sections of Cu tape indicating time slice(s)/step average investigated.

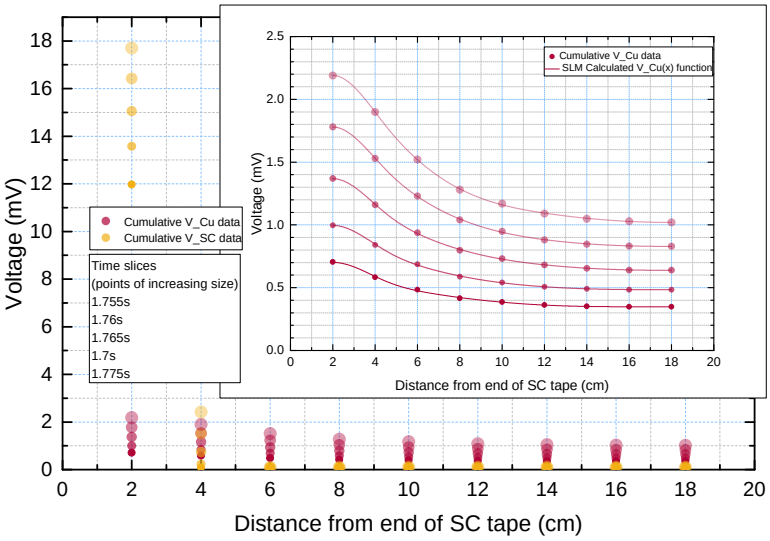

(b) Main figure: Measured cumulative voltage drop profiles for SC and Cu tapes; Inset: Measured cumulative voltage drop profile and continuous SLM spline approximation for Cu tape.

Figure 5.36: Plots for 33 K, no tape heater, 351 A applied, bolts loosened scenario; L-Phase current sharing (continued in figure 5.37).

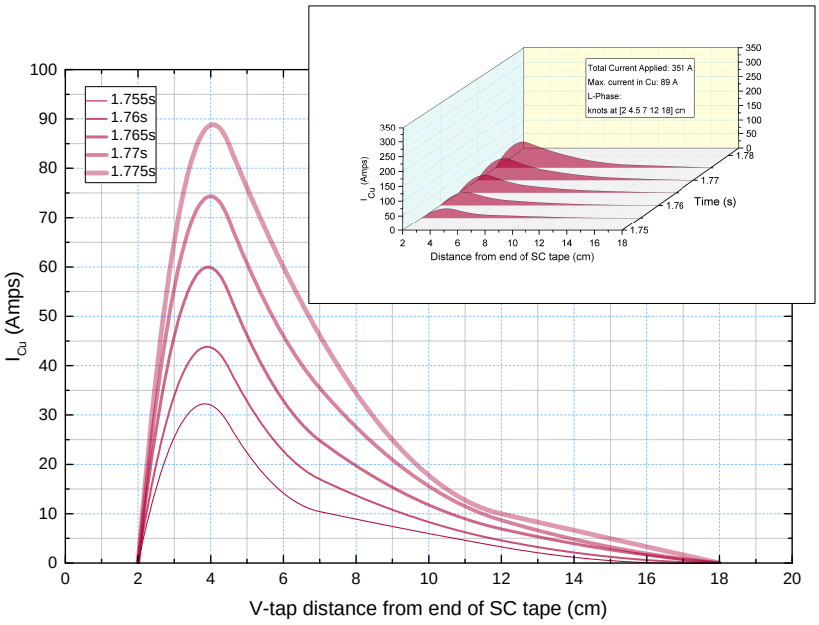

(a) Current carried by the Cu tape as a function of position along tape length, continuous function derived from differentiation of SLM curves in figure 5.36b (Inset) - Main figure: 2D plot, zoomed scale; Inset: 3D plot showing evolution with time, scale reflects total applied current.

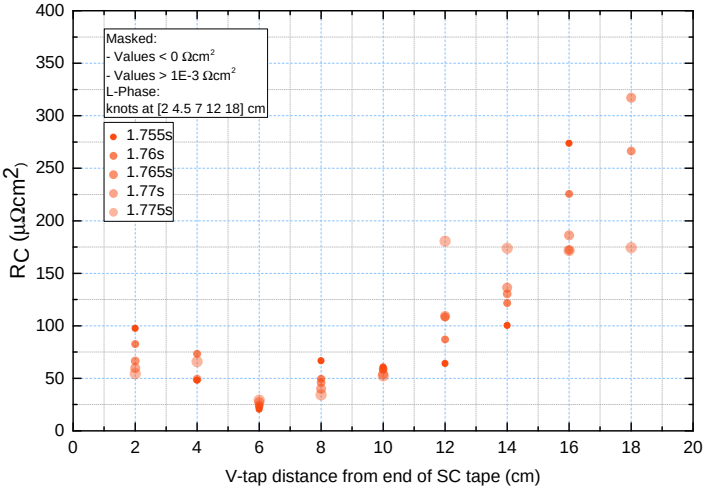

(b) Contact resistance approximation along tape length as calculated using the SLM spline method.

Figure 5.37: Continued plots for 33 K, no tape heater, 351 A applied, bolts loosened scenario; L-Phase current sharing.

5.2.6 Summary of No Tape Heater Scenarios and Reliability of Results

In the BT scenarios without application of the tape heater, in which the tapes were held under a pressure of approximately 5.6 MPa, the mean value of R_C was calculated to be 32.7 $\mu\Omega\text{cm}^2$ with a standard deviation of 18.1 $\mu\Omega\text{cm}^2$, excluding 'outliers', values below 0 and above 100 $\mu\Omega\text{cm}^2$, (R_C of 31.5 $\mu\Omega\text{cm}^2$ with a standard deviation of 29.9 $\mu\Omega\text{cm}^2$ including outliers). In the BL scenarios without application of the tape heater, in which the tapes were held under a pressure of approximately 2.1 MPa, the mean value of R_C was calculated to be 126.3 $\mu\Omega\text{cm}^2$ with a standard deviation of 116.5 $\mu\Omega\text{cm}^2$, excluding 'outliers', values below 0 and above 1000 $\mu\Omega\text{cm}^2$, (R_C of 129.4 $\mu\Omega\text{cm}^2$ with a standard deviation of 163.5 $\mu\Omega\text{cm}^2$ including outliers). This, and the variation in the shapes of the $I_{Cu}(x)$ curves, have shown the effects of the change in contact pressure using the adjustable clamp sample holder.

However, due to the presence of a higher R_C on the RHS of the sample, which was observed consistently throughout the tests carried out on this sample and is discussed in greater detail in section 5.2.8, a more accurate picture can be painted by looking at the mean R_C values and there standard deviations for each position along the tape length. These are presented in tables 5.2 (BT) and 5.3 (BL). Although an increase in R_C between the BT and BL cases is observed across the length of the sample, this is particularly apparent on the RHS where the increase is almost by a factor of 10.

It is noted that both when all values are considered and when looking at individual positions along the tape length, the effect of the outliers on the mean R_C values is not as great as it is on the standard deviations, as positive and negative outliers were observed in roughly equal numbers.

R_C values for each time slice for each no tape heater scenario are plotted against position along sample length in figures 5.38 (BT) and 5.39 (BL), along with the mean R_C values and standard deviation for each position.

Position (cm)	**2**	**4**	**6**	**8**	**10**	**12**	**14**	**16**	**18**
$\overline{R_c}$ **($\mu\Omega$cm^2)**	21.3	16.3	21.4	37.5	40.6	30.1	30.0	53.6	43.0
$\overline{R_c}$ ***($\mu\Omega$cm^2), with outliers***	*21.3*	*14.5*	*21.4*	*31.7*	*40.4*	*18.0*	*39.5*	*53.6*	*43.0*
Standard Deviation ($\mu\Omega$cm^2)	14.2	11.9	5.1	17.9	19.7	9.0	12.3	15.5	15.0
Standard Deviation ($\mu\Omega$cm^2), with outliers	*14.2*	*12.3*	*5.1*	*21.9*	*27.0*	*44.3*	*51.0*	*15.5*	*15.0*

Table 5.2: Mean R_c values and standard deviations for each position along the tape length (shown in cm away from the end of the SC tape), with and without 'outliers' (values below 0 and above 100 $\mu\Omega$cm^2), for all BT scenarios without the tape heater. All values given to one decimal place.

Position (cm)	**2**	**4**	**6**	**8**	**10**	**12**	**14**	**16**	**18**
$\overline{R_c}$ **($\mu\Omega$cm^2)**	74.6	44.1	40.7	40.7	52.1	209.7	167.8	210.5	304.0
$\overline{R_c}$ ***($\mu\Omega$cm^2), with outliers***	*74.6*	*35.6*	*38.8*	*40.7*	*52.1*	*209.7*	*167.8*	*210.5*	*334.8*
Standard Deviation ($\mu\Omega$cm^2)	28.0	37.9	22.5	28.8	8.3	133.3	40.3	41.0	158.5
Standard Deviation ($\mu\Omega$cm^2), with outliers	*28.0*	*55.9*	*23.8*	*28.8*	*8.3*	*133.3*	*40.3*	*41.0*	*359.2*

Table 5.3: Mean R_c values and standard deviations for each position along the tape length (shown in cm away from the end of the SC tape), with and without 'outliers' (values below 0 and above 1000 $\mu\Omega$cm^2), for all BL scenarios without the tape heater. All values given to one decimal place.

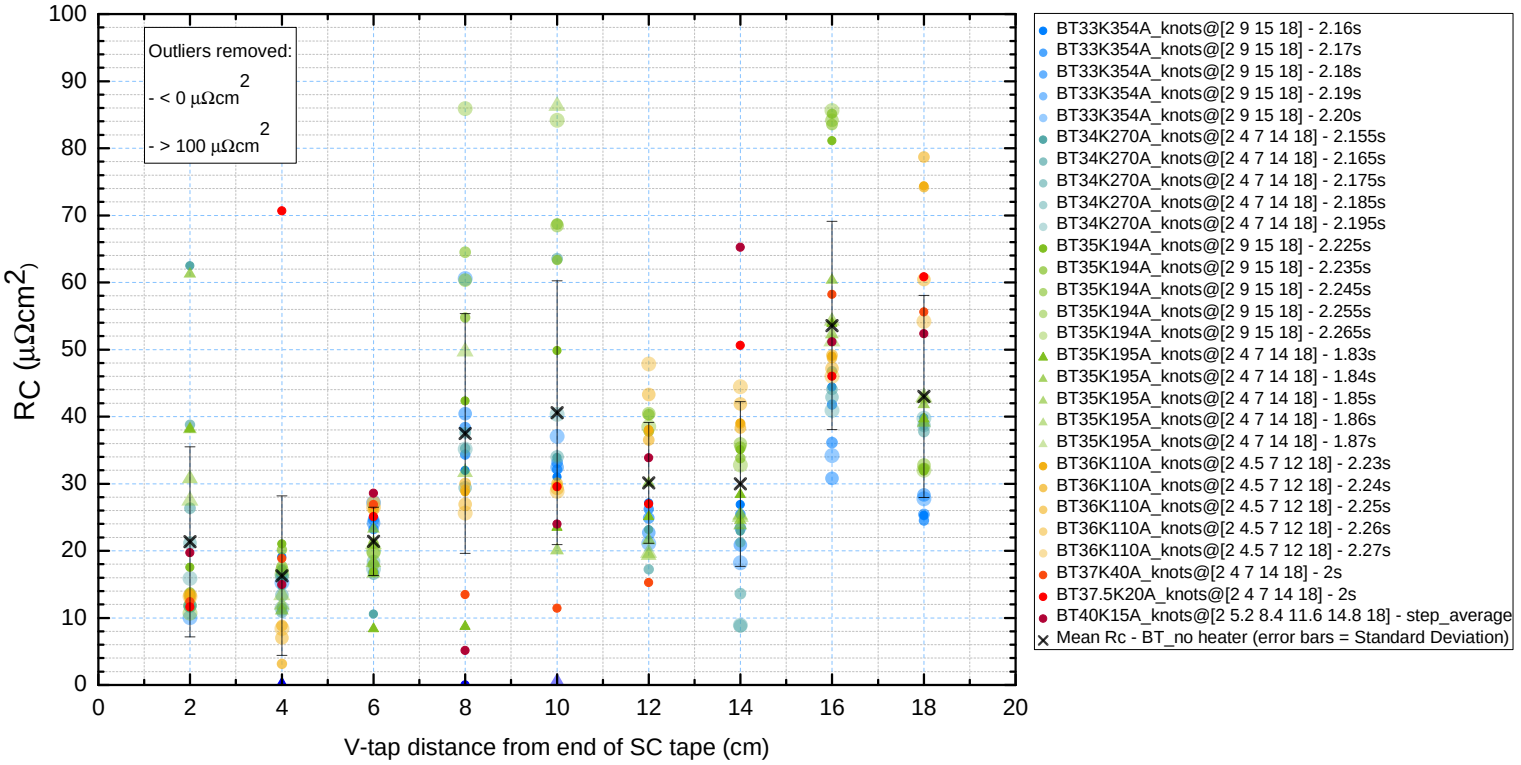

Figure 5.38: All BT, no tape heater scenario R_c values calculated, including each time slice depicted by symbols of increasing size, plotted against position along sample length.

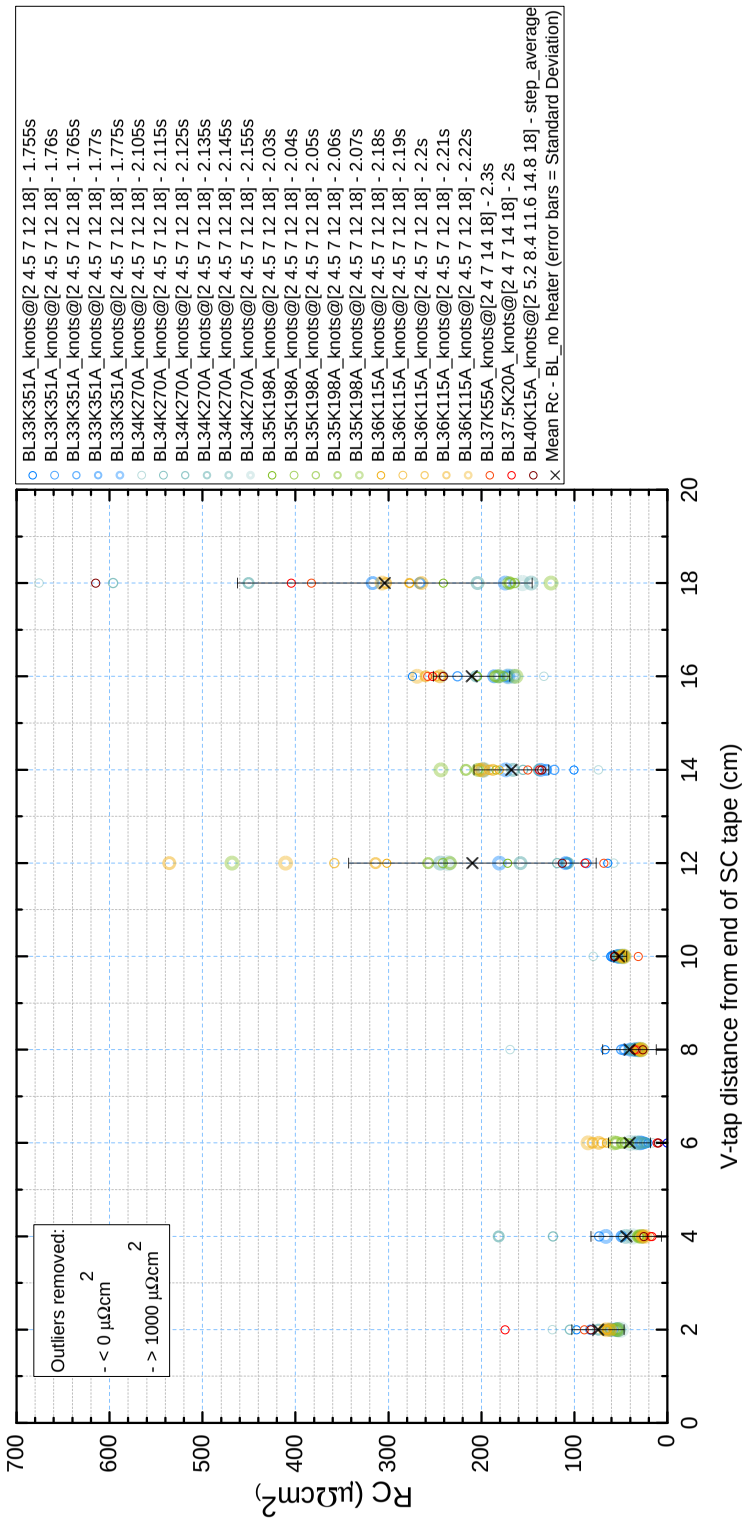

Figure 5.39: All BL, no tape heater scenario R_c values calculated, including each time slice depicted by symbols of increasing size, plotted against position along sample length.

5.2.6.1 Variable Current Sharing and Unexpected Increase in I_{quench}

Additionally, it has been seen that the sample appears to have higher R_C on the RHS of the sample. This is identified as one of the mechanisms determining the current sharing regime in the non-heated scenarios, including being a driving factor behind the current sharing phase, the maximum current shared with the Cu tape and the shape of the $I_{Cu}(x)$ curve, but not the sole mechanism. It is possible that there are inhomogeneities in the I_c distribution throughout the SC tape, and that the interaction of this non-linear phenomenon with the linear effect of the higher R_C on the RHS are what give rise to the various current sharing regimes.

The capture of R-Phase current sharing at 35 K and 33 K in the BT scenarios suggests, for example, that part of the tape on the RHS had a lower local I_c than the rest of the tape, driving current to initially share with the Cu tape here. It is highly likely that this was always the case in the BT scenarios but it is unusual that it was only captured in these cases. This is not seen in the BL scenarios. One theory is that when the R_C is increased, the sample is not able to undergo this local sharing on the RHS, so the SC tape carries the excess current, heating resistively, until the whole tape starts to transition, including the LHS where current starts to share more easily - and, hence, only L-Phase current sharing has been observed in the BL scenarios below 37 K. However, this theory has a flaw in that this proposed resistive current carrying on the RHS has not been measured. Unless the non-linear nature of the phenomenon means that this resistive current carrying on the RHS existed for such a short period of time and/or led to such a low voltage that it was hidden in the signal noise (less than 10 μV), therefore, it is unlikely to be the case.

This would, however, explain the higher I_{quench} values recorded in the BL scenarios than the BT scenarios, which is somewhat counter-intuitive; it would be expected that the 'better' contact and improved sharing possibilities would make the system more stable, more robust and more difficult to quench - as was shown in the large cable tests - and that I_{quench} would therefore be seen to be higher in the BT scenarios, which was not the case. Other possible explanations for this include:

- By putting the sample under the maximum pressure the rig could create (approximately 5.6 MPa), consequent stresses in the SC tape caused temporary degra-

dations in I_c (temporary since the BL measurements took place after the BT measurements),

- That the nominal temperatures assumed were not consistent between measurements - from figure 5.2a, a difference of approximately 0.25 K or less would account for the I_{quench} differences observed between BT and BL scenarios.

However, neither of these phenomena would account for the R-Phase and US-Phase current sharing observed.

5.2.6.2 Reliability of R_C Values Around Zero-Points

It has also been noted that the R_C values calculated around the zero-points are not reliable values. This is where it was most common for either negative or uncharacteristically small or large R_C values to be calculated.

As mentioned, since current was injected into and out of the SC tape only, in order to share current with the Cu tape it must have transferred both to and from the tape within the Cu tape length. Therefore, there is a point, generally in the middle region of the tape, although often to the left or right depending on the current-sharing phase, at which the current flow changes direction from SC-to-Cu to Cu-to-SC. This is denoted by a maximum in the $I_{Cu}(x)$ curve and so $\frac{d\sigma_{Cu}(x)}{dx} = 0$ A m^{-2} at this point, and is very small around this point. This point should correspond with the x-value at which $V_{Cu}(x)$ is equal to $V_{SC}(x)$ or at which $V_{SC-Cu}(x) = 0$ V (for example, around $x = 8$ cm in figure 5.3).

However, as mentioned previously, there may have been discrepancies between the actual position of the v-taps with reference to the end of the SC tape and the nominal or assumed positions, of up to 1.5 mm or half a groove width, as the nominal positions are taken to be in the centre of the grooves in the aluminium clamps and the v-tap connections were all aligned with the grooves. There also may have been some error in the position of the grooves with reference to the end of the SC tape adding to the x-error in the position of the v-taps and therefore of the $V_{SC-Cu}(x)$ function. Furthermore, with the spline approximation of the $V_{Cu}(x)$ curve from which the $\frac{d\sigma_{Cu}(x)}{dx}$ term is derived, it is likely that the estimated x-value of the zero-point does not exactly correspond to the physical position of the zero-point. This 'misalignment' of the zero-points in the $\frac{d\sigma_{Cu}(x)}{dx}$ and $V_{SC-Cu}(x)$ terms leads either to division of or by very small values

resulting in insensibly high or low $R_C(x)$ values; or a change of sign occurring in one term before the other resulting in negative values of $R_C(x)$ which have no meaning. More reliable values of $R_C(x)$ close to the centre could be found in scenarios in which the tape heater was used.

5.2.7 Results With Tape Heater

Using the tape heater allowed greater control over the current transfer in the sample and, by increasing the current transfer taking place near the zero-point, made consequent R_C values calculated around this point more accurate. Consequently, there is some divergence of calculated R_C values at the ends of the tape where the current transfer is smaller. However, overall there is seen to be more consistency in the R_C values calculated from the tape heater scenarios than those without it, including less variation with time, temperature and position along tape length. There still remains an unreliable result at the position closest to the zero-point.

Figures 5.40 to 5.55 show: the time slices investigated indicated in the $V_{Cu}(t)$ plots and, for these time slices, the cumulative voltage drops and the calculated $V_{Cu}(x)$, $I_{Cu}(x)$ and R_C profiles. In all cases H-Phase current sharing is observed and higher currents were required to force a measurable thermal runaway in the BL scenarios than the BT scenarios, as was seen when the tape heater was not used; in the tape heater scenarios, the difference in I_{quench} between the BT and BL scenarios is bigger (10-16 A) than those at the same temperatures without the tape heater (0-5 A).

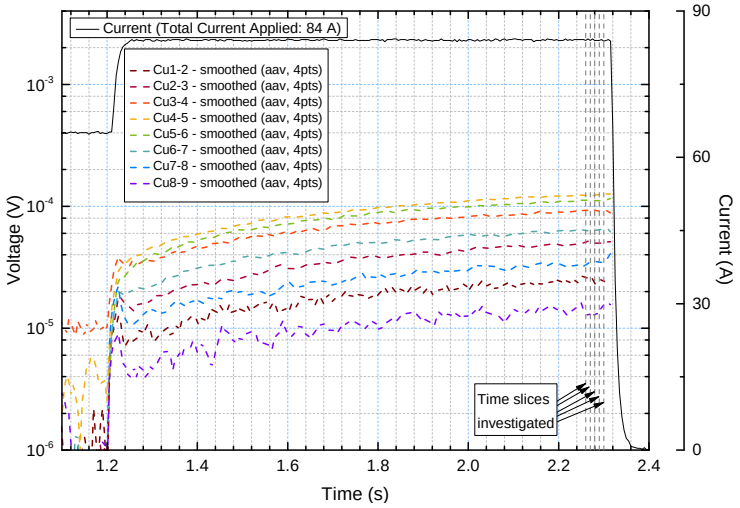

(a) Voltage-time traces for sections of Cu tape indicating time slice(s)/step average investigated.

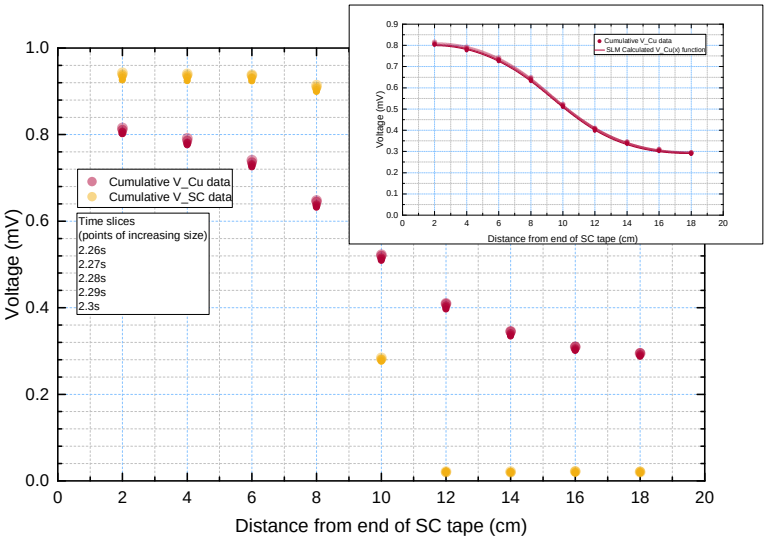

(b) Main figure: Measured cumulative voltage drop profiles for SC and Cu tapes; Inset: Measured cumulative voltage drop profile and continuous SLM spline approximation for Cu tape.

Figure 5.40: Plots for 36 K, tape heater applied, 84 A applied, bolts tightened scenario; H-Phase current sharing (continued in figure 5.41).

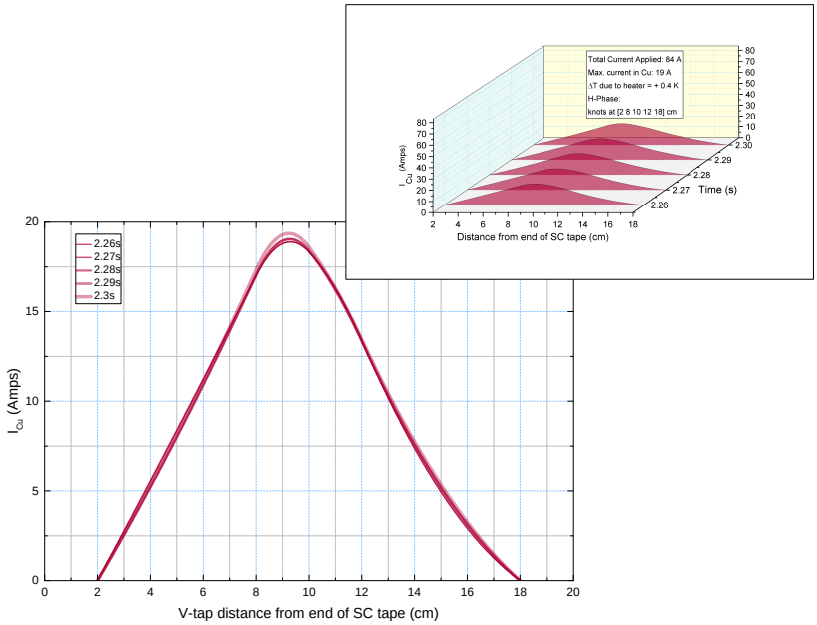

(a) Current carried by the Cu tape as a function of position along tape length, continuous function derived from differentiation of SLM curves in figure 5.40b (Inset) - Main figure: 2D plot, zoomed scale; Inset: 3D plot showing evolution with time, scale reflects total applied current.

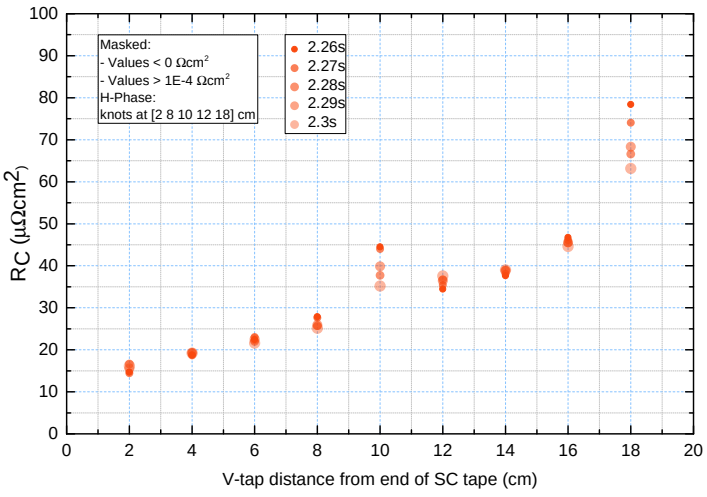

(b) Contact resistance approximation along tape length as calculated using the SLM spline method.

Figure 5.41: Continued plots for 36 K, tape heater applied, 84 A applied, bolts tightened scenario; H-Phase current sharing.

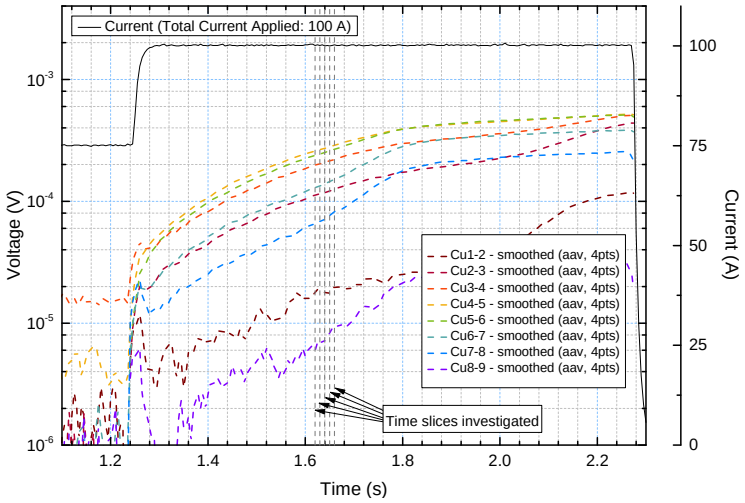

(a) Voltage-time traces for sections of Cu tape indicating time slice(s)/step average investigated.

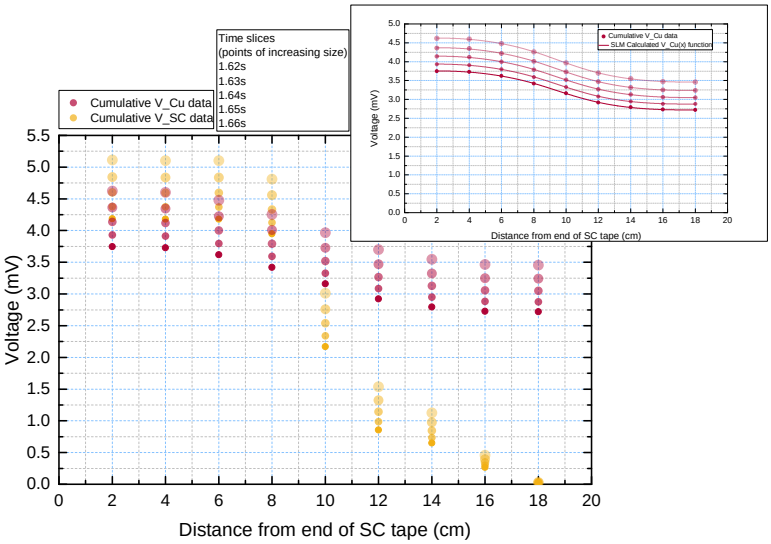

(b) Main figure: Measured cumulative voltage drop profiles for SC and Cu tapes; Inset: Measured cumulative voltage drop profile and continuous SLM spline approximation for Cu tape.

Figure 5.42: Plots for 36 K, tape heater applied, 100 A applied, bolts loosened scenario; H-Phase current sharing (continued in figure 5.43).

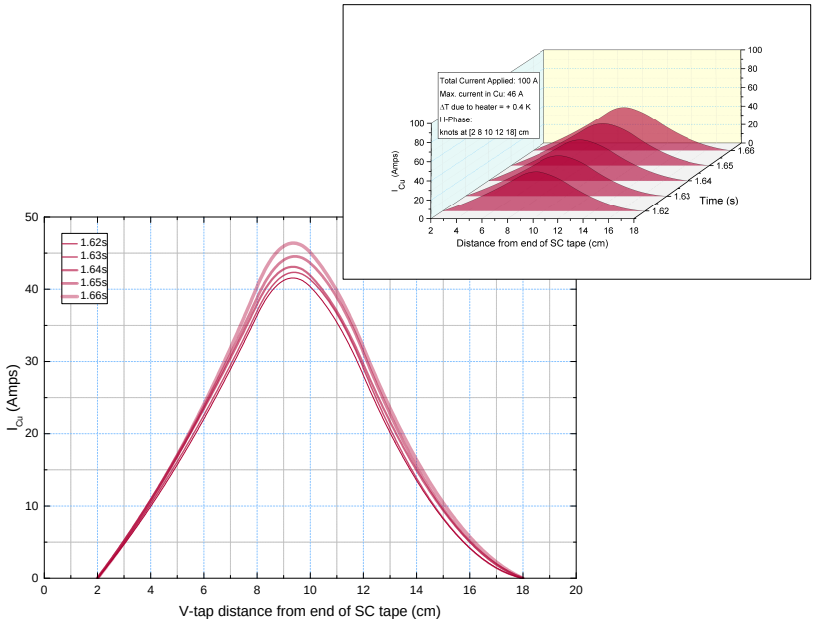

(a) Current carried by the Cu tape as a function of position along tape length, continuous function derived from differentiation of SLM curves in figure 5.42b (Inset) - Main figure: 2D plot, zoomed scale; Inset: 3D plot showing evolution with time, scale reflects total applied current.

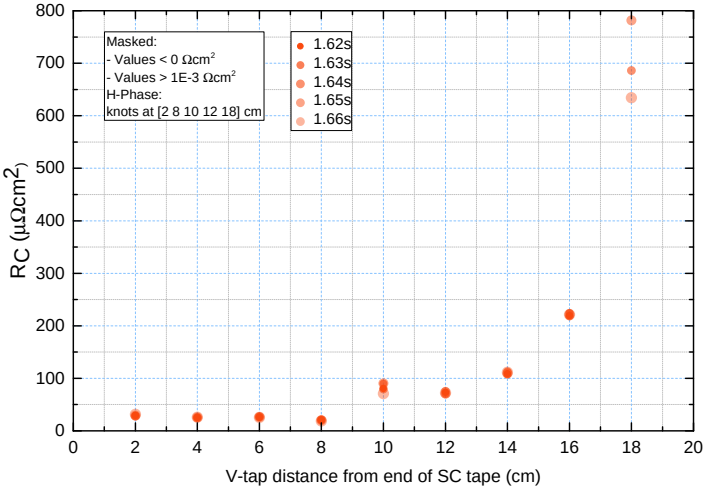

(b) Contact resistance approximation along tape length as calculated using the SLM spline method.

Figure 5.43: Continued plots for 36 K, tape heater applied, 100 A applied, bolts loosened scenario; H-Phase current sharing.

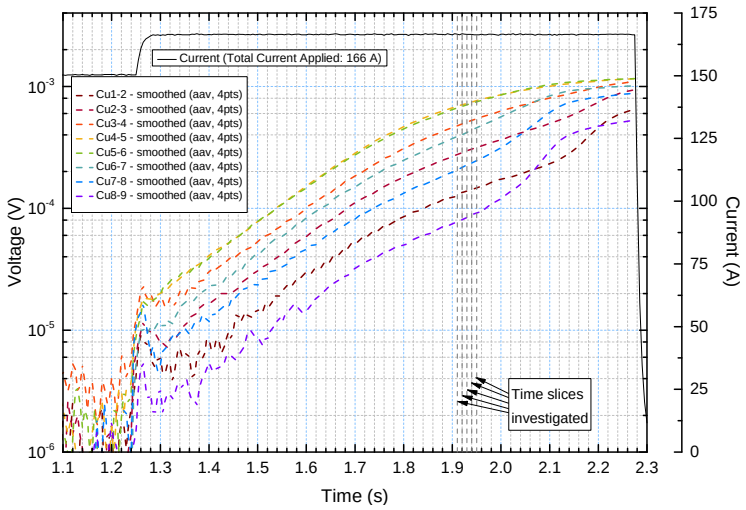

(a) Voltage-time traces for sections of Cu tape indicating time slice(s)/step average investigated.

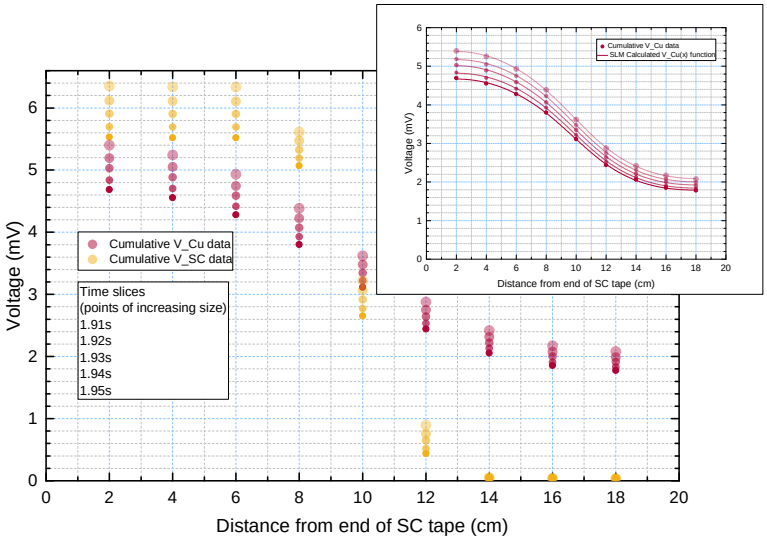

(b) Main figure: Measured cumulative voltage drop profiles for SC and Cu tapes; Inset: Measured cumulative voltage drop profile and continuous SLM spline approximation for Cu tape.

Figure 5.44: Plots for 35 K, tape heater applied, 166 A applied, bolts tightened scenario; H-Phase current sharing (continued in figure 5.45).

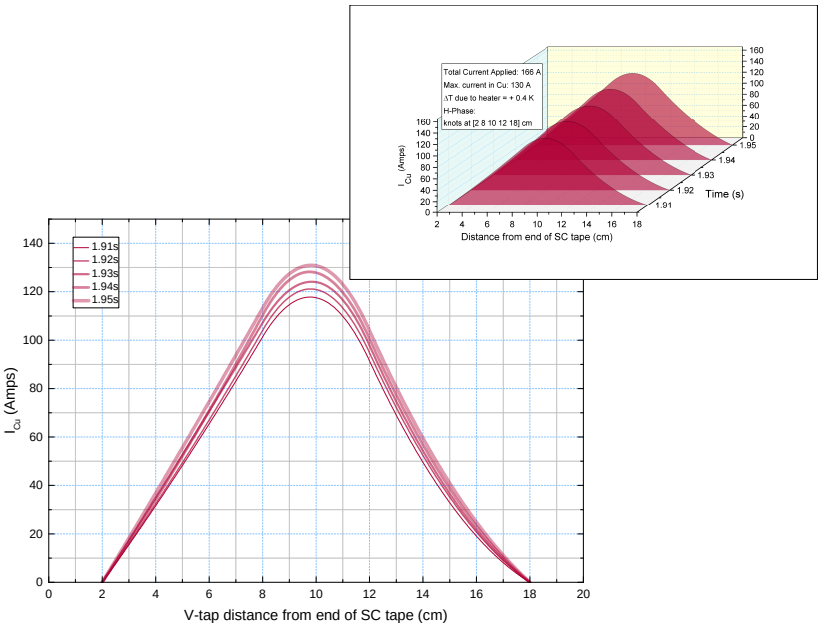

(a) Current carried by the Cu tape as a function of position along tape length, continuous function derived from differentiation of SLM curves in figure 5.44b (Inset) - Main figure: 2D plot, zoomed scale; Inset: 3D plot showing evolution with time, scale reflects total applied current.

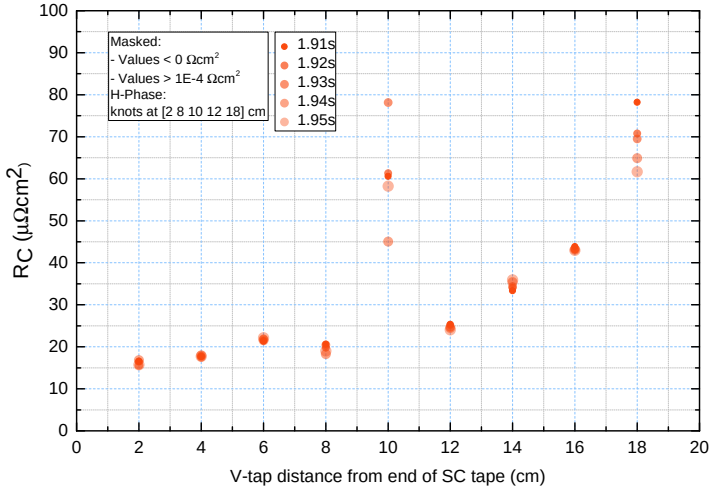

(b) Contact resistance approximation along tape length as calculated using the SLM spline method.

Figure 5.45: Continued plots for 35 K, tape heater applied, 166 A applied, bolts tightened scenario; H-Phase current sharing.

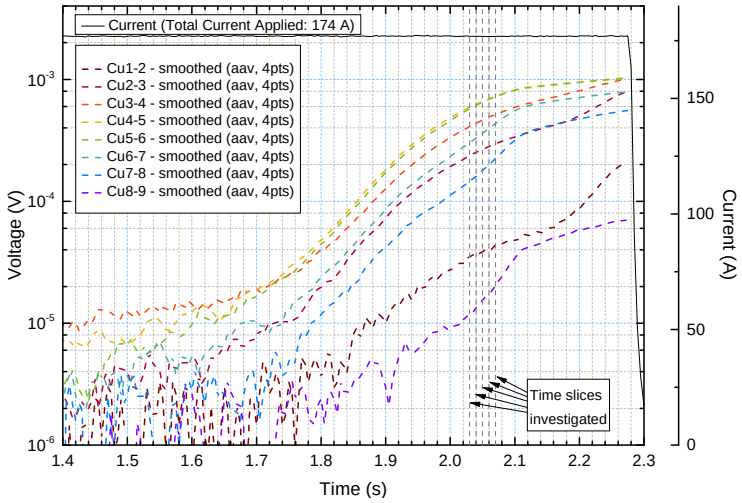

(a) Voltage-time traces for sections of Cu tape indicating time slice(s)/step average investigated.

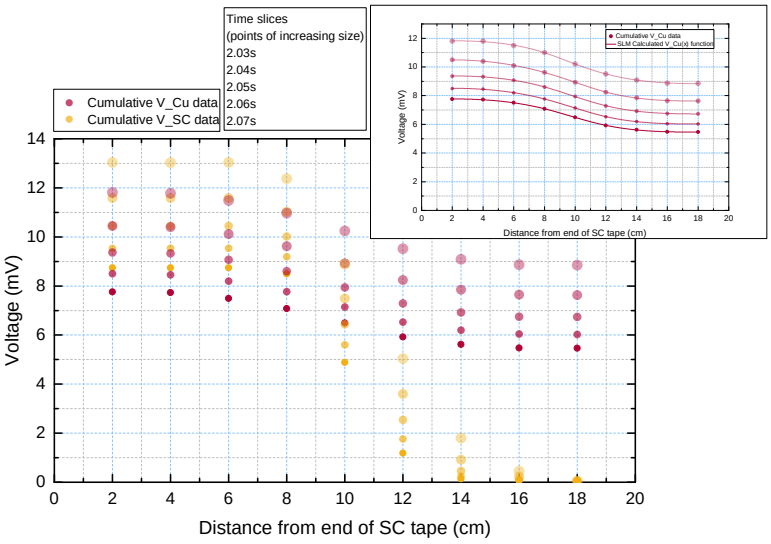

(b) Main figure: Measured cumulative voltage drop profiles for SC and Cu tapes; Inset: Measured cumulative voltage drop profile and continuous SLM spline approximation for Cu tape.

Figure 5.46: Plots for 35 K, tape heater applied, 174 A applied, bolts loosened scenario; H-Phase current sharing (continued in figure 5.47).

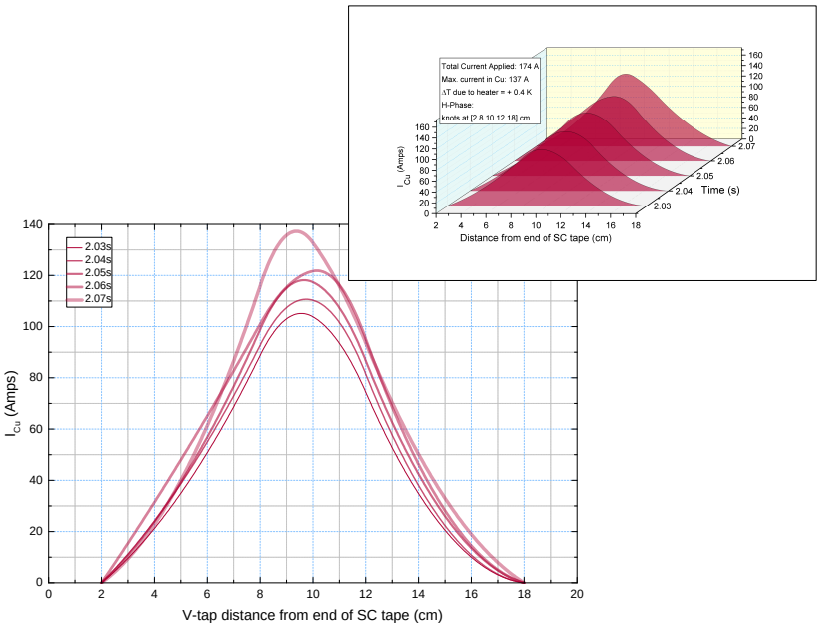

(a) Current carried by the Cu tape as a function of position along tape length, continuous function derived from differentiation of SLM curves in figure 5.46b (Inset) - Main figure: 2D plot, zoomed scale; Inset: 3D plot showing evolution with time, scale reflects total applied current.

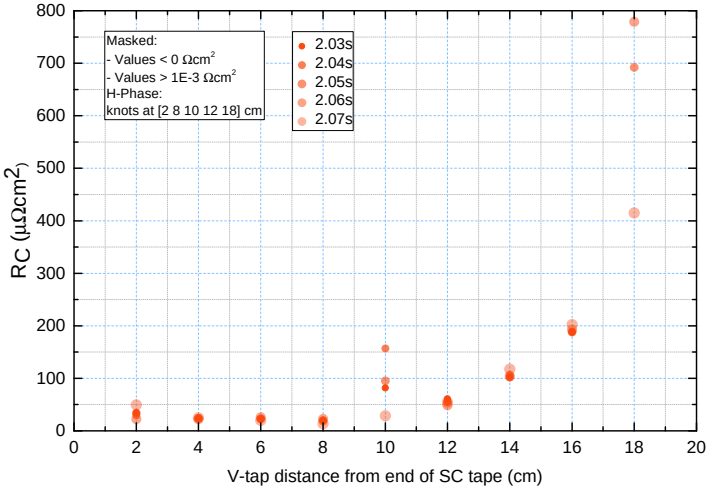

(b) Contact resistance approximation along tape length as calculated using the SLM spline method.

Figure 5.47: Continued plots for 35 K, tape heater applied, 174 A applied, bolts loosened scenario; H-Phase current sharing.

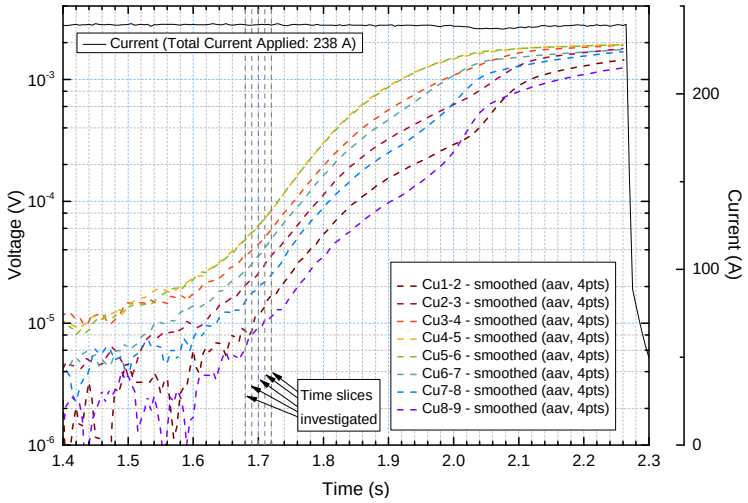

(a) Voltage-time traces for sections of Cu tape indicating time slice(s)/step average investigated.

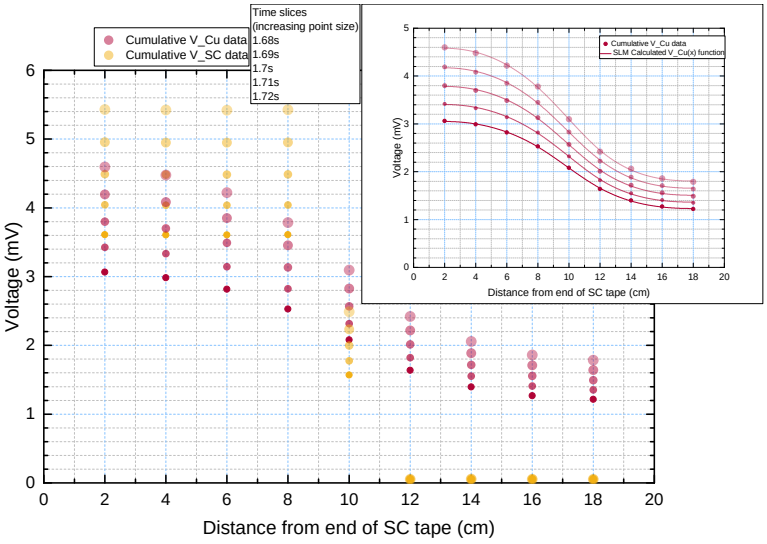

(b) Main figure: Measured cumulative voltage drop profiles for SC and Cu tapes; Inset: Measured cumulative voltage drop profile and continuous SLM spline approximation for Cu tape.

Figure 5.48: Plots for 34 K, tape heater applied, 238 A applied, bolts tightened scenario; H-Phase current sharing (continued in figure 5.49).

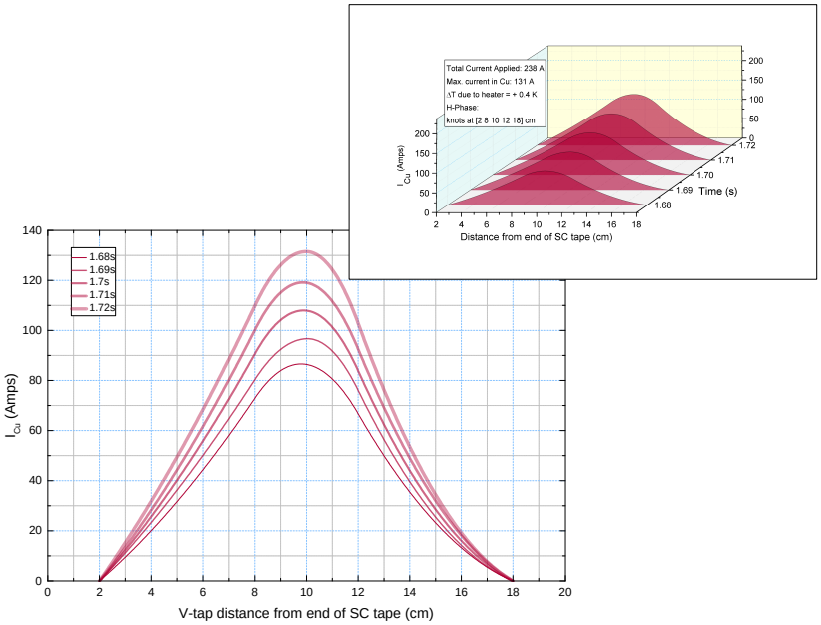

(a) Current carried by the Cu tape as a function of position along tape length, continuous function derived from differentiation of SLM curves in figure 5.48b (Inset) - Main figure: 2D plot, zoomed scale; Inset: 3D plot showing evolution with time, scale reflects total applied current.

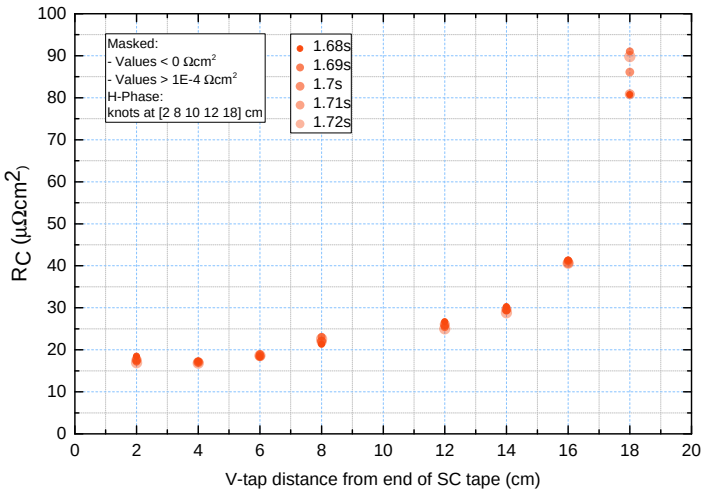

(b) Contact resistance approximation along tape length as calculated using the SLM spline method.

Figure 5.49: Continued plots for 34 K, tape heater applied, 238 A applied, bolts tightened scenario; H-Phase current sharing.

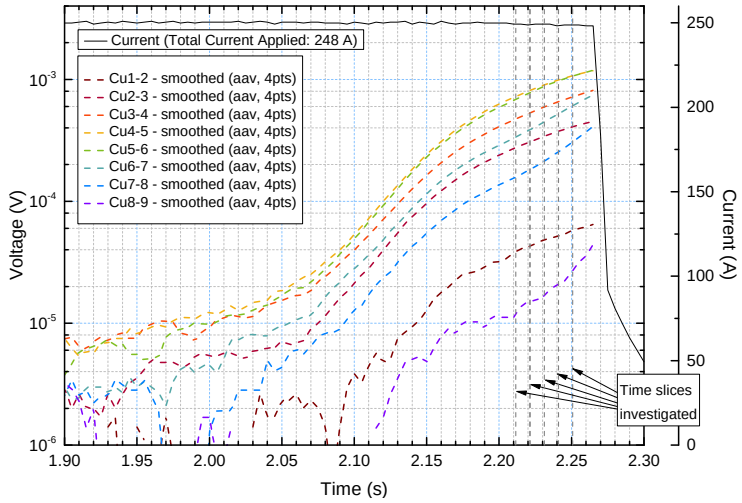

(a) Voltage-time traces for sections of Cu tape indicating time slice(s)/step average investigated.

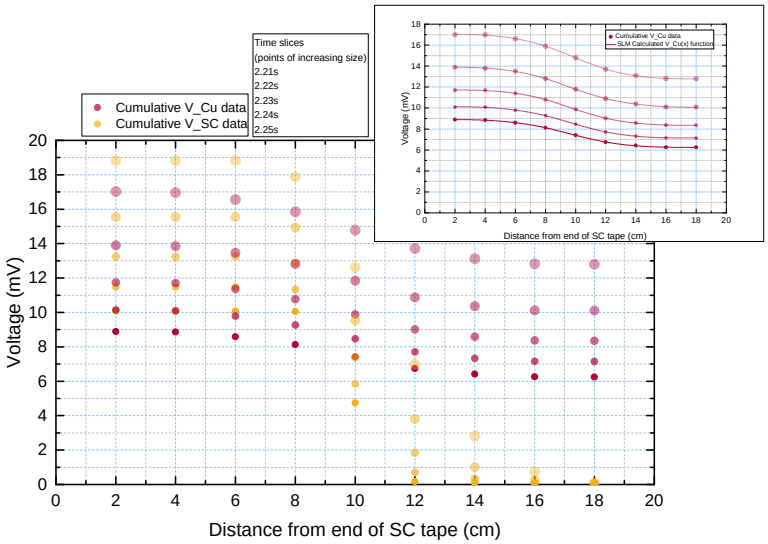

(b) Main figure: Measured cumulative voltage drop profiles for SC and Cu tapes; Inset: Measured cumulative voltage drop profile and continuous SLM spline approximation for Cu tape.

Figure 5.50: Plots for 34 K, tape heater applied, 248 A applied, bolts loosened scenario; H-Phase current sharing (continued in figure 5.51).

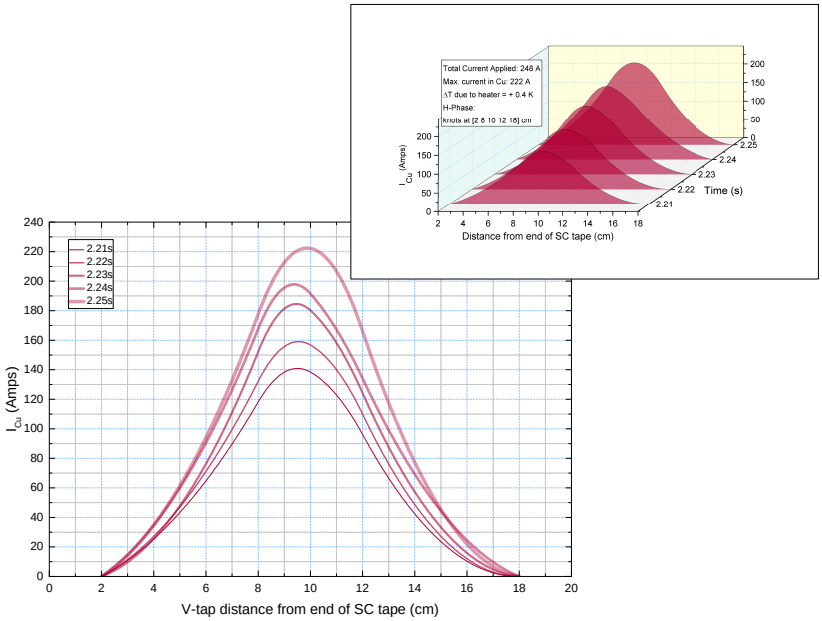

(a) Current carried by the Cu tape as a function of position along tape length, continuous function derived from differentiation of SLM curves in figure 5.50b (Inset) - Main figure: 2D plot, zoomed scale; Inset: 3D plot showing evolution with time, scale reflects total applied current.

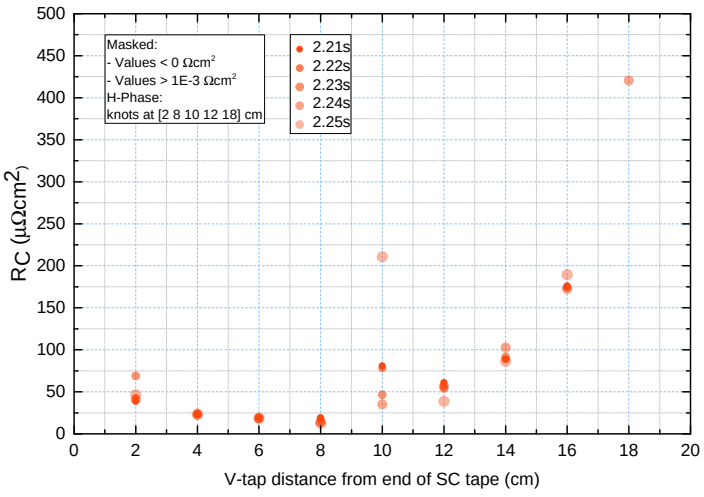

(b) Contact resistance approximation along tape length as calculated using the SLM spline method.

Figure 5.51: Continued plots for 34 K, tape heater applied, 248 A applied, bolts loosened scenario; H-Phase current sharing.

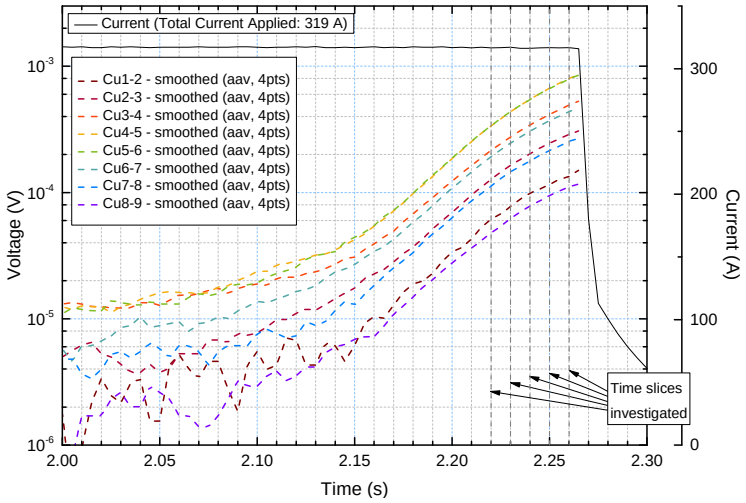

(a) Voltage-time traces for sections of Cu tape indicating time slice(s)/step average investigated.

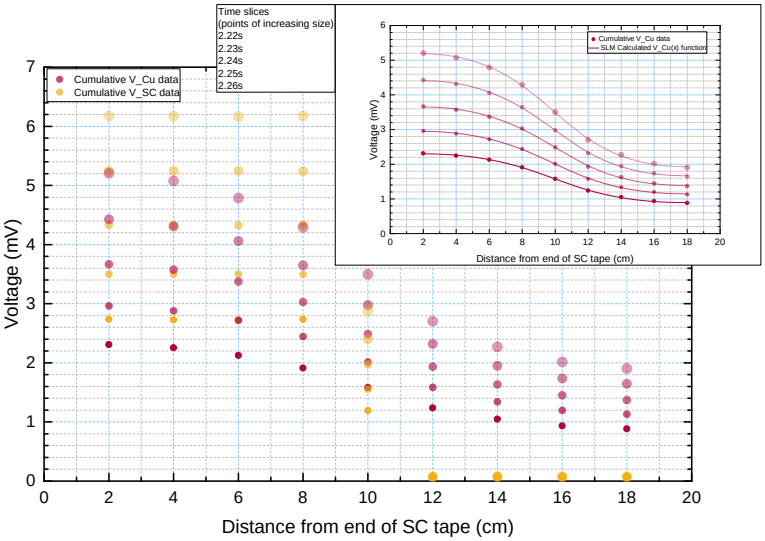

(b) Main figure: Measured cumulative voltage drop profiles for SC and Cu tapes; Inset: Measured cumulative voltage drop profile and continuous SLM spline approximation for Cu tape.

Figure 5.52: Plots for 33 K, tape heater applied, 319 A applied, bolts tightened scenario; H-Phase current sharing (continued in figure 5.53).

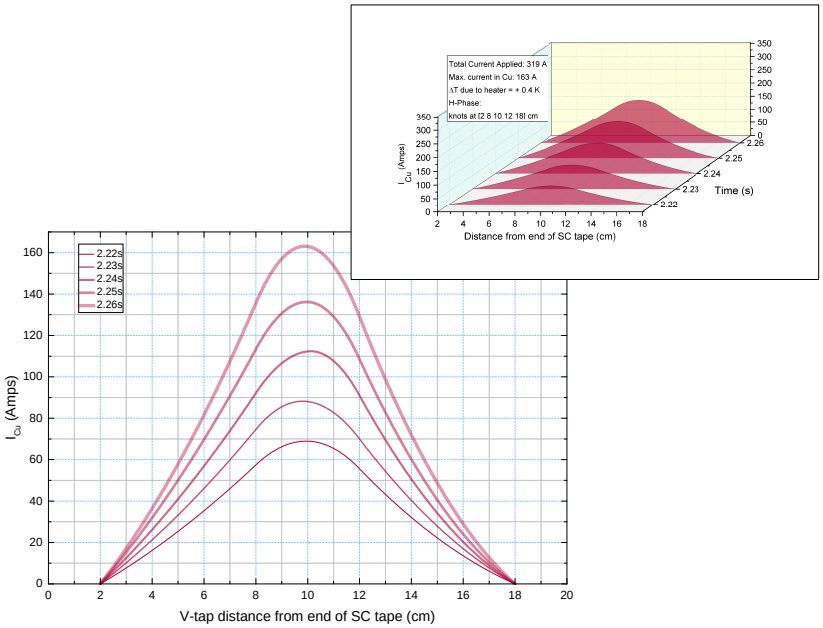

(a) Current carried by the Cu tape as a function of position along tape length, continuous function derived from differentiation of SLM curves in figure 5.52b (Inset) - Main figure: 2D plot, zoomed scale; Inset: 3D plot showing evolution with time, scale reflects total applied current.

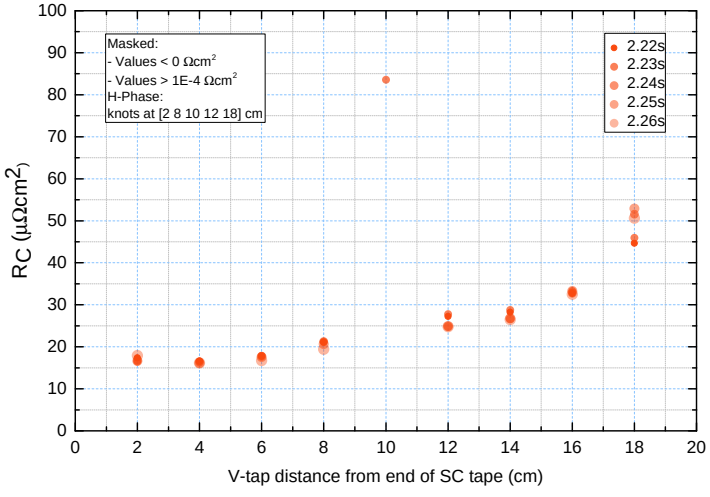

(b) Contact resistance approximation along tape length as calculated using the SLM spline method.

Figure 5.53: Continued plots for 33 K, tape heater applied, 319 A applied, bolts tightened scenario; H-Phase current sharing.

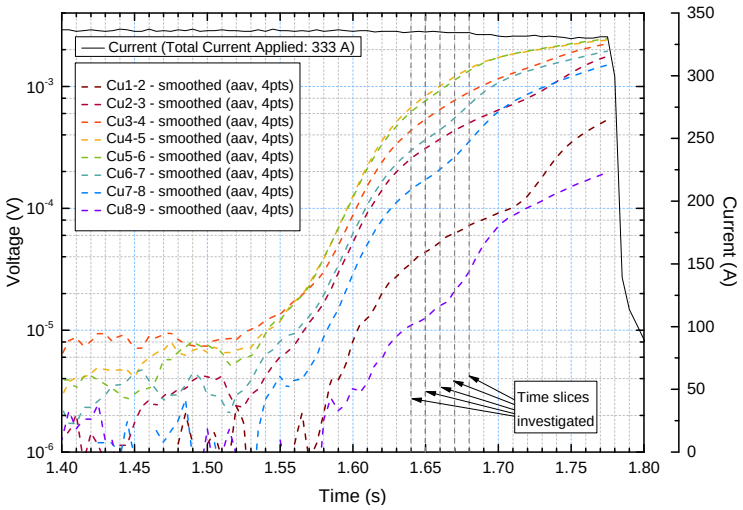

(a) Voltage-time traces for sections of Cu tape indicating time slice(s)/step average investigated.

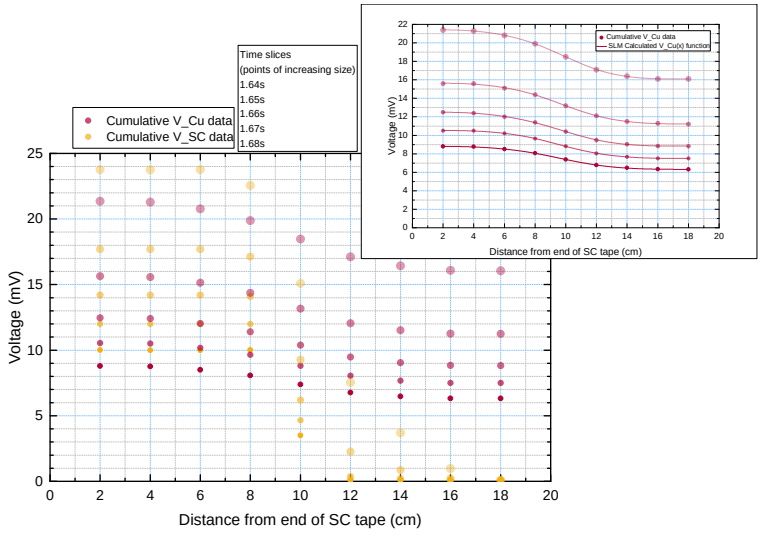

(b) Main figure: Measured cumulative voltage drop profiles for SC and Cu tapes; Inset: Measured cumulative voltage drop profile and continuous SLM spline approximation for Cu tape.

Figure 5.54: Plots for 33 K, tape heater applied, 333 A applied, bolts loosened scenario; H-Phase current sharing (continued in figure 5.55).

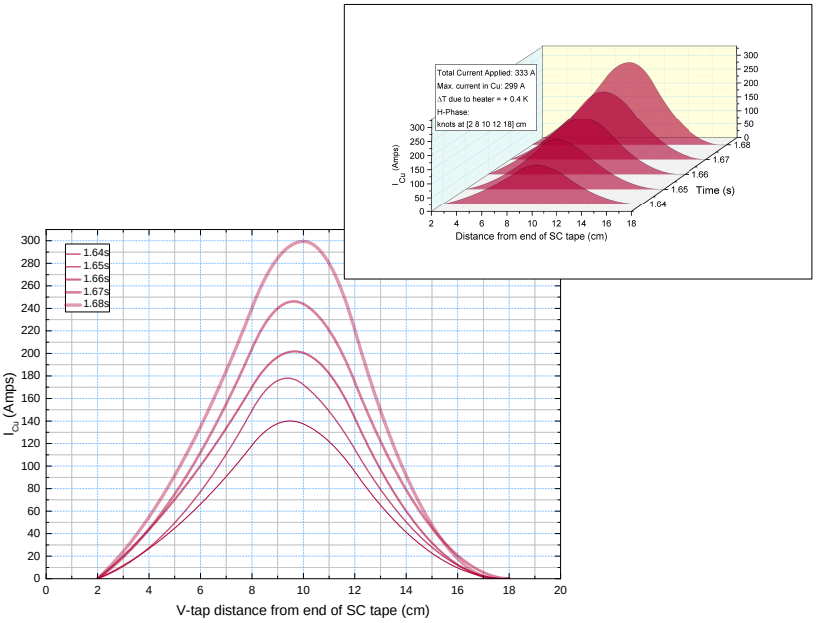

(a) Current carried by the Cu tape as a function of position along tape length, continuous function derived from differentiation of SLM curves in figure 5.54b (Inset) - Main figure: 2D plot, zoomed scale; Inset: 3D plot showing evolution with time, scale reflects total applied current.

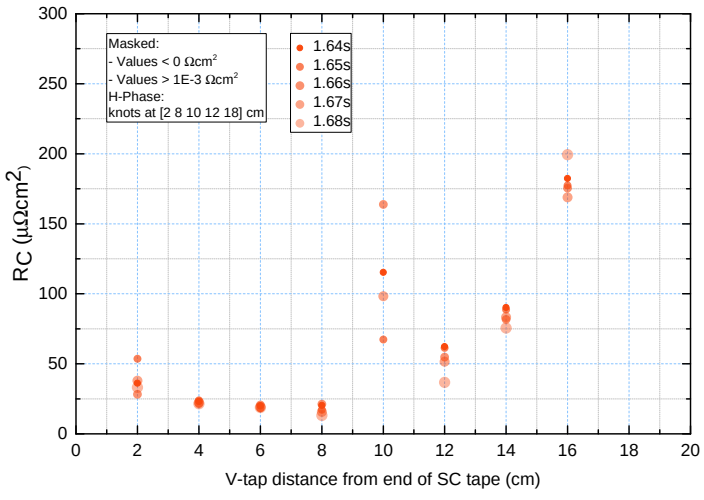

(b) Contact resistance approximation along tape length as calculated using the SLM spline method.

Figure 5.55: Continued plots for 33 K, tape heater applied, 333 A applied, bolts loosened scenario; H-Phase current sharing.

Overall, the measurements with the tape heater led to more consistent R_C results than those without. In the BT scenarios a standard deviation decrease of up to 15.1 $\mu\Omega cm^2$ was seen without outliers considered (and a decrease of up to 46.4 $\mu\Omega cm^2$ in cases with outliers considered). In the BL scenarios a standard deviation decrease of up to 122.7 $\mu\Omega cm^2$ was seen both with and without outliers considered. R_C comparisons for both BT and BL scenarios at 33 K are given in figures 5.56 and 5.57 respectively, where it can be seen that the tape heater results show less variation over time in both the BT and BL cases.

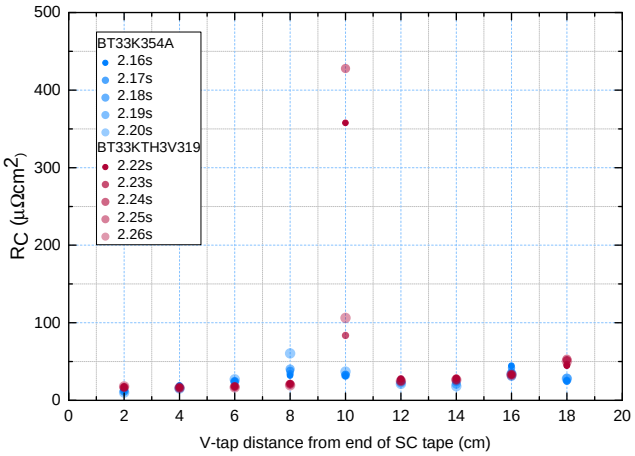

(a) BT tape heater (red) vs no tape heater (blue) R_C comparison; overall view (all points shown).

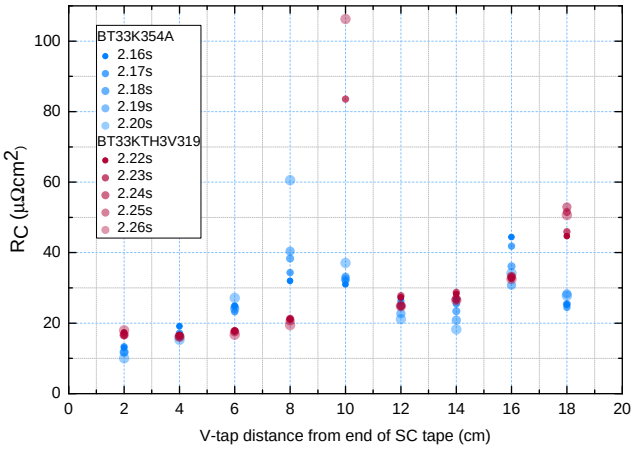

(b) BT tape heater (red) vs no tape heater (blue) R_C comparison; zoomed scale (some points out of scale).

Figure 5.56: Contact resistance comparison plots at 33 K, no tape heater vs tape heater, for both BT scenarios, as calculated using the SLM spline model.

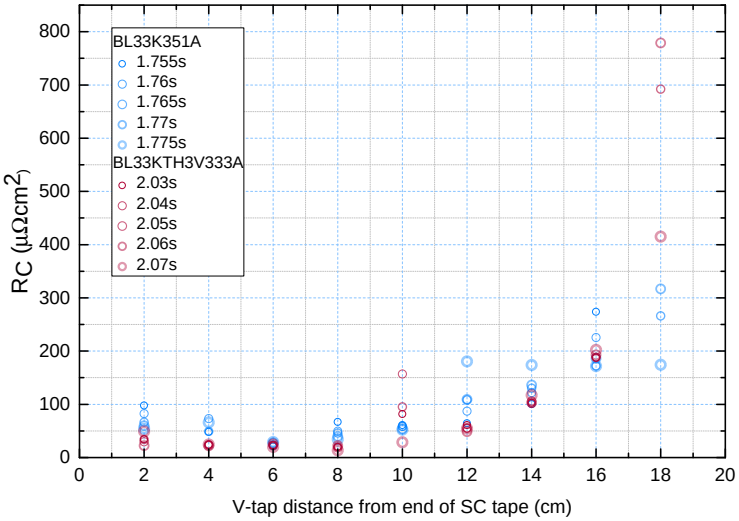

(a) BL tape heater (red) vs no tape heater (blue) R_C comparison; overall view (all points show).

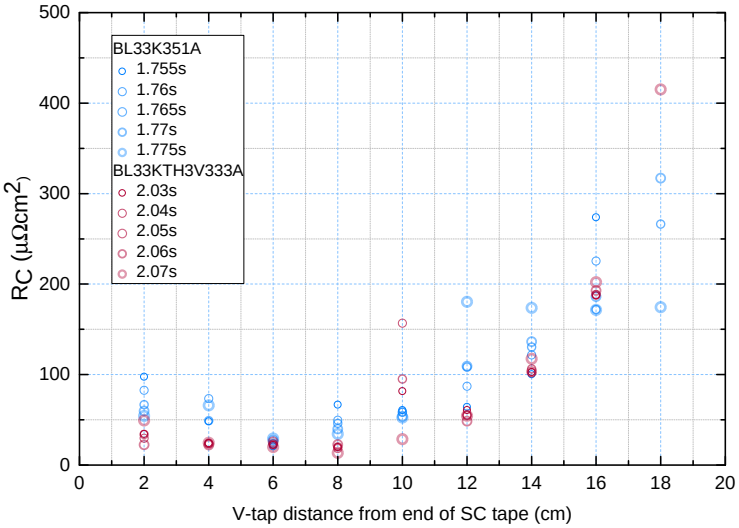

(b) BT tape heater (red) vs no tape heater (blue) R_C comparison; zoomed scale (some points out of scale).

Figure 5.57: Contact resistance comparison plots at 33 K, no tape heater vs tape heater, for BL scenarios, as calculated using the SLM spline model.

In the heated scenarios, as in the non-heated scenarios, an increase of R_C of approximately a factor of ten is seen between the BT scenarios and the BL scenarios, and a higher R_C is observed on the RHS than on the LHS. Interestingly, for the 33 K example used in figures 5.56 to 5.58, the R_C on the LHS in the BL scenarios with the tape heater is calculated to be lower than those without, being around 25 $\mu\Omega\text{cm}^2$ compared to up to 100 $\mu\Omega\text{cm}^2$. Figure 5.58 compares BT and BL R_C at 33 K with the tape heater.

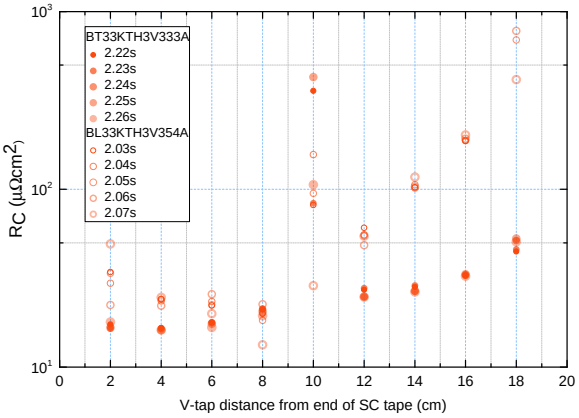

(a) Overall view comparison; log scale.

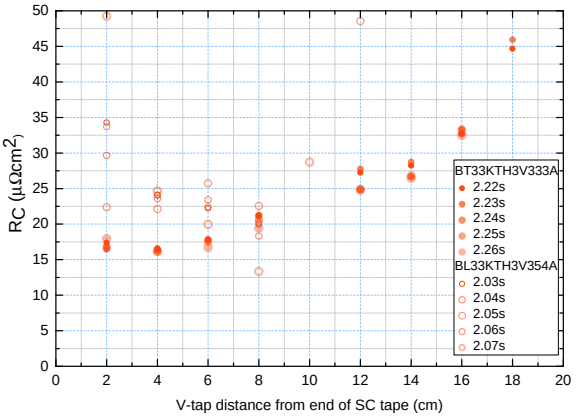

(b) Close-up comparison without unreliable central points; linear scale.

Figure 5.58: Contact resistance comparison: BT (319 A applied) and BL (333 A applied); calculated using the SLM spline model; H-Phase current sharing, 33 K, 3 V on tape heater.

5.2.8 R_C Inhomogeneity Along Tape Length

When calculating the contact resistance using both the preliminary and the final method, it was noted that R_C appeared to be much higher on the RHS than on the LHS. Using the data from the scenarios in which the tape heater was used:

- In the BT scenarios, this difference was approximately 40 $\mu\Omega cm^2$ between 30 $\mu\Omega cm^2$ on the LHS and 70 $\mu\Omega cm^2$ on the RHS,
- In the BL scenarios this difference was approximately 500 $\mu\Omega cm^2$ with between up to 150 $\mu\Omega cm^2$ on the LHS and 650 $\mu\Omega cm^2$ on the RHS.

This consistent difference in contact resistance between ends of the sample suggested either inhomogeneities in the tapes or that, despite efforts to make the clamp system apply a homogeneous pressure, it was not in fact the case. This inhomogeneity of clamping could have been caused, for example, by differences arising in the surface finish of the clamps which were cleaned and sometimes polished between tests to ensure no debris could break the Kapton tape and cause the samples to come into contact with the clamps. Furthermore, slight differences in the angles between the clamps or the clamps and the tapes due to inaccuracies in the manufacture of the assembly parts could also have played a part in creating the inhomogeneous contact.

Another possible explanation for this discrepancy is a small amount of damage to the clamps which occurred. As noted in the description of the sample holder, section 4.3.2.1, the bolts holding the clamps together were fixed to one of the clamps (which had 3 mm tapped i.e. threaded holes) and were free to move in the other clamp (clearance holes). Aluminium being a relatively soft material, in one of the holes on the RHS the thread became worn and disappeared. It was assumed that since the clamping pressure came primarily from the tightening of the nuts and care was taken to make sure that the bolt did not spin around when tightening and that it was tightened evenly with the rest of the nut-bolt pairs, this would have little effect on the system. However, it may be that this extra degree of freedom contributed to lower clamping pressures at the end of the sample where it was situated and hence to the calculation of higher contact resistance on the RHS.

5.3 Conclusions

A new method for calculating contact resistance along a length of MgB_2 tape stabilised with an additional copper tape has been devised, tested and validated. The contact resistance has been changed by altering the applied pressure creating 'good' contact (BT, 5.6 MPa pressure applied) and 'bad' contact (BL, 2.1 MPa pressure applied) scenarios and the effects of this observed, both in the nature of the calculated current profiles or current sharing phases and in the calculated contact resistance values.

Contact resistance data has been calculated over a range of temperatures from 33 K through to 40 K, using snapshots in time of various points in quench development under different transitions and good agreement has been seen in the results. This suggests that the method is robust.

By using a measurement set-up similar to that used in the cable assembly tests described in chapter 3, rather than the standard two-point contact resistance measurement set-up described at the beginning of chapter 4, this method has laid the groundwork for being able to measure contact resistance between superconducting and stabilising tapes *in situ*, using instrumentation that could also be used to gather other data e.g. for quench detection. There are still some limitations of the method which would need to be overcome, such as the fact that this relies on the knowledge that all current is initially injected into the superconducting tape and that any current in the stabilising tape has transferred there from the superconducting tape. In a sandwich stack such as those described in previous chapters, with multiple superconducting and stabilising tapes and current injected into all tapes simultaneously, the method would need to be refined to account for the distribution of current across the tapes. Further suggestions of method refinement are given in section 5.4.

An unexpected inhomogeneity in the contact between tapes led to the further observance of the effects of contact resistance on current transfer between the superconducting and stabilising tapes, including an unexpected increase in I_{quench} which was observed when contact resistance was increased. Furthermore, it has been identified that mechanisms other than the contact resistance are driving the current transfer. Potential additional mechanisms driving these observations have been identified as: inhomogeneities in the I_c distribution across the tape length; a temporary change in tape I_c caused by the stress of applying the clamping pressure; and differences in the

nominal recorded temperatures and the actual temperatures. Further information is required to confirm the presence of any of these mechanisms.

5.4 Future Work

As described and discussed above, the current model uses a constant copper resistivity, ρ_{Cu}, value for each scenario i.e. that correlating to the nominal temperature in the data in figure 4.18. This limits the R_C calculations in two ways:

1. **The accuracy of the** $I_{Cu}(x)$ — If heating during a quench is not taken into effect, the ρ_{Cu} will be underestimated and, therefore, the inversely proportional I_{Cu} will be overestimated.

2. **The data available to calculate** R_C — It was observed that only early in a thermal runaway or self-heating event could the ρ_{Cu} be assumed to be constant before the effects of heating meant that the overestimated I_{Cu} gave unreasonable results. Only this 'early' data could therefore be used at which measured voltages were still relatively low, most likely leading to greater error. By accounting for the change in ρ_{Cu} with temperature, higher voltage data would become available.

It is therefore recommended that to improve the presented R_C calculation method, a method for accounting for the dependence of the ρ_{Cu} on temperature and the dependence of temperature on both position and time (or the dynamic nature of local temperature and therefore local copper tape resistivity) is constructed. Progress on this aspect of the work to date is discussed below.

Using the sample TCs it was possible to measure temperature profiles of the sample and also, by interpolating from the data in figure 4.18, resistivity profiles of the copper tape. However, here we encounter our first problem which must be solved. The TC at position nine along the tape, i.e. 18 cm from the end of the superconducting tape, referred to as 'TC9', was observed to pick up stray voltage signals. This is most likely due to a slight gap between the copper and constantan wires meaning that as well as the thermoelectric effect, the wire pair was also picking up voltage signals due to current flow in the tape to which it was soldered. This was observed in the form of TC9 signals changing inversely to the other TCs during heating when current was applied i.e. during a quench but changing with the same polarity as the other TCs when the

sample was heated or cooled but no current was applied. Attempts to mitigate this effect were trialled by, for example, taking this zero-current data and using it to help separate the with-current voltage signal into thermoelectric effect and current flow. This showed some promising results but was highly time-consuming and no final method was realised in the scope of this project. If this method were to be developed further, it is recommended that it is applied to all TC signals to see if there is a significant voltage contribution to those too as, although they all changed in a way which correlated with changes in temperature, it is possible that there was some additional voltage signal which is adding error to the interpolated temperatures.

Assuming that all TCs apart from TC9 gave temperature readings within a reasonable error margin, the measured TC and interpolated ρ_{Cu} profiles could still be used e.g. by assuming the temperature at point 9 was either: the same as the temperature at point 8; the same as the nominal temperature; or interpolated from the difference between the the temperature at point 8 and the nominal temperature as these would be, in effect, the neighbouring points of measurement.

Here we reach the second conundrum which must be dealt with to make use of this data for more accurate R_C calculations, namely that the ρ_{Cu} profile available is that of discrete points rather than a continuous curve. There are two possible paths to tread:

1. Use only discrete point data for the R_C calculation from the point of calculating the $I_{Cu}(x)$ profile (equation 4.11), thus losing the subtlety that gives this method its strength.

2. A continuous function interpolation of the ρ_{Cu} profile is made and used in the calculations, e.g. via the same SLM spline method used to interpolate the continuous $V_{Cu}(x)$ function, thus introducing error.

The second option appears at first to be the most promising and a first recommendation would be to adapt the MATLAB® code to trial this and compare results to see if the introduced error is acceptable. However, some thought must also be given to the nature of ρ_{Cu} as a function of position along tape length, the variable against which V_{Cu} is differentiated. Equations 4.12 to 4.16 would become:

$$E_{Cu}(x) = \rho(T[x]) \times J_{Cu}(x), \tag{5.1}$$

$$I_{Cu}(x) = A_{Cu} \times J_{Cu}(x) = A_{Cu} \times \frac{E_{Cu}(x)}{\rho_{Cu}(T[x])} = A_{Cu} \times \frac{1}{\rho_{Cu}(T[x])} \times -\frac{dV_{Cu}(x)}{dx}, \quad (5.2)$$

$$\frac{d\sigma_{Cu}(x)}{dx} = \frac{A_{Cu}}{w_{Cu}} \times \frac{d}{dx}(\frac{1}{\rho_{Cu}(T[x])}) \times -\frac{d^2V_{Cu}}{dx^2} = t_{Cu} \times \frac{d}{dx}(\frac{1}{\rho_{Cu}(T[x])}) \times -\frac{d^2V_{Cu}}{dx^2} \quad (5.3)$$

where all terms are as defined previously. Interpreting the term $\frac{d}{dx}(\frac{1}{\rho_{Cu}(T[x])})$ requires further investigation.

It is also suggested that further investigation is carried out into the effects of twisting the strands on I_c distribution, current sharing and contact resistance. To this end a prototype twisted adjustable clamp sample holder has been designed and a rapid prototype model 3D printed to verify the design. The final clamp pieces would be able to hold 200 mm-long samples in a single- or half-sandwich configuration in a 90° turn with the twist pitch of 0.4 m used in the CERN cable design.

6

Conclusions

As part of the HiLumi upgrade project, designing the CERN HL-LHC, CERN have designed a novel, 150m-long, superconducting power transmission cable consisting of superconducting MgB_2 tapes sandwiched between copper tapes to form a strand; with two strands (electrically insulated from each other by Kapton wrapping) twisted together to form a twisted-pair. Unlike other superconducting power transmission cables, the CERN design is both DC feeding individual magnet circuits (as opposed to being built into existing 3-phase AC infrastructure) and gas-cooled, due to the large volume of cold helium gas available in the LHC, rather than liquid- or conduction-cooled. A 5 m-long cable consisting of 23 current-carrying twisted-pairs has been tested at the University of Southampton. The work for this PhD centred around the tests carried out on this cable for CERN and subsequent investigations into the mechanisms behind the phenomena discovered and in explaining the behaviour of the cable.

The following tests were carried out during the project:

- **Cable specification tests** — The cable design was tested within the given working specification of 600 A at 25 K and it has been shown that this is well within the capabilities of the cable.

- **Thermal stability tests** — By attaching resistance heaters to individual strands within the test cable it was possible to apply point-like heat deposition and simulate point disturbances such as that which the cable may experience when in use. Properties such as minimum quench energy (MQE) and resistive zone propagation velocity (v_p) have been measured under a number of conditions by varying

operating temperature, current applied and contact resistance between MgB_2 and copper tapes within the strand. It has been shown that the addition of the copper tapes increases the MQE, meaning that the cable is more robust than it would be without the additional copper and able to withstand greater disturbances before the phenomenon known as 'quench' or thermal runaway (a positive feedback loop which leads to exponential heating and potentially irrecoverable system damage) occurs. However, this comes at the cost of reduced v_p so that, should a sufficient disturbance occur and the cable quench, the heated zone remains localised and an undesirably steep temperature gradient is produced. Furthermore, the voltage read across the heated strand at this time remains low as only small portions of the strand have started the transition from the superconducting state (where no voltage is measured) to the resistive state. Since the majority of quench detection systems currently rely on voltage measurement, and given the large signal noise expected due to the size of the cable, an increase in voltage measured during a quench is desirable. Early estimations of functions describing the variation of MQE and v_p with operating temperature, applied current and tape contact resistance have been made.

- **Contact resistance and current transfer tests** — A small-scale test rig was designed and built to look closely at the transfer of current between the MgB_2 and copper layers within a flat (un-twisted) sandwich under various conditions; and to ascertain whether or not contact resistance, and important property in determining cable stability in a design such as that described above, could be measured on a cable sample *in situ*. With this small-scale rig it was possible to adjust the contact resistance between the layers with more accuracy than simply changing from finite to effectively infinite contact resistance (by separating the MgB_2 and copper tapes) as was the case in the large-scale tests described above. A new contact resistance measurement method was devised, validated and proved robust, with measurements carried out over a range of temperatures from 33 K through to 40 K, using snapshots in time of various points in quench development and under two different contact scenarios. A greater understanding of the current transfer process was also gleaned and important mechanisms driving current transfer investigated.

Using the data generated during the large-scale cable tests and examining the governing equations, progress has begun in finding a greater understanding of the mechanisms driving quench propagation in this cable configuration. Our evidence from the small-scale tests suggests that the mechanisms driving current transfer are:

- Local contact between SC and stabilising tapes, and,
- Local I_c.

Both of these may be inhomogeneous along the sample length. Contact homogeneity depends on the clamps and clamping process. Local I_c inhomogeneities make exist due to:

- The manufacturing process,
- The twisting process,
- Temporary I_c degradation due to stresses caused by clamping,
- Local temperature differences due to inhomogeneities in heating and cooling.

Contact resistance appears to have a linear relationship with current sharing as in the higher the contact resistance the less current is shared in that region; whereas the relationship with local I_c inhomogeneities is more complex. There still remain questions as to the exact nature of the effects of changing contact resistance on the I_{quench} of the sample and therefore its effect on detectability of quench and robustness of cable design. However, it has been shown that even in the 'worse' contact or lower contact pressure scenarios, the copper stabiliser tapes are still carrying excess current in reaction to a disturbance and therefore making the cable design more robust to disturbances; it is therefore feasible to suggest that contact between superconducting and stabilising layers could be optimised for quench detectability without compromising robustness of design.

These results have paved the way towards an analysis of the optimisation of the cable design. As well as optimising for both thermal stability (or resistance to quench) and detectability of quench, it is also anticipated that the minimum number of voltage taps required to successfully be able to detect quench anywhere along the cable length could be found. This is important in the CERN HL-LHC Point 7 links cable operation

given that there will be 48 strands each 150 m long requiring constant detection; and equally valid in future power transmission projects where cables may be more accessible but they would likely be much longer.

The following areas have been highlighted as potential sources of future work outside the scope of this project:

- **Refinement of contact resistance calculation method** — To account for: ρ_{Cu} changing with temperature; additional superconducting and stabilising layers; and current injection into multiple tapes.
- **Critical current degradation and small-scale twisted-pair tests** — In order to further investigate the effect of the mechanical twisting process on I_c degradation a set of prototype twisted clamps have been designed and a rapid prototype 3D printed. Based on the clamp design used in this project (section 4.3.2) the twisted clamps also create a 90° twist in the sample over the same pitch length as that in the cable design.
- **Non-standard quench detection** — Initial investigations have been made into unconventional quench detection methods; rather than measuring the voltage appearance, it may be possible to detect a quench by measuring the accompanying temperature increase. Temperature could be measured by laying optical fibres along the cable length which have promising response times and accuracies at low temperatures.

7

Appendix: MATLAB® Code

MATLAB® code used to calculate contact resistance using SLM as described in section 4.5.2. Note the data files used in each case are .csv files containing three columns of data:

- Position (in cm from end of SC tape),
- Cu tape cumulative voltage data (in volts),
- Measured transfer voltage between SC and Cu tapes.

Function: SLM Filename Knots Plot All

Using SLM function, takes a file name and no. of knots or knot positions, makes multiple plots and stores data in a .txt file. Used for generating data which was analysed.

```
1  %% SLM Filename Knots Plot All
2  % ARGUMENT NOTES
3  % rho_Cu must be in ohm-cm
4  %
5  % Function which takes a filename, number of knots/knot
       positions
6  %       and rho_cu and returns plots and data in .txt files
       for:
7  %       - V_Cu(x) interpolation
8  %       - I_Cu(x) based on this interpolation
9  %       - Rc(x) based on this interpolation
10 % The interpolation applies the specified number of knots to
       the
```

```
%   interpolation prescription.
% Created: 10/11/15
% JCS

%% Function definition

function [] = slmfilenameknotsplotall(filename, noknots,
    rho_cu)
%% Constants and .txt file set-up variables
% Declare sample constants
% NB:- rho_Cu assumed constant here
% rho_cu given (in ohm-cm)
t_cu = 0.02; % cm
w_cu = 0.3; % cm
a_cu = t_cu*w_cu; % cm^2

% Load and unpack data from file
data_packed = importdata(filename);
data_array = data_packed.data;
pos1 = data_array(:, 1);
vcu = data_array(:, 2);
vsccu = data_array(:, 3);

% Get current directory
parentfolder = cd;

% Make new folder for .txt files
foldername = filename(1:(length(filename)-4));
mkdir(foldername);
path(path, foldername);
cd(foldername);

% Create file prefix, data file names from filename and no.
    knots
underscorestr = '_';
noknotsstr = num2str(noknots);
knotsstr = 'knots';
txtsuffix = '.txt';
pos1str = 'pos1-based data';
xevstr = 'xev-based data';

fileprefix = [foldername underscorestr noknotsstr knotsstr
    underscorestr];
```

```
pos1dataname = [fileprefix pos1str txtsuffix];
xevdataname = [fileprefix xevstr txtsuffix];

%% Continuous curve data (x = xev)
% Create and plot interpolation of V_Cu(x) data
slm = slmengine(pos1, vcu, 'plot', 'on', 'knots', noknots, '
    leftslope', 0, 'rightslope', 0);
title('V_{Cu}(x)');
xlabel('Distance from end of SC tape (cm)');
ylabel('Voltage (volts)');
legend('Interpolated curve', 'Knot positions');
xev = linspace(2, 18, 1001);
vcuinterp = slmeval(xev, slm, 0);

% Evaluate first derivative of interpolated function
dvcudx = slmeval(xev, slm, 1);

% Calculate E_Cu(x)
ecux = -dvcudx;

% Calculate J_Cu(x) assuming constant rho_Cu
jcux = ecux/rho_cu;

% Calculate and plot I_Cu(x)
icux = jcux*a_cu;
figure
plot(xev, icux);
title('I_{Cu}(x)');
xlabel('Distance from end of SC tape (cm)');
ylabel('Current (amps)');
grid on;

% Transpose all xev-based variables
xevtrans = transpose(xev);
vcuinterptrans = transpose(vcuinterp);
dvcudxtrans = transpose(dvcudx);
ecuxtrans = transpose(ecux);
jcuxtrans = transpose(jcux);
icuxtrans = transpose(icux);

% Make new .txt file with xev-based variables
xevtable = [xevtrans, vcuinterptrans, dvcudxtrans, ecuxtrans,
    jcuxtrans, icuxtrans];
```

```
save (xevdataname, 'xevtable', '-ascii', '-tabs');

%% Data point data (x = pos1)
% Evaluate second derivative of interpolated function
d2vcudx2 = slmeval(pos1, slm, 2);

% Calculate dSigma_Cu(x)/dx
dsigmadx = -d2vcudx2*t_cu/rho_cu;

% Calculate and plot Rc(x)
rc = vsccu./dsigmadx;
figure
plot(pos1, rc, 'o');
title('R_C(x)');
xlabel('Distance from end of SC tape (cm)');
ylabel('Contact resistance (ohm-cm^2)');
grid on;

% Make new .txt file with pos1-based variables
pos1table = [pos1, vcu, vsccu, d2vcudx2, dsigmadx, rc];
save (pos1dataname, 'pos1table', '-ascii', '-tabs');

%% Return to parent folder
cd(parentfolder)
end
```

Function: SLM Compare R_C Knot Range

Using SLM function, plots R_C values for a knots in a given range e.g. 3-9 knots. Used when ascertaining best knot numbers and positions. Limited to creating a range of evenly spaced knots.

```
%% SLM Compare Rc Knot Range
% ARGUMENT NOTES
% rho_Cu must be in ohm-cm
% pos1table cols:
%   Position; V_Cu(x); V_SC-Cu(x); d2V_Cu(x)/dx; dSigma_Cu(x)/
    dx; Rc(x)
% xevtable cols:
%   Position; V_Cu(x); dV_Cu(x)/dx; E_Cu(x); J_Cu(x); I_Cu(x)
%
```

```
% Function which takes a filename and a range of knot numbers and for each
%  knot number uses function 'slmfilenameknotsrc' to:
%      - return data in .txt files for:
%          - V_Cu(x) interpolation
%          - I_Cu(x) based on this interpolation
%          - Rc(x) based on this interpolation.
%      - plot Rc(x) on a comparison plot.
% Created: 11/11/15
% JCS

%% Function definition

function [] = slmcomparercknotrange(filename, knotrange, rho_cu)
    legendarray = [];
    for i = 1:length(knotrange)
        knotno = knotrange(i);
        legendlabel = slmfilenameknotsrc(filename, knotno, rho_cu);
        legendarray = [legendarray; legendlabel];
        legend(legendarray);
    end
end
```

Function: SLM Filename Knots R_C

Using SLM function, takes a file name and no. of knots or knot positions, plots $R_C(x)$ only and holds 'on' so that when looped (e.g. in 'slmcomparercknotrange.m') generates a comparison plot, and stores all data in a .txt file.

```
%% SLM Filename Knots Rc
% ARGUMENT NOTES
% rho_Cu must be in ohm-cm
% po1table cols:
%   Position; V_Cu(x); V_SC-Cu(x); d2V_Cu(x)/dx; dSigma_Cu(x)/dx; Rc(x)
% xevtable cols:
%   Position; V_Cu(x); dV_Cu(x)/dx; E_Cu(x); J_Cu(x); I_Cu(x)
%
% Function which takes a filename, number of knots and a rho_Cu value and
```

```
%   returns data in .txt files for:
%       - V_Cu(x) interpolation
%       - I_Cu(x) based on this interpolation
%       - Rc(x) based on this interpolation.
% Plots Rc(x) only and holds 'on' so that when looped generates a
%   comparison plot.
% The interpolation applies the specified number of knots to the
%   interpolation prescription.
%
% NB:- Future Adaptation: take temperature interpolate rho_Cu from data!
% Created: 11/11/15
% JCS

%% Function definition

function [legendlabel] = slmfilenameknotsrc(filename, noknots, rho_cu)
% Declare sample constants
% NB:- rho_Cu assumed constant here
% rho_cu given (in ohm-cm)
t_cu = 0.02; % cm
w_cu = 0.3; % cm
a_cu = t_cu*w_cu; % cm^2

% Load and unpack data from file
data_packed = importdata(filename);
data_array = data_packed.data;
pos1 = data_array(:, 1);
vcu = data_array(:, 2);
vsccu = data_array(:, 3);

% Get current directory
parentfolder = cd;

% Make new folder for .txt files
foldername = filename(1:(length(filename)-4));
mkdir(foldername);
path(path, foldername);
cd(foldername);

```

```
% Create legend label, graph title, file prefix, data file names from
%   filename and no. knots
underscorestr = '_';
spacestr = ' ';
dashstr = '-';
noknotsstr = num2str(noknots);
knotsstr = 'knots';
rcxstr = 'R_C(x)';
txtsuffix = '.txt';
pos1str = 'pos1-based data';
xevstr = 'xev-based data';

legendlabel = [noknotsstr spacestr knotsstr];
titlestr = [rcxstr spacestr dashstr spacestr foldername];
fileprefix = [foldername underscorestr noknotsstr knotsstr underscorestr];
pos1dataname = [fileprefix pos1str txtsuffix];
xevdataname = [fileprefix xevstr txtsuffix];

% Create, calculate and save to .txt files all data necessary to
%   calculate Rc(x), plot Rc(x)
% Create and save to .txt file V_Cu(x) interpolation
slm = slmengine(pos1, vcu, 'plot', 'off', 'knots', noknots, 'leftslope', 0, 'rightslope', 0);

xev = linspace(2, 18, 1001);
vcuinterp = slmeval(xev, slm, 0);
% save xev.txt xev -ascii -tabs;
% save vcuinterp.txt vcuinterp -ascii -tabs;

% Evaluate first derivative of interpolated function
dvcudx = slmeval(xev, slm, 1);
% save dvcudx.txt dvcudx -ascii -tabs;

% Calculate E_Cu(x)
ecux = -dvcudx;
% save ecux.txt ecux -ascii -tabs;

% Calculate J_Cu(x) assuming constant rho_Cu
jcux = ecux/rho_cu;
% save jcux.txt jcux -ascii -tabs;
```

```
88
89  % Calculate I_Cu(x)
90  icux = jcux*a_cu;
91  % save icux.txt icux -ascii -tabs;
92
93  % Create, plot and save to .txt file Rc(x) data
94  % Evaluate second derivative of interpolated function
95  d2vcudx2 = slmeval(pos1, slm, 2);
96  % save d2vcudx2.txt d2vcudx2 -ascii -tabs;
97
98  % Calculate dSigma_Cu(x)/dx
99  dsigmadx = -d2vcudx2*t_cu/rho_cu;
100 % save dsigmadx.txt dsigmadx -ascii -tabs;
101
102 % Calculate Rc(x)
103 rc = vsccu./dsigmadx;
104 % save rc.txt rc -ascii -tabs;
105
106 % Plot Rc(x)
107 markeredgecolors = jet(9);
108 markers = ['x','*','o','s','d','v','^','<','>'];
109
110 plot(pos1, rc, markers(noknots), 'color', markeredgecolors(
      noknots,:), 'MarkerFaceColor', markeredgecolors(noknots,:))
      ;
111 title(titlestr);
112 xlabel('Distance from end of SC tape (cm)');
113 ylabel('Contact resistance (ohm-cm^2)');
114 grid on;
115 hold on;
116
117 % Make new file with pos1-based variables
118 pos1table = [pos1, vcu, vsccu, d2vcudx2, dsigmadx, rc];
119 save (pos1dataname, 'pos1table', '-ascii', '-tabs');
120
121 % Transpose all xev-based variables
122 xevtrans = transpose(xev);
123 vcuinterptrans = transpose(vcuinterp);
124 dvcudxtrans = transpose(dvcudx);
125 ecuxtrans = transpose(ecux);
126 jcuxtrans = transpose(jcux);
127 icuxtrans = transpose(icux);
128
```

```
129 % Make new file with xev-based variables
130 xevtable = [xevtrans, vcuinterptrans, dvcudxtrans, ecuxtrans,
      jcuxtrans, icuxtrans];
131 save (xevdataname, 'xevtable', '-ascii', '-tabs');
132
133 cd(parentfolder)
134 end
```

7. APPENDIX: MATLAB® CODE

References

[1] Y. Yang, E. A. Young, W. O. S. Bailey, C. Beduz, and A. Ballarino. **First Electrical Characterization of Prototype 600 A HTS Twisted-pair Cables at Different Temperatures**. *Physics Procedia*, **36**:1337–1342, 2012. x, xxi, xxiv, 33, 34, 35, 39, 40, 42, 46, 50

[2] Oxford Instruments Cryospares. **GE Low Temperature Varnish**, 2015. xxvi

[3] Lakeshore Cryotronics. **Varnish: VGE-7031**, 2015.

[4] Lakeshore Cryotronics. **Epoxy, Grease & Varnish: Varnish Varnish - VGE-7031 Varnish**. Technical report. pp 147. xxvi

[5] CERN. **LHC Magnet Types**, 2013. xxviii

[6] Martin N. Wilson. *Superconducting Magnets*. Oxford Science Publications, 1983. xxi, xxix, 13, 65, 67

[7] H Kamerlingh Onnes. **The liquefaction of helium**. *Koninklijke Nederlandse Akademie van Wetenschappen Proceedings Series B Physical Sciences*, **11**:168–185, 1908. 1

[8] Nobelprize.org. **The Nobel Prize in Physics 1913**, 2015. 1

[9] Dirk van Delft and Peter Kes. **The discovery of superconductivity**. *Physics Today*, **63**(9):38–43, 2010. 2

[10] H Kamerlingh Onnes. **The superconductivity of mercury**. *Comm. Phys. Lab. Univ. Leiden*, **13-14**:122–124, 1911. ix, 2, 4

[11] H Kamerlingh Onnes. **Further experiments with liquid helium. D. On the change of electric resistance of pure metals at very low temperatures, etc.** *Comm. Phys. Lab. Univ. Leiden*, **133d**, 1913. 2

[12] Anaïs Vernède. **Centenary of the discovery of superconductivity**. *CERN Bulletin*, (15-16), 11 April 2011 2011. ix, 2

[13] Pradeep Haldar and Abetti Pier. **Superconductivity's First Century**. *IEEE Spectrum*, 28 Feb 2011 2011. 3

[14] CERN. **Taking a Closer Look at the LHC - Superconductivity in Short**, 2014. 5

REFERENCES

[15] Lyndon Evans. *The Large Hadron Collider: A Marvel of Technology*. CRC Press, 2009. 5

[16] Walther Meissner and Robert Ochsenfeld. **Ein neuer effekt bei eintritt der supraleitfähigkeit**. *Naturwissenschaften*, **21**(44):787–788, 1933. 4, 6

[17] Andrey Geim. **Everyone's magnetism**. *Physics Today*, **51**(9):36–39, 1998. ix, 6, 7

[18] Fritz London and Heinz London. **The electromagnetic equations of the supraconductor**. In *Proceedings of the Royal Society of London A: Mathematical, Physical and Engineering Sciences*, **149**, pages 71–88. The Royal Society, 1935. 9

[19] Emanuel Maxwell. **Isotope Effect in the Superconductivity of Mercury**. *Physical Review*, **78**(4):477–477, 1950. PR. 9

[20] C. A. Reynolds, B. Serin, and L. B. Nesbitt. **The Isotope Effect in Superconductivity. I. Mercury**. *Physical Review*, **84**(4):691–694, 1951. PR. 9

[21] James William Rohlf. *Modern Physics from α to Z^0*. 1994. Image used is representation of printed image taken from in Hyperphysics website (URL given). ix, 10

[22] J. Bardeen, L. N. Cooper, and J. R. Schrieffer. **Theory of Superconductivity**. *Physical Review*, **108**(5):1175–1204, 1957. PR. 10

[23] Lev Petrovich Gorkov. **Microscopic derivation of the Ginzburg-Landau equations in the theory of superconductivity**. *Sov. Phys. JETP*, **9**(6):1364–1367, 1959. 10

[24] J. G. Bednorz and K. A. Müller. **Possible high Tc superconductivity in the Ba-La-Cu-O system**. *Zeitschrift für Physik B Condensed Matter*, **64**(2):189–193, 1986. 10

[25] M. Wu, J. Ashburn, C. Torng, P. Hor, R. Meng, L. Gao, Z. Huang, Y. Wang, and C. Chu. **Superconductivity at 93 K in a new mixed-phase Y-Ba-Cu-O compound system at ambient pressure**. *Physical Review Letters*, **58**(9):908–910, 1987. 11

[26] S. Connor. **Why the world is running out of helium**, August 2012. 11, 20

[27] Airbus Group. **E-Thrust**, 2014. ix, 16

[28] Nigel Fox. **Power Transmission Losses Data**. Personal Correspondance (Email), June 2012. Project Manager, ControlConnect, UK Transmission, National Grid. 15

[29] National Grid plc. **2011 National Electricity Transmission System (NETS) Seven Year Statement**, May 2011. 17

[30] Sohn Associates Ltd. **Electricity Distribution Systems Losses - Non-Technical Overview**. Report, Offgem, 2009. 17

[31] Jason Palmer. **Superconductors got hot 25 years ago**, 2011. 17

[32] P C Michael, L Bromberg, A J Dietz, K J Cragin, and C Gold. **Design and Test of a Prototype 20 kA HTS DC Power Transmission Cable**. *Applied Superconductivity, IEEE Transactions on*, **25**(3):1–5, 2015. 17

[33] A. Kalam, H. Al-Khalidi, and D. Willen. **HTS cable and its anticipated effects on power transmission networks**. In *AC and DC Power Transmission, 2006. ACDC 2006. The 8th IEE International Conference on*, pages 50–53, 2006. 17

[34] A. Sierra, A. Prez, J. L. Nieto, A. Gonzalez, M. Maya, and F. Ortiz. **Superconducting transmission 23kV/2kA cable - first in Latin America**. *Revista Mexicana de Fisica*, **49**(6):489–492, 2003. 17

[35] S. Fleshler, D. Buczek, B. Carter, P. Cedrone, K. DeMoranville, J. Gannon, J. Inch, X. Li, J. Lynch, A. Otto, E. Podtburg, D. Roy, M. Rupich, S. Sathyamurthy, J. Schreiber, C. Thieme, E. Thompson, D. Tucker, K. Nagashima, and M. Ogata. **Scale-up of 2G wire manufacturing at American Superconductor Corporation**. *Physica C: Superconductivity*, **469**(1520):1316–1321, 2009. ix, 19

[36] Sumitomo Electric. **Specifications - DI-BSCCO**, 2007. ix, 20

[37] Jun Nagamatsu, Norimasa Nakagawa, Takahiro Muranaka, Yuji Zenitani, and Jun Akimitsu. **Superconductivity at 39 K in magnesium diboride**. *Nature*, **410**(6824):63–64, 2001. 10.1038/35065039. 20

[38] Chauncey Starr. **The Hydrogen-Electric Energy Supergrid (White Paper)**. Report, EPRI, 2006. 20, 24

[39] K. Vinod. *Studies on development of MgB2 superconductor with improved in-field critical current density*. PhD thesis, Cochin University of Science and Technology (CUSAT), 2010. 20

[40] Paul M. Grant. **Potential Electric Power Applications for Magnesium Diboride**. Technical report, Electric Power Research Institute (EPRI), 2001. 20

[41] A. Ballarino. **Design of an MgB2 feeder system to connect groups of superconducting magnets to remote power converters**. *Journal of Physics: Conference Series*, **234**(3):032003, 2010. x, 20, 27, 33

[42] Columbus Superconductors. **For Superconducting Magnets**, 2011. ix, 21

[43] A. Ballarino, K. H. Mess, and T. Taylor. **Extending the Use of HTS to Feeders in Superconducting Magnet Systems**. *IEEE Transactions on Applied Superconductivity*, **18**(2):1455–1458, 2008. x, 22, 32

[44] Yifeng Yang, E. A. Young, W. O. S. Bailey, C. Beduz, T. Taylor, and A. Ballarino. **Critical Current and Stability of MgB2 Twisted-Pair DC Cable Assembly Cooled by Helium Gas**. *IEEE Transactions on Applied Superconductivity*, **23**(3):4801204–4801204, 2013. x, 22, 26, 39, 41, 43

[45] V. Baglin, A. Ballarino, F. Cerutti, R. Denz, P. Fessia, K. Foraz, M. Fuerstner, W. Herr, M. Karppinen, N. Kos, H. Mainaud-Durand, A. Mereghetti, Y. Muttoni, D. Nisbet, R. Ostojic, H. Prin, J-P. Tock, R. van Weelderen, E. Wildner, and L. Williams. **Conceptual Design of the LHC Interaction Region Upgrade Phase-I**. Report, CERN, 2008. 22, 26, 28

REFERENCES

[46] A. Anghel, B. Jakob, G. Pasztor, R. Wesche, A. M. Fuchs, G. Vecsey, H. Bieri, H. Bauman, and F. X. Hansen. *Design, construction and operation of a neon refrigeration system for a HTS power transmission cable.* Plenum, New York, NY, ETATS-UNIS, 2000. Advances in Cryogenic Engineering v.45 p.1419 (photocopied from library). 22

[47] Sastry Pamidi, Chul Han Kim, Jae-Ho Kim, Danny Crook, and Steinar Dale. **Cryogenic helium gas circulation system for advanced characterization of superconducting cables and other devices**. *Cryogenics*, **52**(46):315–320, 2012. 23

[48] H. Rodrigo, F. Salmhofer, D. S. Kwag, S. Pamidi, L. Graber, D. G. Crook, S. L. Ranner, S. J. Dale, and D. Knoll. **Electrical and thermal characterization of a novel high pressure gas cooled DC power cable**. *Cryogenics*, **52**(46):310–314, 2012. 23

[49] J. F. Maguire, J. Yuan, W. Romanosky, F. Schmidt, R. Soika, S. Bratt, F. Durand, C. King, J. McNamara, and T. E. Welsh. **Progress and Status of a 2G HTS Power Cable to Be Installed in the Long Island Power Authority (LIPA) Grid**. *IEEE Transactions on Applied Superconductivity*, **21**(3):961–966, 2011. 23

[50] Craid Dyke. **Conversation with Energy, Strategy & Policy, Market Operation, The National Grid**. Personal Correspondance (Telephone), November 2012. 23

[51] Roddy Wilson. **Conversation with System Planning, SHETL, SSE**. Personal Correspondance (Telephone), October 2012. 24

[52] Jon Berry. **Conversation with Innovation and Low Carbon Engineer, WPD**. Personal Correspondance (Telephone), November 2012. 24

[53] Paul M. Grant. **Cryo-delivery Systems for the Co-transmission of Chemical and Electrical Power**. *AIP Conference Proceedings*, **823**(1):291–301, 2006. 24

[54] P. M. Grant. **The supercable: dual delivery of hydrogen and electric power**. In *Power Systems Conference and Exposition, 2004. IEEE PES*, pages 1745–1749 vol.3, 2004. 24

[55] S. Yamada, Y. Hishinuma, T. Uede, K. Schippl, N. Yanagi, T. Mito, and M. Sato. **Conceptual design of 1 GW class hybrid energy transfer line of hydrogen and electricity**. *Journal of Physics: Conference Series*, **234**(3):032064, 2010. 25

[56] Pasquale Balena, Giovanna Mangialardi, and Carmelo Torre. *A BEP Analysis of Energy Supply for Sustainable Urban Microgrids Computational Science and Its Applications at ICCSA 2012*, **7334** of *Lecture Notes in Computer Science*, pages 116–127. Springer Berlin / Heidelberg, 2012. 25

[57] M. G. Molina and P. E. Mercado. **Power Flow Stabilization and Control of Microgrid with Wind Generation by Superconducting Magnetic Energy Storage**. *Power Electronics, IEEE Transactions on*, **26**(3):910–922, 2011. 25

[58] U. A. Khan, W. J. Shin, J. K. Seong, S. H. Oh, S. H. Lee, and B. W. Lee. **Feasibility analysis of the application and positioning of DC HTS FCL in a DC microgrid through modeling and simulation using Simulink and SimPowerSystem**. *Physica C: Superconductivity*, **471**(21-22):1322–1326, 2011. 25

[59] Poonum Agrawal. **Overview of DOE Microgrid Activities**. Report, Office of Electricity Delivery and Energy Reliability, Montreal Symposium on Microgrids, 2006. 25

[60] A. Ballarino. **Application of High Temperature Superconductors to Accelerators**. Report, CERN, 2000. 26

[61] A. Ballarino. **HTS in the LHC & in the LHC Upgrades**. Report, CERN, 2006. 26

[62] A. Ballarino, K. Hubert Mess, and T. Taylor. **Extending the application of HTS in particle accelerators**. *Journal of Physics: Conference Series*, **97**(1):012288, 2008. 26

[63] A. Ballarino, A. N. Bruchanov, V.S. Kruglov, S. T. Latushkin, A. N. Lubinov, A. I. Ryazanov, S. V. Shavkin, T. M. Taylor, and P. V. Volkov. **Effect of fast neurtron irradiation on current transport properties of HTS materials**, 2003. 26

[64] W. Scandale and F. Zimmermann. **LHC Phase-2 Upgrade Scenarios**. Report, CERN, 2008. 26, 35

[65] A. Ballarino. **Superconducting Links for the LHC machine**. Report, CERN, 2013. ix, 29

[66] F.W. Grover. *Inductance Calculations: Working Formulas and Tables*. Dover Publications, 2004. 30

[67] A. Ballarino, J. Fleiter, J. Hurte, M. Sitko, and G. Willering. **First Tests of Twisted-Pair HTS 1 kA Range Cables for Use in Superconducting Links**. *Physics Procedia*, **36**(0):855–858, 2012. xxi, 30, 31, 33, 34, 39

[68] A. Ballarino. **Alternative Design Concepts for Multi-Circuit HTS Link Systems**. *IEEE Transactions on Applied Superconductivity*, **21**(3):980–983, 2011. 31, 37

[69] J.P. Todd and H.B. Ellis. *Applied heat transfer*. Harper & Row, 1982. 43

[70] Minyi Fu, Xiaofeng Xu, Zhengkuan Jiao, H. Kumakura, K. Togano, Liren Ding, Futang Wang, and Jinglin Chen. **Minimum quench energy and normal zone propagation velocity in MgB_2 superconducting tape**. *Physica C: Superconductivity*, **402**(3):234–238, 2004. 63, 67

[71] E. Martínez, F. Lera, M. Martínez-López, Y. Yang, S. I. Schlachter, P. Lezza, and P. Kováč. **Quench development and propagation in metal/MgB_2 conductors**. *Superconductor Science and Technology*, **19**(1):143, 2006.

[72] U. Gambardella, A. Saggese, P. Sessa, A. Guarino, S. Pace, G. Masullo, A. Matrone, E. Petrillo, and R. Quarantiello. **Stability Measurements in Multifilamentary MgB_2 Tapes**. *IEEE Transactions on Applied Superconductivity*, **17**(2):2937–2940, 2007.

[73] E. Martínez, O. Munoz, L. A. Angurel, Yang Yifeng, and S. I. Schlachter. **Analysis of the Quench Onset and Propagation in MgB_2 Conductors**. *IEEE Transactions on Applied Superconductivity*, **19**(3):3533–3536, 2009. 65

[74] P. Kováč, E. Martínez, T. Melišek, L. Kopera, and I. Hušek. **Stability of multi-core MgB_2/Ti/Cu/SS wires**. *Cryogenics*, **51**(1):16–20, 2011. 63, 65, 67

[75] Jorge Pelegrín Mosquera. *Study of thermal stability processes in MgB_2 and REBCO wires and tapes*. Thesis, Universidad de Zaragoza, 2013. 65

[76] Y. Yang. **Minimum Quench Energy of Power-law Superconductors/Magnets**. Conference prestentation, EUCAS 2013, 2013. 65

[77] V. S. Vysotsky, A. L. Rakhmanov, and Y. Ilyin. *Novel Approaches to Describe Stability and Quench of HTS devices*, chapter 9. Nova Publishers, Superconductivity Research Developments, 2008. 65

[78] R. Holm. *Electric Contacts*. Almqvist & Wiksells akademiska handböcker. H. Geber, 1946. xii, 77, 79, 80

[79] S. Timsit. **Electrical contact resistance: properties of stationary interfaces**. In *Electrical Contacts, 1998. Proceedings of the Forty-Fourth IEEE Holm Conference on*, pages 1–19, 1998. 77, 79

[80] R. S. Timisit. **ELECTRICAL CONTACT RESISTANCE: REVIEW OF ELEMENTARY CONCEPTS**, 2007. xii, 78

[81] A. Nijhuis, Yu Ilyin, W. Abbas, and H. H. J. ten Kate. **Evolution of contact resistance and coupling loss in prototype ITER PF NbTi conductors under transverse cyclic load**. *Applied Superconductivity, IEEE Transactions on*, **13**(2):2388–2391, 2003. 79

[82] Oh Dong Keun, Oh Sangjun, Kim Hyoung Chan, Choi Heekyung, Lee Chulhee, Park Wonwoo, and Kim Keeman. **Transverse Load Versus Mechanical Characteristics and Inter-Strand Resistances in the Cable of the "Option 2" Specification for ITER TF Conductor**. *Applied Superconductivity, IEEE Transactions on*, **20**(3):495–498, 2010.

[83] E. P. A. van Lanen, L. Feng, R. P. P. van Meerdervoort, W. A. J. Wessel, and A. Nijhuis. **Interstrand Resistance Measurements on the Conductor Terminations of TF-PRO2 and JATF3 SULTAN Samples**. *Applied Superconductivity, IEEE Transactions on*, **20**(3):474–477, 2010.

[84] Mori Nobuyuki, J. Yoshida, T. Maebatake, R. Teranishi, M. Mukaida, K. Yamada, M. Miura, M. Yoshizumi, and T. Izumi. **Effects of uniaxial constant pressures on the joint properties of REBCO coated conductors**. *Journal of Physics: Conference Series*, **234**(2):022023, 2010.

[85] J. Järvelä, A. Stenvall, R. Mikkonen, and M. Rindfleisch. **Contact resistance simulations and measurements of MgB2-MgB2 lap joints**. *Cryogenics*, **51**(7):400–407, 2011. See hard copy. 79

[86] E. Preisler, J. Bayersdorfer, M. Brunner, J. Bock, and S. Elschner. **Electrical contacts on bismuth-based bulk high-temperature superconductors in high-current applications**. *Superconductor Science and Technology*, **7**(6):389, 1994. 79

[87] A. J. Dietz, W. E. Audette, L. Bromberg, J. V. Minervini, and B. K. Fitzpatrick. **Resistance of Demountable Mechanical Lap Joints for a High Temperature Superconducting Cable Connector**. *Applied Superconductivity, IEEE Transactions on*, **18**(2):1171–1174, 2008. 79

[88] A. Stenvall, A. Korpela, J. Lehtonen, and R. Mikkonen. **Current transfer length revisited**. *Superconductor Science and Technology*, **20**(1):92, 2007. 79

[89] K. W. See, X. Xu, J. Horvat, C. D. Cook, and S. X. Dou. **Transport critical current of MgB2 wires: pulsed current of varying rate compared to direct current method**. *Superconductor Science and Technology*, **24**(10):105009, 2011. 79

[90] Bauer Springs. **Product Data Sheet for Products 105578 and 112650 (Belleville Washers)**. Technical report, 2013. Available direct from Bauer Springs - for general info follow URL link. xiii, 89, 90, 91

[91] Copper Development Association Inc. **Cryogenic Properties of Copper: Electrical Resistivity vs. Temperature**, 2015. xiv, 105, 106